



# Electronic and Photoelectronic Processes in Multiferroic Materials

## Dissertation

zur Erlangung des

Doktorgrades der Naturwissenschaften (Dr. rer. nat.)

der Naturwissenschaftlichen Fakultät II - Chemie, Physik und  
Mathematik

der Martin-Luther-Universität Halle - Wittenberg

vorgelegt

von **Herrn Akash Bhatnagar**

geboren am 12.09.1986 in Neu Delhi, Indien

angefertigt am Max-Planck-Institut für Mikrostrukturphysik

in Halle an der Saale

*Gutachter:*

1. Prof. Dietrich Hesse
2. Prof. Kathrin Dörr
3. Prof. Andrei Kholkin

Halle (Saale), Februar 2014

verteidigt am 1. Juli 2014



# Contents

<b>1</b>	<b>Introduction</b>	<b>1</b>
<b>2</b>	<b>Basics</b>	<b>3</b>
2.1	Ferroelectrics and Multiferroics . . . . .	3
2.1.1	Ferroelectrics . . . . .	3
2.1.2	Multiferroics . . . . .	5
2.1.3	Bismuth Ferrite ( $\text{BiFeO}_3$ ) . . . . .	6
2.1.3.1	Structure . . . . .	6
2.1.3.2	Ferroelectricity . . . . .	8
2.1.3.3	Types of domains . . . . .	9
2.1.3.4	Anti-ferromagnetism . . . . .	10
2.2	Photovoltaic Effect . . . . .	10
2.2.1	In Semiconductors . . . . .	11
2.2.2	In Ferroelectrics . . . . .	12
2.3	Trap level assisted conduction . . . . .	15
2.4	Summary . . . . .	17
<b>3</b>	<b>Experimental and characterization methods</b>	<b>19</b>
3.1	Sample synthesis . . . . .	19
3.1.1	Pulsed laser deposition . . . . .	19
3.1.2	Electrode fabrication . . . . .	20
3.2	Scanning probe microscopy - Morphology and domain analysis . . . . .	21
3.2.1	Atomic Force Microscopy . . . . .	22
3.2.2	Piezo Force Microscopy . . . . .	23
3.2.3	PFM study in $\text{BiFeO}_3$ . . . . .	25
3.3	Structural Analysis . . . . .	26
3.3.1	X-ray diffraction . . . . .	26
3.3.1.1	$2\theta - \omega$ scan . . . . .	27
3.3.1.2	Reciprocal space maps . . . . .	28
3.3.2	Transmission electron microscopy . . . . .	29
3.4	Electrical characterization . . . . .	29
3.4.1	Ferroelectric measurements . . . . .	29

3.4.2	Photoelectric measurements . . . . .	30
3.4.3	Trap level spectroscopy . . . . .	31
3.5	Summary . . . . .	34
<b>4</b>	<b>Bulk photovoltaic effect in epitaxial BiFeO<sub>3</sub> films</b>	<b>35</b>
4.1	Growth . . . . .	36
4.1.1	BiFeO <sub>3</sub> films grown on bare substrates . . . . .	36
4.1.2	BiFeO <sub>3</sub> films grown on buffered substrates . . . . .	39
4.2	Structural investigations . . . . .	40
4.2.1	2 $\theta$ - $\omega$ scans . . . . .	40
4.2.2	Reciprocal space map investigations . . . . .	41
4.2.3	TEM investigation . . . . .	44
4.3	PFM studies . . . . .	45
4.4	Ferroelectric characteristics . . . . .	49
4.5	Photoelectric measurements . . . . .	51
4.5.1	Abnormal photovoltaic effect . . . . .	52
4.5.2	Temperature dependent open circuit voltages . . . . .	53
4.5.3	Bulk photovoltaic effect . . . . .	54
4.5.3.1	Two-resistance model . . . . .	56
4.5.3.2	Calculation of photovoltaic response . . . . .	56
4.6	Summary . . . . .	63
<b>5</b>	<b>Persistent photoconductivity in strained BiFeO<sub>3</sub> films</b>	<b>65</b>
5.1	Growth . . . . .	66
5.1.1	BiFeO <sub>3</sub> films on LaAlO <sub>3</sub> substrates . . . . .	66
5.1.2	BiFeO <sub>3</sub> films on (La,Sr)MnO <sub>3</sub> -buffered substrates . . . . .	68
5.2	Structural analysis . . . . .	70
5.2.1	BiFeO <sub>3</sub> films grown on LaAlO <sub>3</sub> substrates . . . . .	70
5.2.1.1	TEM investigations . . . . .	74
5.2.2	BiFeO <sub>3</sub> films on (La <sub>0.7</sub> Sr <sub>0.3</sub> )MnO <sub>3</sub> -buffered substrates . . . . .	76
5.3	PFM studies . . . . .	79
5.4	Ferroelectric characteristics . . . . .	82
5.5	Electronic characterization . . . . .	84
5.5.1	Current-voltage characteristics . . . . .	84
5.5.2	Thermally stimulated current/conductivity . . . . .	87
5.5.3	Spectral distribution . . . . .	92
5.6	Summary . . . . .	96
<b>6</b>	<b>Summary and Outlook</b>	<b>98</b>
	<b>Bibliography</b>	<b>i</b>

## List of Figures

2.1	Schematic of the crystal structure of BaTiO <sub>3</sub> to show ferroelectricity. . .	4
2.2	Hysteretic behavior shown by various ferroic materials under the influence of an external force. . . . .	5
2.3	Phase diagram of the system of Bi <sub>2</sub> O <sub>3</sub> and Fe <sub>2</sub> O <sub>3</sub> . . . . .	6
2.4	Rhombohedral unit cell of BiFeO <sub>3</sub> in the ferroelectric state and accommodation of two perovskite unit cells into one rhombohedral cell. . . . .	7
2.5	Paraelectric state and ferroelectric states in BiFeO <sub>3</sub> . . . . .	8
2.6	Depiction of different polarization directions possible in BiFeO <sub>3</sub> and corresponding structural variants. . . . .	9
2.7	Photovoltaic effect in semiconductors. . . . .	11
2.8	Schematic for bulk photovoltaic effect in ferroelectric materials. . . . .	14
2.9	Schematic for recombination processes. . . . .	16
2.10	Band diagram under equilibrium conditions and the presence of quasi-fermi levels in non-equilibrium conditions. . . . .	17
3.1	Schematic of the pulsed laser deposition technique. . . . .	20
3.2	Schematic of the photo-lithography procedure. . . . .	21
3.3	Schematic of the AFM setup. . . . .	22
3.4	Schematic of the PFM setup. . . . .	24
3.5	PFM study in BiFeO <sub>3</sub> . . . . .	25
3.6	Bragg's diffraction of X-rays and the XRD setup. . . . .	26
3.7	Selection of plane for reciprocal space map. . . . .	28
3.8	Triangular voltage pulse of frequency $f$ applied across the sample to measure the polarization. . . . .	30
3.9	Schematic of the setup used for performing photoelectric measurements. .	31
3.10	Process flow for the steps involved in the TSC technique in terms of temperature and the current behavior. . . . .	32
4.1	Schematic showing charge build-up on either side of the domain wall. . .	35
4.2	Accommodation of four pseudocubic unit cells of BFO in the (110) <sub>o</sub> plane of TSO and transformation of the orthorhombic coordinate system to pseudocubic coordinate system. . . . .	37

4.3	AFM images of annealed TSO and STO substrates alongwith BFO films grown on them. . . . .	38
4.4	AFM image of BFO films grown on LSMO and SRO buffered TSO and STO substrates. . . . .	39
4.5	$2\theta$ - $\omega$ scans obtained for BFO films grown on TSO and STO substrates with or without LSMO and SRO as the buffer layers. . . . .	41
4.6	RSM contours obtained from BFO films grown on TSO substrate. . . . .	42
4.7	RSM contours obtained from BFO films grown on TSO and STO substrate with LSMO and SRO buffer layer, respectively. . . . .	44
4.8	TEM micrographs for BFO film with $109^\circ$ and $71^\circ$ domain walls. . . . .	45
4.9	AFM and PFM images for a BFO film with $109^\circ$ domain walls. . . . .	47
4.10	AFM and PFM images of size for a BFO film with $71^\circ$ domain walls. . . . .	48
4.11	AFM and PFM images for a BFO film with both, $71^\circ$ and $109^\circ$ domain walls. . . . .	49
4.12	Investigation of ferroelectric characteristics by measuring the ferroelectric polarization and switching current. . . . .	50
4.13	Investigation of ferroelectric characteristics by PFM. . . . .	51
4.14	Schematic showing the patterned electrodes on top of a film in PPDW and PLDW geometries with majority $71^\circ$ and $109^\circ$ domain pattern. . . . .	52
4.15	IV characteristics under illumination with monochromatic light of BFO thin films comprising $109^\circ$ and $71^\circ$ periodic stripe domains. . . . .	53
4.16	Temperature-dependent $V_{oc}$ . . . . .	54
4.17	Dark and photo conductivity measured with temperature in PLDW and PPDW geometries. . . . .	55
4.18	Two resistance model. . . . .	57
4.19	Schematic showing measurement of BPV effect. . . . .	58
4.20	Schematic of the measurement geometry for a sample with alternating $71^\circ$ domains parallel to the electrodes (PLDW) along with the lab coordinate system. . . . .	60
4.21	PV current measured and predicted by varying the angle $\theta$ that the light polarization axis makes with the direction of current flow in PLDW geometry and PPDW geometry for a film consisting of $71^\circ$ domains. . . . .	62
5.1	Depiction of the growth of a BFO unit cell on LAO substrate. . . . .	66
5.2	AFM images of LAO substrate and BFO grown on LAO at 5 Hz. . . . .	67
5.3	AFM image of BFO films grown on LAO at 10 Hz. . . . .	68
5.4	AFM image of BFO films grown on LAO with LSMO as the buffer layer. . . . .	69
5.5	$2\theta - \omega$ scans of BFO films grown on LAO substrate. . . . .	71
5.6	RSM contours measured for BFO films grown on LAO substrate. . . . .	72
5.7	Schematic explaining the $M_a/M_b$ and $M_c$ structures. . . . .	73
5.8	AFM image to describe the stripes in morphology of BFO film grown on LAO. . . . .	74
5.9	TEM images and GPA analysis for BFO films grown on LAO. . . . .	75
5.10	$2\theta - \omega$ scans for BFO films grown on LAO with LSMO as the buffer layer. . . . .	77
5.11	RSM contours obtained from BFO films grown on LAO with LSMO as the buffer layer. . . . .	78
5.12	Possible polarization variants in the $M_c$ phase. . . . .	80
5.13	PFM analysis for 20 nm thick BFO film grown on LAO. . . . .	81

---

5.14	PFM analysis for 80 nm thick BFO film grown on LAO. . . . .	82
5.15	Investigation of ferroelectric characteristics by measuring the ferroelectric polarization (blue) and switching current (red) loops at a) room temperature, b) 150 K and c) 120 K. . . . .	83
5.16	Investigation of ferroelectric characteristics by PFM. . . . .	83
5.17	Current-voltage (IV) characteristics with (photo, red) and without (dark, black) illumination for a) 20 nm and b) 80 nm BFO films grown on LAO. . . . .	85
5.18	Persistent photo-conductivity in BFO film grown in LAO. . . . .	86
5.19	TSC measurement, for an 80 nm thick BFO film. . . . .	88
5.20	Arrhenius plot for a TSC measurement and TSC measurement with different heating rates. . . . .	89
5.21	Simulated and measured TSC response for BFO film grown on LAO. . . . .	90
5.22	Comparison of TSC measurements subjected to different intensities and duration of illumination. TSC measurement for a 20 nm thick BFO film. . . . .	92
5.23	Spectral distribution acquired for 80 nm and 20 nm thick films by varying the wavelength. . . . .	93
5.24	Energy band diagrams corresponding to spectral measurements. . . . .	94
5.25	Spectral distribution from the rhombohedral and monoclinic phase of BFO. . . . .	95

## List of abbreviations and nomenclature

### Abbreviations

**AFM** atomic force microscopy

**BFO** bismuth ferrite

**BPV** bulk photovoltaic

**DWs** domain walls

**LAO**  $\text{LaAlO}_3$

**LPFM** lateral PFM

**LSMO**  $\text{LaSr}_{0.3}\text{Mn}_{0.7}\text{O}_3$

**PFM** piezo force microscopy

**PLDW** parallel to domain walls

**PPDW** perpendicular to domain walls

**PV** photovoltaic

**SRO**  $\text{SrRuO}_3$

**STO**  $\text{SrTiO}_3$

**TEM** transmission electron microscopy

**TSO**  $\text{TbScO}_3$

**VPFM** vertical PFM

**XRD** X-ray diffraction



## Nomenclature

**Å** angstrom

$\beta$  bulk photovoltaic coefficient

**cm** centimeters

**°C** degree Celsius

**E<sub>a</sub>** activation energy in electron volts (eV)

*G* Glass coefficient

*I* intensity

**J** current density

**K** Kelvin

**mbar** millibar

**μm** micrometers

**nm** nanometers

$\sigma$  conductivity

**V<sub>oc</sub>** open circuit voltage



Materials which exhibit a co-dependence between their ferroelectric, magnetic and stress control properties are known as multiferroic materials [1]. The revitalized interest in these materials is largely driven by the possibility to control the electrical charges by the application of a magnetic field, and a realignment of the spin orientations under an electrical voltage [2] [3]. Additionally, multiferroic materials might also have the ability to undergo a change or a distortion in their crystal structure due to a variation in polarization or magnetization which makes them a lucrative option for the sensor industry [4]. Another aspect about these materials which has emerged in the recent past, and also has been a subject of numerous studies, is the enhanced conductivity at the domain walls in comparison to the conductivity of the bulk of the material [5] [6] [7].

Bismuth ferrite with the chemical formula  $\text{BiFeO}_3$  (BFO) has risen to be one of the prime candidates to study the interplay between all of the above mentioned properties in multiferroic materials. Even though the multiferroic capabilities of BFO were known in the past from the work of Smolenskii et. al. [8] [9], the true potential of this material was demonstrated only recently after successful fabrication of thin films [10]. Thereafter, studies were directed to enhance the polarization values [11], reduce the leakage current and understand the domain arrangements [12] [13]. From the electronic point of view, theoretical calculations predicted a band gap with values ranging between 1.9 eV [14] to 2.8 eV [15] which lies in or near the visible range of the electromagnetic spectrum and is considerably lower than the band gap values of other ferroelectric materials like  $\text{BaTiO}_3$  [16],  $\text{PbTiO}_3$  [17],  $\text{LiNbO}_3$  [18] or  $\text{Pb}(\text{Zr},\text{Ti})\text{O}_3$  [19].

In the initial works, by utilizing the low band gap of BFO, the photoconductive [20], photovoltaic and switchable-diode like behavior [21] of BFO was investigated. Subsequent studies revealed the possibility of obtaining above band-gap open circuit voltages in BFO films under illumination [22] that is unlike the case of conventional semiconductors where the open circuit voltage is restricted by the band gap of the material. A model was proposed according to which the domain walls, separating the ferroelastic domains, are at the origin of this effect. But the validity of this model has been under deliberation and scrutiny due to some of the results from the measurements that were performed on the microscale [23] [24]. Nevertheless, the generation of a photovoltaic current and a high open circuit voltage in a ferroelectric material under illumination is not new. It has been studied in the past in materials like  $\text{LiNbO}_3$  [25] or  $\text{BaTiO}_3$  [26], where the effect was attributed to a tensorial property of the material and was termed as the bulk

photovoltaic effect (BPV). As a result till now the origin of this effect in BFO films and the role of domains walls, if any, is under speculation and needs to be resolved.

However till now, the majority of studies in BFO, including the photovoltaic effect, have been focused on its inherent room temperature rhombohedral phase. Lately, the “tetragonal-like” phase of BFO, which is stabilized at room temperature under epitaxial compressive strain, has also generated much interest [27] [28]. One of the main attractions of this strained system is the presence of small amounts of a secondary phase which is embedded in the parent “tetragonal-like” phase and the ability to switch between these two phases by electric field. The corresponding boundary between the two phases has been referred to as the *strain driven morphotropic phase boundary* [28]. Besides, the simplified magnetic structure in comparison to the magnetic structure in the rhombohedral phase [29] [30], and the potential to have large polarization values [27] makes this strained system of BFO a lucrative alternative for future spintronic devices. Keeping in perspective the changes in physical and magnetic structure induced by strain, one might also speculate on a variation in the electronic structure.

The objective of this Thesis is to study and explain the electronic and photoelectronic processes in strained and unstrained multiferroic BiFeO<sub>3</sub> thin films along with their ramifications. In chapter 2, entitled Basics, principles of ferroelectric and multiferroic materials will be discussed with special emphasis on BFO. The structure of BFO will be discussed and how it eventually leads to the evolution of various ferroelastic/electric domains. Henceforth the photoelectronic and electronic processes, namely the photovoltaic effect and some trapping phenomenon will be elaborated.

In chapter 3, various techniques and tools will be detailed that have been employed in the present work. The technical protocol for the present Thesis has been to fabricate the samples, perform structural and domain analysis with subsequent ferroelectric and electronic characterizations.

In chapter 4, the bulk photovoltaic effect in epitaxial BFO thin films is described. The topic involves the fabrication of epitaxial single crystalline thin films of BFO in the rhombohedral phase which will be validated by structural analysis. Thereafter, a thorough domain analysis via PFM is presented that is essential to determine the manifestation of different types of ferroelastic domains in the films. Accordingly, the results of electrical and photoelectric measurements are elaborated to decipher the role of the domains and domain walls in the photovoltaic effect in these films.

In chapter 5, the phenomenon of persistent photoconductivity in strained BFO films is introduced. Firstly, the growth of epitaxial BFO films on a largely mismatched substrate is presented. It will be shown by X-ray and TEM analysis how BFO crystallizes in a monoclinic phase under a compressive strain. In the PFM analysis, the complex domain pattern will be resolved and explained. The existence of enhanced and persistent photoconductivity in these films will be explained. Henceforth the results of temperature and wavelength resolved measurements will be presented. Based on these results, the trapping phenomenon which is responsible for the persistent photoconductivity in these films will be revealed.

Finally in chapter 6, all the results will be summarized and an outlook will be presented to compare certain properties of the relaxed (rhombohedral phase) and strained (monoclinic phase) system of BFO films .

## 2.1 Ferroelectrics and Multiferroics

### 2.1.1 Ferroelectrics

A ferroelectric crystal is defined as a crystal which can possess two or more different orientational polarization states in the absence of any electric field. However it should be possible to switch between any of these states by the application of an electric field. These states are identical in structure but are different with respect to the direction of their electric polarization vector [31]. The presence of these states can be attributed to the non-centrosymmetric structure of these materials. Out of the 21 different classes of non-centric crystals known, ferroelectric materials belong to a class of materials which show a piezoelectric effect and have a unique polar direction along which they show a spontaneous polarization [31] [32].

Piezoelectricity can be defined as the linear coupling between the applied mechanical stress ( $X$ ) and the induced electrical polarization ( $P$ ). It can be expressed in the form of the following equation [33]:

$$P_i = d_{ijk}X_{kl} \quad (2.1)$$

where  $P$  is the polarization vector,  $X$  is a second rank tensor for stress and  $d_{ijk}$  is a third rank tensor which comprises the piezoelectric coefficients. Additionally, the converse piezoelectric effect relates the applied electric field ( $E$ ) to the induced strain ( $\epsilon$ ) and can be described as :

$$\epsilon_{ij} = d_{ijk}E_k \quad (2.2)$$

The piezoelectric coefficients remain the same in either of the effects. Since the spontaneous polarization is also temperature dependent, these crystal classes also exhibit a pyroelectric effect. The pyroelectric effect can be expressed as [33]

$$\Delta P_i = p_i \Delta T \quad (2.3)$$

where  $\Delta P_i$  is the change in polarization vector,  $p_i$  is the pyroelectric coefficient and  $\Delta T$  is the change in temperature. Hence forth, ferroelectric materials form a subclass of pyroelectric and piezoelectric materials [31] [32]. In many aspects, ferroelectricity and ferromagnetism are analogous to each other. The hysteresis-like behavior of magnetization under magnetic field is similar to the behavior of polarization under the influence of an

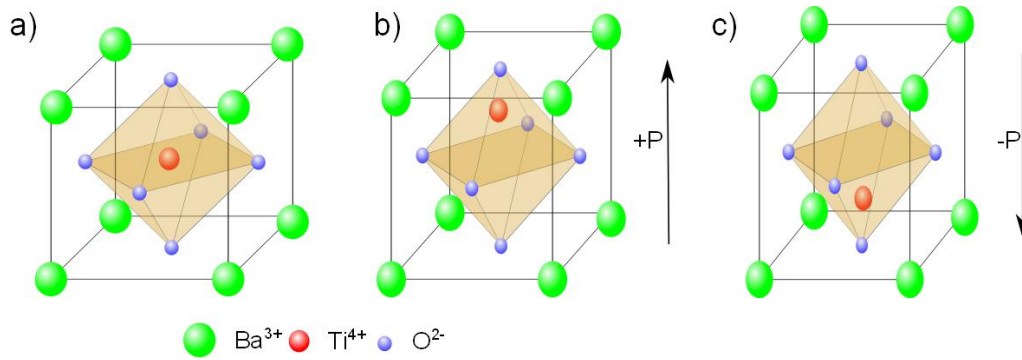


**Figure 2.1:** a) Schematic of the crystal structure of BaTiO<sub>3</sub> above its Curie temperature in its paraelectric state. BaTiO<sub>3</sub> undergoes a phase transition below its Curie temperature to a tetragonal phase which results in, e.g., two possible polarization variants (b) up or (c) down.

applied electric field. Also, like magnetic domains in ferromagnetic materials, ferroelectricity can also be characterized by the presence of domains with different polarizations.

One of the main characteristics of a ferroelectric material is the ability to undergo a phase transition from a high temperature centrosymmetrical phase to a non-centrosymmetric phase below a certain temperature known as the Curie temperature. The most widely studied ferroelectric materials are oxides with perovskite structure which are of the type ABO<sub>3</sub>. A and B are the cations in the structure with oxygen ions forming an octahedral cage which surrounds the cation B. Examples of such materials are BaTiO<sub>3</sub>, PbTiO<sub>3</sub>, BiFeO<sub>3</sub>, LiNbO<sub>3</sub> etc. The mechanism of ferroelectricity may vary in different kinds of these oxide perovskites.

In the case of BaTiO<sub>3</sub>, the material exhibits a centrosymmetric cubic perovskite structure at high temperatures, with the Ti<sup>4+</sup> ion located in the center of the oxygen octahedron as shown in Figure 2.1a. The center of positive charges coincides with the center of negative charges. So, the material at this temperature behaves like an ordinary dielectric which can obtain a polarization under an electric field, but the polarization goes to zero on the removal of the field. This state is known as the paraelectric state. Below the Curie temperature, the material undergoes a phase transition to a tetragonal state. As a result, the Ti<sup>4+</sup> ion shifts away from its central position and is placed, e.g., either in the upper or lower half of the octahedron (Figure 2.1b,c). Additionally there is also a change in the positions of oxygen ions. Due to these new positions, the charge neutrality is destroyed and a dipole is generated which results in a spontaneous polarization. Thus the direction of polarization depends upon the position of the Ti<sup>4+</sup> ions. Regions with same directions of polarizations are known as ferroelectric domains. By the application of an electric field it is possible to switch between the different polarization or ferroelectric states [34] [35].

In the case of PbTiO<sub>3</sub>, the ferroelectric polarization states are also realized due to the displacement of the Ti<sup>4+</sup> ion. However, unlike the case of BaTiO<sub>3</sub>, the role of the A site cation is substantial. The Pb ion has a lone pair of electrons in its outermost 6s shell. This lone pair undergoes hybridization with the 2p electron of the oxygen ion. Theoretically it has been proven that this hybridization stabilizes the tetragonal phase in PbTiO<sub>3</sub> at low temperatures [36] [37].

## 2.1.2 Multiferroics

The term *ferroic* was first introduced to describe all those materials in which one or more vectorial properties can be changed to another orientational state on the application of a force [1]. Moreover, the orientational state should exhibit a hysteretic behavior under the application of external force. The components can be strain ( $\epsilon$ ), spontaneous polarization ( $P_s$ ) or spontaneous magnetization ( $M_s$ ). The forces can be either mechanical stress ( $\sigma$ ), electrical field ( $E$ ) or magnetic field ( $M$ ). For example, in case of ferroelectric materials an electric field can be used to switch between different polarization states, with the polarization possessing hysteresis like behavior under the electric field (Figure 2.2a). Similarly in a ferromagnetic material, switching between different magnetization states can be achieved by the application of a magnetic field (Figure 2.2a). Ferroelastic materials show likewise behavior but with stress and strain. The term *multiferroic* [1] [4] was

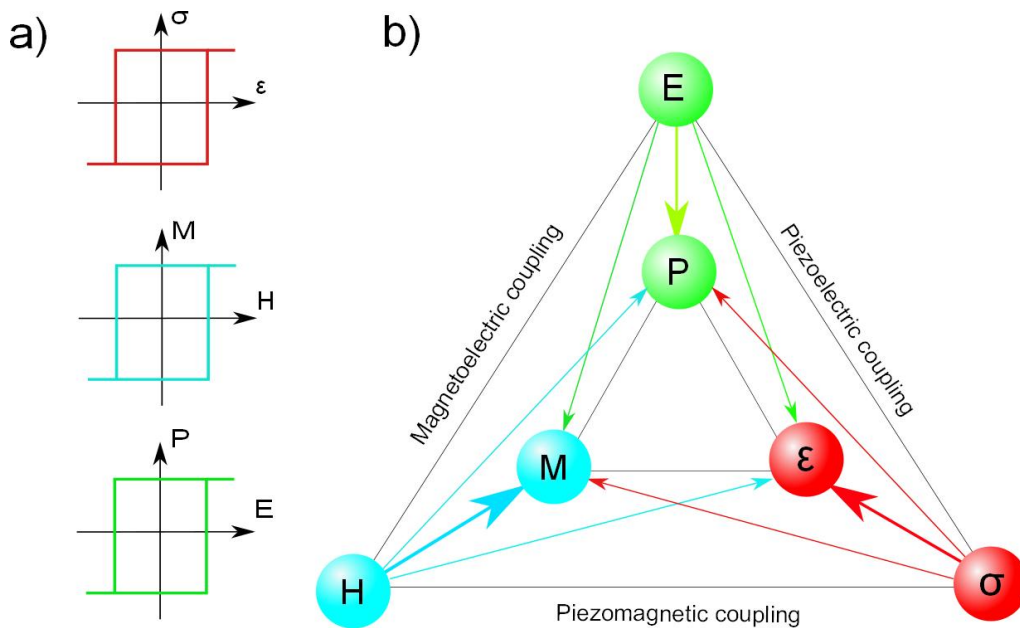


**Figure 2.2:** Hysteretic behavior shown by various ferroic materials under the influence of an external force. a) In ferroelectric materials:  $P_s$  vs  $E$ , in ferromagnetic materials:  $M_s$  vs  $H$  and in ferroelastic materials:  $\sigma$  vs  $\epsilon$ . b) Schematic depicting the variety of couplings possible in a multiferroic material between different ferroic properties [4] [33].

unveiled to characterize those materials which can exhibit two or more of these ferroic properties. A schematic to depict the properties demonstrated by multiferroic materials and their corresponding dependencies is shown in Figure 2.2b (adapted from [4]). In a multiferroic material it is possible to have a coupling between two or more ferroic properties. As can be implied from Figure 2.2b, apart from the usual ferroelectric and ferromagnetic properties, switching of the magnetization is attainable by an electric field. Conversely, the polarization can be switched by a magnetic field. Specifically this coupling, which is termed as magnetoelectric coupling, has been responsible for stirring immense amounts of interest in the field of multiferroic materials.

However, there are only few materials capable of showing such properties in single phase, for example  $\text{BiFeO}_3$ ,  $\text{TbMnO}_3$  and  $\text{TbMn}_2\text{O}_5$ . The main reason behind the scarcity of finding multiferroic materials with high magnetoelectric coupling can be attributed to the *d<sup>0</sup>-ness* [37]: Usually in all the ferroelectric perovskite materials, the B

position cation has no electrons in the d-shell. But for the existence of magnetic moments it is imperative to have the presence of unpaired d-shell electrons. In this perspective  $\text{BiFeO}_3$  has attracted lots of attention because the ferroelectricity is due to the A site cation ( $\text{Bi}^{3+}$ ) and the anti-ferromagnetic nature is due to the B site cation ( $\text{Fe}^{3+}$ ) [37] [14].

### 2.1.3 Bismuth Ferrite ( $\text{BiFeO}_3$ )

As mentioned in section 2.1.2,  $\text{BiFeO}_3$  is one of the few materials which shows multiferroic properties in single phase. It is ferroelectric and antiferromagnetic at room temperature. These properties of  $\text{BiFeO}_3$  can be primarily attributed to its crystal structure. Moreover, the presence of different kinds of ferroelastic domains with corresponding domain walls and the possibility to engineer them makes the material attractive to study the interplay between the ferroic orders.

#### 2.1.3.1 Structure

The phase diagram of  $\text{Bi}_2\text{O}_3$  and  $\text{Fe}_2\text{O}_3$  has been well investigated and studied [38] [39]. From the phase diagram (Figure 2.3) it can be implied that approximately equal parts of  $\text{Bi}_2\text{O}_3$  and  $\text{Fe}_2\text{O}_3$  are required to prepare  $\text{BiFeO}_3$ . However the phase transitions in  $\text{BiFeO}_3$  are rather complicated. The material dissociates above  $960^\circ\text{C}$ . A similar dissoci-

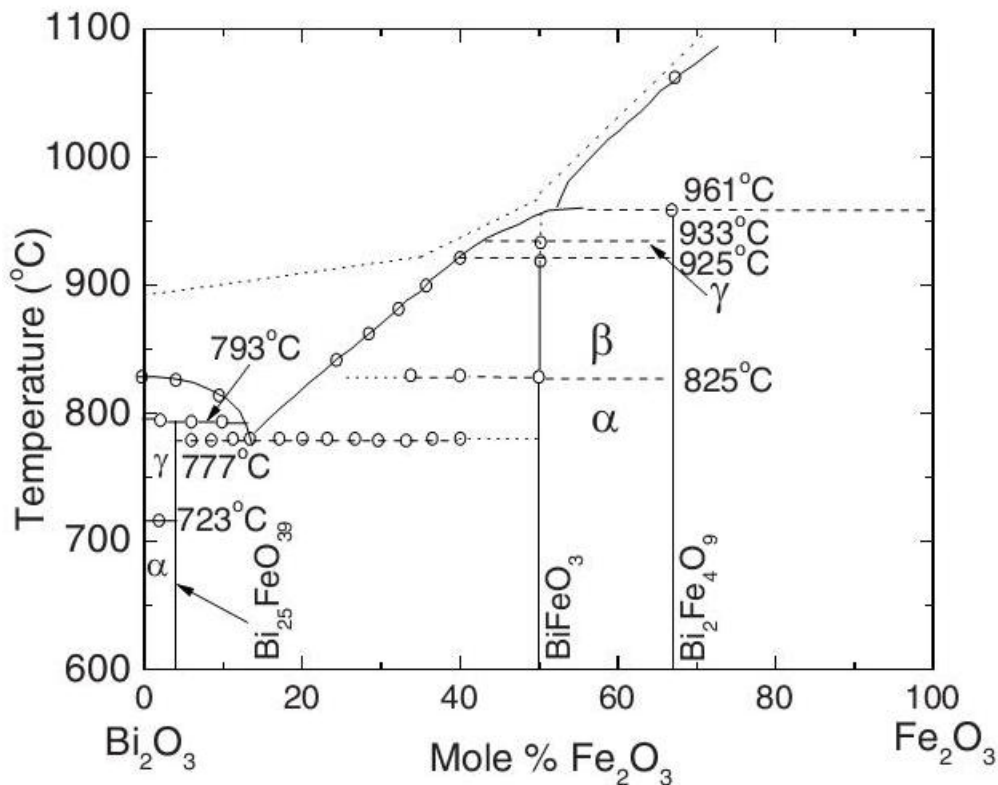


**Figure 2.3:** Phase diagram of the system of  $\text{Bi}_2\text{O}_3$  and  $\text{Fe}_2\text{O}_3$ . Equal proportions of either material result in  $\text{BiFeO}_3$ . The high temperature  $\gamma$  and  $\beta$  phases are paraelectric phases. The Curie temperature is approx.  $825^\circ\text{C}$ . The low temperature  $\alpha$  phase is the ferroelectric phase [39].

ation is observed when  $\text{BiFeO}_3$  is subjected to electric fields in the range of  $200\text{ kV cm}^{-1}$



at room temperature. Below  $960^\circ\text{C}$ , it forms the  $\gamma$  phase which is a cubic and metallic phase. At roughly  $925^\circ\text{C}$  there is a transition to the  $\beta$  phase. The structure of the  $\beta$  phase has been under intensive investigation. It has been argued to be orthorhombic but some reports have also proposed a pseudotetragonal or monoclinic structure. Despite varied results from studies, it has been suggested that the  $\beta$  phase is paraelectric [40]. At  $825^\circ\text{C}$  (Curie temperature) there is the transition which results in the formation of the stable rhombohedral phase. This phase has the point group  $R3c$  and is ferroelectric.

From X-ray analysis, it has been concluded that the unit cell in the rhombohedral phase, of the type shown in Figure 2.4a, is bimolecular when compared to an ideal perovskite structure [41], i.e. the rhombohedral unit cell consists of two  $\text{BiFeO}_3$  perovskite units. This is presented in the schematic shown in Figure 2.4b where two perovskite

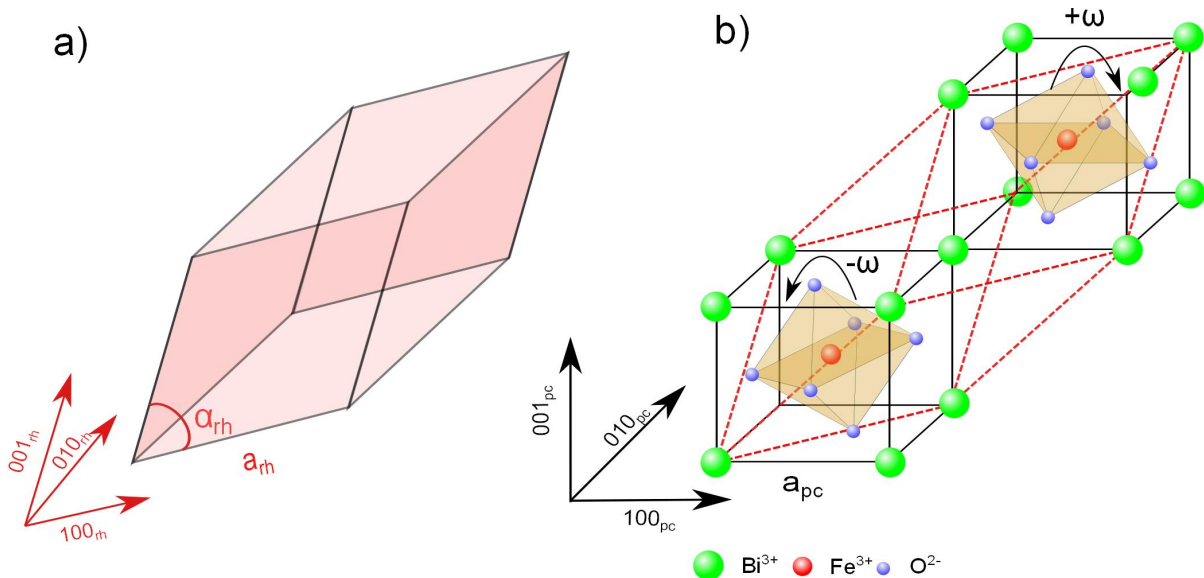


**Figure 2.4:** a) Rhombohedral unit cell of  $\text{BiFeO}_3$  in the ferroelectric  $\alpha$  phase where  $\alpha_{rh}$  is the rhombohedral angle and  $a_{rh}$  is the lattice parameter. b) Accommodation of two perovskite unit cells into one rhombohedral cell (red dotted line). The perovskite cells are connected along their  $[111]$  body diagonal with the oxygen octahedra tilted by an angle of  $\pm\omega$ . The  $a_{pc}$  is the lattice parameter of the pseudocubic structure.

structures are connected along their body diagonal  $[111]$ . The red-dashed line shows the outline of the rhombohedral unit cell. Furthermore, the two oxygen octahedra are rotated by an angle  $+\omega$  and  $-\omega$  around the  $[111]$  direction with  $\omega = 13.8^\circ$  degrees. To compensate for this rotation, the bond distances O-O and Fe-O change and finally the bismuth atom is shifted from its center position. The cubic perovskite unit cell undergoes a slight rhombohedral distortion as result of which the lattice angle changes from the ideal  $90^\circ$  to  $89.45^\circ$  (not shown in Figure 2.4) [42]. Owing to such a comparison with the ideal perovskite structure, the lattice constants for  $\text{BiFeO}_3$  can be expressed in pseudo-cubic (pc) and rhombohedral (rh) notations. The lattice constants  $a_{pc}$  and  $a_{rh}$  have been reported to be  $3.965 \text{ \AA}$  and  $5.6336 \text{ \AA}$ , respectively. The rhombohedral angle  $\alpha_{rh}$  is  $59.348^\circ$  [42] [43].

### 2.1.3.2 Ferroelectricity

The ferroelectricity in  $\text{BiFeO}_3$  has been primarily attributed to the displacement of the  $\text{Bi}^{3+}$  ion along the  $[111]_{pc}$  direction [37] [14], i.e. the ferroelectricity is due to the A-site cation. This is unlike the case of classical perovskite ferroelectrics like  $\text{BaTiO}_3$ ,  $\text{PbTiO}_3$  or  $\text{KNbO}_3$ , where the ferroelectricity is caused due to the B-site cation shift as explained in section 2.1.1.

The valence state configuration of Bi is  $6s^2p^3$ . Therefore the trivalent Bi ion in  $\text{BiFeO}_3$  possesses a lone pair of electrons in the 6s shell. The role of this lone pair at the A-site has also been investigated in  $\text{BiMnO}_3$  and  $\text{PbTiO}_3$  where it has been found to be stereochemically active [36] [44]. In the case of  $\text{BiFeO}_3$ , below the Curie temperature the rhombohedral phase is stabilized due to the hybridization between the lone pair and the  $\text{O}^{2-}$  p orbitals. Due to this hybridization the  $\text{Bi}^{3+}$  ion is driven to the off center position which eventually is responsible for the ferroelectricity [14]. Moreover, x-ray and neutron diffraction studies have shown that along with  $\text{Bi}^{3+}$ , there is also a shift of the  $\text{Fe}^{3+}$  ion. But the displacement of the  $\text{Fe}^{3+}$  ion is approximately four times less than that of  $\text{Bi}^{3+}$  [42].

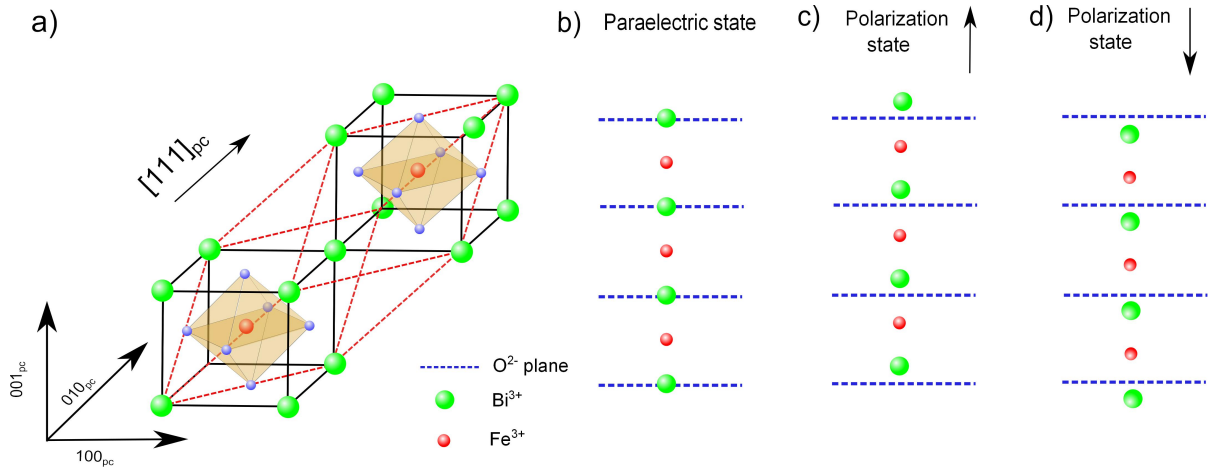


**Figure 2.5:** a) Unit cell of  $\text{BiFeO}_3$ . Cross-section view of the unit cell cut along the  $[111]_{pc}$  direction and the relative positions of different ions in b) paraelectric state and ferroelectric states with polarization directions c) up and d) down.

Figure 2.5a shows the two pseudo cubic unit cells of  $\text{BiFeO}_3$ , connected along their  $[111]$  direction, with the outline of the rhombohedral unit cell. Figures 2.5b-d depict the cross-section views of the unit cells along the  $[111]_{pc}$  direction. In the paraelectric state,  $\text{BiFeO}_3$  has a cubic perovskite cell. As a result, the faces of the oxygen octahedra are parallel to  $\langle 111 \rangle$  planes and the  $\text{Bi}^{3+}$  ion lies in these planes in the cross-section view. The  $\text{Fe}^{3+}$  ion is placed exactly in the middle of two oxygen planes. Below the Curie temperature, due to the hybridization, the  $\text{Bi}^{3+}$  ion tends to move nearer to the oxygen planes. Additionally, the  $\text{Fe}^{3+}$  ion shifts to an off-center position [42]. The movements of these ions (up or down) in reference to the oxygen planes culminate into two polarization states (Figures 2.5c-d). The displacement of the  $\text{Bi}^{3+}$  ion relative to its position in the paraelectric state has been calculated to be  $0.54 \text{ \AA}$  and for the  $\text{Fe}^{3+}$  ion it is  $0.134 \text{ \AA}$  [42].

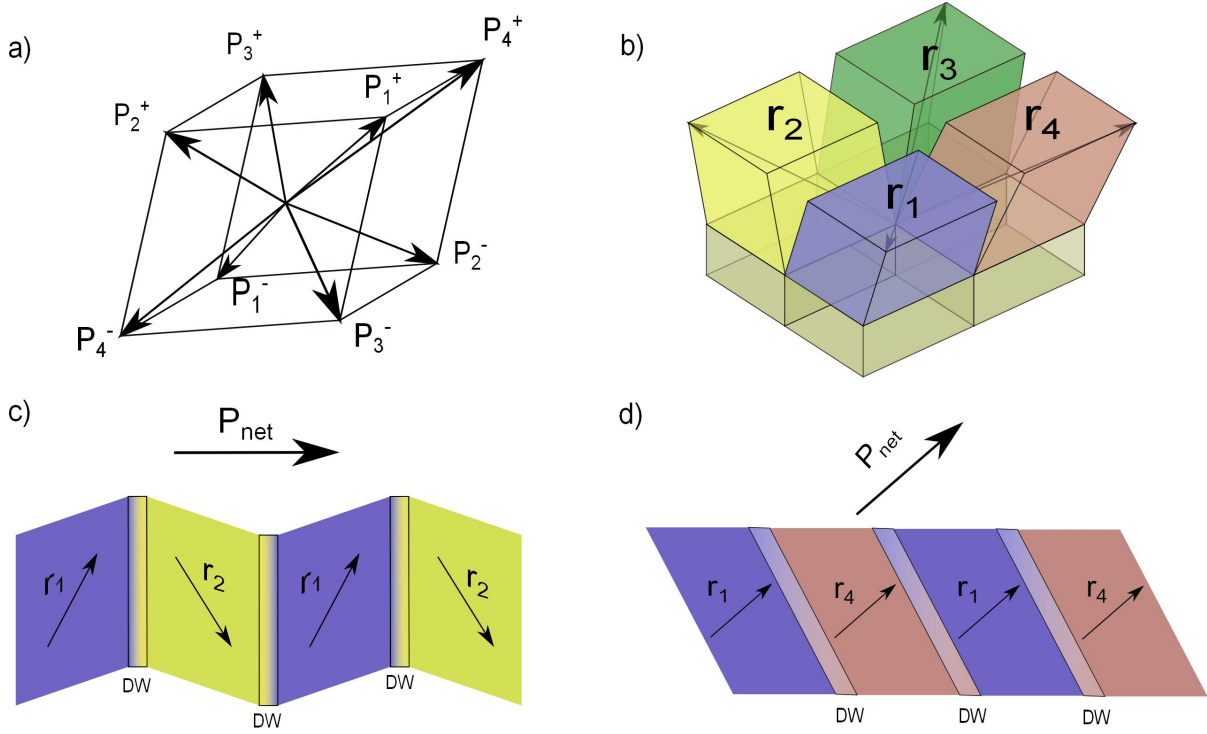


**Figure 2.6:** a) Depiction of eight different polarization directions possible in  $\text{BiFeO}_3$ . All the directions belong to the  $\langle 111 \rangle$  family of directions. b) Four ( $r_1$ - $r_4$ ) variants of ferroelastic distortions corresponding to eight polarization directions. c) The  $109^\circ$  domain walls which belong to the  $\{100\}$  family of planes with net in-plane polarization. d) The  $71^\circ$  domain walls which belong to the  $\{101\}$  family of planes and make an angle of  $45^\circ$  with the  $(001)$  film surface. The net polarization also has a component out of plane.

### 2.1.3.3 Types of domains

As explained in section 2.1.1, a spontaneous polarization is generated in a ferroelectric material when it is cooled below the Curie temperature. The spontaneous polarization goes abruptly to zero at the surface or at any defect which results in a depolarizing field. Since most ferroelectric materials are strong insulators, this depolarizing field cannot be compensated by simple charge conduction. In order to compensate for the energy related to these depolarizing fields, different regions in the material polarize in different directions. Regions with the same direction of polarization are called domains and the interface between two different domains is called domain wall [31].

In  $\text{BiFeO}_3$ , the spontaneous polarization is along the  $\langle 111 \rangle$  family of directions in the cubic notation. Figure 2.6a depicts these polarizations in a schematic where  $P_i^+ = -P_i^-$  with  $i = 1 - 4$ . As can be observed from Figure 2.6a, there is a possibility of having eight different polarization directions. However, for the same value of  $i$ , the positive and negative polarization will induce an identical strain [45]. As result of this there are only four variants of deformation states feasible,  $r_1$ - $r_4$ , as shown in Figure 2.6b. These variants are separated from each other by ferroelectric/ferroelastic domain walls. The type of domain wall is defined by the angle which the direction of the polarizations, of the two domains separated by the wall, make with each other. Taking into consideration the rhombohedral  $R3c$  symmetry of some ferroelectric materials and assuming  $(001)$  oriented films, Streiffer et.al. [45] have calculated the possible domain wall configurations. The

results allow the existence of domain walls in only two family of planes:  $\{100\}$  and  $\{101\}$  (the indices are in cubic notation). The  $\{100\}$  planes are perpendicular to the film surface whereas the  $\{101\}$  planes make an angle  $45^\circ$  with the film surface. Therefore in  $\text{BiFeO}_3$  there are two types of ferroelastic domains:  $109^\circ$  walls wherein the domains are separated from each other by vertical domain walls which belong to  $\{100\}$ , and  $71^\circ$  domain walls in which the domains are separated by walls inclined at an angle of  $45^\circ$  and are a part of  $\{101\}$ . The  $109^\circ$  domains are shown in Figure 2.6c for the case of variants r1/r2. The net polarization in this case is in plane. In case of  $71^\circ$  domains, which are shown by variants r1/r4 in Figure 2.6d, the net polarization has a component which exits out of plane.

### 2.1.3.4 Anti-ferromagnetism

$\text{BiFeO}_3$  is anti-ferromagnetic below its Néel temperature  $T_N$  of  $340^\circ\text{C}$ , but such a transition is not accompanied with any kind of structural modifications. The anti-ferromagnetic character in  $\text{BiFeO}_3$  is induced due to the  $\text{Fe}^{3+}$  cation. The outermost shell electronic configuration for Fe is  $3d^64s^2$ . In the trivalent state, the  $\text{Fe}^{3+}$  ion has the configuration of  $3d^5$  which results in unpaired electrons and consequently local magnetic moments [40] [46] [47].

$\text{BiFeO}_3$  is a G-type anti-ferromagnet which means that each  $\text{Fe}^{3+}$  spin is surrounded by six other anti-parallel spins. However the spins are not perfectly anti-parallel but are slightly canted due to the lack of inversion symmetry. The canted spins result in a net magnetic moment. This moment is spatially canceled out due to a cycloid-like rotation of the canted spins which propagates along the  $[110]$  direction. The spin cycloid can be suppressed, and thus result in a net non-zero moment, by application of a large magnetic field or by stress due to epitaxial strain in thin films [48, 49] [50].

## 2.2 Photovoltaic Effect

The photovoltaic effect can be defined as an electronic process wherein charge carriers are excited in a material from the valence band to the conduction band under illumination. The energy of the illumination should be higher than the band gap of the material. Due to the excitation, an excess number of carriers is available in the conduction band resulting in the generation of a photovoltaic current under short circuit conditions. Under open-circuit conditions, there is a corresponding open-circuit voltage. The magnitude of this open-circuit voltage depends upon the photovoltaic current [51].

Traditionally, the photovoltaic phenomenon is primarily related to semiconducting materials like silicon. These materials have a band gap which lies in the visible range of the light spectrum. Hence, they are the prime candidates for the fabrication of solar cells which make use of the photovoltaic effect to produce electrical energy.

The photovoltaic phenomenon has also been reported and studied in ferroelectric materials with high band gaps like  $\text{BaTiO}_3$ ,  $\text{LiNbO}_3$ ,  $\text{KNbO}_3$  [52]. Like in the case of photovoltaics in semiconductors, there is generation of photovoltaic current and voltage. But the origin of this phenomenon in ferroelectric materials is largely different from that of semiconductors.

### 2.2.1 In Semiconductors

The photovoltaic (PV) effect in semiconductors is realized by the help of a  $pn$  junction. A  $pn$  junction fundamentally is a single crystal material in which one region is doped with an acceptor impurity to form a p-type region. The adjacent region is doped with donor impurities to form an n-type region. In equilibrium conditions the electrons from the n-type region tend to diffuse into the p-type region. The same is valid for holes which try to diffuse into the n-type region. As a result a space charge region (SCR) is created which has an electric potential ( $V_b$ ) opposing any further diffusion. This is depicted in Figure 2.7a. For zero bias voltage, the band diagram in equilibrium conditions has been shown in Figure 2.7b. As can be seen from Figure 2.7b, the conduction ( $E_c$ ) and valence ( $E_v$ ) bands bend along the SCR. Additionally, the intrinsic Fermi level ( $E_F$ ) also bends at the SCR [51] [53]. Under an illumination, which has a higher energy than the band

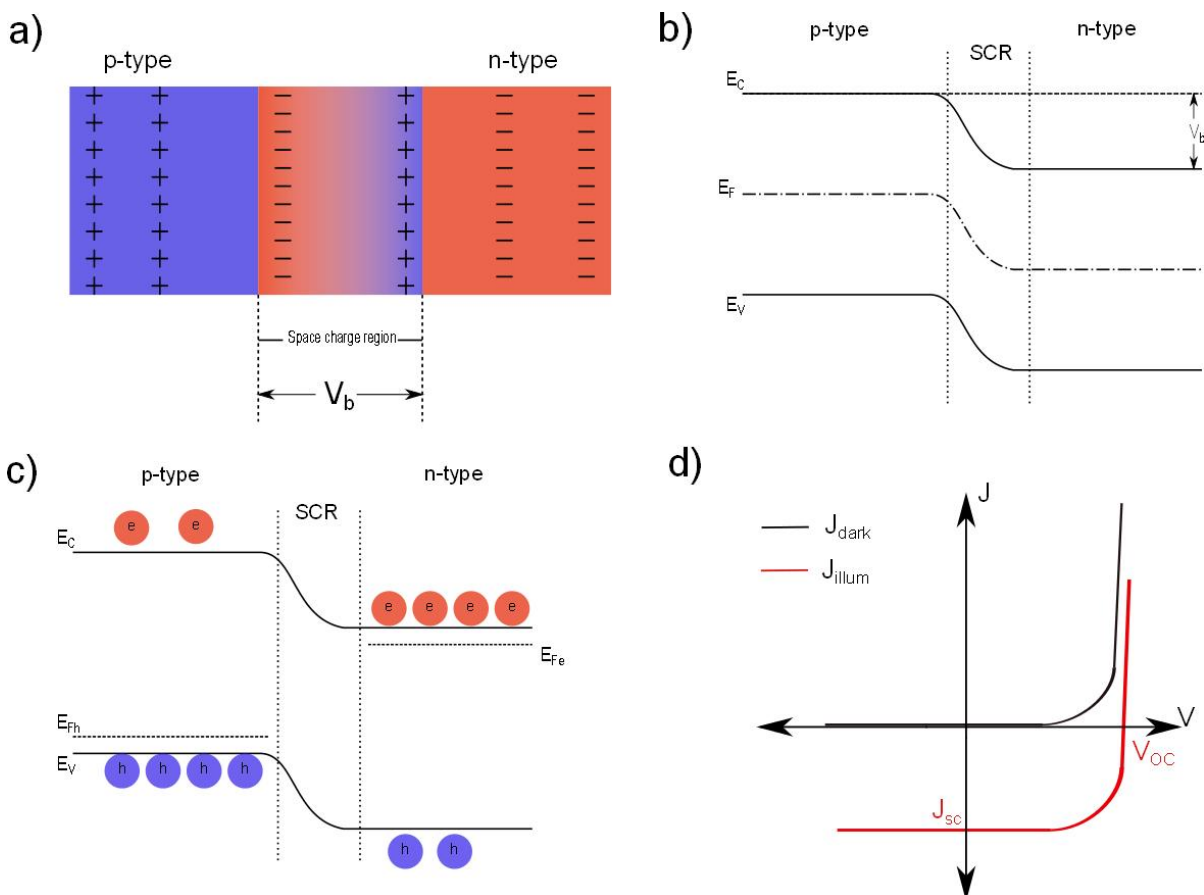


**Figure 2.7:** a) Appearance of a space charge region at the interface between an n-type and p-type region due to the diffusion of charge carriers. b) Bending of the energy levels at the interface due to the SCR resulting a potential  $V_b$ . c) Generation of quasi Fermi ( $E_{Fh}$  and  $E_{Fe}$ ) levels under illumination. d) IV characteristics of the  $pn$ -junction in dark (black) and under illumination (red) where  $V_{oc}$  is the open circuit voltage,  $J_{sc}$  is the short circuit current.

gap, electron-hole pairs are generated in both regions (Figure 2.7c). As a result, the intrinsic Fermi level is split into a quasi Fermi level for holes ( $E_{Fh}$ ) and one for electrons ( $E_{Fe}$ ). In the n-type region excess amounts of electrons are generated in an already electron-populated environment. Similarly an excess number of holes is generated in the

p-type region. But due to the presence of the SCR, inter-diffusion of carriers is inhibited which results in the reduction of recombination rates and subsequent higher lifetimes. Eventually, all of these processes culminate into large photovoltaic currents.

The current-voltage (I- V) characteristics (Figure 2.7d) for a non-illuminated [51] *pn* junction can be expressed by the equation

$$J_{dark} = J_s \left[ \exp \left( \frac{eV}{k_B T} \right) - 1 \right] \quad (2.4)$$

where  $J_s$  is the saturation current,  $e$  is the elementary charge value,  $k_B$  is the Boltzmann constant,  $T$  is the temperature and  $V$  is the applied voltage. The I-V characteristics for an illuminated [51] *pn*-junction is given by

$$J_{illum} = J_s \left[ \exp \left( \frac{eV}{k_B T} \right) - 1 \right] - J_{ph} \quad (2.5)$$

where  $J_{ph}$  is the photovoltaic current generated. The short circuit current ( $J_{sc}$ ) is calculated by putting the voltage equal to zero in equation 2.5 and is equal to  $-J_{ph}$ . The open circuit voltage ( $V_{oc}$ ) is calculated by setting equation 2.5 to zero. Hence the  $V_{oc}$  is estimated to be

$$V_{oc} = \frac{k_B T}{e} \left[ \ln \left( \frac{J_{sc}}{J_s} \right) + 1 \right] \quad (2.6)$$

It can be implied from equation 2.6 that in order to obtain a higher  $V_{oc}$ , the ratio of  $J_{sc}/J_s$  should be as high as possible. Thus a reduction in dark current can help in attaining increased values of  $V_{oc}$  [51].

## 2.2.2 In Ferroelectrics

The photovoltaic effect in ferroelectric materials was first reported in 1955 by A.G. Cheynoweth [26]. He observed a steady generation of photocurrent under illumination and without any bias voltage. The effect was observed in single crystals of  $\text{BaTiO}_3$  below the Curie temperature. Historically, the photovoltaic effect in ferroelectrics has been referred to with different terminologies, for example it has been labeled to be the bulk photovoltaic (BPV) effect, the anomalous photovoltaic (APV) effect, or simply the photogalvanic effect. For maintaining consistency, hence forth in this work it will be called the *bulk photovoltaic effect*.

The existence of the BPV effect has been observed in a variety of single crystalline ferroelectric materials [52] [54]. The effect has been observed in regions of these crystals which have no internal electric field and no gradient in the concentration of charge carriers. Hence these crystals were completely homogeneous [52] [55]. This aspect is in complete contrast to the photovoltaic effect observed in semiconductors where the effect is a consequence of illuminating an inhomogeneity, *i.e.* the *pn* junction. Even though the materials can be single crystalline in semiconductors, but the presence of a *pn* junction is imperative to induce a gradient in the concentration of carriers. Moreover, the magnitude of the open circuit voltage ( $V_{oc}$ ) in semiconductors is limited to the barrier height of the junction and the band gap of the material. This is unlike the case of the BPV effect in ferroelectrics where some of the reported  $V_{oc}$  values have exceeded the band gap of the material by orders of magnitude.

In order to determine and evaluate the necessary conditions for the existence of the BPV effect, Ruppel et. al. [56] in their theoretical work used the Boltzmann transport equation [57] of the form which can be expressed as :

$$\frac{\delta f}{\delta t} + v_k \nabla_r f - \frac{eE}{\hbar} \nabla_k f = G + R + S \quad (2.7)$$

where  $k$  is the wave vector of an electron,  $f$  is the distribution function,  $E$  is the electric field,  $v_k$  is the velocity of an electron which is given by

$$v_k = \frac{1}{\hbar} \nabla_k E_k \quad (2.8)$$

with  $E_k$  being the wave vector dependence of the energy in the band from where the electron originates. In equation 2.7, the second term on the left hand side represents the diffusion current due to the spatial variation of the particle concentration and the third term represents the drift current due to the electric field. The term on the right hand side, collectively, is indicative of the various time-dependent scattering mechanisms. The mechanisms have been separated into a) generation of carriers with rate  $G$ , b) recombination between electrons and holes with rate  $R$  and c) the scattering rate  $S$  between same kind of carriers.

In thermodynamic equilibrium, the distribution function  $f$  is given by the Fermi distribution which is independent of time and is given by:

$$f(r, k) = f[E(k)] = \frac{1}{1 + e^{\frac{E(k) - E_F}{k_B T}}} \quad (2.9)$$

where  $E_F$  is the Fermi level or electrochemical potential. The distribution function given in equation 2.9 will change under external perturbation, like illumination. As a result, the new distribution function  $f_{ph}(r, k)$  will be of the form

$$f_{ph}(r, k) = f_{eq}[E(k) - E_F(r)] + \delta f(r, k) \quad (2.10)$$

where  $\delta f(r, k)$  describes the change due to the external perturbation. Noteworthy in equation 2.10 is the  $r$ -space dependency of the Fermi level  $E_F$  which earlier in equation 2.9 was spatially independent.  $E_F(r)$  indicates the local Fermi level which is also known as quasi Fermi level. The relation between the optical generation rate  $G_{opt}(r, k)$  and the change  $\delta f(r, k)$  is given by

$$\delta f(r, k) = \tau G_{opt}(r, k) + \frac{\delta f(E_F)}{\delta E} v_k \nabla_r E_F(r) \quad (2.11)$$

where  $\tau$  is the relaxation time from an excited state back to the equilibrium state. In equilibrium conditions,  $f(k) = f(-k)$  and as a result there will be no flow of current. In order for a current to flow, the distribution function must have an asymmetric part ( $f^{as}(r, k)$ ). The current that will be generated due to  $f^{as}(r, k)$  can be expressed as:

$$j(r) = \frac{-2}{V} \sum_k e v_k f^{as}(r, k) \quad (2.12)$$

One of the ways to induce such an asymmetry in the distribution function, according to equation 2.11, is to have non-symmetric optical excitations in  $k$ -space [56]. This

is possible in materials which have no center of symmetry and have a polar axis, for example in ferroelectric and pyroelectric materials. In these materials the generation rates  $G(k) \neq G(-k)$  along the polar axis as is depicted in the schematic shown in Figure 2.8a. As a result the asymmetric distribution function  $f^{as}(r, k)$ , based on equation 2.11, will be

$$f^{as}(r, k) = \frac{1}{2}[G(+k) - G(-k)]\tau \quad (2.13)$$

However, equation 2.13 is valid only under the condition that the recombination processes are different from the reverse generation process. Alternatively, the recombination process collectively must progress in ways other than just emission of a phonon or a photon. This situation can be realized by the presence of trap levels below or above the conduction or valence band, respectively. A charge carrier trapped in one of these levels is always capable of being in thermal equilibrium with the bands. Hence it has a certain probability to be emitted from or recaptured at the trap level. Nevertheless, the presence of these trap levels makes the recombination process different from the reverse generation process. From the above discussion it can be concluded that there are primarily two requirements for the existence of a BPV effect: first, asymmetric generation of carriers which is possible in non-centro symmetric materials, and second, the presence of trap levels [56] [58].

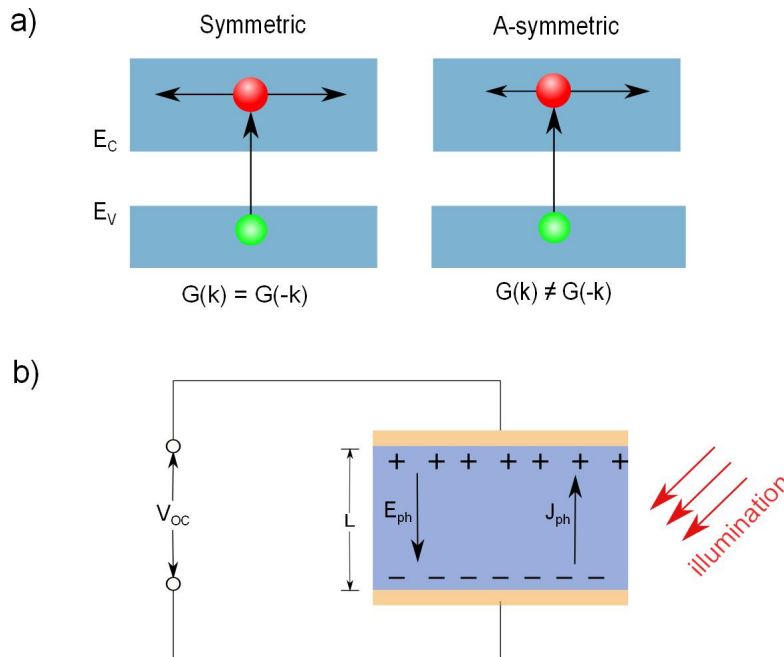


**Figure 2.8:** a) Depiction of the symmetric generation of charge carriers in centrosymmetric materials and asymmetric generation of charge carriers in non-centrosymmetric materials. b) Generation of a photovoltaic current ( $J_{ph}$ ) in non-centrosymmetric materials due to the bulk photovoltaic effect.

Since the presence of a BPV effect can only be manifested in a non-centro symmetric material, it can be inherently observed only in pyroelectric and ferroelectric materials [52]. Phenomenologically, the BPV effect can be described by the following equation [52] [59]

$$J_{(ph)i} = I\beta_{ijk}e_j e_k \quad (2.14)$$



According to the equation 2.14, when a homogeneous ferroelectric crystal is illuminated with a linearly polarized light of intensity  $I$ , a photovoltaic current ( $J_{ph}$ ) is generated. The generation of current primarily depends upon a third rank bulk photovoltaic tensor which is given by  $\beta_{ijk}$ . This tensor is analogous to the piezoelectric tensor mentioned in equation 2.1. The magnitude and direction of the photovoltaic current depends upon the projections,  $e_j$  and  $e_k$ , which the electric field of the linearly polarized light makes on the plane of measurement. It is apparent from equation 2.14 that the generation of the photovoltaic current is completely independent from the direction of polarization in the material. In open circuit conditions a voltage ( $V_{oc}$ ) is measured corresponding to the electric field ( $E_{ph}$ ) generated due to the flow of photovoltaic current (Figure 2.8b). The open circuit voltage can be described by

$$V_{oc} = \frac{J_{ph}}{\sigma_{ph} + \sigma_{dark}} L \quad (2.15)$$

where  $\sigma_{ph}$  and  $\sigma_{dark}$  are the photo and dark conductivities of the material, respectively and  $L$  is the gap between the measurement electrodes. The values of  $V_{oc}$  are inversely related to the total conductivity of the material. Consequently, the values of  $V_{oc}$  are not restricted by the band gap of the material [52, 59, 60]. In some ferroelectric materials like  $\text{LiNbO}_3$ , the values of  $V_{oc}$ 's obtained have been reported to be several orders of magnitude higher than the band gap. The main reason behind these high values can be attributed to the inherent low total conductivity ( $\sigma_{ph} + \sigma_{dark}$ ) in ferroelectric materials [54].

## 2.3 Trap level assisted conduction

In intrinsic semiconductors and insulators under equilibrium conditions the number of holes ( $p$ ) in the valence band are equal to the number of free electrons ( $n$ ) in the conduction band. As a result  $n = p = n_i$  and the product  $np = n_i^2$ . Any perturbation from this equilibrium condition results in triggering of recombination processes which tend to restore the equilibrium [51]. In the absence of any levels in the band gap, the recombination is band-band in which the transition of an electron from the conduction to the valence band is accompanied with the emission of either a photon (radiative process) or a phonon (Auger process) as shown in Figure 2.9a. However if some levels or a band of levels exist within the band gap then the recombination process becomes a bit more complicated. Figure 2.9b depicts the recombination processes occurring *via* the trap levels existing at energy level  $E_t$  between the conduction ( $E_c$ ) and valence band ( $E_v$ ).

Under equilibrium conditions, the distribution function for electrons or holes is given by the Fermi function which is expressed as

$$f(E) = \frac{1}{1 + e^{\frac{E - E_F}{k_B T}}} \quad (2.16)$$

According to the theory formulated by Shockley and Read in 1952 [61], the occupational function used to describe the distribution function of carriers in non-equilibrium conditions is similar to the one described in equation 2.16. Although, in this case the Fermi levels are replaced with the quasi-Fermi levels. The quasi Fermi levels are different for electrons ( $E_F^n$ ) and holes ( $E_F^p$ ) as shown in Figure 2.10b. The introduction of quasi Fermi levels is based on the assumption that under non-equilibrium conditions the distribution

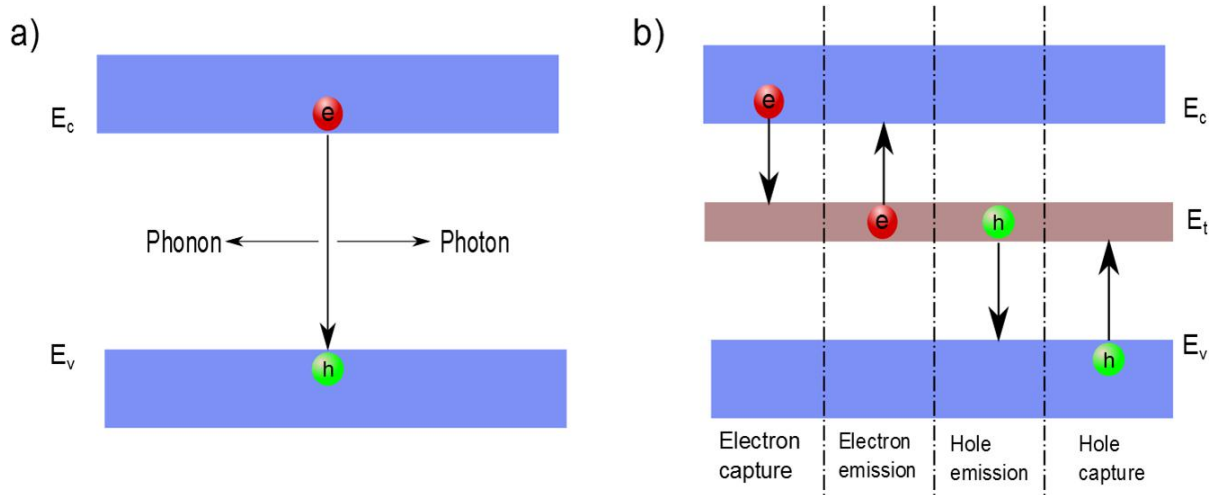


**Figure 2.9:** a) Band-band recombination process in which an electron from the conduction band combines with a hole in the valence band resulting in the generation of either a photon or a phonon. b) Recombination process occurring via a trap level which might lead to either electron emission, electron capture, hole emission, or hole capture.

of charge carriers over certain available levels is determined by the thermal equilibrium between the levels. As a result the number of electrons in the conduction band ( $n_c$ ) can be expressed as [62]

$$n_c = N_c \exp[-(E_c - E_F^n)/k_B T] \quad (2.17)$$

where  $N_c$  is the number of available states in the conduction band.

One of the purposes for using the concept of quasi Fermi levels is to categorize and distinguish the levels as shallow or deep. The deep levels have also been labeled as ground states in some studies. In this work, for consistency, they will be referred to as deep levels. The position of the level with respect to the quasi Fermi level is the main criteria to determine whether a level is shallow or deep as has been depicted in Figures 2.10c-d [63]. The shallow levels lie between the quasi Fermi levels ( $E_F^n$  or  $E_F^p$ ) and the band edges ( $E_c$  or  $E_v$ ) whereas the deep levels lie between the two quasi Fermi levels ( $E_F^n$  and  $E_F^p$ ) (Figures 2.10c-d). Therefore the shallow levels are always in thermal equilibrium with their respective bands edges. Consequently a charge carrier falling into one of the shallow levels has a high probability to be re-excited into the band. But, a charge carrier trapped in one of the deep levels has a high probability to be recombined before it can be re-excited back into one of the bands. Apparently this distinction between the shallow and deep trap levels is purely statistical and can be changed by the temperature [62] [63]. For instance, at lower temperatures the quasi Fermi levels tend to recede towards their respective band edges. As a result, a level which might be shallow at a certain temperature may become a deeper level at a different temperature. Conversely, as the temperature increases, a previously deep level might become a shallow level as the quasi Fermi level passes through it. The ratio of number of carriers trapped in a shallow trap ( $n_t$ ) to the number of free carriers in the conduction band ( $n_c$ ) is given by [64]:

$$\frac{n_t}{n_c} = \frac{N_t}{N_c} e^{\frac{\Delta E}{kT}} \quad (2.18)$$

where  $\Delta E$  is the difference between the energy of the trap level and the respective band,  $N_t$  is the number of available trap states. When an insulating or a strong dielectric

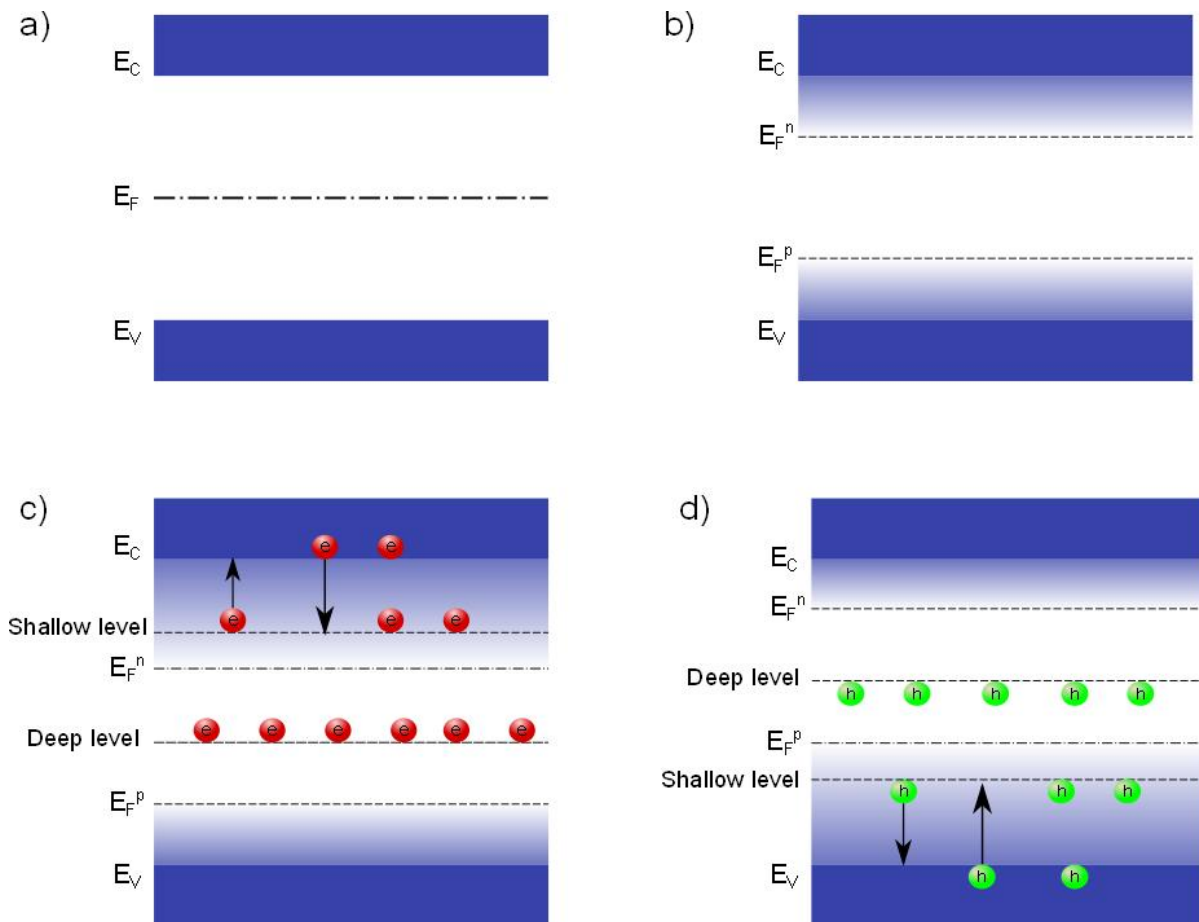


**Figure 2.10:** a) Band diagram under steady state equilibrium conditions. b) Band diagram under non-equilibrium conditions resulting in the formation of quasi Fermi levels  $E_F^n$  for the electrons and  $E_F^p$  for the holes. Thermal equilibrium between the charge carriers [c) electrons, d) holes] present in the band with the carriers trapped in the shallow levels. The carriers trapped in deeper states have high probability of recombining.

material, which has no levels within the band gap and the conduction is via band-band transition, is illuminated for a short period of time then the observed decay time of photo-induced current is approximately equal to the lifetime of a carrier in the material. However in the presence of an active shallow trap level, the observed decay time of current exceeds the lifetime of the carriers. The same is valid for the rise time of the currents. This occurs as a consequence of the fact that during the illumination process, the carriers might be first excited to the trap level and then the conduction band which results in extended rise times. Also, when the illumination is removed, the decay of the carriers, due to the recombination processes, occurs *via* the trap level which leads to higher decay times. It can be implied from equation 2.18 that in the case of insulating materials with trap levels, where inherently the value of  $n_c$  is negligible, the entire photo-excitation process can be largely dependent on the trap level [64] [63].

## 2.4 Summary

In this chapter the concepts of ferroelectric and multiferroic materials were introduced. Special emphasis was given to the multiferroic material  $\text{BiFeO}_3$  which is the main ma-

terial of the present study. The structure of  $\text{BiFeO}_3$  was discussed which is primarily responsible for different functional properties like ferroelectricity, different domain wall configurations and antiferromagnetism. The basic photovoltaic phenomenon along with its manifestation in semiconductor and ferroelectric materials were explained. Finally the trap assisted conduction mechanisms were elaborated and their relevance in case of photo excitation phenomena in a strong dielectric material like  $\text{BiFeO}_3$  was presented.

## Experimental and characterization methods

### 3.1 Sample synthesis

In the present work, thin films of  $\text{BiFeO}_3$  were grown on single crystalline substrates, with definite orientation, *via* pulsed laser deposition (PLD). In some cases bottom electrodes with perovskite structure were deposited between the  $\text{BiFeO}_3$  film and the substrate for ferroelectric characterization. For photoelectric measurements, top electrodes were used instead of bottom electrodes to avoid short-circuits. The top electrodes were fabricated using a conventional lift off technique followed by *dc* sputtering.

#### 3.1.1 Pulsed laser deposition

Pulsed laser deposition or PLD (as it is commonly known) can be categorized as one of the physical vapor deposition processes. The technique has been widely used in the field of deposition of complex materials. Features such as stoichiometric transfer of material from the target onto the substrate, generation of high energy species and the possibility to have reaction between the background gas and the released cations from the material makes this technique lucrative for depositing oxide materials [65].

The basic principle of PLD the technique primarily involves exposing the material to be deposited to high-energy laser pulses. The effective energy of the laser is described in terms of the fluence, which is defined as laser energy per unit square area ( $\text{J}/\text{cm}^2$ ). For a low fluence, the laser pulse will only heat the target. However with increasing fluence a threshold of energy is reached where the material will ablate or evaporate and eventually condense on the surface of the substrate [65]. A schematic to depict the PLD setup used for the present work is shown in Figure 3.1.

The setup consists of a chamber which is connected to a vacuum pump system. There is a possibility to introduce oxygen or argon gas via a gas inlet. The partial pressure for either of the gases can be fully controlled. The substrate is placed directly above the target at a distance of approximately  $5.5\text{ cm}$ . The substrate is placed on a heating stage (not shown) so that the incoming material particles have enough energy at the substrate surface for epitaxial growth. The laser beam enters the chamber through an optical setup of lenses (not shown). As a result the laser spot size on the target can be optimized to obtain the required fluence. The target is a ceramic disc which is made up of the materials mixed to the required stoichiometry. However in case of bismuth ferrite, the target is composed of approximately 10% in excess of bismuth to compensate for

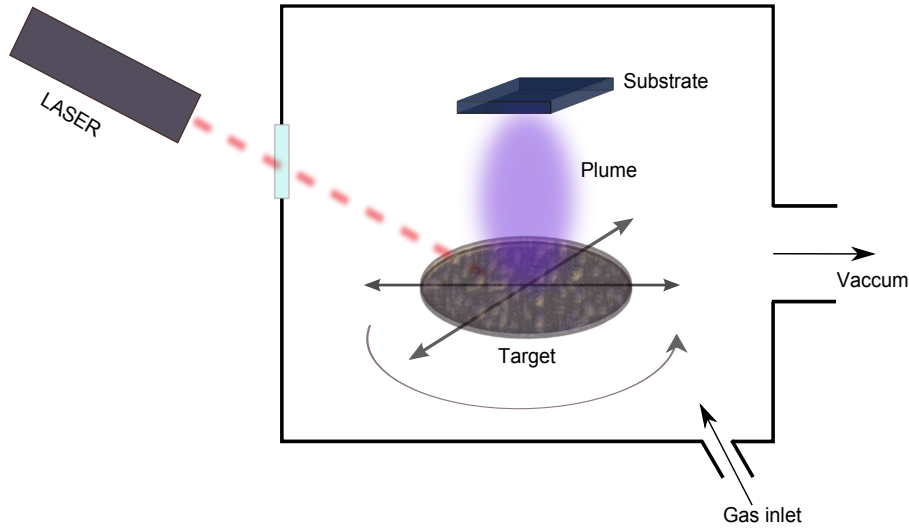


**Figure 3.1:** Schematic of the pulsed laser deposition technique.

the volatile nature of bismuth. The target is mounted on a holder which is capable of rotations and translational movements during the ablating process. These movements are necessary to avoid any kind of damage to the target surface due to repeated exposures to the laser pulses. The details regarding the deposition parameters of the materials which were deposited using PLD have been listed in Table 3.1.

**Table 3.1:** Deposition parameters

Material	Bismuth ferrite (BFO)	Lanthanum strontium manganate (LSMO)	Strontium ruthenate (SRO)
Target composition	$\text{Bi}_{1.1}\text{FeO}_3$	$\text{La}_{0.7}\text{Sr}_{0.3}\text{MnO}_3$	$\text{SrRuO}_3$
Target diameter	2 inches	2 inches	2 inches
Sample to target distance	5 cm	5 cm	5 cm
Ablation energy	55 - 60 mJ	65 - 70 mJ	65 - 70 mJ
Fluence energy	0.30 - 0.33 J/cm <sup>2</sup>	0.36 - 0.38 J/cm <sup>2</sup>	0.36 - 0.38 J/cm <sup>2</sup>
Growth rate	0.16 - 0.3 Å / sec	0.2 Å / sec	0.4 Å / sec
Substrate temperature	650 °C	600 °C	700 °C
Partial pressure of O <sub>2</sub>	0.14 - 0.16 mbar	0.2 mbar	0.14 mbar
Heating rate	20 K/min	20 K/min	20 K/min
Cooling rate	15 K/min	20 K/min	20 K/min

### 3.1.2 Electrode fabrication

For photoelectric and thermally stimulated current spectroscopy measurements, electrodes were deposited on top of the BFO film. Correspondingly the BFO films were deposited directly on the substrate without any bottom electrode. In order to fabricate the electrodes at the top of the BFO film, a conventional photo-lithography procedure was followed by a subsequent lift-off process. A schematic of the photo-lithography procedure has been shown in Figure 3.2. The sample with a BFO film grown directly on the

substrate is spin coated with a p-type photo-resist (Figure 3.2b). Thereafter the sample is exposed to UV-light for a definite time through a mask which comprises of the pattern of the electrodes (Figure 3.2c). The sample is then developed in a solution to remove the exposed part of the resist (Figure 3.2d). Subsequently a layer of platinum (Pt) is *dc* sputtered on top of the resist (Figure 3.2e). The photo-resist is then lifted off by cleaning the sample with acetone which eventually results in the desired electrode pattern on top of the BFO film (Figure 3.2f). The thickness of the electrodes was approximately between 50 and 80 nm.

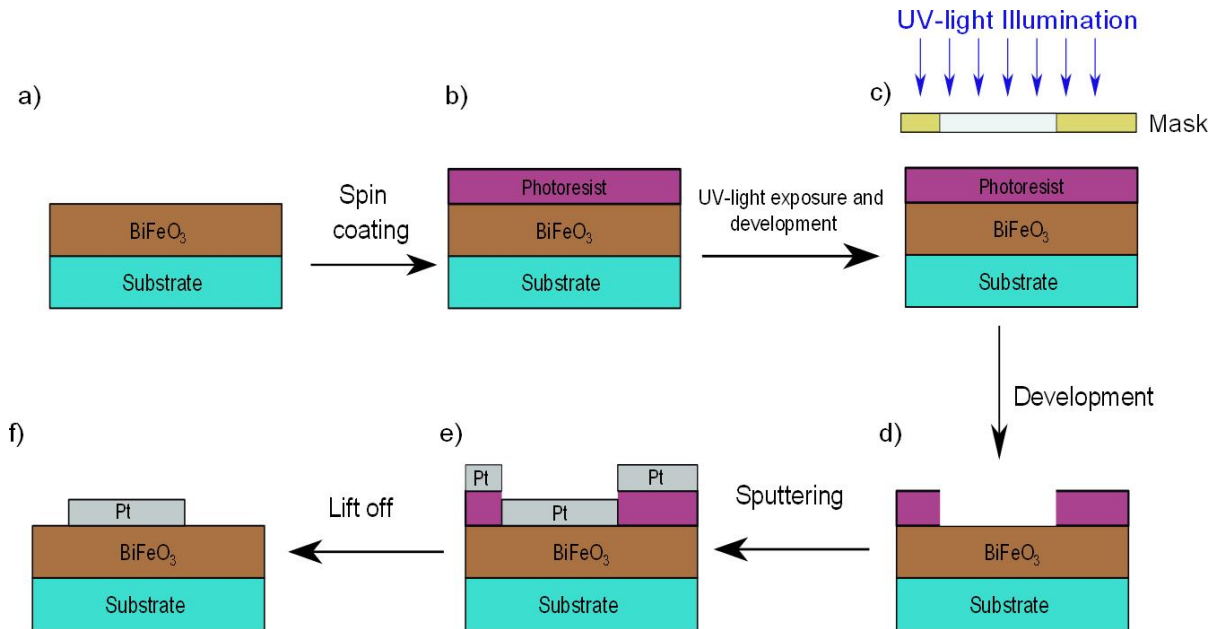


**Figure 3.2:** Schematic of the photo-lithography procedure.

For ferroelectric measurements, a thin epitaxial layer of LSMO was first grown on top of the substrate followed by the growth of BFO. Thereafter Pt was deposited on top of the BFO film. The deposition of Pt was performed *via rf* sputtering through a hard mask. The mask consisted of an array of square holes of size  $10 \times 10 \mu\text{m}$ . As a result, a capacitor-like geometry was obtained of the type *Substrate/LSMO/BFO/Pt*.

## 3.2 Scanning probe microscopy - Morphology and domain analysis

The main principle of scanning probe microscopy is the interaction between the tip, which is mounted at the end of a soft cantilever, and the surface of the material. As the tip is scanned along the surface of the sample, the cantilever undergoes a deflection which is a measure of the type of interaction. Different kinds of interactions can be measured based on the type of material and tip, like electrical (piezo force microscopy, conductive force microscopy), magnetic (magnetic force microscopy) and mechanical (atomic force microscopy). In the present work atomic force microscopy (3.2.1) was used to investigate the sample surfaces whereas piezo force microscopy (3.2.2) was used for characterizing the ferroelectric domains.

### 3.2.1 Atomic Force Microscopy

Atomic force microscopy or AFM is a widely used technique to investigate the sample surface of a variety of materials like polymers, metals, insulators, bio-materials etc. In AFM, the tip of the cantilever is scanned along the surface of the material. Depending upon the type of morphology, the cantilever undergoes different extents of bending. This bending is a measure of the deformities at the surface. The resultant signal due to the deflection is fed into a feedback loop which compares the deflection with a reference value. The output of the comparison is transferred to a piezoelectric actuator which maintains a constant distance between the tip and surface. Hence the output from the feedback loop is a measure of the surface morphology [66] [67].

A basic schematic of an AFM setup is shown in Figure 3.3a. The deflection which

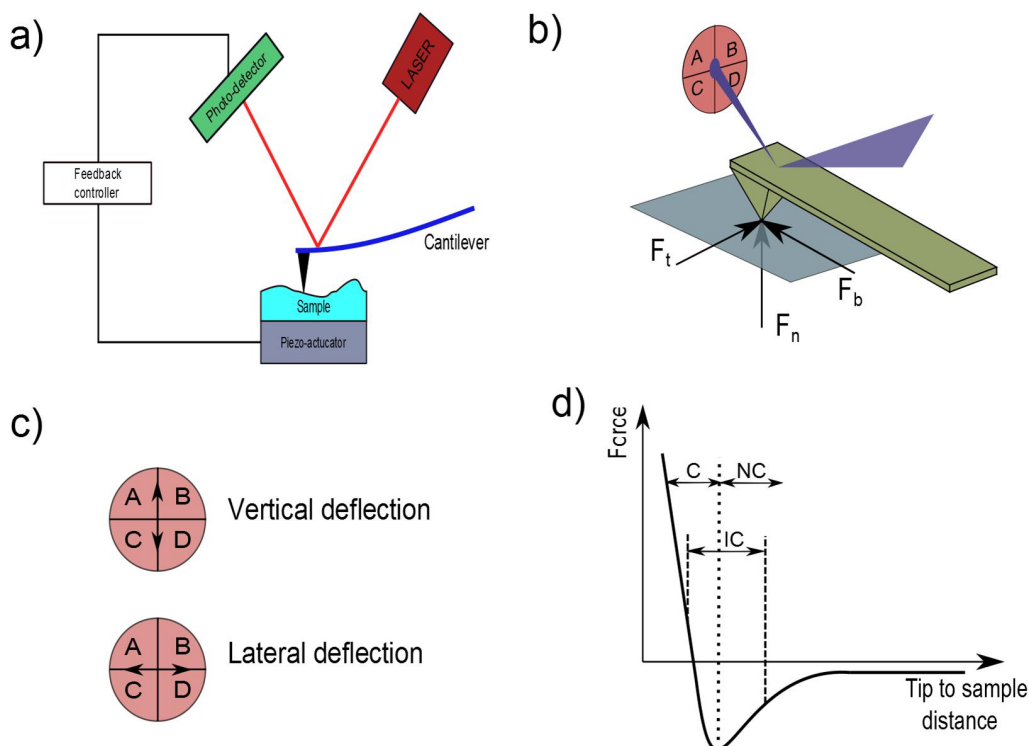


**Figure 3.3:** a) Schematic of the AFM setup. b) The optical lever arrangement which is used to detect and measure deflections. c) The vertical deflection calculated as  $(A + B) - (C + D)$  and the lateral deflection as  $(A + C) - (B + D)$ . d) The force measured due to the Lennard-Jones potential as a function of the tip-to-sample distance. The contact mode (C), the non-contact mode (NC) and the intermediate contact (IC) mode operate in the repulsive, attractive and intermittent range of forces.

is experienced by the cantilever is measured by the help of an optical lever setup. In such a setup, as can be seen from Figure 3.3b, a laser beam is directed on the surface of the cantilever which gets reflected onto a four-piece photo detector. The forces acting on the tip upon interaction with the surface can be categorized as normal force ( $F_n$ ) which acts perpendicular to the tip, torsion force which acts along the lateral direction ( $F_t$ ) and bending forces which are acting parallel or anti-parallel to the tip ( $F_b$ ) [68]. As a result of these forces the tip undergoes deflection which is detected by the four-piece photo detector. Effectively any vertical deflection is detected as the signal from  $(A + B) - (C + D)$  (Figure 3.3c). Additionally, any lateral deflection is measured as the



signal  $(A+C) - (B+D)$ . The normal forces acting on the tip can be efficiently described by the Lennard-Jones potential [57] which can be expressed by the following equation

$$V(z) = 4\epsilon \left[ \left( \frac{\sigma}{z} \right)^{12} - \left( \frac{\sigma}{z} \right)^6 \right] \quad (3.1)$$

where  $\sigma$  is the distance is the distance for  $V(z) = 0$ ,  $\epsilon$  is the potential depth and  $z$  is the distance between the tip and the surface.

Based on the extent of the distance between the tip and the surface, the AFM technique can be categorized into three types, namely contact mode, non-contact mode and intermediate or tapping mode. It can be seen from Figure (3.3d) that in the contact mode the tip and surface distance is in the range of high repulsion forces. As a result the cantilever experiences bending which is overcome by an applied set-point force. Any deviation from this set point is a measure of surface deformity. However, a constant contact with the surface might lead to tip damage, and the noise due to frictional forces limits the resolution. To circumvent the problems of constant contact, the non-contact mode can be used. In this mode the tip is in the attractive range of forces. In the intermediate contact mode, which is also referred to as the tapping mode, the tip is made to oscillate at a resonance frequency and the tip-to-surface distance is adjusted so that the tip touches the sample surface for only a short time [66].

### 3.2.2 Piezo Force Microscopy

Piezo force microscopy or PFM can be considered to be one of the variants of AFM which is used for visualizing the domains in ferroelectric materials. The technique makes use of the principle that all ferroelectric materials are also piezoelectric in nature, as was discussed in section 2.1.1. Since the PFM is based on the piezoelectric response of the ferroelectric material, it can also be used to measure the corresponding piezoelectric coefficients of the material. The operation of a PFM is based on the converse piezoelectric effect which results in coupling between strain and applied electric field. In PFM an  $ac$  voltage is applied between the tip and the bottom electrode as is shown in Figure 3.4a. Due to the converse piezoelectric effect the surface of the material under the tip tends to expand or contract, depending upon the sign of the voltage at the tip. These contractions and expansions are detected by the tip. The out-of-plane and in-plane deflection of the tip are converted into electrical signals by the photo-diodes which then are fed into two different lock-in amplifiers (only one is shown). The  $ac$  signal applied to the tip is also fed as the reference signal to the lock-in amplifiers. It is possible to extract the net piezoelectric response from the lock-in amplifier by comparing the reference signal with the deflection signal. The piezoelectric response comprises of information regarding the phase and the amplitude [69] [70]. Hence, it is possible to acquire simultaneously the in-plane and out-of-plane piezo responses from a given scan area of the sample by using two lock-in amplifiers. In this study the in plane response will be referred to as lateral PFM or LPFM and the out-of-plane response as vertical PFM or VPFM.

It can be implied from equation 2.2 stated in section 2.1.1, that the piezoresponse from a given ferroelectric material primarily depends upon the values of the coefficients of the third rank tensor ( $d_{ijk}$ ). A general third rank tensor consist of 27 elements. But since the strain is symmetrical in nature i.e.  $\epsilon_{ij} = \epsilon_{ji}$ , therefore only 18 of the 27 elements remain independent. Moreover the presence of crystal symmetry reduces the number of

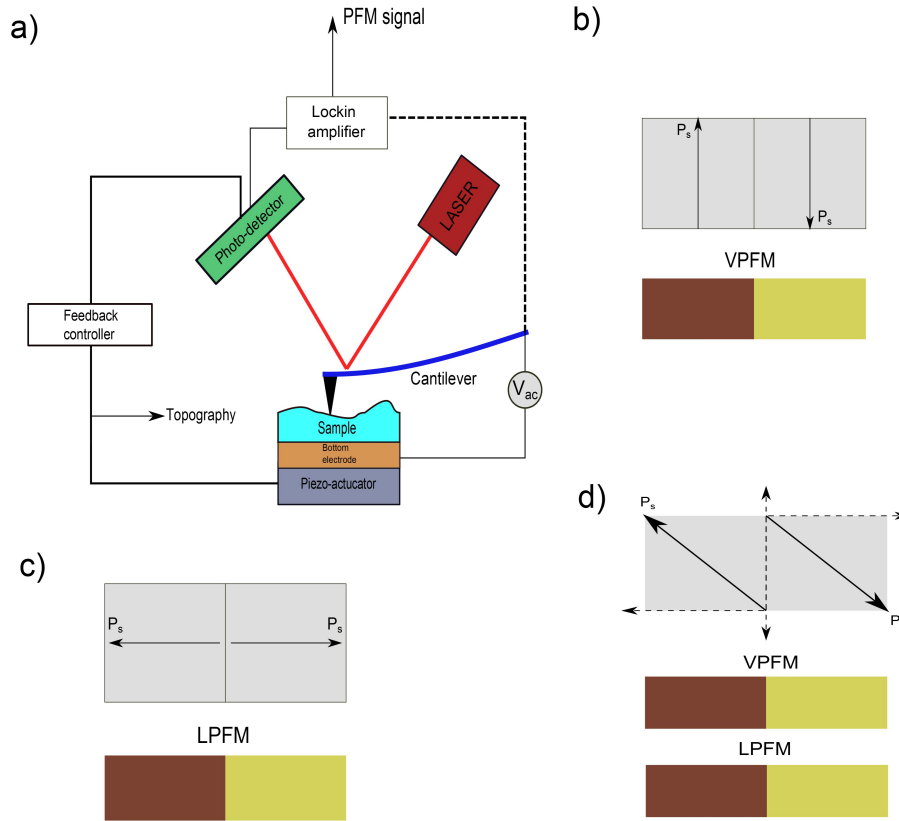


**Figure 3.4:** a) Schematic of the PFM setup. b) Vertical PFM signal when the spontaneous polarization ( $P_s$ ) changes only out-of-plane. c) Lateral PFM signal when  $P_s$  changes only in-plane. d) Vertical and lateral PFM signal when  $P_s$  is at an angle with the film surface.

independent coefficients even further [33]. For instance, in case of BFO due to the  $R3c$  symmetry the equation 2.2 can be elaborated as

$$\begin{pmatrix} \epsilon_1 \\ \epsilon_2 \\ \epsilon_3 \\ \epsilon_4 \\ \epsilon_5 \\ \epsilon_6 \end{pmatrix} = \begin{pmatrix} 0 & -d_{22} & d_{31} \\ 0 & d_{22} & d_{31} \\ 0 & 0 & d_{31} \\ 0 & 0 & d_{33} \\ 0 & d_{15} & 0 \\ d_{15} & 0 & 0 \\ -2d_{22} & 0 & 0 \end{pmatrix} \begin{pmatrix} E_1 \\ E_2 \\ E_3 \end{pmatrix} \quad (3.2)$$

Due to the combined effects of distribution of electric field under the PFM tip and the variety of coefficients, the net response from the material can be rather complex. However in ferroelectric materials it is safe to assume that the response is largely governed by the expansion or contraction along the direction of spontaneous polarization [68] [70]. For example, when a voltage  $V$  is applied to the tip which is in contact with a film of thickness  $x$ , the resultant change in the film thickness  $\Delta x$  can be described by [70] [67]

$$\Delta x = d_{33}V \quad (3.3)$$

Equation 3.3 is valid under the assumption that the polarization for such a film is oriented completely out-of-plane. Whether the film undergoes contraction or expansion depends upon the sign of the voltage at the tip. While measuring if the tip scans over an area which

comprises of two different polarizations (up  $\uparrow$  and down  $\downarrow$ ), the change of film thickness or the amplitude will remain the same in either of the cases. However in the phase image there will be a  $180^\circ$  shift. Additionally, in another extreme case when the polarization is completely in plane, the response in VPFM will vanish with phase variations observed only in LPFM. However in a more conceivable case when the polarization makes an angle ( $\alpha$ ) with the sample surface, the responses in VPFM and LPFM compose of the projections of the polarization in vertical and lateral direction, respectively. All these three cases are shown in a schematic in Figures 3.4b-d. Apparently, in case of LPFM the orientation of the cantilever must be perpendicular to the direction of the spontaneous polarization or its projections for causing any deflection due to the torsional forces [68] [67].

### 3.2.3 PFM study in BiFeO<sub>3</sub>

As mentioned in the previous section, the piezoresponse in ferroelectric films is largely dominated by the expansions and contractions along the direction of the spontaneous polarization [67] [12, 13]. In BFO this direction is of type  $\langle 111 \rangle$  in pseudo cubic notation which leads to eight possible polarization variants. As a consequence the signals from LPFM and VPFM consist of lateral and vertical projections of the polarization. However it is possible to decipher the type of domains present in the film by analyzing and comparing the PFM scans obtained along different crystallographic directions of the film.

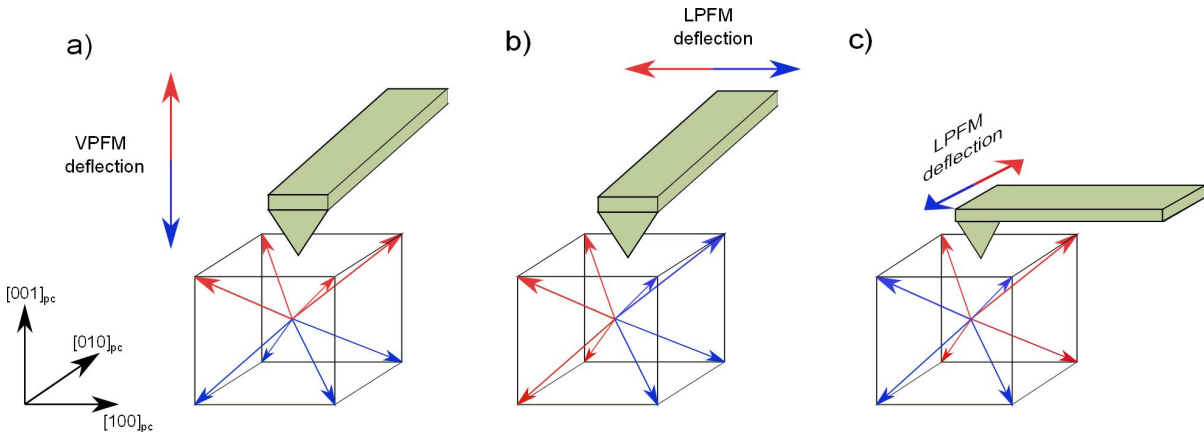


**Figure 3.5:** Schematic of the different polarization variants which can be detected by scanning along specific crystallographic directions. a) Out-of-plane polarization variants can be detected irrespective of scanning direction. Distinguishing between in-plane polarization variants is susceptible to scanning along b)  $\langle 100 \rangle_{pc}$  or c)  $\langle 010 \rangle_{pc}$ .

Figure 3.5 depicts the different polarization variants which can be detected by scanning along particular crystallographic directions. In the VPFM (Figure 3.5a), irrespective of the scanning direction it is always possible to determine the direction of the polarization by detecting the deflection in  $[001]_{pc}$  direction. However the signal in LPFM is largely susceptible to scanning direction. As can be seen from Figure 3.5b, when the cantilever is oriented along  $[010]_{pc}$  direction, only the polarization variants which have lateral projections along  $[100]_{pc}$  or  $[\bar{1}00]_{pc}$  will be visible, since only these projections will result in a torsional force on the cantilever. Similarly, when the cantilever is placed

along the  $[100]_{pc}$  direction (Figure 3.5c), only the polarization variants with projections along the  $[010]_{pc}$  or  $[0\bar{1}0]_{pc}$  can be distinguished. Therefore it is possible to develop a convincing approximation about domain orientation in BFO by combining the knowledge obtained after scanning along two crystallographic directions which are perpendicular to each other [12, 13].

### 3.3 Structural Analysis

The structural analysis in the present work was done by x-ray diffraction (XRD) studies and transmission electron microscopy (TEM) investigations. All the TEM images in this work have been acquired and provided by Dr. Young Heon Kim and Dr. Hakan Deniz with support from Dr. Eckhard Pippel.

#### 3.3.1 X-ray diffraction

X-ray diffraction is one of the standard techniques for characterizing a solid in terms of its crystallinity, structure and to a certain extent chemical composition. The technique is based on the interaction of X-ray photons with the solid under investigation. The diffracted x-rays are then analyzed, which contain information regarding the structure. The X-rays are generated whenever a charged particle with high enough kinetic energy

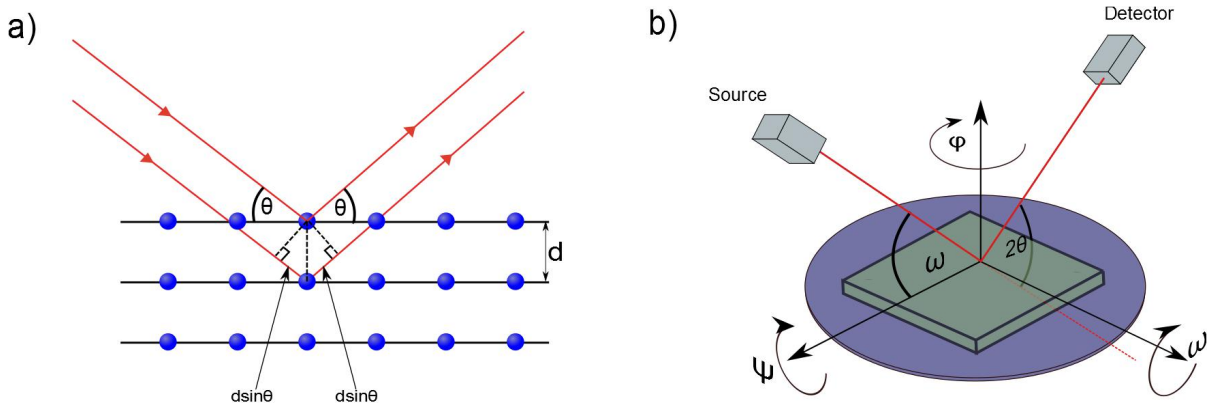


**Figure 3.6:** a) Bragg's diffraction of X-rays with wavelength  $\lambda$  by atomic planes which are separated by a distance  $d$  with  $\theta$  as the angle of incidence. b) Schematic of the XRD setup along with different possible angular movements  $\phi$ ,  $\psi$  and  $\omega$ .

decelerates. This is realized by applying large voltages across two electrodes. The large voltage promptly draws electrons from the cathode towards the anode and the deceleration is caused by the help of a target material which is kept at the anode on which the electrons strike. The resulting X-rays from the target have varied wavelengths and intensities. This type of radiation is known as *Bremsstrahlung* or white radiation. However, when the voltage applied across the electrodes is increased above a certain threshold value then the radiation with wavelength that are characteristic to the target material are emitted. These rays are categorized as *K*, *L*, *M* type etc [71].

When an electron with high kinetic energy strikes a target material atom, it might knock out one of the electrons from the K-shell of the atom. This shell is then filled up again by an electron from an outer shell. This results in an electron losing its energy in the form of a photon and the corresponding radiation is the characteristic *K*-radiation

of the target material. Moreover, the type of radiation emitted can be subclassified depending upon the level from which the electron falls to fill up the K-shell. For example  $K\alpha$  refers to the radiation emitted when an electron from the  $L$ -shell fills up the vacant  $K$ -shell, and  $K\beta$  when the electron comes from the  $M$ -shell.

Since the wavelength of X-ray radiation is in the order of 1-2 Å, it can undergo diffraction in crystals which possess periodicity in their structure of the same order of magnitude. The main condition for the diffraction of X-rays in crystals is defined by Bragg's law which is expressed as

$$n\lambda = 2d\sin\theta \quad (3.4)$$

where  $\lambda$  is the wavelength of the X-ray beam,  $\theta$  is the angle which the X-ray beam makes with the atomic planes,  $n$  is an integral value which is equal to the number of wavelengths and  $d$  is the interplanar distance between atomic planes. Bragg's law can be interpreted as a condition for constructive interference between two rays, which is: if the path difference between the two rays (given by  $2d\sin\theta$ ) is an integral value times the wavelength, then the rays can exhibit constructive interference [71].

The schematic of the XRD setup (Phillips X'Pert MRD, type 3050/65) which was used in the present study is shown in Figure 3.6b. The target material used for generating X-rays was copper. When the Cu target is struck with high energy electrons, *Bremsstrahlung* is generated along with all the characteristic wavelengths of copper. Copper  $K\alpha_1$  and  $K\alpha_2$  wavelengths were used for diffraction since they have the highest intensities with wavelengths  $\lambda(K\alpha_1) = 1.5406\text{Å}$  and  $\lambda(K\alpha_2) = 1.5444\text{Å}$ . The other characteristic wavelengths were suppressed by using a nickel filter. The X-rays which are emitted from the source are radiated in all directions. Therefore a *Soller* slit is used at the source to realize parallel beam conditions at the surface of the sample.

In the present study, two kinds of XRD measurements were performed, namely the  $2\theta - \omega$  scan and reciprocal space maps, which are explained in the following sections.

### 3.3.1.1 $2\theta - \omega$ scan

In a  $2\theta - \omega$  scan the sample is analyzed in a Bragg-Brentano geometry. The angle between the incident beam and the sample surface ( $\omega$ ) is varied in steps by  $\Delta\omega$ . Correspondingly, the angle between the diffracted beam and the incident beam is also changed simultaneously by an amount  $\Delta 2\theta = 2\Delta\omega$ . As a consequence Bragg's condition is maintained. The intensity of the diffracted beam is measured at each angle position. Apparently during such a scan the crystallographic plane under investigation remains unchanged. This enables to measure different orders of diffraction ( $n$ ) and ultimately calculate the distance between the inter-atomic planes ( $d$ ) by using equation 3.4. If the investigated plane contains the surface of the thin film then the value of  $d$  is the out-of-plane lattice parameter ( $c$ ). Also the presence of secondary phases can be detected if their planes are parallel to the film surface plane.

In order to perform a  $2\theta - \omega$  scan, the sample is first oriented by selecting the surface plane of the substrate as the reference. For this the  $2\theta$  value corresponding to the plane is chosen. Subsequently the sample alignment is adjusted so that the maximum intensity is obtained in the  $\phi$  and  $\psi$  scan.

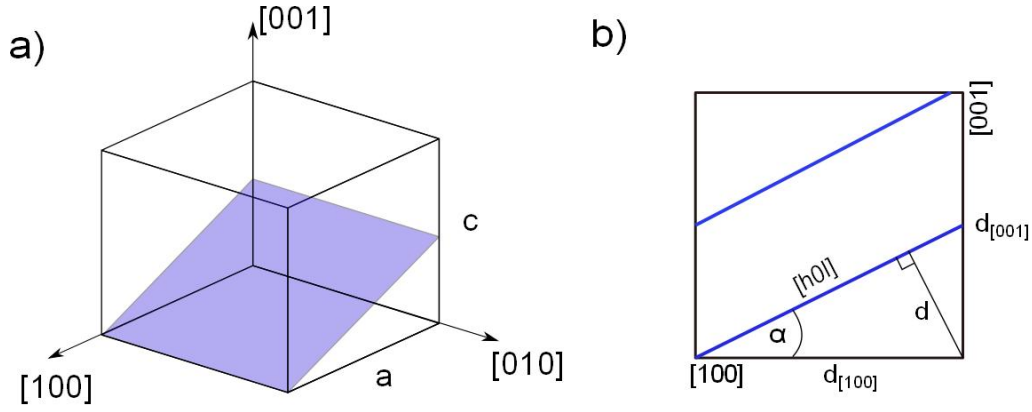


**Figure 3.7:** a) Schematic of the  $(h0l)$  plane in a cubic system which contains information about in-plane ( $a$ ) and out of plane lattice parameters ( $c$ ). b) View of the cubic unit cell shown in (a) along the  $[010]$  direction, with the interplanar distance  $d$  and the offset angle  $\alpha$ .

### 3.3.1.2 Reciprocal space maps

As discussed in section 3.3.1.1, the main information obtained from a  $2\theta - \omega$  scan is the value of out-of-plane lattice parameter. However the knowledge of the in-plane lattice parameter ( $a$ ) of the film is essential to completely analyze the epitaxial relation of the film with the substrate. This eventually assists in calculating the strain in the film due to the lattice parameter mismatch with the substrate.

To calculate the in-plane lattice parameter, a crystallographic plane which contains  $a$  is chosen. Usually an odd plane of the type  $(h0l)$  or  $(0kl)$  is selected. As can be seen in Figure 3.7a, the  $(h0l)$  plane comprises of information about  $a$ . The film is then oriented so that the x-rays are incident on the chosen plane by incorporating the angle  $\alpha$  which is the offset between the film surface and the odd plane. The  $2\theta - \omega$  scans are then obtained for a range of values of  $\alpha$  which accommodate  $\alpha_{film}$  and  $\alpha_{substrate}$ . The measured interplanar distance ( $d$ ) can then be resolved along the  $[100]$  and  $[001]$  directions (Figure 3.7b) as:

$$d_{[100]} = \frac{d}{\sin\alpha} \quad (3.5)$$

$$d_{[001]} = \frac{d}{\cos\alpha} \quad (3.6)$$

Henceforth, the in-plane and out-of-plane lattice parameters can be obtained by multiplying the corresponding Miller indices with the values of  $d_{[100]}$  and  $d_{[001]}$  which are expressed as:

$$a = hd_{[100]} \quad (3.7)$$

$$c = ld_{[001]} \quad (3.8)$$

The above mentioned treatment in case of a tetragonal or cubic structure will yield single peaks from the film in the eventually obtained contours. When the structure under investigation exhibits monoclinic distortions, then as result of epitaxy, the in-plane projection of  $d$  i.e  $d_{[100]}$  will be the same for all the orientations of distortion. But the out-of-plane projection ( $d_{[001]}$ ) will vary for different orientations. As a result in the contours obtained in the RSM, the peak from the film will be split depending upon the number of distortion orientations present.

### 3.3.2 Transmission electron microscopy

Transmission electron microscopy or TEM, as it is usually referred, is one of the most powerful techniques to investigate the structural properties of materials. As the name suggests, the technique makes use of a beam of electrons which is incident on the sample and the transmitted electrons are then analyzed to determine the structure. Therefore the investigated samples are thinned down to a minimal thickness in the range of few tens of nm to enable an efficient transmission of electrons [72].

In TEM, structural information can be acquired either in an image or a diffraction pattern. The images obtained can be categorized as dark-field image which is produced by analyzing those electrons which undergo diffraction from the atomic planes, or a bright-field image in which the transmitted electrons are assessed. Based on the interaction between the electrons and the sample, different contrasts can be generated depending upon the mass, inter-atomic distances and electrostatic potentials. In case of ferroelectric films, the crystallographic properties of the various ferroelectric and/or ferroelastic domains may be used to visualize these domains.

In the present work, the samples for TEM investigations were prepared either by ion milling or focused ion beam. Thereafter the samples were analyzed in TEM CM20T (Phillips, 200 keV) and JEM-4010 (JEOL, 400 keV). For certain cases, high angle annular dark field (HAADF) imaging along with scanning transmission electron microscopy (STEM) was used to analyze the samples.

## 3.4 Electrical characterization

Different types of electrical measurements were performed in the present work to characterize the photoelectric and ferroelectric properties of the material. In some cases temperature dependent studies were required to achieve a better understanding of the band structure of the material.

### 3.4.1 Ferroelectric measurements

Ferroelectric properties of materials are primarily characterized by their polarization values and corresponding switching/coercive fields. The ferroelectric properties of BiFeO<sub>3</sub> films were investigated in samples which have La<sub>0.7</sub>Sr<sub>0.3</sub>MnO<sub>3</sub> as bottom electrodes and platinum as the top electrode (sections 3.1.1 and 3.1.2).

A commercially available TF Analyzer 2000 setup (aixACCT) was used for the measurements. The top electrode is contacted with the setup *via* gold coated probes. The circuit was completed by applying silver paste to connect the bottom electrode and the ground of the setup. For the measurement, triangular voltage pulses with frequency  $f$  (Figure 3.8) are applied across the sample and the corresponding current generated is integrated over time to calculate the charge involved. The current which is produced has contributions from the leakage mechanisms, trapped charges and displacive phenomena. The displacement current depicts the ferroelectric nature of the material. Voltage pulses at high frequencies are applied in order to minimize the effect from leakage and trapped charges and emphasize on the displacive current contribution. The amount of charge can be estimated by

$$Q = \int I dt \quad (3.9)$$

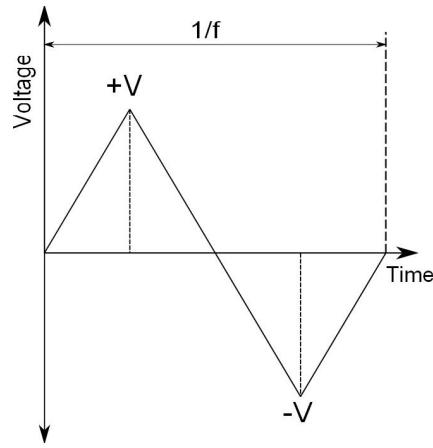


**Figure 3.8:** Triangular voltage pulse of frequency  $f$  applied across the sample to measure the polarization.

and the spontaneous polarization is calculated according to the relation

$$P_s = \frac{Q}{A} \quad (3.10)$$

where  $A$  is the effective area under the electrodes.

### 3.4.2 Photoelectric measurements

The photoelectric properties of the BFO material were investigated in thin films which were deposited directly on the substrate. The measurement electrodes were fabricated on top of the film (section 3.1.2). Different kinds of illumination sources were used in these measurements.

- LASER (Model LQC405-85E) from Newport with wavelength 405 nm and maximum power of 85 mW was used.
- White light generated from a Xenon lamp was used along with a monochromator to perform wavelength dependent studies.

In all the photoelectric measurements, the voltage across the electrodes was applied by a high input impedance electrometer from Keithley (Model: K6517) with simultaneous measurement of current. The sample was placed inside an optical cryostat from Janis (Model: VPF-700) with connections to electrodes fed out of the cryostat. The electrodes were connected to the cryostat terminals *via* copper wires and silver paste.

A schematic of the measurement setup is shown in Figure 3.9a. The pattern of fabricated electrodes is shown in Figure 3.9b. Such an arrangement of electrodes allowed for measurements with varying distance between the electrodes. The measurements were performed by centering the illumination in between the connected electrodes (Figure 3.9b). This was confirmed by measuring the current during the positioning of the illumination and obtaining the maximum photocurrent. In case of illumination *via* laser, the intensity of the laser was controlled by modulating the operational voltage of the laser.

For the experiments involving the white light-monochromator arrangement, suitable photo-detectors were used to determine the power emitted by the white light at each wavelength in the range of interest. The wavelength dependent studies can assist in



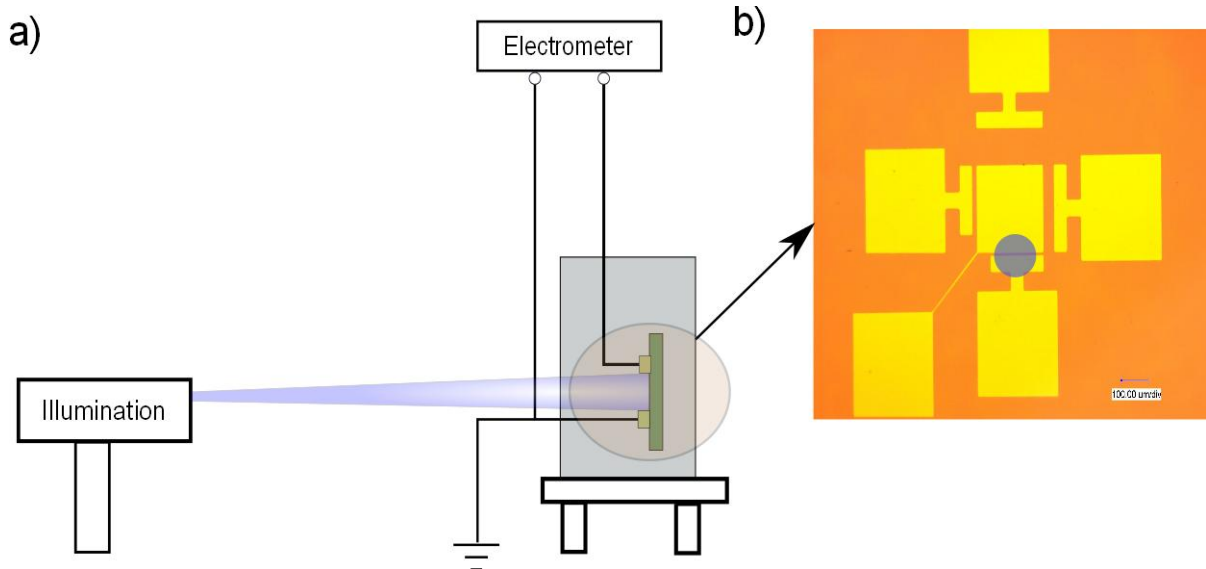


**Figure 3.9:** a) Schematic of the setup used for performing photoelectric measurements. The illumination can be either laser or white light with monochromator (not shown). b) Depiction of the illumination falling in between the measurement electrodes

determining the existence of sub-band levels which can be activated under illumination of appropriate energy or wavelength.

### Polarization dependent analysis

It was required for certain experiments to change the angle between the axis of light polarization and the flow of current. This was achieved by using a linear polarizer in tandem with a photo detector. Initially the polarizer was fixed at  $0^\circ$  and the laser was rotated till a zero intensity was obtained. This process was repeated for every  $30^\circ$  rotation of the polarizer and the corresponding laser rotations were marked which were required for zero intensity. As a result, the laser position was calibrated for different angles which the polarization axis makes with the sample orientation.

### 3.4.3 Trap level spectroscopy

One of the conventional measurements in the study of insulating or strong dielectric materials is the estimation of the activation energy of the conduction mechanism. This is realized by cooling the sample to a lower temperature and then heating at a consistent rate with a bias voltage. Simultaneously the current ( $I$ ) is recorded as a function of increasing temperature ( $T$ ). The plot of  $\ln I$  vs  $T^{-1}$  (Arrhenius plot) yields a straight line, the slope of which gives an approximation of the activation energy [73]. In case of materials with trap levels within the band gap, a similar measurement is performed with an additional operation of stimulating the material. The measurement is referred to as thermally stimulated conductivity (TSC) technique [74].

In the TSC technique the material is illuminated at a lower temperature with a light of appropriate wavelength. As a result, excess amounts of carriers are generated which might get trapped in the levels within the band gap. However, the temperature at which the material is illuminated should be low enough so that the trapped carriers do not have

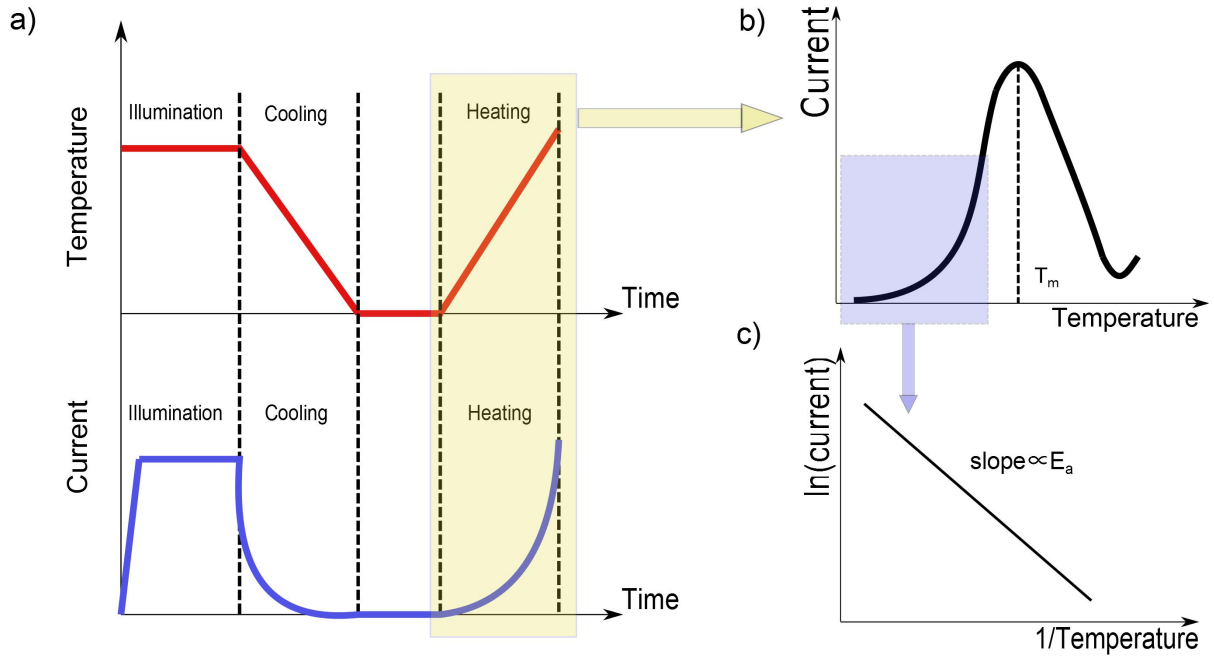


**Figure 3.10:** Process flow for the steps involved in the TSC technique in terms of temperature and the current behavior. b) Schematic of a typical plot exhibiting the behavior of the thermally stimulated current during the heating process. c) Arrhenius plot of the TSC curve in the initial rise of the current [blue area in (b)] which yields the value of  $E_a$ .

sufficient energy to be thermally released. Then the material is cooled down rapidly in order to freeze the carriers in their respective levels. Thereafter, the material is heated at a constant heating rate with simultaneous measurement of current. The process flow of the TSC technique is depicted in the schematic shown in Figure 3.10a. The current which is measured as a function of temperature during the heating process is called the thermally stimulated current [74] [75]. The typical behavior exhibited by the thermally stimulated current during the heating process is shown in Figure 3.10b. A mathematical treatment of the thermally stimulated current was reported in the work of R.H. Bube in 1960 [74] [76] which was based on the contribution from trap filling and emptying with temperature. For a given temperature, the probability ( $P$ ) of a charge carrier to escape from a trap level which is at energy level  $E_a$  below the conduction band is given by

$$P = N_{eff} v \beta_t \exp\left(\frac{-E_a}{k_b T}\right) \quad (3.11)$$

where  $v$  is the thermal velocity of the carrier at temperature  $T$ ,  $\beta_t$  is the capture cross section of the trap and  $N_{eff}$  is the effective density of states in the conduction or valence band. As a result, the rate at which the charge carriers ( $n_t$ ) are emitted from the trap level is a function of the escape probability ( $P$ ) and is expressed as

$$\frac{dn_t}{dt} = -n_t P \quad (3.12)$$

The solution of the differential equation 3.12 is given by

$$n_t = n_{t0} e^{-Pt} \quad (3.13)$$

where  $n_{t0}$  is the initial number of trapped carriers. Therefore, the change in the number of free charge carriers ( $n$ ) in a short interval of time ( $dt$ ) is given by

$$\Delta n = -\frac{dn_t}{dt}\tau \quad (3.14)$$

where  $\tau$  is the lifetime of a carrier after it is emitted from the trap. Substituting equation 3.13 into equation 3.14 results in the expression of the rate of decay of charge carriers which were trapped in the level

$$\Delta n = n_{t0}\tau P e^{-Pt} \quad (3.15)$$

In case of insulating or dielectric materials like  $\text{BiFeO}_3$ , inherently the number of thermally generated charge carriers are negligible; therefore it is convenient to assume  $\Delta n \approx n$ . As a result equation 3.15 can be written as

$$n \approx n_{t0}\tau P e^{-Pt} \quad (3.16)$$

During the TSC measurement, the temperature is increased at a constant rate; therefore  $dT = \gamma dt$  where  $\gamma$  is the rate at which the temperature (T) changes with time (t). Apparently the probability P will also depend on the variation of temperature. As a result equation (3.12) will take the form

$$\frac{dn_t}{dt} = -n_t P \exp\left(-\int \frac{P}{\gamma} dT\right) \quad (3.17)$$

Eventually, the current behavior in the TSC measurement due to the emptying of the traps can be approximated by incorporating the length (L) of the measurement gap and using equation 3.17 which leads to an expressions

$$I_{TSC} \approx \frac{1}{2} e L n_{t0} P \exp\left[\frac{-1}{\gamma} \int P dT\right] \quad (3.18)$$

Equation 3.18 can be elaborated by substituting the value of P from equation 3.11 and expressed as [77]:

$$I_{TSC} \approx \frac{1}{2} e L n_{t0} N_{eff} v \beta_t \exp\left(\frac{-E_a}{k_b T}\right) \exp\left[\frac{-v N_{eff} \beta_t k_B T^2}{\gamma E_a} \exp\left(\frac{-E_a}{k_b T}\right)\right] \quad (3.19)$$

The term before the square brackets represents the current behavior at low temperatures when the trap levels are nearly full. Apparently, for low temperatures a plot of  $\ln(I_{TSC})$  vs  $T^{-1}$  gives a straight line the slope of which gives an approximation of the activation energy ( $E_a$ ) as is shown in Figure 3.10c. This method of calculating the trap depth is known as decayed TSC [76]. The temperature at which the current  $I_{TSC}$  reaches its maximum value ( $T_m$ ) (Figure 3.10b) is obtained by differentiating equation 3.19 and equating it to zero. This results in an expression

$$E_a = k_B T_m \ln \left[ \frac{k_B T_m^2 N_{eff} v \beta_t}{\gamma E_a} \right] \quad (3.20)$$

It must be mentioned here that equations 3.19 and 3.20 are valid only in the case when a single discrete trap level exists. Moreover, for simplicity and convenience, the temperature dependencies of parameters like  $v$ ,  $N_{eff}$  and  $\beta_t$  have been neglected [76]. The area

A under the  $I_{TSC}$  curve can be obtained by integrating between two temperatures which leads to a relation

$$A \propto \gamma n_{t0} \quad (3.21)$$

It can be implied from relation 3.21 that the area under the  $I_{TSC}$  curve is directly dependent upon the heating rate ( $\gamma$ ) and gives an approximation of the initial filling of the trap level which is a direct measure of the trap level density [77].

### 3.5 Summary

In this chapter, the experimental and technical details of the various procedures performed in the present Thesis were discussed. Basic concepts of PLD which was used to fabricate thin films of BFO and LSMO were discussed. The main steps involved in photolithography technique were presented which was used to pattern top electrodes. Concepts of AFM were considered which is an important tool for surface characterization. Essential aspects pertaining to PFM along with its relevance in visualizing domains configuration in  $\text{BiFeO}_3$  thin films were elaborated. Structural properties of the thin films were investigated by XRD and TEM analysis. Specifically, XRD can be efficiently used to determine the strain and various distortion variants present in thin films. By ferroelectric testing, the polarization behavior of the films can be deciphered. Different photoelectric measurements were performed by varying the wavelength, intensity and polarization axis of light to investigate the electronic structure of the films. Finally, trap level spectroscopy was discussed which over the years has been one of the most widely used technique to detect and characterize trap levels in insulating and dielectric materials. A mathematical treatment was provided to analyze the resultant curves which are obtained.

## Bulk photovoltaic effect in epitaxial BiFeO<sub>3</sub> films

Recently the entire field of photoferroelectrics has been revitalized by reports of an abnormal photovoltaic (PV) effect in BiFeO<sub>3</sub> (BFO) thin films. The main characteristics of this abnormal PV effect are very large open circuit ( $V_{oc}$ ) photovoltages exceeding the band gap of the material. For instance, in high quality BFO thin films  $V_{oc}$  is several times larger than the band gap ( $\approx 2.7$  eV). However, reports on the photovoltaic effect in different BFO systems are rather contradictory. In a specific in-plane geometry of measuring electrodes with respect to the domain pattern, films with periodic ferroelectric/ferroelastic stripe domain patterns show  $V_{oc}$  values above [22] or below the band gap [78]. In the normal plane-parallel capacitor geometry the measured  $V_{oc}$  value has always been below the band gap values [20] [79]. Single crystals show, or do not show, large  $V_{oc}$  values depending on the source or perhaps the crystal growth details [23] [21] [80]. In ceramics, the reported values of  $V_{oc}$  have always been under the band gap [81].

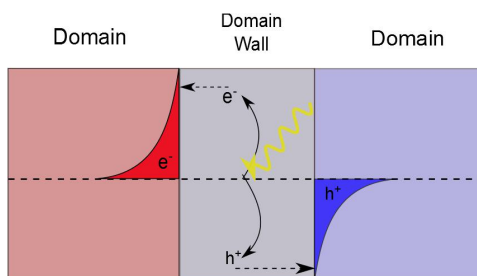


**Figure 4.1:** Separation of photo excited charge carriers in the domain wall resulting in charge build-up on either side of the domain wall (adapted from [22])

In the initial report on the abnormal PV effect [20], based on epitaxial BFO films, it was shown that  $V_{oc}$  values as large as 15 V can be obtained. However the high voltages can be obtained only in a specific geometry when the ferroelectric/ferroelastic domain walls are running parallel to the macroscopic electrodes (henceforth will be referred to as PLDW). There was no sizable PV effect if the ferroelectric domains or domain walls are perpendicular to the electrodes (which henceforth will be referred to as PPDW). In this case only a photoconductive effect was detected. Additionally in an earlier work it was proven that the domain walls in epitaxial BFO films have a conductive nature when compared to the conductivity of the domain itself [5]. Henceforth, *via* TEM and DFT studies, the existence of a potential step across the domain walls was found to be at the origin of conducting domains walls [5].

Combining the observations regarding the high  $V_{oc}$  only in PLDW geometry and the potential step across the domain wall, the following mechanism was hypothesized to explain the generation of high voltages: The carriers (electron hole pairs), under illumination, are generated equally in all of the film. But the carriers generated in the bulk will tend to recombine quickly, while the carriers at the domain wall will be under the potential that is active across the wall. As a result there is an efficient separation of carriers at the walls as is shown in Figure 4.1. Consequently, there is a voltage built up owing to the accumulation of charges across each and every domain wall. Cumulatively, the small voltages across the domain walls add up which leads to the observation of photovoltage when measured in PLDW geometry. In the past, a similar analysis has also been postulated to explain the anomalous photovoltage in zinc sulphide (ZnS) comprising of stacking faults [82]. In this case, the material was made up of alternating lattices of cubic and hexagonal structures. The charge buildup was assumed to be at the interface between the two lattices [83].

Subsequent microscopic measurements, performed *via* scanning a conductive tip in conductive force microscopy mode under illumination, in BFO single crystals revealed that high  $V_{oc}$  values can be achieved in all of the crystal irrespective of the tip position, i.e. within the domain or at the domain wall [23]. Moreover, on a microscopic scale, it has been proven that the recombination rate in the domain is not much different from that at the domain wall, which is in contrast to the initial assumptions [24]. Recently, theoretical studies, based on ab-initio calculations, have predicted that the shift currents, which are attributed to the bulk photovoltaic (BPV) effect, are at the origin of the generation of the photovoltaic current in thin BFO films [84].

Hence till now, the true origin of the anomalous photovoltaic effect in BFO is under deliberation and needs to be resolved to harness the true potential of this effect. In section 4.1 the growth of epitaxial BFO films will be studied, which will be followed by structural characterization in section 4.2. The domain analysis via PFM will be detailed in section 4.3. Subsequently, the electrical and photovoltaic properties will be elaborated in section 4.5.

## 4.1 Growth

In this section, growth and morphology of the BFO films deposited on two different substrates, namely SrTiO<sub>3</sub> and TbScO<sub>3</sub>, will be discussed. In section 4.1.1, BFO films grown on bare substrates will be investigated, while in section 4.1.2, the influence of (La,Sr)MnO<sub>3</sub> and SrRuO<sub>3</sub> buffer layers will be considered.

### 4.1.1 BiFeO<sub>3</sub> films grown on bare substrates

Epitaxial BFO films were deposited on top of TbScO<sub>3</sub> (TSO) and SrTiO<sub>3</sub> (STO) single crystalline substrates *via* pulsed laser deposition using the parameters described in table 3.1 of section 3.1.1. TSO and STO exhibit orthorhombic and cubic structures, respectively.

The TSO substrates with (110)<sub>o</sub> orientation were used for the deposition. The lattice parameters of orthorhombic TSO are:  $a_o = 5.4654 \text{ \AA}$ ,  $b_o = 5.7292 \text{ \AA}$ , and  $c_o = 7.9170 \text{ \AA}$  [85]. The (110)<sub>o</sub> plane of TSO can accommodate four pseudocubic unit cells of BFO as shown in Figure 4.2a. This is possible due to the validity of the following relations in the

$(110)_o$  plane by which the orthorhombic parameters can be converted into equivalent pseudocubic parameters (Figure 4.2b, c):

$$b_{pc} = \frac{c_o}{2} \quad (4.1)$$

$$a_{pc} = \frac{\sqrt{a_o^2 + b_o^2}}{2} \quad (4.2)$$

The calculated pseudocubic parameters of TSO in the  $(110)_o$  plane are:  $a_{pc} = 3.95 \text{ \AA}$ , and  $b_{pc} = 3.95 \text{ \AA}$ . In comparison to the pseudocubic parameters of BFO ( $a_{pc} = 3.96 \text{ \AA}$ ), the lattice mismatch between TSO and BFO is about  $-0.2 \%$ . As a result, BFO will tend to grow on TSO substrate under a compressive strain to maintain the pseudomorphic relation i.e.  $a_{pc}(BFO) = a_{pc}(TSO)$ .

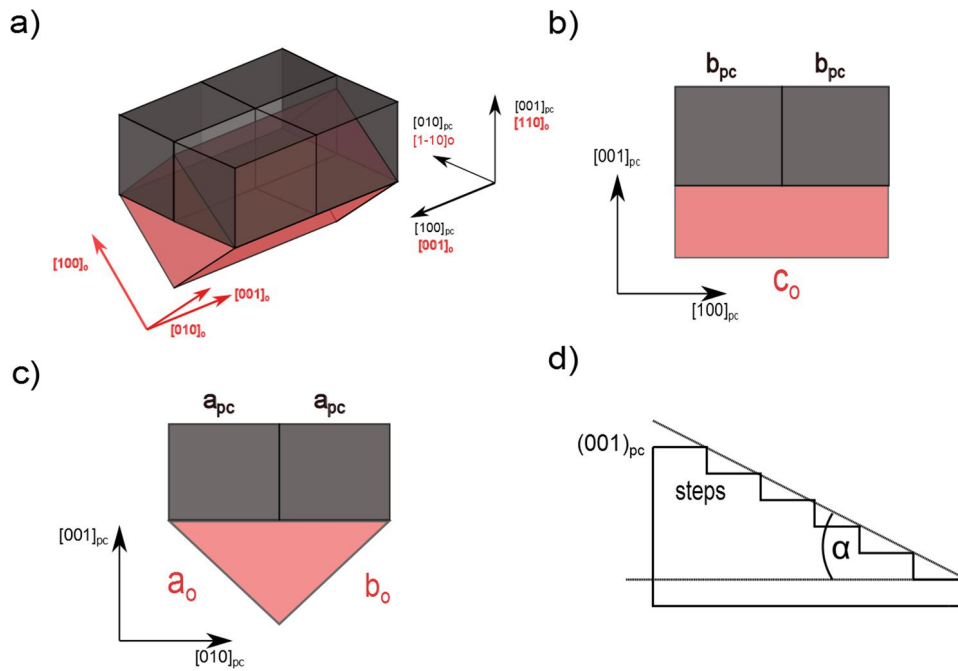


**Figure 4.2:** a) Accommodation of four pseudo cubic unit cell of BFO (black cubes) in the  $(110)_o$  plane of TSO (red wedge) and transformation of the orthorhombic coordinate system ( $o$ ) to the pseudocubic coordinate system ( $pc$ ). b) Relation between the pseudocubic parameter  $b_{pc}$  and the orthorhombic parameter  $c_o$  when viewed along the  $[001]_{pc}$  direction. c) Relation between the pseudocubic parameter  $a_{pc}$  and orthorhombic parameters  $a_o$  and  $b_o$  when viewed along the  $[100]_{pc}$  direction. d) Schematic depicting the steps on the  $(001)_{pc}$  oriented substrate with  $\alpha$  as the offcut angle.

STO substrates with  $(001)$  orientation were used. The lattice parameter of STO is  $3.905 \text{ \AA}$  [86] which makes the lattice mismatch with BFO of approximately  $-1.4 \%$ , and the pseudomorphic growth is realized under compressive stress.

In either of the substrates, there was an offcut angle of  $0.1^\circ$  with respect to the  $(001)_{pc}$  orientation. The offcut angle is defined as the angle which the plane of the substrate surface makes with the plane of terraces as is shown in Figure 4.2d. Consequently the substrates were subjected to a treatment prior to deposition. The STO substrates were etched in a solution containing 50 ml of de-ionized water, 1.5 ml of  $\text{NH}_4\text{F}$  and 0.5 ml of HF. The etching process was performed for approximately 13 to 14 seconds. Thereafter,

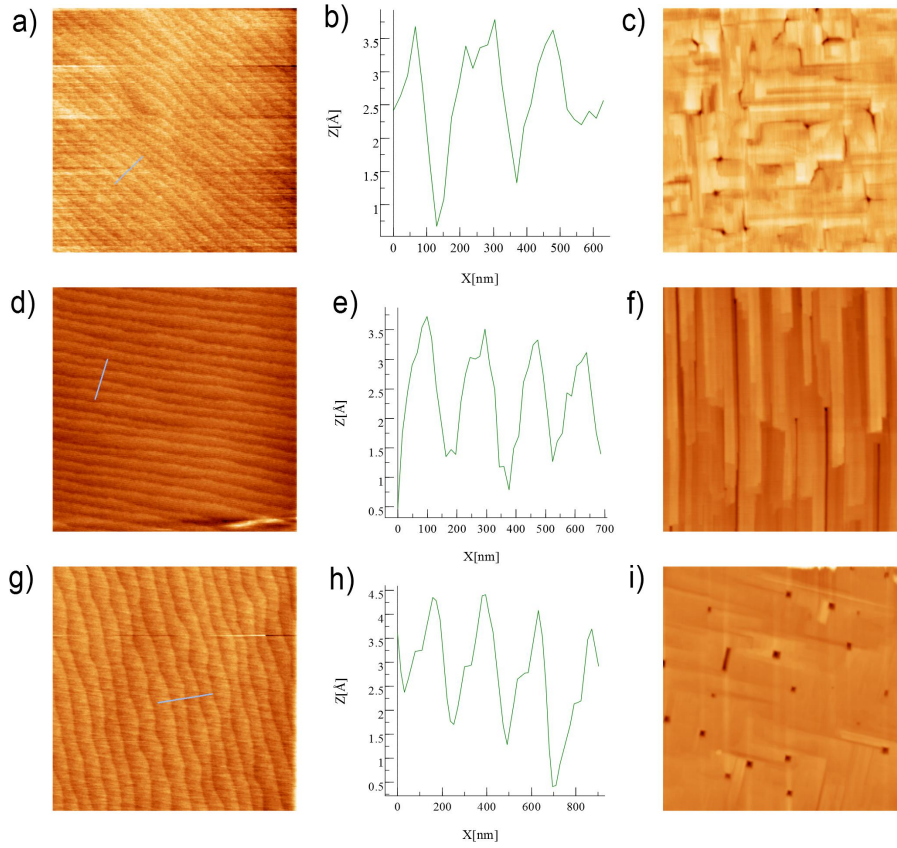


**Figure 4.3:** a) AFM image of size  $4 \times 4 \mu\text{m}$  of a STO substrate after the etching and annealing procedure. b) Profile of the line scan indicated in Figure a. c) AFM image of size  $4 \times 4 \mu\text{m}$  of a 100 nm thick BFO film grown on annealed STO. d) AFM image of size  $4 \times 4 \mu\text{m}$  of a TSO substrate after the annealing process. e) Profile of the line scan indicated in Figure d. f) AFM image of size  $4 \times 4 \mu\text{m}$  of a 100 nm thick BFO film grown on annealed TSO. g) AFM image of size  $4 \times 4 \mu\text{m}$  of a TSO substrate after annealing in  $\text{O}_2$ . h) Profile of the line scan indicated in Figure g. i) AFM image of size  $3.4 \times 3.4 \mu\text{m}$  of a 100 nm thick BFO film grown on TSO annealed in  $\text{O}_2$ .

the substrates were annealed at  $950^\circ\text{C}$  for 2 hours. The preparation of TSO substrates involved just an annealing process for 2 hours at  $1100^\circ\text{C}$ . In some cases the TSO substrates were annealed at  $1100^\circ\text{C}$  under an  $\text{O}_2$  gas flow of about 200 sccm for 2 hours.

In the STO substrates, the etching and annealing procedure results in surfaces that are dominantly terminated with  $\text{TiO}_2$  [87] [88]. In the case of scandate substrates of the type  $\text{ReScO}_3$ , at least for  $\text{DyScO}_3$ , normal annealing results in a surface which is terminated with  $\text{ScO}_2^-$ , while annealing under  $\text{O}_2$  environment results in dominant  $\text{ReO}^+$  surface termination [89]. After the annealing process, the terraces at the surface, due to the offcut angle, are revealed and are shown in Figure 4.3a for STO, Figure 4.3d for TSO and Figure 4.3g for TSO annealed in  $\text{O}_2$  environment. The line profiles acquired across the terraces in all the substrates (Figures 4.3b, e, and h) result in a step height between  $3.5 \text{ \AA}$  and  $3.7 \text{ \AA}$  which is comparable to the  $a_{pc}$  of either.

The morphology of the 100 nm thick BFO films grown directly on bare STO and TSO substrates is shown Figure 4.3c and f, respectively. The root mean square (RMS) roughness for the BFO film grown on STO is 1.5 nm and the one grown on TSO is 1.92 nm. In either of the morphologies, the steps from the substrates are not transferred to the



film which suggests a 3-D growth mode. The BFO films on STO have a mosaic kind of pattern, while films on TSO have stripe-like morphology. The stripe-like morphology on TSO has also been predicted in theoretical studies by considering the mechanical and electrostatic constraints for the coexistence of different variants of ferroelastic domains.

However the BFO film grown on TSO that was annealed in O<sub>2</sub> environment has a different morphology, as shown in Figure 4.3i, as compared to the film grown on TSO subjected to normal annealing. The stripe-like morphology is replaced with stripes which are crossing each other at 90°. The different morphology can be attributed to a different termination of the TSO substrate due to the annealing in O<sub>2</sub>. The deposition of BFO is performed at 650 °C which is below its Curie temperature. As a result there is an in-situ domain formation during the growth process. As described in section 2.1.3.3, BFO has a possibility to form different variants of ferroelastic domains which can also affect the morphology. A different termination might favor the formation of certain variants more than of others, as a result of which the morphology will also change. The different domains corresponding to different morphologies will be discussed in the subsequent sections.

### 4.1.2 BiFeO<sub>3</sub> films grown on buffered substrates

In certain samples, a thin layer of a conducting perovskite material was grown on the substrate, prior to the deposition of the BFO film, to allow for the investigation of the ferroelectric characteristics of the BFO film. Two types of conducting perovskite were used, namely, (La<sub>0.7</sub>Sr<sub>0.3</sub>)MnO<sub>3</sub> (LSMO) and SrRuO<sub>3</sub> (SRO). LSMO and SRO have rhombohedral and orthorhombic structures at room temperature, respectively. Likewise as in the case of rhombohedral BFO and orthorhombic TSO, the lattice parameters of the two conducting perovskites can be given in pseudocubic notation and are  $a_{pc(LSMO)} = 3.78 \text{ \AA}$ , and  $a_{pc(SRO)} = 3.92 \text{ \AA}$ .

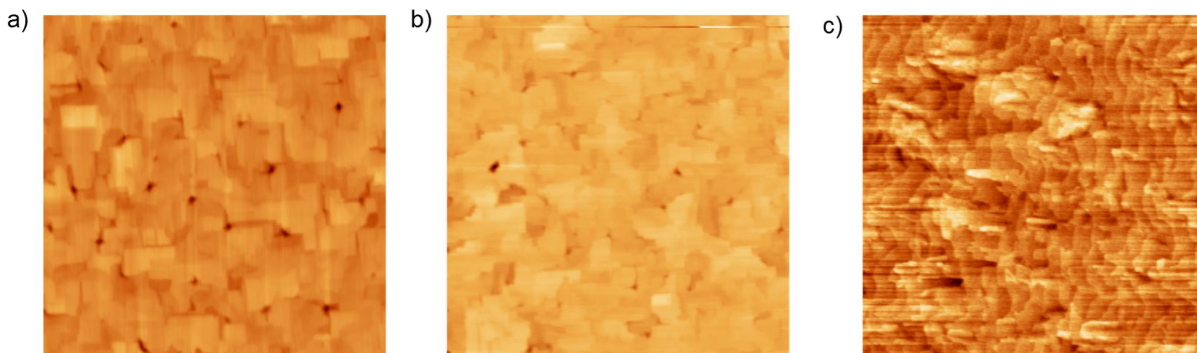


**Figure 4.4:** AFM image of size 4x4 μm of a 100 nm thick BFO film grown on an annealed STO with a) LSMO and b) SRO as the bottom electrode. c) AFM image of size 4x4 μm of a 100 nm thick BFO film grown on an annealed TSO with LSMO as the bottom electrode.

For the STO substrate, SRO and LSMO were used as bottom electrodes, whereas for the TSO substrate LSMO was chosen as the conducting layer. Figures 4.4a and b show the AFM images of 100 nm thick BFO films grown on STO substrate with LSMO and SRO as the bottom electrode, respectively. The change in the morphology in reference to the BFO film that was grown on bare STO (Figure 4.3c) is evident. Also, irrespective of the bottom conducting layer, the surface roughness in either of the film is between

1.5 and 1.7 nm. The absence of the steps from the substrate indicates 3-D growth. It must be mentioned here that reports have exhibited the step flow growth of BFO on SRO in thin films in the range of 20 to 30 nm [67] [90]. Nevertheless, the change in the morphology, for the same thickness of BFO as that was deposited on bare substrate, might be due to the role of the type of termination at the surface of the conducting layer. It has been proven in the case of SRO that the diffusivity at the surface is highly affected by the type of termination which in turn can also affect the type of growth [91]. A similar observation can be made in the case of the 100 nm thick BFO film grown on LSMO-buffered TSO substrate (Figure 4.4c). The stripe-like morphology of the BFO film on bare TSO (Figure 4.3f) is completely lost, and the corresponding RMS surface roughness is 1.49 nm.

## 4.2 Structural investigations

In this section structural aspects of the films deposited on different substrates will be investigated. Emphasis will be given to the films that are deposited on bare TbScO<sub>3</sub> substrate since they are the basis of the study of the bulk photovoltaic effect in BiFeO<sub>3</sub>. The films were analyzed by performing  $2\theta$ - $\omega$  scans (of section 3.3.1.1). Reciprocal space maps or the RSMs (as mentioned in section 3.3.1.2) were acquired for some films to analyze the manifestation of different ferroelastic domains and to validate the pseudomorphic relation between the substrate and the film.

### 4.2.1 $2\theta$ - $\omega$ scans

In order to acquire the  $2\theta$ - $\omega$  scans, the  $(001)_{pc}$  plane was chosen as the reference for the films deposited on SrTiO<sub>3</sub> and TbScO<sub>3</sub> substrates. By analyzing the position of the peaks in terms of  $2\theta$  and using the Bragg equation, it is possible to calculate the out-of-plane parameters for the respective materials.

In Figure 4.5a and b the  $2\theta$ - $\omega$  scans for BFO films grown on bare TSO substrate and LSMO-buffered TSO substrate are shown, respectively. It is evident from Figure 4.5a, that the peaks originating from the  $(001)_{pc}$  plane of the film and substrate are hardly distinguishable from each other. The lattice mismatch between the BFO and TSO is about -0.25% which results in a minimal change in the out-of-plane lattice parameter ( $c_{pc(BFO)}$ ) of BFO in comparison to the  $c_{pc(TSO)}$  due to which the peak from BFO is overshadowed by that of the TSO substrate. On the other hand, the lattice mismatch between LSMO and TSO is about +2.02%, as a result of which LSMO grows on top of TSO under tensile strain, which tends to reduce the  $c_{pc}$  of LSMO. This is also observed in the  $2\theta$ - $\omega$  scan shown in Figure 4.5b where the  $(001)_{pc}$  peak from LSMO appears on the right side of the BFO and TSO peaks. The resultant  $c_{pc}$  of LSMO due to the tensile strain is about 3.85 Å.

The  $2\theta$ - $\omega$  scans obtained for the BFO films grown on STO substrates with LSMO and SRO as the buffer layer are shown in Figures 4.5c and d, respectively. The BFO grows under a compressive strain of -1.5% on STO as a result of which the  $c_{pc}$  of BFO expands to about 4.06 Å as is calculated from the scan shown in Figure 4.5c. Reports have suggested that the growth of BFO on STO is accompanied with monoclinic distortion. Also the high  $c/a$  ratio ( $\approx 1.04$ ) that is obtained is considered as one of the ways of enhancing the ferroelectric polarization value. However, recently a better alternative for

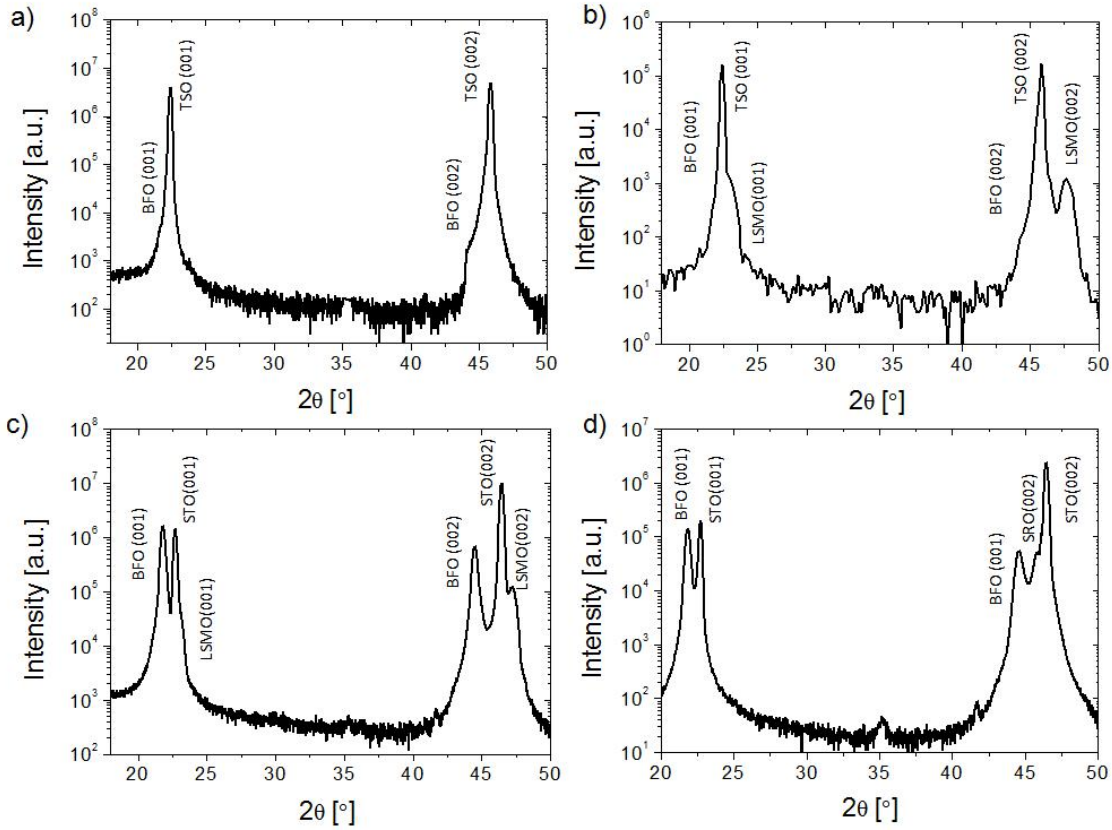


**Figure 4.5:**  $2\theta$ - $\omega$  scans obtained around the  $(001)_{pc}$  plane for 100 nm thick BFO film deposited on a) annealed TSO, b) annealed TSO with 10 nm thick LSMO as the bottom electrode, c) annealed STO with 20 nm thick LSMO and d) annealed STO with 60 nm thick SRO.

this purpose has been explored in BFO films grown on  $\text{LaAlO}_3$  substrate. Such a system has also been investigated, and is discussed in chapter 5. The effect of strain, due to the pseudomorphic relation with the substrate, is also observed in the growth of the LSMO buffer layer. LSMO, as in the case of TSO, grows under a tensile strain on STO which causes its  $c_{pc}$  to reduce to a lower value of  $3.83 \text{ \AA}$ . Similar details are also evident for the BFO film grown on top of SRO with STO as the substrate as shown in Figure 4.5d. The  $c_{pc}$  of BFO is about  $4.06 \text{ \AA}$ . The pseudomorphic growth of SRO on top of STO is realized under a strain of about  $-0.46 \%$  which leads to a slight expansion of its  $c_{pc}$ . As a result, the  $(001)_{pc}$  peak of SRO is overshadowed by that of STO. Nevertheless, the peak due to SRO separates out when the peaks from the  $(002)_{pc}$  planes are considered.

### 4.2.2 Reciprocal space map investigations

As mentioned in section 3.3.1.2, the investigation of reciprocal space maps (RSM) can provide information to prove the pseudomorphic relation between the film and the substrate, i.e. to analyze whether  $a_{film} = a_{substrate}$ . Moreover, in the scenario where the polarization leads to structural distortion (also referred to as ferroelastic domains), which is the case in BFO, RSM can be regarded as one of the tools to observe different types of distortion variants.

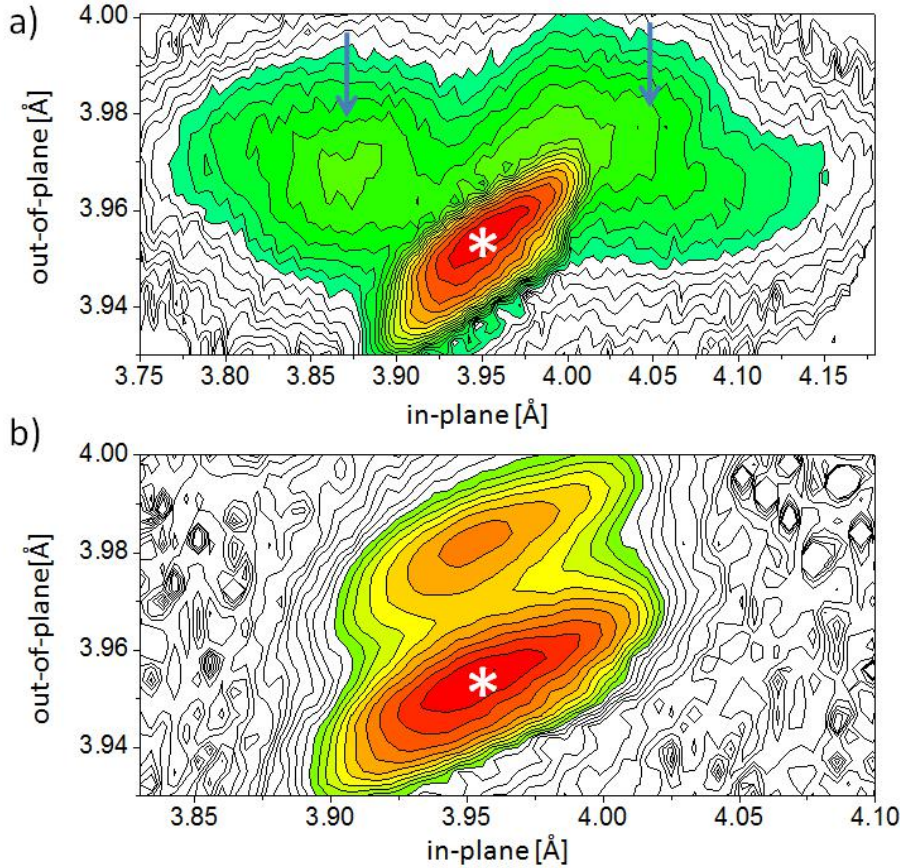


**Figure 4.6:** RSM obtained around the  $(103)_{pc}$  plane for a 100 nm thick BFO film deposited on a) an conventionally annealed TSO substrate and b) an O<sub>2</sub> annealed TSO substrate. The arrows indicate the two variants and the peaks from the substrates are marked with a white star.

To perform RSM investigations, a plane which includes information about the in-plane lattice parameter was chosen for reference. In the case of BFO films that were deposited on the TSO substrate, the  $(113)$  plane of orthorhombic symmetry was chosen as the reference plane. This plane translates into a  $(103)$  plane in the pseudocubic notation. Figure 4.6 shows the RSM contours obtained around the  $(103)_{pc}$  plane of the TSO substrate. The substrate peaks have been marked for convenience and the contours are presented in the out-of-plane ( $c$ ) and in-plane ( $a$ ) lattice parameters.

It has been proven, theoretically [92] and experimentally [93], that the deposition of BFO on bare TbScO<sub>3</sub> or on any other orthorhombic scandate (ReScO<sub>3</sub>) substrate results in the formation of 109° domain patterns in the films. This has been analyzed by considering the energies corresponding to the depolarization field ( $F_d$ ), elastic energy ( $F_e$ ) due to the substrate/film interface and the domain wall energy ( $F_{dw}$ ) [92]. Additionally, as was shown in Figure 2.6c of section 2.1.3.3, the polarization vector alternates between up and down directions in consecutive domains in the case of 109° domain pattern. This feature considerably reduces the energy due to the depolarization field and assists the system in attaining an overall minimum energy state which makes the formation of a 109° domain pattern more favorable. The formation of a 109° domain pattern means the dominance of only two out of the four variants possible which were shown in Figure 2.6b

in section 2.1.3.3, i.e. only one pair of variants can be present. This is also visible in Figure 4.6a where the RSM obtained from a 100 nm thick BFO film that was deposited on bare TSO is shown. The peak arising due to the  $(103)_{pc}$  plane of the BFO film is split into two which indicates the dominance of two variants. However it is not possible to clearly distinguish which pair amongst the four possible (r1-r2, r2-r3, r3-r4 or r4-r1) is dominant since all the pairs will result in a similar contour in the RSM.

Nevertheless, there are different theories which have been proposed to explain the criterion that controls and decides the dominance of only one pair of variants. The slight mismatch between the two in-plane lattice parameters of the orthorhombic scandate substrates has been postulated as one of the reasons for the suppression of all the other pairs except one [93]. Another explanation takes into account the monoclinic distortion in the pseudocubic unit cell of the scandate substrate. The distortion tends to reduce the symmetry in such a way that only two out of the four structural variants of BFO will be preferred [67] [90].

The RSM around the  $(103)_{pc}$  plane for a BFO film that was deposited on a TSO substrate which was annealed in an atmosphere of  $O_2$  is shown in Figure 4.6b. The peak from the  $(103)_{pc}$  plane of the BFO film is evident with the second peak barely spreading out. The peak splitting seems to be more prominent in the case shown in Figure 4.6a than in Figure 4.6b. This could be due to the presence of the variants which have a polarization either all up or down, as a result of which the distortions corresponding to all the domains exist also in one direction i.e. either up or down. Such kind of arrangement of domains is also relevant when the film contains a  $71^\circ$  domain pattern. This is unlike the case of a  $109^\circ$  domain pattern where the distortion alternates up and down, in consecutive domains, making the peaks due to either of the variants more apparent. One of the ways of visualizing a more evident peak split can be to select a different order of planes for reference.

A similar RSM analysis was performed on BFO films that were deposited on substrates buffered with conducting perovskite layers (i.e. LSMO and SRO) and the corresponding contours obtained are presented in Figure 4.7. Figure 4.7a shows the RSM contour acquired around the  $(103)_{pc}$  plane for a BFO film deposited on TSO substrate that was buffered with LSMO as the conducting layer. The thickness of LSMO and BFO films is approximately 10 nm and 100 nm, respectively. The dotted line shows that apparently both the films, LSMO and BFO, have adopted the  $a_{pc}$  of the substrate. Also it is noteworthy to mention the position of the peak arising due to the  $(103)_{pc}$  plane of LSMO which appears on the left side of the TSO substrate peak. This proves that the growth of LSMO is under a tensile strain on TSO, which results in a reduced  $c_{pc}$  of LSMO in comparison to that of the relaxed LSMO.

The RSM corresponding to the BFO film grown on STO buffered with SRO is shown in Figure 4.7b. The thickness of the SRO and BFO films is approximately 80 nm and 100 nm, respectively. Either of the films have adapted to the  $a_{pc}$  of the STO substrate which proves the pseudomorphic growth.

It is noteworthy to mention that in either of the contours shown in Figure 4.7, a faint BFO peak elongation is evident that is rather similar to the contour given in Figure 4.6b. From this one might speculate that the BFO grown on buffered substrates is dominated by variants which have the polarization directed all up or down, which eventually makes the peak splitting less apparent. However, in the case of SRO-buffered STO substrates it has been reported that by increasing the thickness of SRO and keeping the thickness

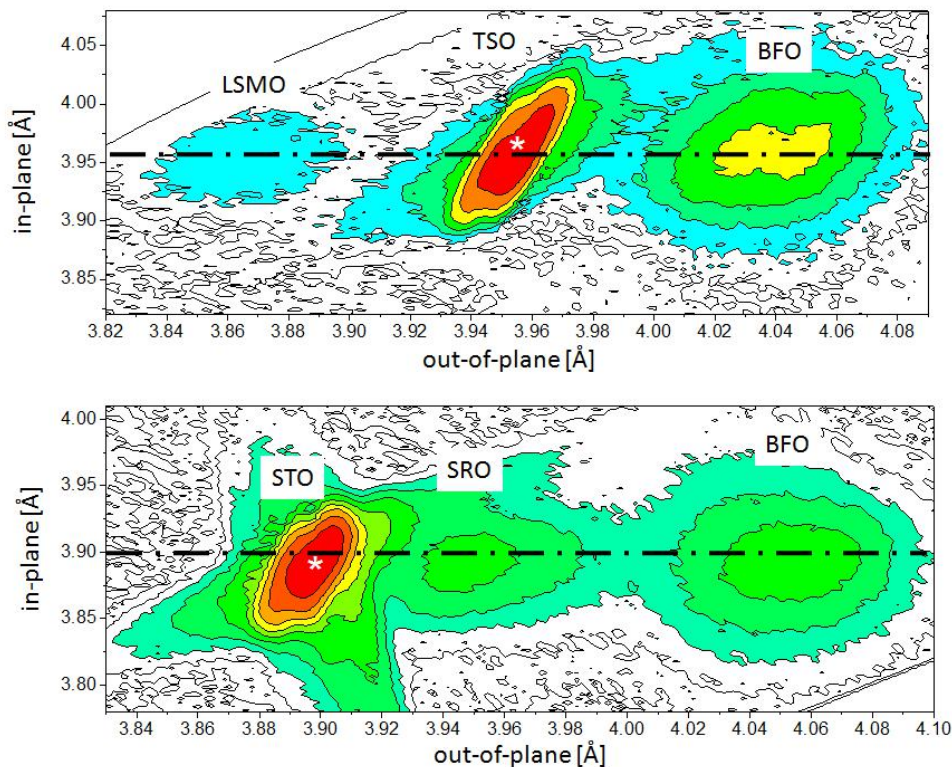


**Figure 4.7:** RSM obtained around the  $(103)_{pc}$  plane for a 100 nm thick BFO film deposited on a) TSO substrate with 10 nm thick LSMO as the buffer layer and b) STO substrate with 80 nm thick SRO as the buffer layer. The peaks from the substrates are marked with a white star.

of BFO film constant, there is a gradual change in the type of domain pattern which changes from  $109^\circ$  to  $71^\circ$  [94].

### 4.2.3 TEM investigation

TEM investigations were performed on approximately 100 nm thick BFO films deposited on bare TSO substrates that were normally annealed and annealed under O<sub>2</sub> atmosphere. Figure 4.8a shows a bright-field TEM micrograph obtained from the BFO film on normally annealed TSO substrate. The dark and bright contrast indicates the presence of different domains or structural variants. The vertical boundaries that appear are in the  $(100)_{pc}$  family of planes. The orientation of these boundaries is identical to the  $109^\circ$  vertical domain walls proposed by the theory. In Figure 4.8b a high resolution TEM image is shown which depicts the structural coherency on either side of the boundary. The presence of domains separated by  $109^\circ$  domain walls means that the film consists of variants which are distorted in upwards and downwards direction in alternate domains and as a result were more apparently visible in the RSM as well.

Figure 4.8c shows a TEM micrograph for a BFO films deposited on TSO that was annealed in O<sub>2</sub> atmosphere. In this case, the boundaries separating the dark and bright contrast seem to be inclined with respect to the interface. Such boundaries resemble the  $71^\circ$  domain walls described in section 2.1.3.3 that belong to the  $(101)_{pc}$  family of planes.

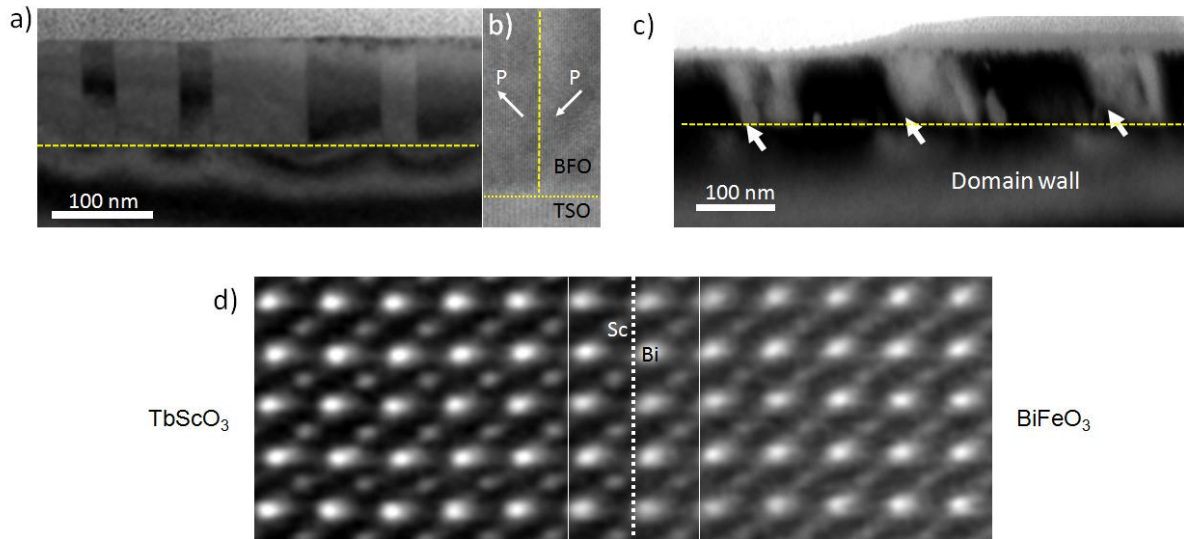


**Figure 4.8:** a) TEM micrograph of a 100 nm thick BFO film grown on an annealed TSO substrate. b) HR-TEM image image obtained at the interface between two domains in image a. c) TEM micrograph of a 100 nm thick BFO films grown on an O<sub>2</sub> annealed TSO substrate. d) High-resolution HAADF-STEM image obtained from the substrate-film interface region of image a. The horizontal yellow dotted line in figures a-c indicate the substrate-film interface.

The distortion in such variants or domains that are separated by such boundaries remains either upwards or downwards as also speculated from RSM.

Figure 4.8d is a HAADF-STEM image acquired from the interface of BFO film whose TEM image is shown in Figure 4.8a. Since in HAADF-STEM images, also named Z-contrast images (where Z refers to the atom number of the elements) the brightness of atoms is monotonically increasing with Z, in Figure 4.8d we can assign the elements to the dots in the image in both TSO and BFO, as shown by the symbols Sc and Bi. This means that TSO has a ScO<sub>2</sub><sup>-</sup> termination is also in agreement with previous studies on DyScO<sub>3</sub> which show a ScO<sub>2</sub><sup>-</sup> termination under conventional annealing. This result was confirmed by EELS investigation by Dr. Y. H. Kim in our group (not shown here).

From the above discussions the presence of 109° and 71° domain walls can be validated in films grown on bare TSO that were annealed normally and under O<sub>2</sub> atmosphere, respectively. In the subsequent section regarding PFM studies, the manifestation of these two types of domain walls and the corresponding domain arrangements will be explained.

## 4.3 PFM studies

As was mentioned in section 3.2.2, PFM can be regarded as one of the important tools to analyze and examine the presence of different kinds of domains in a ferroelectric material. In this section, emphasis will be given to the domains formed in BFO films that were deposited on bare TSO substrates, since these films were eventually used to accomplish the final motive of understanding the role of domain and domain walls in the abnormal photovoltaic effect in BFO.

Following from the discussion presented in section 3.2.3 regarding the importance of the cantilever alignment with respect to the polarization directions, PFM scans were performed in two orientations. Figure 4.9 shows the topography and the corresponding PFM images obtained for a 100 nm thick BFO film deposited on bare TSO substrate. A stripe pattern in the topography is apparently visible in Figure 4.9a. The stripes run along the  $[010]_{pc}$  direction. In the first orientation the PFM cantilever is oriented parallel to the direction of stripes. In the VPFM-phase image shown in Figure 4.9c, stripes with alternating yellow and brown colors were obtained which indicates the projection of polarization switches between up and down directions. In the LPFM-phase image shown in Figure 4.9e, a mosaic-like pattern was obtained. It is noteworthy to mention that areas of the film which show yellow (and brown) patches in the LPFM-phase image show stripes in the VPFM-phase images. Such kind of arrangement of polarization projections can be understood by a schematic that is shown in Figure 4.9f where the polarization directions related to the two structural variants r1 and r2 are indicated. In this orientation, the stripes in the VPFM-phase image can be attributed to either switching between  $P_2^+$  and  $P_1^-$  or between  $P_1^+$  and  $P_2^-$ . Additionally the yellow and brown patches in the LPFM-phase images are due to the left and right deflection of the cantilever, respectively.

To be certain regarding the presence of only two variants, the orientation of the film was changed so that the stripes in the morphology become perpendicular to the cantilever (Figure 4.9g). The PFM images for this orientation are shown in Figures 4.9h-k. Interestingly in this orientation, the phase image of the VPFM (Figure 4.9i) is identical to the phase image of the LPFM (Figure 4.9k). Figure 4.9l shows a schematic to explain such kind of observation. It must be mentioned here that the cube in Figure 4.9l is rotated by  $90^\circ$  in comparison to the cube shown in Figure 4.9f to depict the change of film orientation with the cantilever. From the schematic it is rather evident that the only possibility to have identical phase images in LPFM and VPFM is when the polarization projection alternates between  $P_2^+$  and  $P_1^-$  or  $P_2^-$  and  $P_1^+$  in subsequent unit cells.

Thus taking into account the information obtained from the PFM scans of the two orientations one can conclude the presence of only two structural variants, i.e. r1 and r2, which were also observed in the RSM study of a similar film. Also in either of the orientations the polarization projection alternates only between  $P_2^+$  and  $P_1^-$  or  $P_1^+$  and  $P_2^-$ . Hence the formation of domain walls can be visualized as shown in Figure 4.9m where the polarization switches between  $P_2^+$  and  $P_1^-$ . Another possibility where the polarization switches from  $P_2^-$  to  $P_1^+$  is depicted in Figure 4.9n. In either of the cases the domain walls separate polarizations which make an angle of  $109^\circ$  with each other. Hence these domain walls can be categorized as  $109^\circ$  walls as was also described previously in section 2.1.3.3.

A similar analysis was performed for a 100 nm thick BFO film that was deposited on a TSO substrate subjected to annealing under O<sub>2</sub> atmosphere. The morphology and the corresponding PFM scans for such a film are presented in Figure 4.10. Likewise, as in the case of the film with the  $109^\circ$  domain pattern, for the first orientation the cantilever was aligned along the  $[010]_{pc}$  direction as depicted in Figure 4.10a. However in contrast to the film with  $109^\circ$  domain pattern, in this case the signal acquired in the VPFM image largely corresponded to one direction. This is evident from the VPFM phase image (Figure 4.10c) which consists of one color, i.e. yellow, which means that the projection of polarization is in the upward direction. However the phase image in the LPFM (Figure 4.10e) exhibits alternating stripes of yellow and brown color, which indicates alternating projections of the polarization in left and right, direction respectively. The arrangements



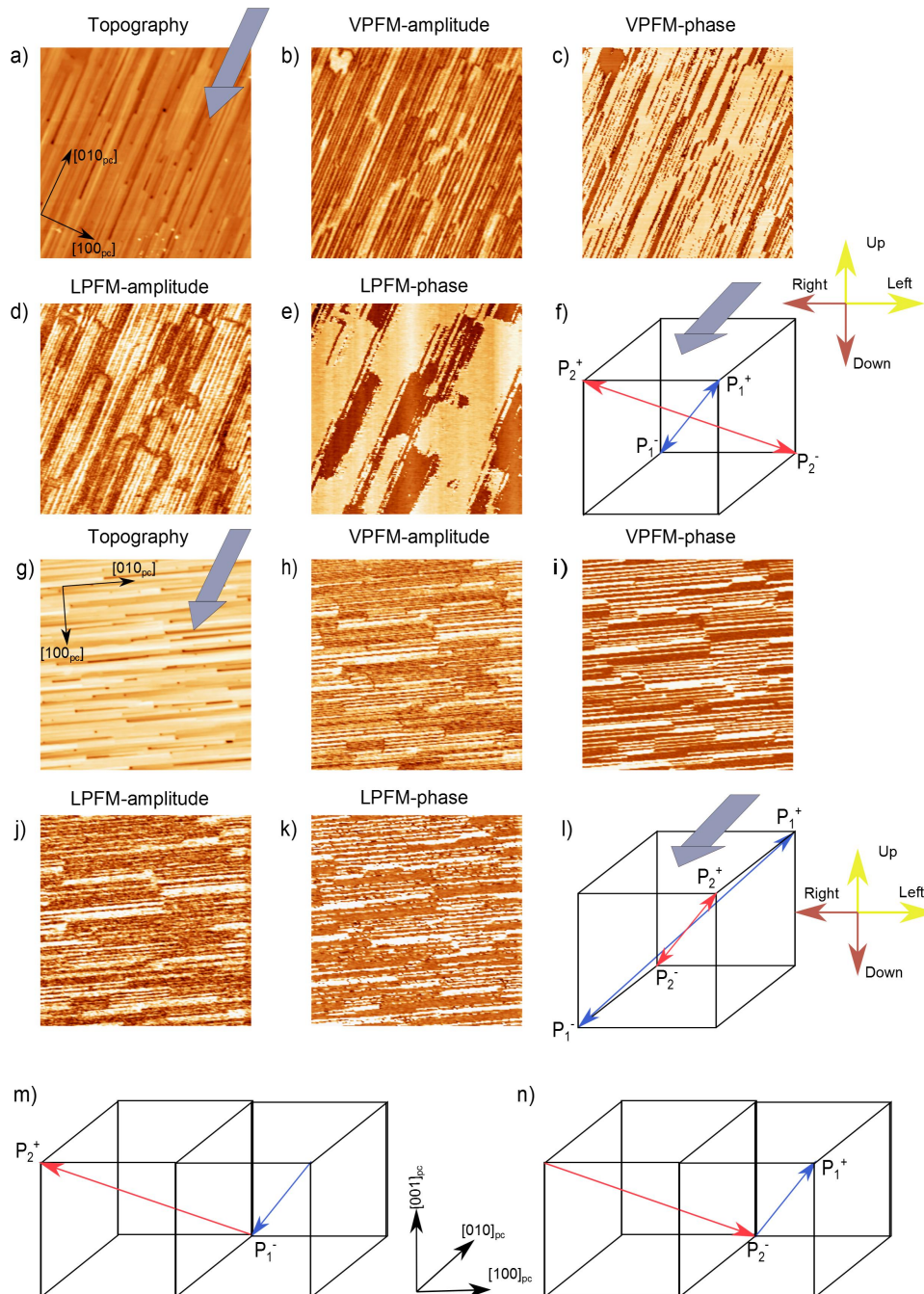


**Figure 4.9:** AFM and PFM images of size  $4 \times 4 \mu\text{m}$  for a 100 nm thick BFO film deposited on bare TSO substrate. Images a-f correspond to the orientation when the cantilever (arrow) is aligned along the  $[010]_{pc}$  direction of the sample and images g-l correspond to the orientation when the cantilever is aligned along the  $[100]_{pc}$  direction of the sample. Images f and l depict a schematic to visualize the possible active polarization variants. The  $109^\circ$  domain walls can be formed by switching between polarization variants m)  $P_1^-$  to  $P_2^+$  or n)  $P_2^-$  to  $P_1^+$ .

of polarization variants that can be responsible for such PFM scans are shown in the schematic in Figure 4.10f; it is identical to the schematic in Figure 4.9f. The single color in the VPFM phase means that the polarization projection remains upwards which can be only due to  $P_1^+$  and  $P_2^+$ . The alternating colors in the LPFM phase can then be attributed

to a sequential change between polarization variants  $P_1^+$  and  $P_2^+$ . The PFM scans in the other orientation (not shown) by aligning the cantilever along  $[100]_{pc}$  resulted in consistent colors in the VPFM and LPFM images indicating all the polarization variants are in one direction. From these observations it can be concluded that the domains in the film comprise of only  $P_1^+$  and  $P_2^+$  polarization variants which are arranged as depicted in Figure 4.10g. The presence of such variants was also speculated in the RSM studies where the dominance of variants with distortions either all up or down was proposed. The resulting striped domain pattern is known as  $71^\circ$  pattern since the angle between the two directions of polarization variants is  $71^\circ$ .

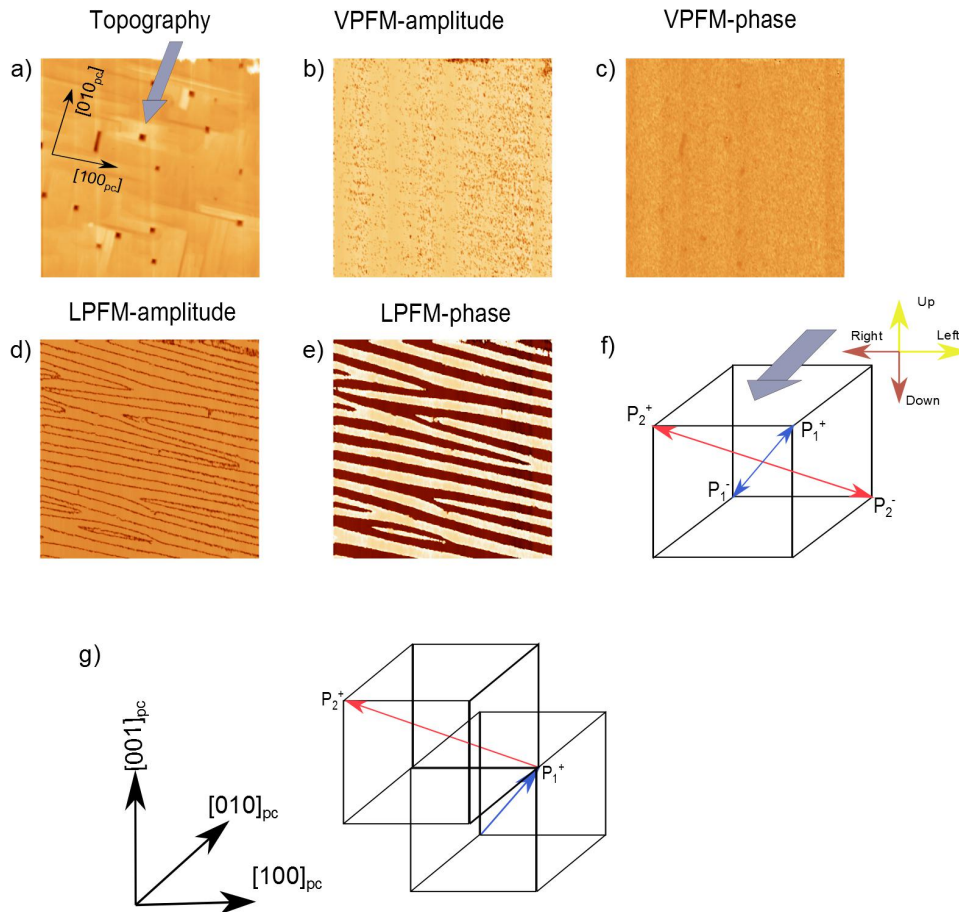


**Figure 4.10:** a) AFM and b-e) PFM images of size  $4 \times 4 \mu\text{m}$  for a 100 nm thick BFO film deposited on  $\text{O}_2$ -annealed TSO substrate when the cantilever (arrow) is along the  $[010]_{pc}$  direction. f) A schematic to visualize the possible active polarization variants. g)  $71^\circ$  domain walls formed by switching between polarization variants  $P_1^+$  to  $P_2^+$ .

It can be concluded from the above analysis of the two domain patterns, i.e.  $71^\circ$  and  $109^\circ$  patterns, that either of the patterns consists of identical structural variants: r1 and r2. This is largely in accordance with the theoretical studies from Streiffer et. al. [45] according to which both the domain patterns consist of the same structural variants. However, the variants in either of the patterns must be arranged at  $90^\circ$  to each other which is also apparent from the above PFM analysis, since the domain walls in the  $109^\circ$  and  $71^\circ$  patterns run along  $[100]_{pc}$  and  $[010]_{pc}$  directions, respectively. Nevertheless, the selection of the dominant polarization variants varies in both these cases and might depend upon the termination of the substrate. In case of  $\text{DyScO}_3$  a change of termination

from the usual  $\text{ScO}_2^-$  to  $\text{DyO}^+$  has been reported by annealing in  $\text{O}_2$ . It is, however, not possible in the present study to confirm such a phenomenon in the case of  $\text{TbScO}_3$ .

Unlike the periodic domain arrangement obtained in the BFO films that were deposited on TSO substrates, the domain pattern observed in the PFM analysis of a BFO film deposited on an annealed STO substrate was rather complex and is shown in Figure 4.11. The PFM response remains similar irrespective of the alignment of the cantilever with the film (only one alignment shown). The presence of a mosaic kind of pattern comprising of yellow and brown colors in the VPFM phase image (Figure 4.11c) indicates that the polarization projection switches between up and down direction without any periodicity. In the LPFM phase (Figure 4.11e), stripe patterns appear only in small patches. The rest of the area is rather scattered which indicates that the polarization projection is switching between left and right directions without much consistency. From such disordered arrangements of domains, the presence of more than two structural variants with their active polarization variants can be speculated.

Therefore, for the electrical and photoelectrical measurements, only the BFO films with periodic domain patterns which were grown on TSO substrates were used, so that the role of domains and domain walls in the photovoltaic effect can be clearly identified.

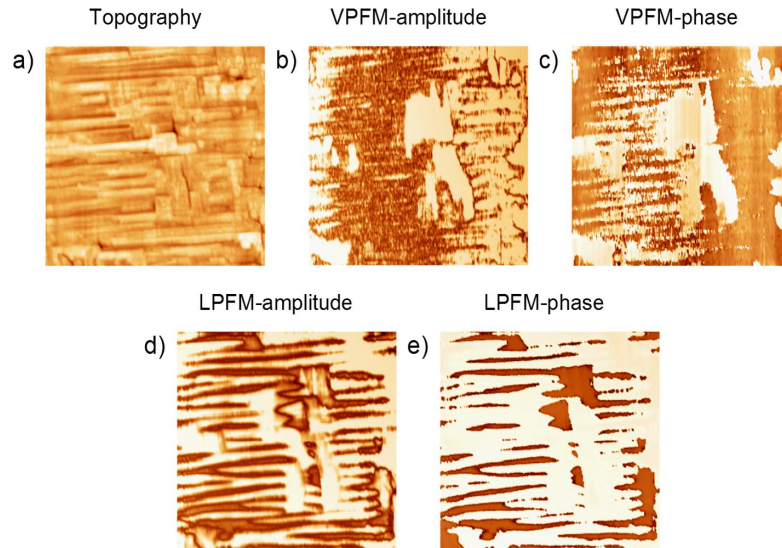


**Figure 4.11:** a) AFM and b-e) PFM images of size  $4 \times 4 \mu\text{m}$  for a 100 nm thick BFO film deposited on an annealed STO substrate.

## 4.4 Ferroelectric characteristics

The ferroelectric nature and behavior of the BFO films was investigated macroscopically and microscopically. In either of the investigations, films with bottom electrodes were used.

The macroscopic investigation was performed by using a setup that was explained previously in section 3.4.1. Platinum electrode pads of size  $10 \times 10 \mu\text{m}$  were fabricated at the top of the film. Figure 4.12 shows the polarization and the corresponding switching current loops. Figure 4.12a shows a measurement acquired at room temperature for a 100 nm thick BFO film with STO as the substrate and 60 nm thick SRO as the bottom

electrode. The inability to well define the position of coercive and saturating fields from the loops indicates towards the activity of leakage mechanisms. However such loops are considered inherent to the ferroelectric nature of BFO films. Some studies have attributed the Pool-Frenkel (PF) emission mechanism as the origin of leakage currents at room temperature [95]. Other investigations have revealed the temperature dependence of leakage mechanisms with space charge limited current behavior dominant at low temperature and PF at higher temperature. Fowler-Nordheim tunneling mechanism have also been proposed under high electric field and temperature [96].

Chemical doping has often been used as one of the ways to to counter the problem of leakage [97]. Doping with elements like Tb, La [98] and Nb [99] have resulted in largely reduced leakage currents with Mn-doping yielding the highest polarization values [100]. Additionally, the polarization values along with corresponding coercive fields are also affected by the in-plane strain applied by the substrate [101]. The polarization and current loops obtained at room temperature for a 100 nm thick BFO film deposited on TSO with 10 nm of LSMO as the buffer layer are shown in Figure 4.12b. Even though the acquired loops are improved in comparison to those obtained on STO/SRO, leakage still seems to be dominant. However, by decreasing the temperature to 150 K the effect of leakage is massively reduced which is validated by more symmetrical and saturated polarization loops as shown in Figure 4.12c. One might suspect from this observation the role of some trap levels which are active at room temperature and which eventually become dormant as the temperature is decreased.

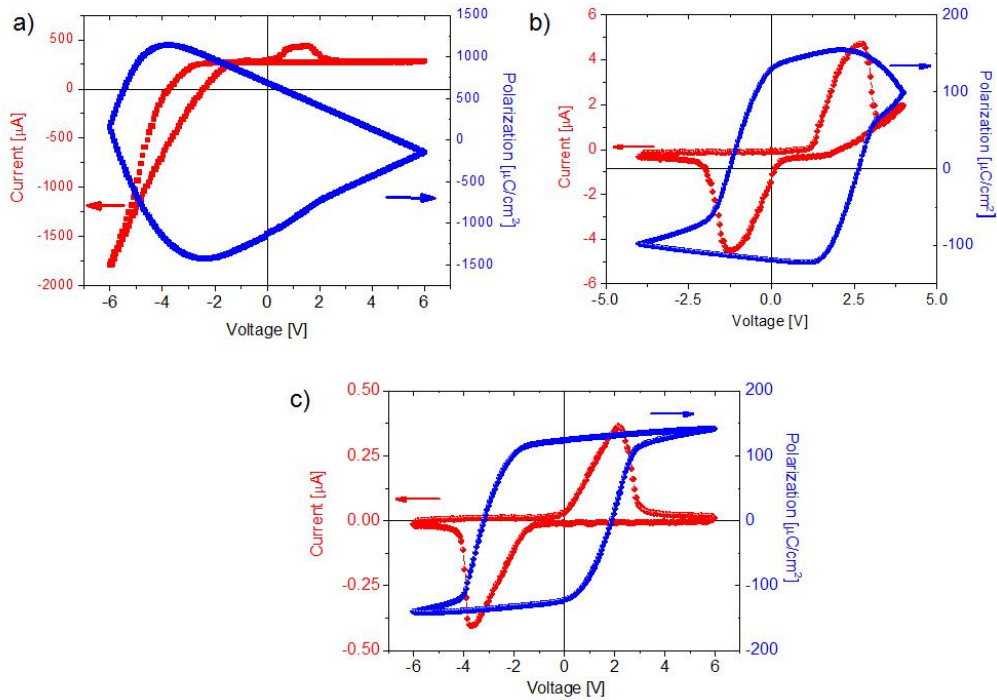


**Figure 4.12:** Investigation of ferroelectric characteristics by measuring the ferroelectric polarization (blue) and switching current (red) loops at room temperature, for 100 nm thick BFO films deposited on a) STO substrate with SRO as the buffer layer; b) TSO substrate with LSMO as the buffer layer. c) Polarization and switching current loops obtained at 150 K for a 100 nm thick BFO film on TSO and LSMO as buffer layer.

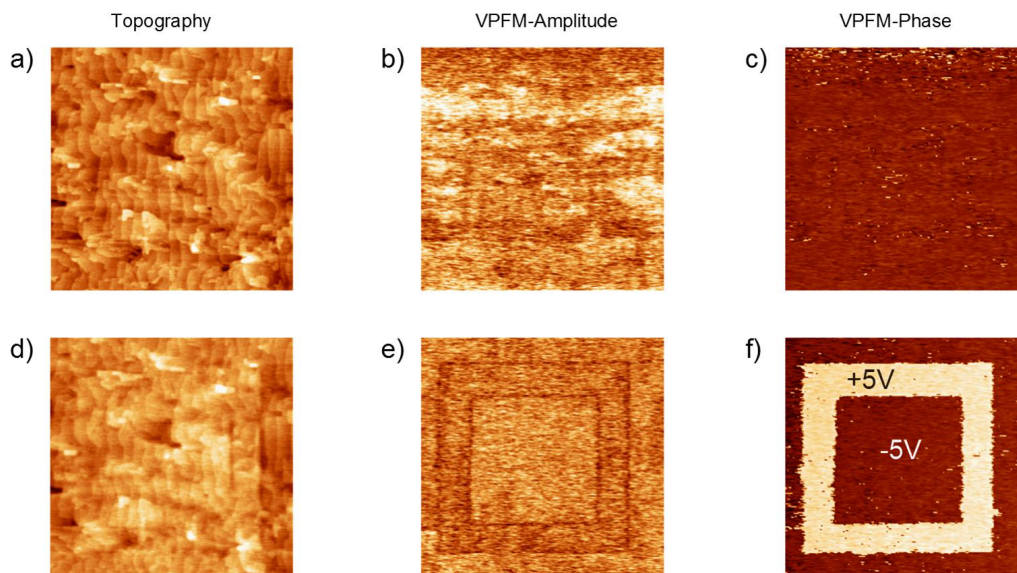


**Figure 4.13:** a) AFM image of size  $4 \times 4 \mu\text{m}$  for a 100 nm thick BFO film on TSO substrate with LSMO as the buffer layer and corresponding VPFM b) amplitude and c) phase images. d) AFM image of size  $4 \times 4 \mu\text{m}$  of the same area shown in image *a* after switching, and the corresponding VPFM images showing e) amplitude and f) phase.

Additionally the ferroelectric nature of the BFO films deposited on TSO with LSMO as the buffer layer was proven by the help of PFM. A region of size  $4 \times 4 \mu\text{m}$  on the surface of the sample was selected, the morphology of which is shown in Figure 4.13a. The VPFM phase image of the area is shown in Figure 4.13c that largely consists of one color i.e. brown which means the area is completely polarized downwards. Thereafter a *dc* bias of +5 V was applied to the PFM tip and an area of size  $3 \times 3 \mu\text{m}$  was scanned to change the polarization of the area upwards. Henceforth, the *dc* bias at the tip was changed to -5 V and an area of size  $2 \times 2 \mu\text{m}$  was scanned to switch the polarization back downwards. Eventually, the complete area of  $4 \times 4 \mu\text{m}$  size was rescanned (morphology shown in Figure 4.13d) under normal PFM mode which resulted in VPFM phase image that is shown in Figure 4.13f with yellow area indicating upward polarization. The co-existence of two different polarization states and the ability of the material to retain the oppositely polarized state depict the ferroelectric nature of the film.

## 4.5 Photoelectric measurements

In the previous sections the phase purity, structural consistency and the ferroelectric nature of the BFO films were discussed and elaborated. The BFO films deposited on bare TSO substrates were then subjected to photoelectric measurements that will be explained in the subsequent sections. For these measurements 100 nm thick BFO films that exhibited dominant  $109^\circ$  and  $71^\circ$  domain wall (DW) patterns were used. This was done to clearly distinguish between the role of domains and DWs. The measurements included acquiring IV (current-voltage) curves with and without illumination over a range of temperatures. In certain cases the measurements were performed by changing the angle between the electric field vector of the incoming light and the direction of current flow.

### 4.5.1 Abnormal photovoltaic effect

In order to have a better insight into the mechanism of the photovoltaic (PV) effect in the BFO films, primarily, two kinds of device geometries were fabricated. In one geometry the electrodes were aligned parallel to the domain walls which will be referred to as the PLDW geometry henceforth. In the other geometry the electrodes were aligned perpendicular to the domain walls which will be referred to as the PPDW geometry. Either of the geometries, both for 71° and 109° domain patterns, are shown in a schematic in Figure 4.14. For realizing the PV effect, a linearly polarized laser illumination of wavelength  $\lambda = 405$  nm (3.06 eV) was used. The illumination was directed at the middle between the measuring electrodes during which the IV curves were acquired.

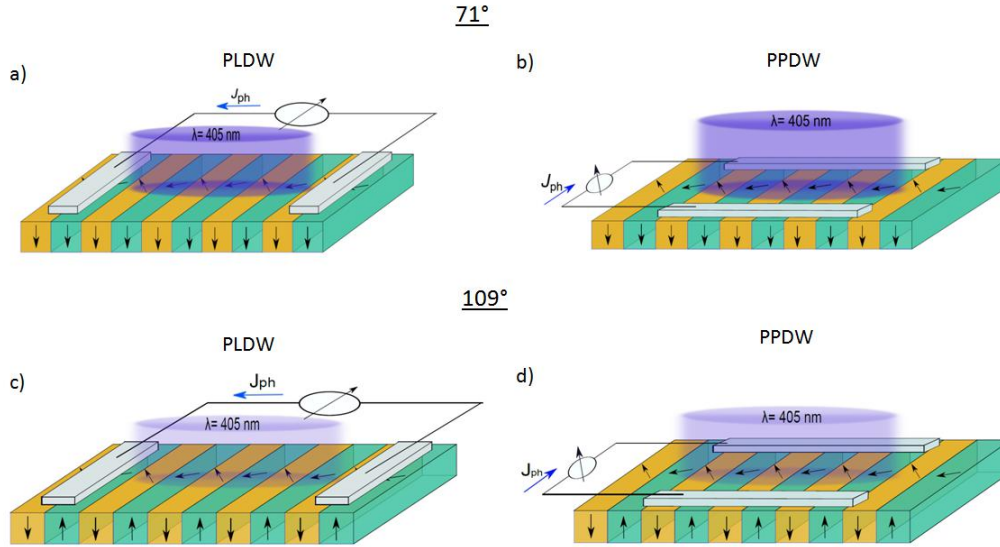


**Figure 4.14:** Schematic showing the patterned electrodes on top of a film with majority 71° (a, b) and 109° (c, d) domain pattern (not to scale) and the fabricated measurement geometries in which the electrodes are running: (a, c) parallel (PLDW) and (b, d) perpendicular (PPDW) to DWs, respectively. The arrows indicate the direction of polarization in out-of-plane (up/down) and in-plane (left/right) directions.

Figure 4.15a and b show the IV curves that were obtained at room temperature under illumination from BFO films comprising of a 109° and 71° DW pattern, respectively. In either of the cases the distance between the electrodes was 100  $\mu\text{m}$ . For the film with 109° DW, in the PLDW geometry an open circuit voltage ( $V_{oc}$ ) of 5.4 V was observed which is higher than the band gap of BFO, whereas no sizable voltage was obtained in the PPDW case as shown in Figure 4.15a. The generation of a  $V_{oc}$  higher than the band gap of the material is termed as abnormal PV effect. Such observation is in accordance with the previous report of the PV effect in BFO films with dominant 109° DWs [78] and seems to follow the model proposed in the earlier work from Ramesh et. al. that allowed above-band gap voltages  $V_{oc}$  only in the PLDW geometry [22]. However, interestingly, at room temperature, the BFO film comprising of 71° DWs exhibits a sizable  $V_{oc}$  in both the configurations, viz.  $\approx -6.6$  V in PPDW and  $\approx -7.6$  V in PLDW geometry, as shown in Figure 4.15b. The generation of an above-band gap voltage  $V_{oc}$  in the PPDW geometry is rather contradictory to the initial model proposed, which predicts only a photoconductive effect in the geometry. Temperature dependent studies were performed to further investigate this anomaly.

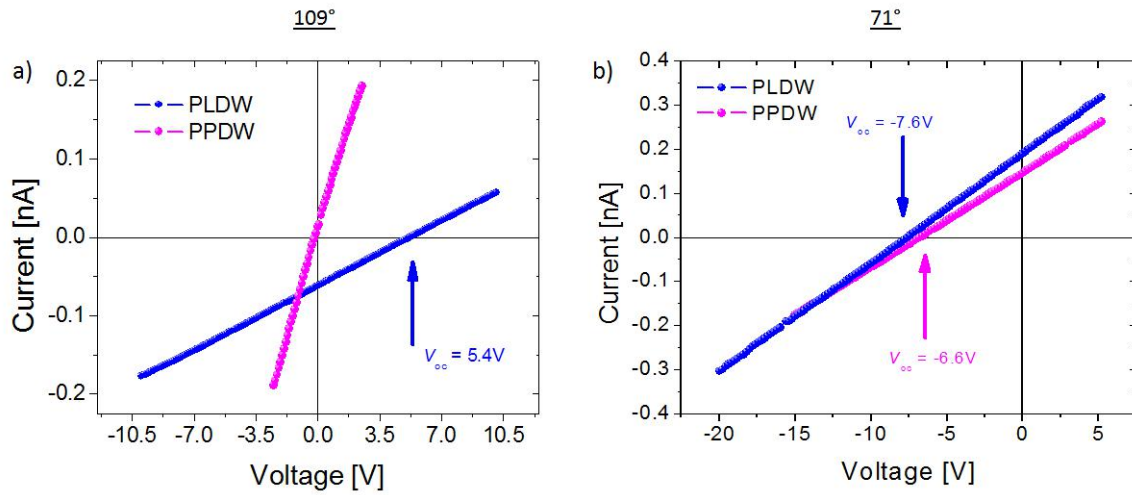


**Figure 4.15:** IV characteristics under illumination with monochromatic light ( $h\nu = 3.05$  eV) of BFO thin films comprising (a)  $109^\circ$  and (b)  $71^\circ$  periodic stripe domains.

### 4.5.2 Temperature dependent open circuit voltages

Photoelectric measurements were conducted by acquiring IV curves of the type shown in Figure 4.15 at temperatures ranging from 80 K to 450 K for both geometries in either of the DW variants. Thereafter, the values of  $V_{oc}$  were extracted from the IV curves. By performing the analysis at different temperatures down to 80 K it was observed that in both the geometries and DW variants by decreasing the temperature well below room temperature the  $V_{oc}$  values increase dramatically. This is shown in Figure 4.16 where the extracted  $V_{oc}$  values have been plotted with temperature.

In the PLDW geometry, the  $V_{oc}$  values in the film with a  $109^\circ$  domain pattern increase to more than 17 V at low temperature (Figure 4.16c) and to more than 50 V for the film with a  $71^\circ$  domain pattern (Figure 4.16d). The most dramatic increase of  $V_{oc}$ , to about 20 times the band gap, is for the  $71^\circ$  DW film. The temperature dependence of  $V_{oc}$  has a similar behavior for both the geometries; it increases at low temperature to values which are in both cases well above the band gap with an obvious increase at temperatures lower than 200 K. For  $109^\circ$  domains in the PPDW geometry the  $V_{oc}$ , which at room temperature was almost zero, becomes at 80 K as large as 12 V (Figure 4.16a). At room temperature in the case of  $71^\circ$  domains in the PPDW geometry, where according to the initial model the open circuit voltage should be below the band gap, the  $V_{oc}$  value is larger than 5 V that increases further to approximately 37 V at low temperature (Figure 4.16b). Another observation that can be made from these measurements is the effect of changing the gap between electrodes. In all the cases, for a given temperature, the value of  $V_{oc}$  tends to increase when the gap between the electrodes is increased from 15  $\mu\text{m}$  to 100  $\mu\text{m}$  irrespective of the measurement geometry.

The sizable  $V_{oc}$  in the perpendicular geometry in the case of  $71^\circ$  domains at room temperature and the dramatic increase of  $V_{oc}$  with decreasing temperature in all cases suggests that those mechanisms within which the domain walls were perceived as the origin of this effect, as it has been previously assumed [22] [102], are not valid and bulk and domain walls should play a different role.

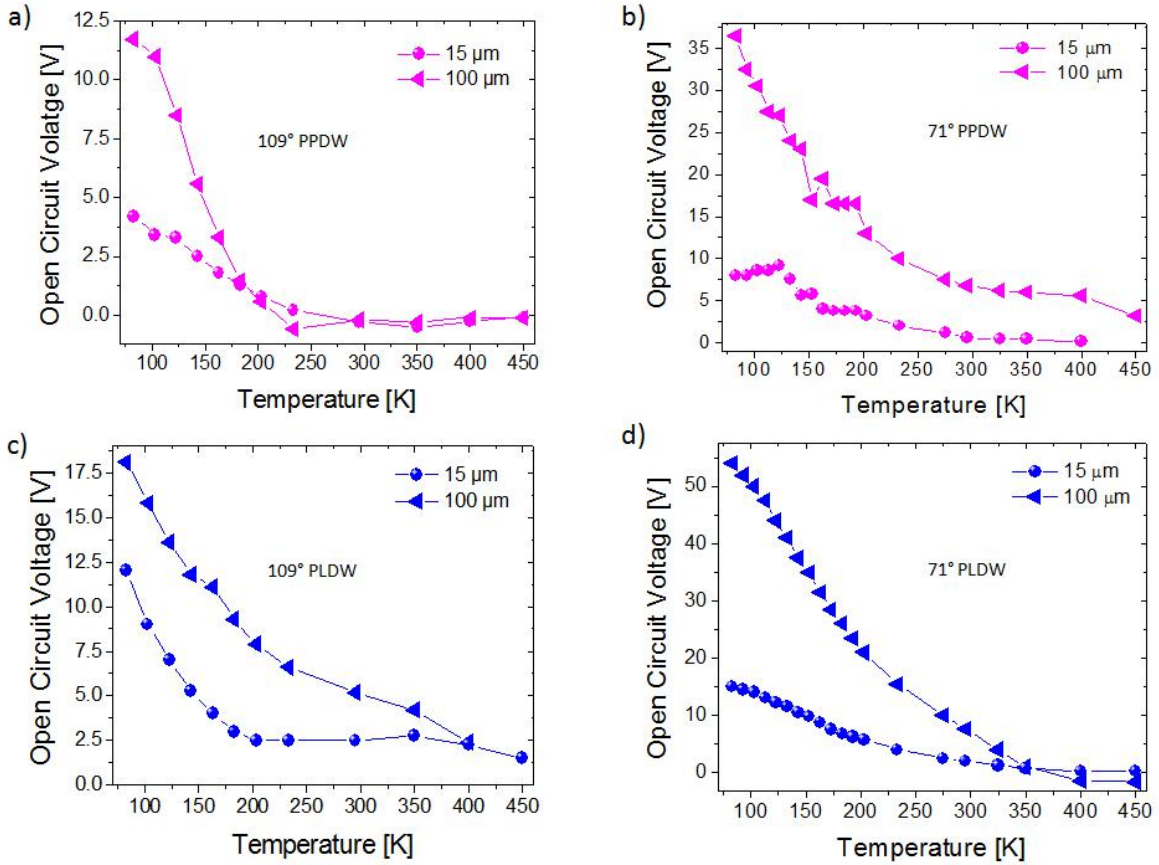


**Figure 4.16:** Temperature dependence of the open circuit voltage for 109° DW in (a) perpendicular and (c) parallel geometry and for 71° DW in (b) perpendicular and (d) parallel geometry for two electrode gap widths, that is, 15 μm and 100 μm.

### 4.5.3 Bulk photovoltaic effect

Keeping in perspective the temperature dependent behavior of  $V_{oc}$ , the only viable alternative explanation for the abnormal PV effect in BFO remains the bulk photovoltaic (BPV) or photogalvanic effect which was discussed previously in section 2.2.2. This effect is largely known in materials lacking inversion symmetry, and has been analyzed phenomenologically by Fridkin [52] and Ruppel et.al. [56] in the past. Accordingly, under uniform illumination the photocurrent  $J_{ph}$  is due to an asymmetric generation in  $k$ -space, and under open circuit conditions the  $V_{oc}$  is given by:

$$V_{oc} = J_{ph}\rho L \quad (4.3)$$

where  $\rho$  is the resistivity and  $L$  is the distance between the electrodes. Moreover, according to the work of Fridkin [52],  $V_{oc}$  scales inverse proportionally with both dark conductivity and photoconductivity, so that equation 4.3 becomes:

$$V_{oc} = \frac{J_{ph}}{\sigma_{ph} + \sigma_{dark}} L \quad (4.4)$$

where  $\sigma_{dark}$  and  $\sigma_{ph}$  are dark conductivity and photoconductivity, respectively. Based on equation 4.4, for a given value  $L$  and under the assumption that the  $J_{ph}$  generated at



all the temperatures is constant, one might speculate that the temperature dependence of the  $V_{oc}$  values is due to the temperature dependent conductivity behavior of the measurement gap. This was validated by measuring the photo and dark-conductivity for all the geometries, shown in Figure 4.17. Both dark and photo-conductivity exhibit an exponentially increasing behavior with increasing temperature. On the other hand the  $V_{oc}$ s show an exponentially decreasing behavior with increase in temperature. The inverse relation between the two entities proves the validity of equation 4.4.

Additionally, the enhanced conductivity in the PPDW geometry is evident when the dark conductivity behavior in the PPDW (Figure 4.17a) and PLDW (Figure 4.17c) geometry is compared. This is also valid for the photoconductivity measurements where the conductivity is higher in the PPDW geometry (Figure 4.17b). These observations imply that the domain walls have an enhanced conductivity and are largely governing both the dark and photoconductivity of the BFO films. This is not surprising since the *dc* dark conductivity of  $109^\circ$  DWs has been already estimated to be at least four orders of magnitude higher than the bulk of BFO [103]. Furthermore, it can be easily seen that both dark and photoconductivity are higher in the case of  $109^\circ$  DWs when compared with  $71^\circ$  DWs. This also has been proven in theoretical calculations that predict higher conductivity in  $109^\circ$  DWs [5] [104].

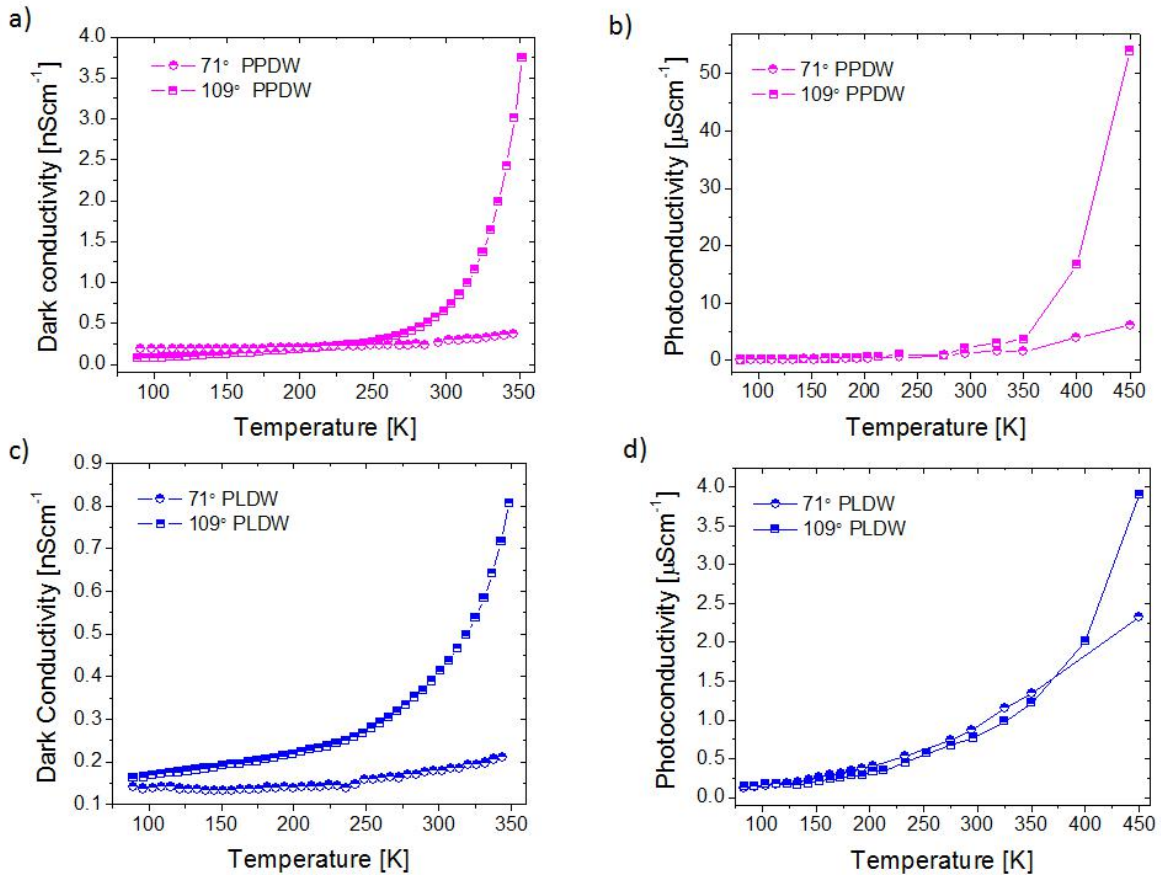


**Figure 4.17:** Temperature dependence of dark conductivity (a, c) and photoconductivity (b, d) measured with the electrodes running perpendicular (PPDW) and parallel (PLDW) to the DWs for both  $109^\circ$  and  $71^\circ$  domains.

### 4.5.3.1 Two-resistance model

Having proven the validity of the relation given in equation 4.4 by  $V_{oc}$  and conductivity measurements, a model can be proposed now in order to explain the existence and/or absence of the abnormal photovoltaic effect and respectively a value of the open circuit voltage  $V_{oc}$  larger than the band gap. It can be assumed that a photocurrent is rather uniformly generated in the entire film due to the bulk photovoltaic effect or, as recently shown using ab-initio calculations [84], by so called shift currents. In the same time the open circuit voltage is established, according to equation 4.4, by the effective conductivity of the BFO film considering both the bulk and the domain wall conductivity. The effective sample conductivity is given by a simple equivalent circuit which is either parallel or serial, depending on the geometrical arrangement of the collecting electrodes relative to the domain walls.

As schematically shown in Figure 4.18b and d, in the perpendicular geometry (PPDW) the equivalent circuit is a parallel circuit and the effective conductivity is given by the sum of both bulk ( $\sigma_{bulk}$ ) and domain wall  $\sigma_{DW}$  conductivities given by

$$\sigma_{total} = \sigma_{bulk} + \sigma_{DW} \quad (4.5)$$

On the other hand, in the parallel geometry (PLDW) (Figure 4.18a and c) the appropriate equivalent circuit is the series circuit and in this case the inverse of the effective conductivity is the sum of the inverse conductivities

$$\frac{1}{\sigma_{total}} = \frac{1}{\sigma_{bulk}} + \frac{1}{\sigma_{DW}} \quad (4.6)$$

According to this simple model, the effective conductivity is higher when the domain walls are running perpendicular to the electrodes and thus the open circuit voltage should be lower in the PPDW geometry. This is valid for all cases as evident from Figure 4.17. For the film with 109° DWs, in which the DWs are much more conductive than in the film with 71° DWs, the  $V_{oc}$  for all the cases was lower than what was measured in the film with 71° DWs.

### 4.5.3.2 Calculation of photovoltaic response

In order to prove the existence of the bulk PV effect (BPV) in the BFO films, the PV current was measured in all the systems by changing the angle between the plane of the linearly polarized light and the direction of current flow ( $\theta$ ). The BPV effect has been studied extensively in non-centrosymmetric materials like KNbO<sub>3</sub> (KNO) [54] [105], BaTiO<sub>3</sub> (BTO) [106] [107], LiNbO<sub>3</sub> (LNO) [25] [108], reduced LiTaO<sub>3</sub> (LTO) [109]. The BPV effect in ferroelectrics, as previously explained in section 2.2.2, can be expressed in the form of an equation given by

$$J_{(ph)i} = I\beta_{ijk}e_je_k \quad (4.7)$$

where  $\beta_{ijk}$  is a third rank tensor, and  $e_je_k$  are the projections of the electric field of the linearly polarized light on the plane of measurement. A PV current ( $J_{ph}$ ) is generated in a non-centrosymmetric material according to the relation given in 4.7 when it is illuminated by a linearly polarized light of intensity  $I$ .

Likewise the case of LiNbO<sub>3</sub> [110] [111], BFO belongs to the space group R3c and the BPV tensor valid for LNO can also be used for BFO [112]. However, many of the 27

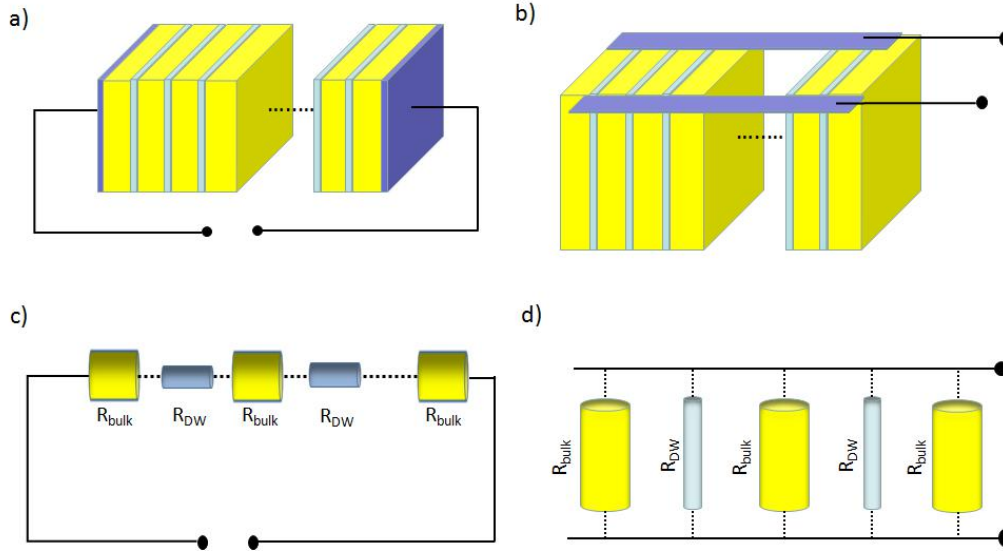


**Figure 4.18:** A schematic showing the periodic arrangement of domains and DW in BFO thin films for the (a) parallel (PLDW) and (b) perpendicular (PPDW) geometry with respect to the DW. An equivalent circuit considering that the domain bulk and DW have different resistances,  $R_{bulk}$  and  $R_{DW}$ , is shown for both the geometries in (c) PLDW and (d) PPDW.

elements of the third rank tensor will be reduced to zero owing to symmetry operations. The tensor thereafter can be contracted into a 3x6 matrix of the form [33]

$$\beta_{ijk} = \begin{pmatrix} 0 & 0 & 0 & 0 & \beta_{15} & -\beta_{22} \\ -\beta_{22} & \beta_{22} & 0 & \beta_{15} & 0 & 0 \\ \beta_{31} & \beta_{31} & \beta_{33} & 0 & 0 & 0 \end{pmatrix} \quad (4.8)$$

The incident light propagating along the Z-axis can be expressed as [111] [113]:

$$E = E_0 \exp[i(kz - \omega t)] \quad (4.9)$$

The electric field vector  $E$  of the light can be resolved into two components along X and Y axes having  $\cos\theta$  and  $\sin\theta$  dependencies, respectively. The components are the projections on the plane of measurement and  $\theta$  is the angle which the vector  $E$  makes with the direction of current flow. Hence

$$E = E_0 [e_x \cos\theta \exp[i(kz - \omega t)] + e_y \sin\theta \exp[i(kz - \omega t)]] \quad (4.10)$$

Based on equation 4.10 and using the Jones notation, the projections of the electric field of the linearly polarized light can be represented by a second rank tensor of the type

$$e_j e_k = I \begin{pmatrix} \cos^2\theta & \cos\theta \sin\theta & 0 \\ \cos\theta \sin\theta & \sin^2\theta & 0 \\ 0 & 0 & 0 \end{pmatrix} \quad (4.11)$$

The matrix given in equation 4.11 can be rearranged in a 6x1 matrix in the following way [113]:

$$e_j e_k = I \begin{pmatrix} \cos^2 \theta \\ \sin^2 \theta \\ 0 \\ 0 \\ 0 \\ \sin \theta \cos \theta \end{pmatrix} \quad (4.12)$$

By substituting the matrices corresponding to  $\beta_{ijk}$  and  $e_j e_k$  in equation 4.7, the PV current generated in X and Y direction can be calculated [114]. However the current in X-direction is in the PPDW geometry and the current in Y-direction is in the PLDW geometry. Hence

$$J_{PPDW} = -I\beta_{22}\sin 2\theta \quad (4.13)$$

$$J_{PLDW} = I\beta_{22}\cos 2\theta \quad (4.14)$$

Figure 4.19a depicts the arrangement of the setup in which the coordinate system shown follows the pseudocubic notation of the BFO film so that the direction X is given by [001], Y is given by [010] and Z is given by [001]. The light illumination is along the Z [001] direction. For these measurements, the angle 0° means that the E vector of the linearly polarized light is parallel to the direction of the current flow, whereas an angle of 90° means that E is perpendicular to the current flow direction. The measurements were performed on the BFO films with 71° and 109° DWs in the PLDW geometry. The normalized values for the measured photovoltaic current by varying the angle between the current direction and the polarization axis of the light are presented in Figure 4.19b.

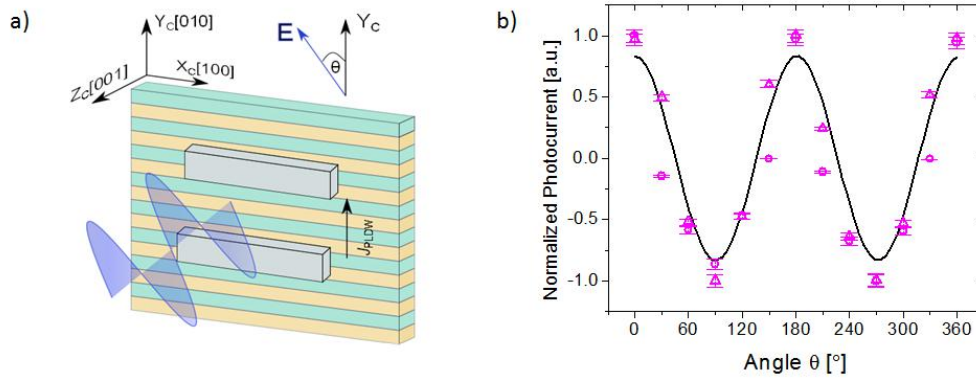


**Figure 4.19:** a) Schematic of a sample showing stripes, which represent the DWs, either of the 109° or 71° stripe domain system. The coordinate system is given by XYZ. The schematic shows how the vector E of the linearly polarized light is aligned with the direction of the current flow J for the PLDW case. (b) Normalized PV current measured at different angles ( $\theta$ ), which the polarization axis of the linearly polarized light makes with the direction of the current flow in the PLDW geometry for samples with 71° (circle) and 109° (triangle) domains, respectively. The solid line represents the fit with equation 4.14.

It is rather evident from the plot shown in Figure 4.19b that in either of the systems there is a definitive angular dependency exhibited by the PV current. For both systems

studied, the normalized PV current fits the cosine function in equation 4.14 proving in this way that the origin of the PV current is the BPV effect. However it must be taken into consideration that equation 4.14 is calculated for rhombohedral symmetry. Therefore in order to predict the exact response which is obtained in the lab coordinates, the bulk photovoltaic tensor must be transformed from rhombohedral to lab coordinates. This transformation has been performed for the films with  $71^\circ$  DWs.

The BPV tensor  $\beta_{ijk}$  is a tensor of third rank. This means it has  $3^3$  elements. These elements can be expressed as:

$$\beta_{ijk} = \begin{pmatrix} \beta_{111} & \beta_{112} & \beta_{113} & \beta_{211} & \beta_{212} & \beta_{213} & \beta_{311} & \beta_{312} & \beta_{313} \\ \beta_{121} & \beta_{122} & \beta_{123} & \beta_{221} & \beta_{222} & \beta_{223} & \beta_{321} & \beta_{322} & \beta_{323} \\ \beta_{131} & \beta_{132} & \beta_{133} & \beta_{231} & \beta_{232} & \beta_{233} & \beta_{331} & \beta_{332} & \beta_{333} \end{pmatrix} \quad (4.15)$$

Since the projections of the electric field of linearly polarized light ( $e_j e_k$ ) are symmetric with respect to each other, it means that the BPV tensor can be assumed to be symmetrical in j and k. Due to this symmetry aspect, there remain only 18 independent  $\beta_{ijk}$  coefficients which can be conveniently represented in a matrix notation of the form [33]:

$$\beta_{ijk} = \begin{pmatrix} \beta_{11} & \beta_{12} & \beta_{13} & \beta_{14} & \beta_{15} & \beta_{16} \\ \beta_{21} & \beta_{22} & \beta_{23} & \beta_{24} & \beta_{25} & \beta_{26} \\ \beta_{31} & \beta_{32} & \beta_{33} & \beta_{34} & \beta_{35} & \beta_{36} \end{pmatrix} \quad (4.16)$$

The coefficients in equation 4.15 are related to the coefficients in equation 4.16 in such an arrangement that the first suffix remains the same in both the notations, whereas the last two notations are related according to the following table [33]:

**Table 4.1:** Tensor to matrix notation

Tensor notation	11	22	33	23, 32	31, 13	21, 12
Matrix notation	1	2	3	4	5	6

However, there is a further reduction in the number of independent tensor coefficients due to the R3c symmetry of BiFeO<sub>3</sub> (BFO). Henceforth, the matrix in equation 4.16 is reduced to [33]:

$$\beta_{ijk} = \begin{pmatrix} 0 & 0 & 0 & 0 & \beta_{15} & -\beta_{22} \\ -\beta_{22} & \beta_{22} & 0 & \beta_{15} & 0 & 0 \\ \beta_{31} & \beta_{31} & \beta_{33} & 0 & 0 & 0 \end{pmatrix} \quad (4.17)$$

It can be observed by comparing equation 4.16 and 4.17 that,  $\beta_{22} = -\beta_{21} = -\beta_{16}$ ,  $\beta_{15} = \beta_{24}$  and  $\beta_{31} = \beta_{32}$ . Therefore the bulk photovoltaic effect in BFO can be completely described by the help of four independent coefficients which are  $\beta_{15}$ ,  $\beta_{22}$ ,  $\beta_{31}$  and  $\beta_{33}$ . By using equation 4.17 and the matrix notations given in table 4.1, we know that

$$\beta_{15} = \beta_{24} = \beta_{113} = \beta_{131} = \beta_{223} = \beta_{232} \quad (4.18)$$

$$\beta_{22} = -\beta_{21} = -\beta_{16} = \beta_{222} = -\beta_{211} = -\beta_{112} = -\beta_{121} \quad (4.19)$$

$$\beta_{31} = \beta_{32} = \beta_{311} = \beta_{322} \quad (4.20)$$

$$\beta_{33} = \beta_{333} \quad (4.21)$$

Based on the relations given in equations 4.18 to 4.21, equation 4.15 can be rewritten to obtain a third rank tensor which would be valid for BFO:

$$\beta_{ijk} = \begin{pmatrix} 0 & -\beta_{112} & \beta_{113} & -\beta_{211} & 0 & 0 & \beta_{311} & 0 & 0 \\ -\beta_{121} & 0 & 0 & 0 & \beta_{222} & \beta_{223} & 0 & \beta_{322} & 0 \\ \beta_{131} & 0 & 0 & 0 & \beta_{232} & 0 & 0 & 0 & \beta_{333} \end{pmatrix} \quad (4.22)$$

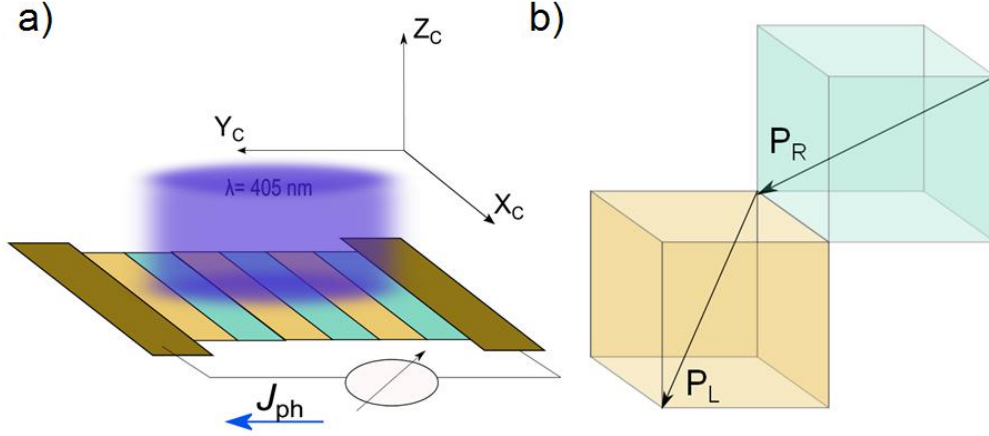


**Figure 4.20:** a) Schematic of the measurement geometry for a sample with alternating 71° domains parallel to the electrodes (PLDW) along with the lab coordinate system. b) Pseudo cubic schematic of two kinds of domains in a sample with 71° domains. P<sub>R</sub> and P<sub>L</sub> show the direction of polarization for the two kinds of domain.

In order to predict the PV current which is measured in the lab coordinates, the BPV tensor must be converted from the rhombohedral to lab coordinates [84]. Additionally, a film comprising of 71° domains, as shown in Figure 4.20, consists of two kinds of rhombohedral unit cells which results in two different domains. These are shown as R-type and L-type in Figure 4.20. Therefore such a conversion must be performed for both the cells and domains. The matrices which are required to transform the rhombohedral coordinate system of the R- and L-type domains to lab coordinates are given by [84]:

$$R = \begin{pmatrix} \frac{-1}{\sqrt{2}} & \frac{1}{\sqrt{6}} & \frac{-1}{\sqrt{3}} \\ \frac{1}{\sqrt{2}} & \frac{1}{\sqrt{6}} & \frac{1}{\sqrt{3}} \\ 0 & \frac{2}{\sqrt{6}} & \frac{-1}{\sqrt{3}} \end{pmatrix} \quad (4.23)$$

$$L = \begin{pmatrix} \frac{-1}{\sqrt{2}} & \frac{-1}{\sqrt{6}} & \frac{-1}{\sqrt{3}} \\ \frac{-1}{\sqrt{2}} & \frac{1}{\sqrt{6}} & \frac{1}{\sqrt{3}} \\ 0 & \frac{2}{\sqrt{6}} & \frac{-1}{\sqrt{3}} \end{pmatrix} \quad (4.24)$$

The BPV tensor in the lab coordinates can then be expressed as a resultant of both the conversions [84]:

$$B_{qrs} = \left( \frac{R_{qi}R_{rj}R_{sk}\beta_{ijk} + L_{qi}L_{rj}L_{sk}\beta_{ijk}}{2} \right) \quad (4.25)$$

Based on the non-zero terms in equation 4.22, equation 4.25 can be elaborated as:

$$\begin{aligned}
 B_{qrs} = & ( - R_{q1}R_{r1}R_{s2}\beta_{112} - R_{q1}R_{r2}R_{s1}\beta_{121} + R_{q1}R_{r1}R_{s3}\beta_{113} + \\
 & R_{q1}R_{r3}R_{s1}\beta_{131} - R_{q2}R_{r2}R_{s1}\beta_{221} + R_{q2}R_{r2}R_{s2}\beta_{222} + \\
 & R_{q2}R_{r2}R_{s3}\beta_{223} + R_{q2}R_{r3}R_{s2}\beta_{232} + R_{q3}R_{r1}R_{s1}\beta_{311} + \\
 & R_{q3}R_{r2}R_{s2}\beta_{322} + R_{q3}R_{r3}R_{s3}\beta_{333} - L_{q1}L_{r1}L_{s2}\beta_{112} - \\
 & L_{q1}L_{r2}L_{s1}\beta_{121} + L_{q1}L_{r1}L_{s3}\beta_{113} + L_{q1}L_{r3}L_{s1}\beta_{131} - \\
 & L_{q2}L_{r1}L_{s1}\beta_{221} + L_{q2}L_{r2}L_{s2}\beta_{222} + L_{q2}L_{r2}L_{s3}\beta_{223} + \\
 & L_{q2}L_{r3}L_{s2}\beta_{232} + L_{q3}L_{r1}L_{s1}\beta_{311} + L_{q3}L_{r2}L_{s2}\beta_{322} + \\
 & L_{q3}L_{r3}L_{s3}\beta_{333})/2
 \end{aligned} \tag{4.26}$$

From the relations given in equations 4.18 to 4.21, equation 4.26 can be rearranged to be:

$$\begin{aligned}
 B_{qrs} = & \frac{1}{2}\beta_{15} (R_{q1}R_{r1}R_{s3} + R_{q1}R_{r3}R_{s1} + R_{q2}R_{r2}R_{s3} + R_{q2}R_{r3}R_{s2} + \\
 & L_{q1}L_{r1}L_{s3} + L_{q1}L_{r3}L_{s1} + L_{q2}L_{r2}L_{s3} + L_{q2}L_{r3}L_{s2}) + \\
 & \frac{1}{2}\beta_{22} (-R_{q1}R_{r1}R_{s2} - R_{q1}R_{r2}R_{s1} - R_{q2}R_{r1}R_{s1} + R_{q2}R_{r2}R_{s2} + \\
 & -L_{q1}L_{r1}L_{s2} - L_{q1}L_{r2}L_{s1} - L_{q2}L_{r1}L_{s1} + L_{q2}L_{r2}L_{s2}) + \\
 & \frac{1}{2}\beta_{31} (R_{q3}R_{r1}R_{s1} + R_{q3}R_{r2}R_{s2} + L_{q3}L_{r1}L_{s1} + L_{q3}L_{r2}L_{s2}) + \\
 & \frac{1}{2}\beta_{33} (R_{q3}R_{r3}R_{s3} + L_{q3}L_{r3}L_{s3})
 \end{aligned} \tag{4.27}$$

Having calculated the BPV tensor in lab coordinates in equation 4.27, the PV current in the lab coordinates can be predicted by:

$$J_{(ph)q} = I\beta_{qrs}e_r e_s \tag{4.28}$$

As explained previously, the lab BPV tensor ( $B_{qrs}$ ) can be reduced to a matrix notation of (3x6) type. Also, we can use the (6x1) matrix notation for the projections of the electric field vector of the incoming light given in equation (4.12). Therefore, equation 4.28 can be solved by a simple matrix multiplication with the result being of the type:

$$\begin{pmatrix} J_{PPDW} \\ J_{PLDW} \\ J_Z \end{pmatrix} = I \begin{pmatrix} B_{12}\sin^2\theta + 2B_{16}\sin\theta\cos\theta + B_{11}\cos^2\theta \\ B_{22}\sin^2\theta + 2B_{26}\sin\theta\cos\theta + B_{21}\cos^2\theta \\ B_{32}\sin^2\theta + 2B_{36}\sin\theta\cos\theta + B_{31}\cos^2\theta \end{pmatrix} \tag{4.29}$$

As can be observed from equation 4.29, the main coefficients required to predict the PV current in PPDW and PLDW geometries are  $B_{12}$ ,  $B_{16}$ ,  $B_{11}$ ,  $B_{22}$ ,  $B_{26}$ ,  $B_{21}$ . By substituting the values from equation 4.23 and 4.24 (using relations given in 4.18 to 4.21) into equation 4.27, these terms can be calculated as follows:

$$B_{12} = 0 \tag{4.30}$$

$$B_{16} = \frac{\beta_{33}}{3\sqrt{3}} - \frac{\beta_{31}}{3\sqrt{3}} + \frac{2\beta_{22}}{3\sqrt{6}} + \frac{\beta_{15}}{3\sqrt{3}} \tag{4.31}$$

$$B_{11} = 0 \quad (4.32)$$

$$B_{22} = \frac{\beta_{33}}{3\sqrt{3}} + \frac{\beta_{31}}{3\sqrt{3}} - \frac{4\beta_{22}}{3\sqrt{6}} + \frac{4\beta_{15}}{3\sqrt{3}} \quad (4.33)$$

$$B_{26} = 0 \quad (4.34)$$

$$B_{21} = \frac{\beta_{33}}{3\sqrt{3}} + \frac{2\beta_{31}}{3\sqrt{3}} + \frac{2\beta_{22}}{3\sqrt{6}} - \frac{2\beta_{15}}{3\sqrt{3}} \quad (4.35)$$

By substituting the values of the coefficients from equations 4.30 to 4.35 in equation 4.29, the calculated PV current in the direction perpendicular to the domain walls or in PLDW geometry is given by:

$$J_{PLDW} = I \left[ \frac{\beta_{33}}{3\sqrt{3}} + \frac{2\beta_{31}}{3\sqrt{3}} + \frac{2\beta_{15}}{3\sqrt{3}}(-\cos 2\theta + \sin^2 \theta) - \frac{2\beta_{22}}{3\sqrt{6}}(-\cos 2\theta + \sin^2 \theta) \right] \quad (4.36)$$

Equation 4.36 can be further simplified by applying trigonometric operations resulting in

$$J_{PLDW} = I \left[ \frac{\beta_{33}}{3\sqrt{3}} + \frac{2\beta_{31}}{3\sqrt{3}} + \frac{\beta_{15}}{3\sqrt{3}} - \frac{\beta_{22}}{3\sqrt{6}} \right] + I \left[ \frac{\beta_{22}}{\sqrt{6}} - \frac{\beta_{15}}{\sqrt{3}} \right] \cos 2\theta \quad (4.37)$$

The current flows in the direction of both ferroelastic distortion and polarization, which is consistent with the theoretical results [84].

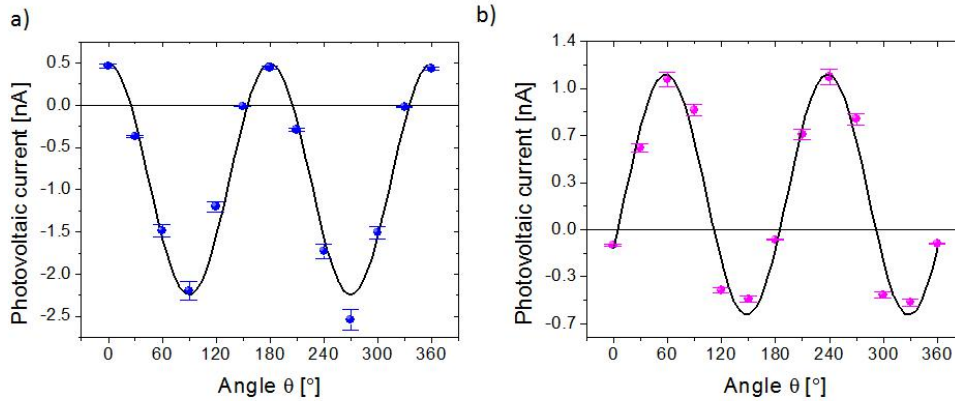


**Figure 4.21:** PV current measured (dots) and predicted (curves) by varying the angle  $\theta$  that the light polarization axis makes with the direction of current flow in a) PLDW geometry and b) PPDW geometry, for a film consisting of 71° domains. In all the plots, a 5% (rough estimate) error has been incorporated in the PV current measurement to compensate for any misalignment in laser beam spot positioning.

From equation 4.37 it can be observed that the current collected in PLDW geometry is composed of two components. The second term due to the BPV effect has a cosine dependency and will oscillate depending on angle  $\theta$ . The first term is also due to the BPV effect but is independent of angle  $\theta$ . This is also evident when we fit equation 4.37 to the data we measured in the PLDW geometry as shown in Figure 4.21a. The  $\theta$ -dependent behavior of the bulk photovoltaic current is shifted by the non-oscillating 1st term of equation 4.37.



The calculated PV current in the direction which is parallel to the domain walls or in the PPDW geometry is given by:

$$J_{PPDW} = I \left[ \frac{\beta_{33}}{3\sqrt{3}} - \frac{\beta_{31}}{3\sqrt{3}} + \frac{2\beta_{22}}{3\sqrt{6}} + \frac{\beta_{15}}{3\sqrt{3}} \right] \sin 2\theta \quad (4.38)$$

The current in PPDW geometry has a sine dependency on angle  $\theta$ . However in order to compensate for the combined effects of factors such as misalignment between the electrodes and domains and a misalignment between the light beam direction and the normal to the sample surface a phase shift of  $\theta_0$  and a constant current  $J_0$  are added to equation 4.38, which eventually can be expressed as:

$$J_{PPDW} = I \left[ \frac{\beta_{33}}{3\sqrt{3}} - \frac{\beta_{31}}{3\sqrt{3}} + \frac{2\beta_{22}}{3\sqrt{6}} + \frac{\beta_{15}}{3\sqrt{3}} \right] \sin(2\theta + \theta_0) + J_0 \quad (4.39)$$

From Figure 4.21b, the agreement between the measured and predicted values from equation 4.39 is obvious. Based on equations 4.37 - 4.39 and the reported value of  $\beta_{22}$ , the values of all the bulk photovoltaic coefficients can be calculated and are given in table 4.2. Additionally, the BPV coefficients are specific to a certain material and depend

**Table 4.2:** Photovoltaic coefficients

Bulk photovoltaic coefficients ( $\beta$ )	Glass coefficients ( $G$ )
$\beta_{22} = 1.1 \times 10^{-4} \text{ V}^{-1}$ [84] [112]	$G_{22} = 4.48 \times 10^{-10} \text{ cm/V}$ [84] [112]
$\beta_{15} = -7.1045 \times 10^{-5} \text{ V}^{-1}$	$G_{15} = -3.946 \times 10^{-10} \text{ cm/V}$
$\beta_{31} = -1.17 \times 10^{-4} \text{ V}^{-1}$	$G_{31} = -6.5 \times 10^{-10} \text{ cm/V}$
$\beta_{33} = 9.74 \times 10^{-5} \text{ V}^{-1}$	$G_{33} = 5.41 \times 10^{-10} \text{ cm/V}$

upon the light absorption coefficient of the material. Glass coefficients are obtained when the BPV coefficients are normalized with respect to the absorption of the material. The corresponding Glass coefficients calculated are given in table 4.2. These coefficients are of the same order of magnitude as obtained for  $\text{LiNbO}_3$  which is also a ferroelectric material with R3c symmetry.

In summary, by investigating the photovoltaic properties of  $\text{BiFeO}_3$  thin films in the low temperature range it was observed that above-band-gap open circuit voltages (as large as 50 V) can be obtained irrespective of the domain wall geometry and the type of the domain wall. The open circuit voltages in all the samples and measurement geometries scaled up roughly exponentially with a decrease of temperature. Thus the bulk photovoltaic effect (or the shift currents) are at the origin of the abnormal photovoltaic effect in BFO. The high dark and photo conductivities of the domain walls tend to inhibit the generation of high  $V_{oc}$  when they are connecting the measurement electrodes.

## 4.6 Summary

$\text{BiFeO}_3$  films were deposited on  $\text{TbScO}_3$  and  $\text{SrTiO}_3$  substrates. The epitaxial nature of the films and their pseudomorphic relation with the substrate was proven by analyzing the  $2\theta$ - $\omega$  scans and RSM contours. The stripe-pattern obtained in the morphology of BFO films deposited on TSO substrates validate the theoretical predictions. An evident

difference was observed between the BFO films deposited on conventionally annealed and O<sub>2</sub> annealed TSO substrates. PFM and TEM investigations revealed that BFO films deposited on conventionally annealed TSO substrates consist of 109° domain patterns whereas BFO films grown on O<sub>2</sub> annealed TSO substrates consist of 71° domains. By analyzing the PFM images, acquired by varying the orientation between the cantilever and the film, it was found that either of the domain patterns are made up of the same structural variants, but the active polarization variants are different. Additionally, in both domain patterns the domain walls were found to be well defined and periodic in nature. Therefore these films were subsequently used for photoelectric measurements to clearly distinguish between the role of domains and domain walls in the abnormal photovoltaic effect in BFO films.

The photoelectric measurements were performed for two geometries: in the PLDW geometry the measuring electrodes were aligned parallel to the domain walls whereas in the PPDW geometry the electrodes were aligned perpendicular to the domains walls. By doing the measurements at lower temperatures it was observed that above-band gap voltages can be obtained in either of the geometries irrespective of the type of domain pattern existing in the film. This proves that the previously proposed model, which assumed that charge accumulation at domain walls is responsible for above-band gap  $V_{oc}$ , is not valid. By performing angle resolved measurements it was observed that the bulk photovoltaic effect is at the origin of the generation of a photovoltaic current in BFO films and accordingly the  $V_{oc}$  values are controlled by the conductivity of the measurement gap. The low or below band gap  $V_{oc}$  value obtained in the PPDW geometry at room temperature can be largely attributed to the high conductivity of the gap since the domain walls tend to act as shunts between the electrodes. However the manifestation of the BPV effect in a sample with periodic domain arrangement is different from the case when the sample consists of a single domain. This was proven mathematically by considering the case of a film with a 71° domain pattern. The conformity between the calculated and measured PV response was evident.

## Persistent photoconductivity in strained BiFeO<sub>3</sub> films

In the recent past, research in the field of multiferroic materials (section 2.1.2) exhibiting more than one phase has gained much momentum. In these materials, enhanced piezoelectric responses can be expected if the composition of the material lies at the boundary between two phases. Phase boundaries of these kind are termed as morphotropic phase boundaries (MPB) [115] [116]. Examples of such materials with high piezoelectric coefficients are PbZr<sub>x</sub>Ti<sub>1-x</sub>O<sub>3</sub> (PZT), PbZn<sub>0.33</sub>Nb<sub>0.67</sub>O<sub>3</sub>-PbTiO<sub>3</sub> (PZN-PT) [117] [118] and Pb(Mg<sub>1/3</sub>Nb<sub>2/3</sub>)O<sub>3</sub>-PbTiO<sub>3</sub> (PMN-PT) [119] [120].

Therefore much work is now being focused on fabricating materials which will not only allow to exploit the use of MPB but are also free of lead. Research has also been directed to find alternative materials in order to circumvent the issue of precise composition control which is one of the prerequisites for an MPB in these materials. In this context, BiFeO<sub>3</sub> thin films grown on lanthanum aluminate (LaAlO<sub>3</sub>) substrates have been of great interest. BFO is generally known to have a rhombohedrally distorted perovskite structure which crystallizes in the R3c space group (section 2.1.3.1). However, due to a lattice mismatch with LaAlO<sub>3</sub>, BFO grows under a compressive strain when fabricated on these substrates. This results in a “tetragonal-like” structure of BFO [27].

First principle calculations predict the “tetragonal” phase of BFO to exhibit large polarization values of approx. 150  $\mu\text{C}/\text{cm}^2$  which are comparable to values obtained for PZT [121]. Moreover, there have been some reports establishing the co-existence of two phases of BFO in the BFO/LAO system, namely “tetragonal-like” and rhombohedral phases [28]. Interestingly, the transition from either phase to the other can be realized by controlling the strain in the film [28] or by the application of an electric field [122]. The high and stable polarization values of the strained BFO system have been successfully realized and applied in case of ferroelectric tunnel junctions [123]. Also a simplified magnetic structure under strain makes the strained BFO/LAO system one of the more attractive areas for future spintronic and magnonic devices [29].

With different properties of the strained BFO system being investigated, it is of utmost importance to study the electronic band structure of this system and the corresponding conduction mechanism involved. In section 5.1, the epitaxial growth of BFO on LAO substrates will be discussed, followed by structural analyses in section 5.2. The domain orientations will be investigated in section 5.3, which will be followed by the elaboration of ferroelectric properties in section 5.4. Hence forth, the electrical properties will be discussed in section 5.5 where a possible conduction mechanism will be presented based on temperature and wavelength dependent studies.

## 5.1 Growth

In this section growth of BiFeO<sub>3</sub> on LaAlO<sub>3</sub> substrates will be studied. In subsection 5.1.1, emphasis will be on the investigation of growth type and morphology of films grown on bare substrates. In subsection 5.1.2 a similar analysis will be performed of films grown on a (La<sub>0.7</sub>Sr<sub>0.3</sub>)MnO<sub>3</sub> buffer layer.

### 5.1.1 BiFeO<sub>3</sub> films on LaAlO<sub>3</sub> substrates

BiFeO<sub>3</sub> films were deposited *via* pulsed laser deposition (section 3.1.1) on top of LaAlO<sub>3</sub> (LAO) single crystal substrates. The substrates were (001)<sub>pc</sub> oriented. LAO is known to have a rhombohedral symmetry (R3m) like other rare earth aluminate materials [124]. The rhombohedral lattice parameter ( $a_{rh}$ ) is 5.35 Å. The pseudo cubic lattice parameter ( $a_{pc}$ ) can be calculated by the following relation :

$$2a_{pc}^2 = a_{rh}^2 \quad (5.1)$$

which results in  $a_{pc} = 3.78$  Å. The substrates chosen had a minimal offcut angle ( $\alpha$ ) in the range of  $0^\circ < \alpha < 0.1^\circ$ . Since the  $a_{pc}$  of LAO is less than the  $a_{pc}$  of BFO (3.96 Å as explained in section 2.1.3.1), the pseudomorphic growth of BFO on LAO (i.e. when  $a_{LAO} = a_{BFO}$ ) is realized under a compressive stress. As a result the out-of-plane lattice parameter of BFO ( $c_{BFO}$ ) undergoes expansion along the [001]<sub>pc</sub> direction to compensate for the in-plane compressive stress along  $\langle 100 \rangle_{pc}$  and  $\langle 010 \rangle_{pc}$  directions as shown in Figure 5.1.

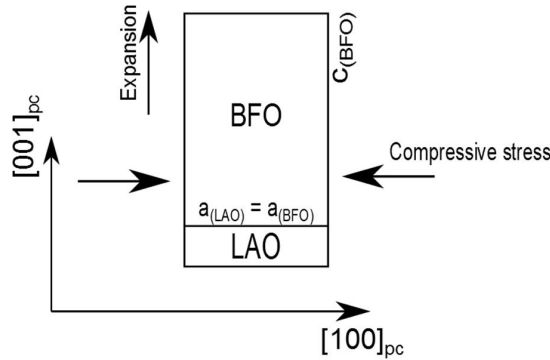


**Figure 5.1:** Depiction of the out-of-plane expansion a BFO unit cell undergoes in order to compensate for the in-plane compressive stress.

The films of BFO were deposited using the parameters stated in table 3.1 in section 3.1.1. Figure 5.2 shows the AFM images acquired from the LAO substrate and the BFO films. From Figure 5.2a, the atomically flat surface of the LAO substrate can be observed. The root mean square (RMS) roughness of the measured area was 2.8 Å. The morphology of the 20 nm thick BFO film deposited on a bare substrate is shown in Figure 5.2b. Atomic terraces are visible which are an indication of layer-by-layer growth [125]. The line scan performed (Figure 5.2d) across the terraces (marked I in Figure 5.2b) gives the step height of approx. 4.2-4.6 Å and width of 50-75 nm. The RMS roughness is approx. 3.9 Å. The morphology of the 80 nm thick BFO film on bare LAO, as shown in Figure 5.2c, was largely different from the 20 nm thick film. Firstly, the roughness increased to approx. 1.2 nm. Secondly, stripe like features appear in the morphology which are not present in

the 20 nm film. The increased roughness can be primarily attributed to the evolution of the stripe like features. The line scan performed (Figure 5.2e) across the stripes (marked II in Figure 5.2c) reveals a periodicity in the range of 90-100 nm and a step height between 0.5 and 2 nm. The profile of the line scan (Figure 5.2f) in a region without

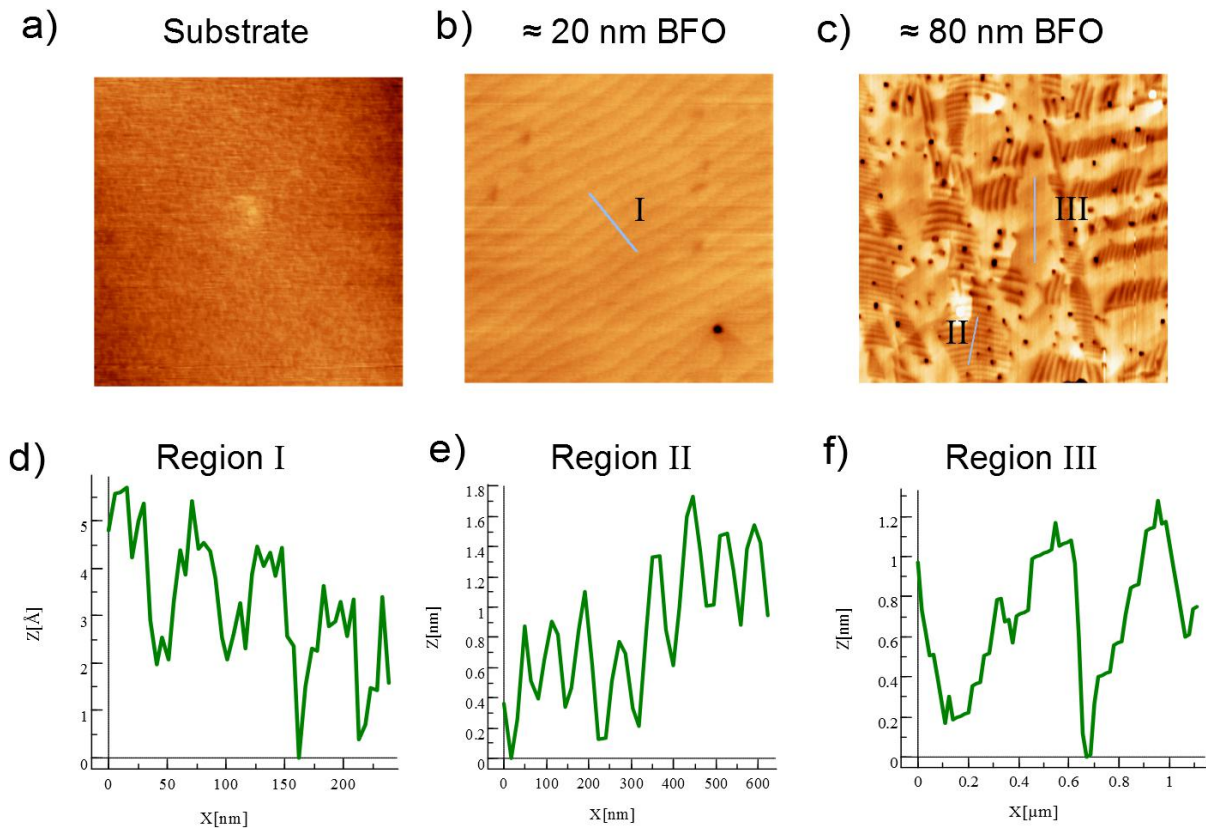


**Figure 5.2:** a) AFM image of the LAO substrate of  $4 \times 4 \mu\text{m}$  size. b) AFM image of 20 nm thick BFO film deposited on top of LAO substrate of  $1 \times 1 \mu\text{m}$  size. c) AFM image of 80 nm thick BFO film deposited on top of LAO substrate of  $4 \times 4 \mu\text{m}$  size. d) Profile of the line scan measured in the area marked *I* in figure b. e) Profile of the line scan measured in the area marked *II* in figure c. f) Profile of the line scan measured in the area marked *III* in Figure c.

stripes (marked III in Figure 5.2c) is similar to the profile shown in Figure 5.2d, but with a larger terrace width. This can be due to the step bunching phenomenon in which the individual terraces coalesce together as the film thickness increases to form terraces of larger width [126] [127]. Therefore it can be stated that the stripes are embedded into a matrix of the type shown in Figure 5.2b. Moreover, with increasing film thickness pinhole-like features also evolved in the morphology. The films, whose morphologies are shown in Figure 5.2b,c, were deposited by ablating the target at a repetition rate of 5 Hz which results in a growth rate of approximately  $0.16 \text{ \AA}/\text{sec}$ . However by increasing the repetition rate to 10 Hz better morphologies are obtained. This is shown in Figure 5.3 where the morphologies of the films prepared at 10 Hz frequency are presented. It can be observed from Figure 5.3a, that the pinhole-like features cease to evolve at higher growth rates.

It can be postulated here that by increasing the deposition rate, more amount of material reaches the substrate surface in a shorter interval of time. The lattice mismatch

between the in-plane lattice parameters of BFO and LAO is approx. 4.7%. As a result the BFO growth on LAO is under compressive stress which disallows the usual rhombohedral symmetry of BFO and forces the film to grow in a metastable state. At low frequency deposition, the film tends to relax in between two ablations and hence release the compressive stress *via* defect formations like pin holes. In a higher frequency deposition, the film has less time to relax between two subsequent ablations which inhibits defect formations.

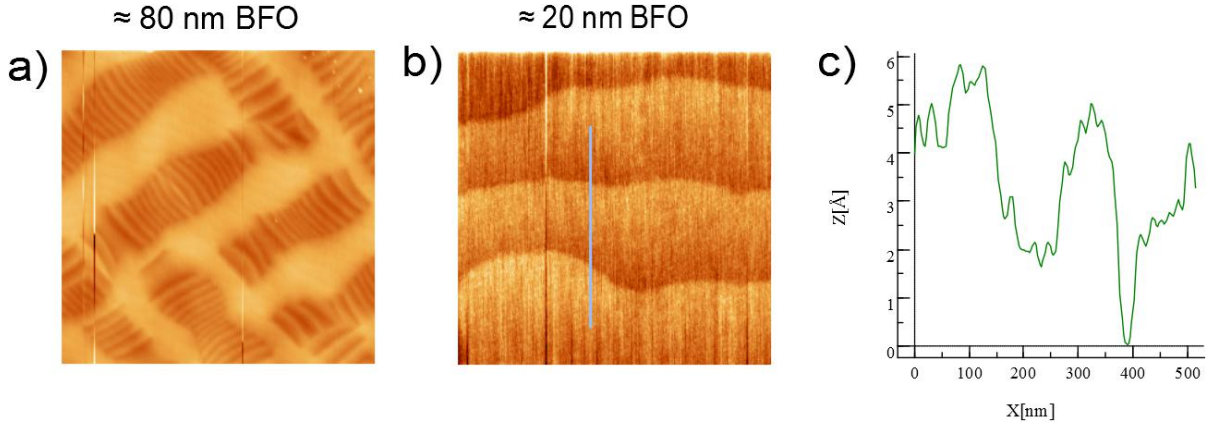


**Figure 5.3:** a) AFM image of size 3.3x3.3  $\mu\text{m}$  of a BFO film 80 nm thick grown at 10 Hz on LAO. b) AFM image of size 800x800 nm of a BFO film 20 nm thick grown at 10 Hz on LAO. c) Profile of the line scan marked in Figure b.

Additionally the atomic terraces of the type shown in Figure 5.2b were also reproduced in the 20 nm thick film grown at 10 Hz. The morphology of such a film is shown in Figure 5.3b. The profile of the line scan obtained across the terraces is shown in Figure 5.3c. The height of the terraces is between 4.4 and 4.7  $\text{\AA}$ . The reported value of the out-of-plane lattice parameter ( $c$ ) of BFO grown on LAO is 4.67  $\text{\AA}$  [27] [28]. Since the step height of the terraces are comparable to the reported value of  $c$ , it can be confirmed that the growth of BFO on LAO is of layer-by-layer type [125].

### 5.1.2 BiFeO<sub>3</sub> films on (La,Sr)MnO<sub>3</sub>-buffered substrates

In order to perform the ferroelectric characterization, a thin layer of (La<sub>0.7</sub>Sr<sub>0.3</sub>)MnO<sub>3</sub> (LSMO) was deposited on top of the LAO substrate, followed by the deposition of BFO film. The films of LSMO were deposited using the parameters stated in table 3.1 in section 3.1.1. Bulk LSMO is known to exhibit a rhombohedral structure at room temperature with a lattice parameter  $a_{rh}=5.506 \text{\AA}$ . Alternatively, likewise in the case of BFO, the lattice parameter can be expressed in pseudo cubic notation as  $a_{pc} \approx 3.87 \text{\AA}$ .

Apparently, due to the mismatch between pseudocubic lattice parameters of LAO and LSMO, the pseudomorphic growth of LSMO on LAO (i.e. when  $a_{pc(LAO)} = a_{pc(LSMO)}$ ) is realized under a compressive stress exerted by LAO which results in an expansion of the out-of-plane lattice parameter of LSMO. As a consequence, the rhombohedral structure of LSMO transforms into an orthorhombic structure [128]. The thickness of LSMO was restricted to approximately 10 nm. Studies have proven that the compressive strain persists in LSMO layers grown on LAO up to a thickness of 30 unit cells, i.e. about 12 nm. Moreover the conducting nature of LSMO is maintained under these strain conditions [129].

Thereafter, as discussed in section 5.1.1, the deposition of about 20 nm BFO film on top of LSMO was performed using a repetition rate of 10 Hz. Figure 5.4a shows the AFM image of the morphology of the resulting BFO film. As can be observed from the image, in contrast to the type of 20 nm thick film grown on bare LAO (Figure 5.3b), island formation is observed in this case. This is also proven by analyzing the profile of

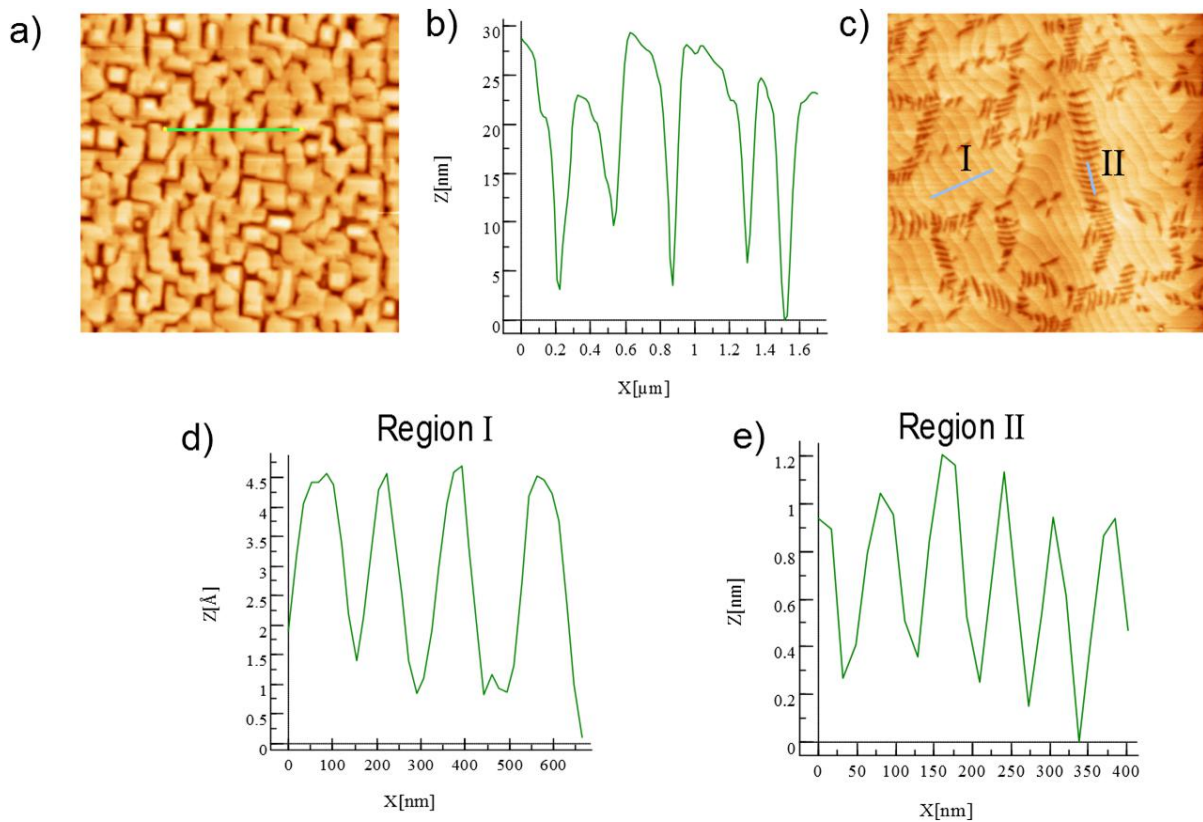


**Figure 5.4:** a) AFM image of size  $4 \times 4 \mu\text{m}$  of a 20 nm BFO film grown at 10 Hz on 10 nm LSMO. b) Profile of the line scan marked in Figure a. c) AFM image of size  $4 \times 4 \mu\text{m}$  of a 20 nm BFO film grown at 3 Hz on on 10 nm LSMO. d) Profile of the line scan marked I in Figure c. e) Profile of the line scan marked II in Figure c.

the line scan measured across a definite distance as is shown in Figure 5.4b. The depth of the pits is in the range of 15 to 20 nm which is approximately equal to the thickness of the film. However, a much better growth was achieved when the repetition rate for the deposition of BFO was reduced to 3 Hz and the corresponding morphology image is shown in Figure 5.4c. The 2-D layer-by-layer growth is confirmed by the step height (between  $3 \text{ \AA}$  and  $4 \text{ \AA}$ ) obtained in the line profile as is shown in Figure 5.4d. Evolution of stripe like patterns, similar to the type observed in the 80 nm thick BFO film on bare LAO substrate (Figure 5.2c), was also observed. By performing a line scan (Figure 5.4e), the resemblance between the nature of these stripes, in terms of their periodicity and height, and those obtained on bare LAO is evident.

It can be concluded from these observations that the stripe-like patterns are indeed related to the stress relaxation phenomenon in BFO films grown on LAO. The relaxation phenomenon can progress either by changing crystal orientation of certain regions or by adopting a different crystal structure under the assumption that the defect formation is neglected [130]. The appearance of these patterns in either thick films (80 nm) grown on

bare LAO or in thin films (20 nm) deposited on LSMO buffered substrates is an indication that the compressive in-plane stress, arising due to substrate-film lattice mismatch, gradually relaxes when the film thickness increases or is due to the existence of a buffer LSMO layer. This relaxation eventually culminates into formation of these patterns. The structural analysis of the thin (20 nm) and thick films (80 nm) is presented in the subsequent sections.

## 5.2 Structural analysis

The structural analysis of the samples was conducted *via* XRD by performing  $2\theta-\omega$  scans (section 3.3.1.1) and by investigating the reciprocal space maps (section 3.3.1.2). Cross-sectional TEM (section 3.3.2) images were obtained to achieve a better understanding on the growth at the substrate-film interface and to validate the presence of different BFO phases.

### 5.2.1 BiFeO<sub>3</sub> films grown on LaAlO<sub>3</sub> substrates

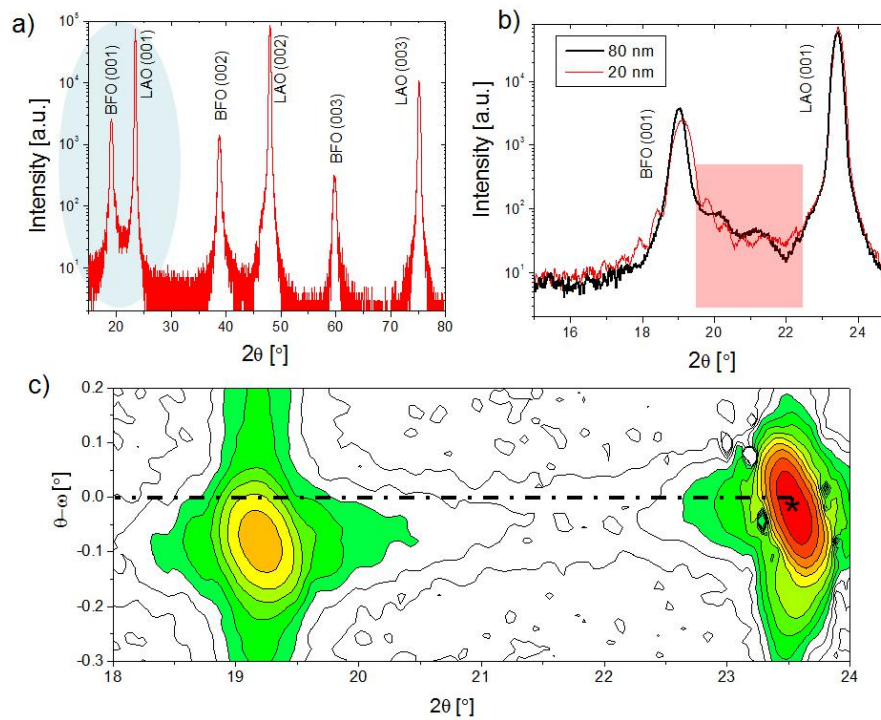
The  $2\theta-\omega$  scans, as explained in section 3.3.1.1, can provide reasonable knowledge about the phase purity of films and their epitaxial relation with the substrate. The  $(001)_{pc}$  plane was chosen as the reference plane to perform the  $2\theta-\omega$  scans on BiFeO<sub>3</sub> films grown on LaAlO<sub>3</sub> substrates.

Figure 5.5a shows the  $2\theta-\omega$  scan for a 20 nm thick BFO film that has a morphology similar to the type presented in Figure 5.3. The peaks in the scan have been indexed for convenience. The absence of any other peak, apart from the ones which are originating from the  $(00l)_{pc}$  of the substrate and the BFO film, indicates the phase purity of the film and indicates epitaxial growth. Additionally, since the growth direction of BFO is along the  $[001]_{pc}$  direction, the distance between the planes will give an approximation of the out of plane lattice parameter ( $c$ ) which can be calculated by using the Bragg relation (equation 3.6). The value of  $c$  comes out to be about 4.67 Å and is in agreement with reported values [27] [28]. This value is substantially larger than the usual lattice parameter of BFO which is 3.96 Å and yields a  $c/a$  ratio of 1.23 assuming  $a_{pc(LAO)} = a_{pc(BFO)}$ . Previous attempts to enhance the  $c/a$  ratio in BFO were realized by growth on SrTiO<sub>3</sub> substrates but it resulted in a meager increase of  $c/a$  onto approximately 1.04 [131] [132]. From this perspective, the BFO growth on LAO has attracted much interest, since ferroelectric materials with high  $c/a$  ratio are predicted to exhibit larger polarization values [133] [134]. Moreover, the high  $c/a$  ratio proves that the BFO crystallizes on LAO in a tetragonal-like symmetry as was previously reported [27]. Also, it is noteworthy to mention the appearance of nearly symmetrical oscillations-like patterns on either side of the BFO  $(001)_{pc}$  peak in the  $2\theta-\omega$  scan. These oscillations are evident when the blue area marked in Figure 5.5a around the  $(001)_{pc}$  BFO peak is zoomed into, as is shown in Figure 5.5b. The presence of these oscillations, also known as Kiessig or thickness fringes, validates a smooth film-substrate interface and a smooth BFO surface which was also proven by AFM investigations presented before.

The  $2\theta-\omega$  measurement from an 80 nm thick film resulted in a scan similar to the type shown in Figure 5.5a. The Kiessig fringes were also observed in the thick film however with lesser periodicity (Figure 5.5b). The  $c$  value obtained in case of 80 nm thickness was about 4.61 Å. This means that the effect of in-plane stress due to substrate-film



pseudomorphy is maintained. The presence of stripe-like features, which were observed in AFM of thick films, does not result in any form of secondary phase peaks. It can be postulated here that either the stripes have a structure which is similar to the structure of the film matrix or the amount of stripes is below the detection limit, at least in case of a  $2\theta - \omega$  scan. Additionally, a reciprocal space map (RSM) was obtained around the  $(001)_{pc}$  plane of BFO for the 20 nm thick film which is presented in Figure 5.5c. The slight offset between the substrate and the film peak on the  $\theta - \omega$  scale is evident and it can be speculated that the  $(001)_{pc}$  plane of the substrate and that of the film are slightly shifted with respect to each other. As a result it can be postulated here that the BFO growth on LAO is not purely in the tetragonal phase but rather involves a few degrees of monoclinic distortion.



**Figure 5.5:** a)  $2\theta - \omega$  scan measured around  $(001)_{pc}$  plane for a 20 nm thick BFO film grown on LAO. b) Zoomed in plot of the area marked in blue in Figure a showing the Kiessig fringes (marked in red) around BFO the  $(001)_{pc}$  peak. c) Reciprocal space map of a 20 nm thick BFO film obtained around the  $(001)_{pc}$  plane of BFO. The substrate peak is labeled with a star and the zero position is marked with a dashed line.

In order to further elucidate the structural properties, off axis reciprocal space maps were obtained for the thin and thick films. As stated in section 3.3.1.2, an odd plane which includes information about the in-plane lattice parameter ( $a$ ), namely  $(103)$ , was chosen as the reference plane for performing the measurements. In Figure 5.6a, the RSM for a 20 nm thick BFO film is presented, and in Figure 5.6b for an 80 nm thick film. The peak which originates from the  $(103)_{film}$  is split roughly into three, with the third peak in Figure 5.6a barely spreading out. This is indicative of a monoclinic structure [135] [136]. For convenience the RSM data are presented in terms of out-of-plane ( $c$ ) and in-plane ( $a$  and  $b$ ) lattice parameters. The value of  $c$  is between 4.6 and 4.7 Å, whereas  $a$  and  $b$  are between 3.7 and 3.8 Å.

The monoclinic structure is accompanied with a distortion angle which will be referred to as  $\beta$  henceforth. Depending upon the plane in which the angle  $\beta$  exists, the monoclinic structure can be categorized as  $M_a$ ,  $M_b$  or  $M_c$  according to the notation introduced by Vanderbilt and Cohen [137]. All of these structures belong to low symmetry phases and can result in ferroelectricity [135] [137]. Such kind of structures also have been reported in a variety of ferroelectric materials with morphotropic phase boundaries [117] [118] and assist in realizing the transition between rhombohedral and tetragonal phases [117] [118]. Consequently the direction of the polarization vector varies in these structures based on the plane of the distortion angle. The distinction between these structures is presented

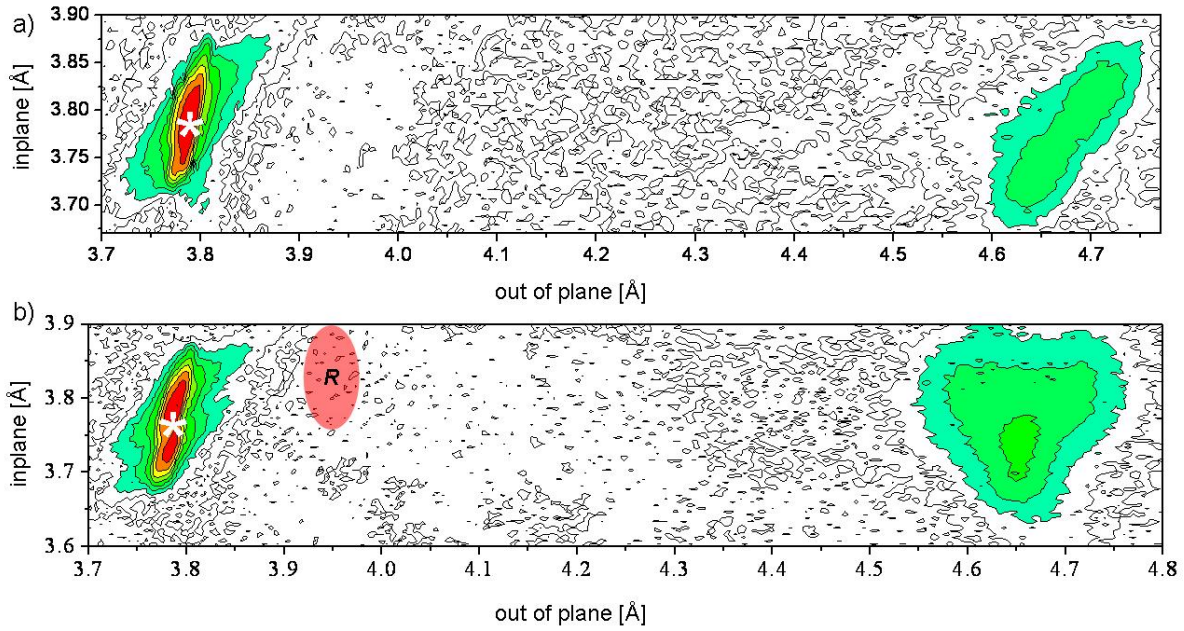


**Figure 5.6:** a) RSM measured around the  $(103)_{pc}$  plane for a 20 nm thick BFO film grown on LAO. b) RSM measured around the  $(103)_{pc}$  plane for an 80 nm thick BFO film grown on LAO with the red area marked “R” indicating the possible position for a peak originating from the rhombohedral phase. The RSMs are presented in terms of out-of-plane ( $c$ ) and in-plane ( $a$ ) lattice parameters. The substrate peaks are labeled with a white star.

in the schematic in Figures 5.7a and b. For better understanding of the monoclinic structures, a tetragonal unit cell (red cell in Figure 5.7a and b) has been used as a reference. In case of  $M_a$  or  $M_b$  structures, the unit cell is rotated by an angle of  $45^\circ$  around the  $[00l]$  axis with respect to the tetragonal unit cell and as a result is aligned along the  $[hh0]$  direction as is shown in Figure 5.7a. The  $\beta$  angle lies in the  $(h\bar{h}0)$  plane and apparently so the polarization ( $P$ ). Despite having similar structures, the magnitudes of the projection of the polarization along the reference axis are different in  $M_a$  and  $M_b$ . In case of the  $M_c$  structure, the unit cell is more close to the reference tetragonal cell with the  $b$  axis aligned along the  $[0k0]$  direction. The angle  $\beta$  lies in the  $(0k0)$  plane and so is the polarization.

The threefold splitting which is observed in the RSM around the  $(103)$  plane in Figures 5.6a,b is attributed to the  $M_c$  structure [135] and can be visualized by the help of a schematic which is presented in Figure 5.7. The schematic depicts the possible variations of the monoclinic distortion when the distortion angle  $\beta$  lies in the  $(0k0)$  plane and the distortion is along  $[h00]$  and  $[\bar{h}00]$  directions which results in two variants. These two

variants are shown in Figures 5.7c and e. A third and a fourth variant can also be conceived where  $\beta$  lies in a direction which is perpendicular to the  $(0k0)$  plane i.e.  $[0k0]$  and  $[0\bar{k}0]$ , as is shown in Figures 5.7d (the splitting is not shown). As a result, when a RSM study is performed on such a system around the  $(103)$  plane, the monoclinic distortion leads to a fourfold splitting of the peak originating from the film with each split peak corresponding to one of the variants presented in Figure 5.7 [138]. Additionally, as stated before, the  $M_c$  phase is known to exhibit ferroelectricity which means each of the variant is also a ferroelastic domain [137]. However, the peaks corresponding to the third and fourth variant tend to overlap with each other due to which only three peaks are visible in an actual RSM measurement. The four peaks can be indexed according to the direction along which the distortion exists i.e.  $(\bar{1}03)$ ,  $(103)$ ,  $(0\bar{1}3)$  and  $(013)$  [135]. The splitting is more evident and visible in the RSM performed around the  $(103)$  plane for an 80 nm thick film as is shown in Figure 5.6b.

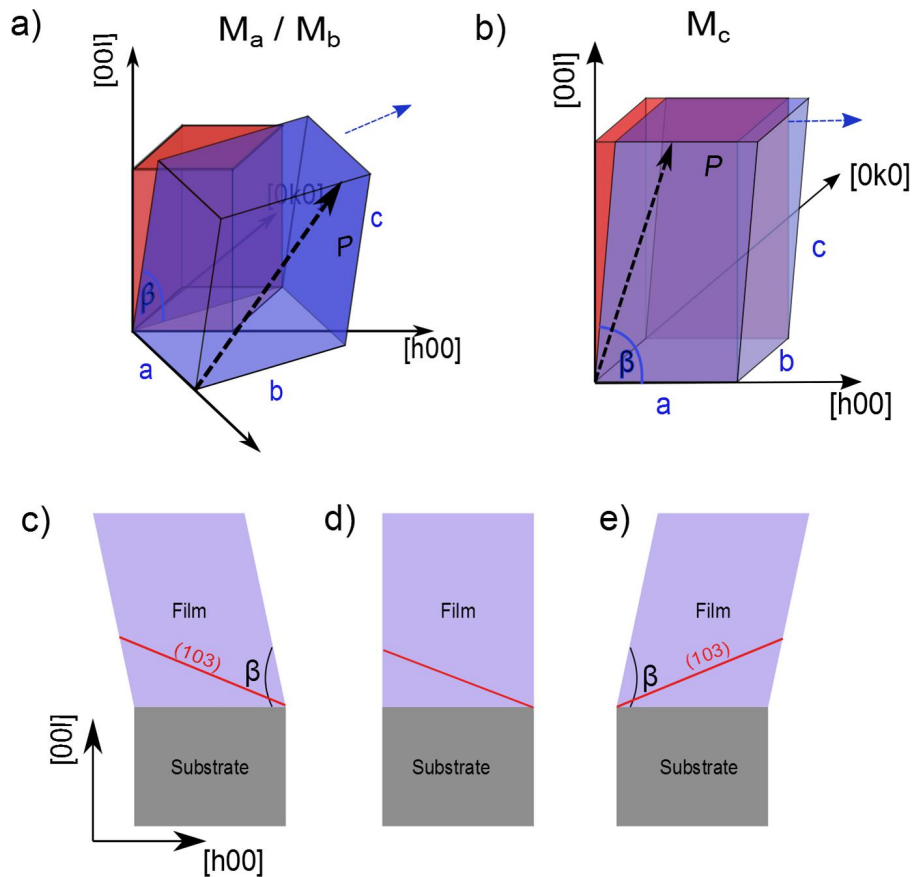


**Figure 5.7:** a) Schematic of a unit cell of  $M_a/M_b$  phase (blue) in comparison to a tetragonal unit cell (red) with the polarization  $P$  and angle  $\beta$  lying in the  $(h\bar{h}0)$  plane. b) Schematic of a unit cell of  $M_c$  phase (blue) in comparison to a tetragonal unit cell (red) with the polarization  $P$  and distortion angle  $\beta$  lying in the  $(0k0)$  plane. Schematic depicting the different variants possible in the  $M_c$  structure when the distortion is along c)  $[\bar{h}00]$  d)  $[0\bar{k}0]$  or  $[0k0]$  and e)  $[h00]$  direction.

By doing geometrical analysis of the reflections of the  $\{103\}$  set of planes and using the equations of the type given in section 3.3.1.2, the in-plane lattice parameters  $a$  and  $b$  along with out-of-plane lattice parameter  $c$  and the distortion angle  $\beta$  can be calculated. The values of these parameters have been calculated for the RSM presented in Figure

5.6b, and are as follows:  $a \approx 3.816 \text{ \AA}$ ,  $b \approx 3.751 \text{ \AA}$ ,  $c \approx 4.613 \text{ \AA}$ , and  $\beta \approx 88.806$ . These values are in agreement with the previously reported values for the monoclinic phase of BFO grown on LAO substrate [28] [139].

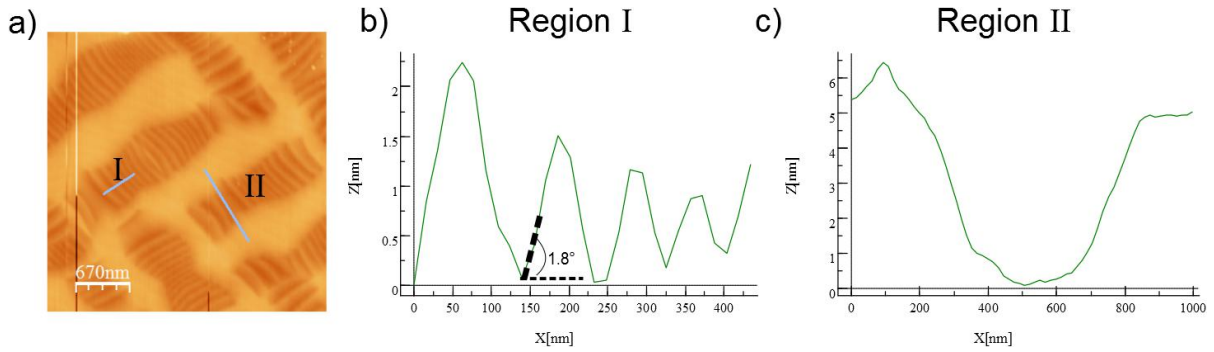


**Figure 5.8:** a) AFM image of size  $3.3 \times 3.3 \mu\text{m}$  of a BFO film 80 nm thick grown at 10 Hz on LAO. b) Profile of the line scan obtained from region I in (a). c) Profile of the line scan obtained from region II in (a).

However, it is rather intriguing that the stripe-like features observed in the AFM analysis of the 80 nm thick film cannot be conclusively observed in the diffraction studies and neither in the RSM patterns obtained. Initial reports claimed that the stripes correspond to the rhombohedral structure [28]. Subsequent studies via PFM revealed mechanisms based on which the stripes (rhombohedral phase) can be changed to the bulk ( $M_c$  phase) and vice versa by the application of an electric field [122]. This is rather contrary to the RSM presented in Figure 5.6b where the possible position of the rhombohedral phase has been marked (red spot) had it been present. From this observation one might suspect that the concentration of these stripes in the films is minimal and below the detection limit of the X-ray scans. Another reason for the absence of the rhombohedral peaks could be the different orientation of the unit cells within the stripes which causes the (103) plane in these unit cells to be differently aligned with respect to the incident x-rays.

The tilting of the unit cells in the stripe-like region can be investigated by analyzing the morphology of the stripe pattern. In Figure 5.8a, the morphology of an 80 nm thick film is presented. The line scan across the stripe (Region I) is presented in Figure 5.8b. The angle which one of the sides of the stripe makes with the bulk surface is approximately  $1.8^\circ$ . Also, the profile of the lateral line scan across one of the steps of the stripe, as is shown in Figure 5.8c, reveals that the stripe is in depressed surface area when compared to the bulk surface. These scans indicate a different orientation of the unit cell, in comparison to the bulk surface, in the striped region. The tilting of these unit cells can also be visualized as one of the mechanisms *via* which the film tends to relax the in-plane strain due to the substrate-film lattice mismatch, without changing the overall out-of-plane lattice parameter. A better insight into the structure of the bulk and strip-like features can be achieved by TEM investigations which are discussed in the subsequent subsection.

### 5.2.1.1 TEM investigations

TEM investigations were performed on BFO films with 20 and 60 nm thickness grown on LAO substrate. The AFM topography images of the films are shown in Figures 5.9a

and e for 20 and 60 nm thick films, respectively. The morphology of the 60 nm thick film (Figure 5.9e) also shows the stripe-like features which were visible in the 80 nm thick film.

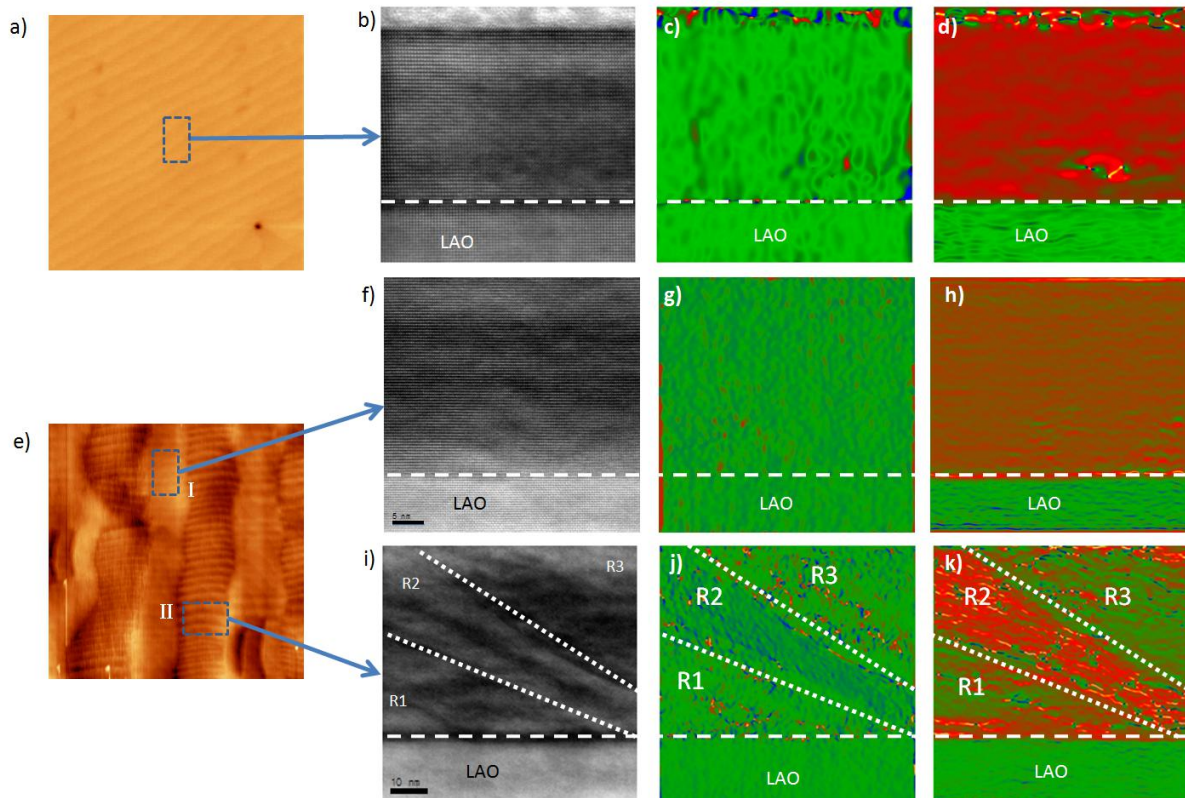


**Figure 5.9:** a) AFM image of size  $1 \times 1 \mu\text{m}$  of a 20 nm thick BFO film grown on LAO. b) HR-TEM image from an area which is of the type indicated in Figure a. Strain maps acquired in the c)  $[110]_{pc}$  and d)  $[001]_{pc}$  directions for the image in Figure b. e) AFM image of size  $3.2 \times 3.2 \mu\text{m}$  of a 60 nm thick BFO film grown on LAO. HR-TEM images from an area indicated as f) Region I and i) Region II in Figure e. Strain maps acquired in  $[110]_{pc}$  direction for g) Region I and j) Region II. Strain maps acquired in  $[001]_{pc}$  direction for h) Region I and k) Region II.

The smooth interface between the film and the substrate, with consequent epitaxial growth is evident from the high resolution TEM (HR-TEM) images shown in Figures 5.9b and f for 20 and 60 nm films, respectively. It should be noted that the image in Figure 5.9f corresponds to the area of the film without stripe-like feature (Region I in Figure 5.9e). From the selected area diffraction (SAED) patterns (not shown here) and by measuring the interplanar distances from HR-TEM images shown in Figures 5.9b and f, it was proven that BFO is in the  $M_c$  phase. The TEM image in Figure 5.9i is acquired from the stripe-like region (Region II in Figure 5.9e). The image has been categorized in three distinct regions based on different contrasts as region R1, R2 and R3. The analysis of the SAED patterns obtained from regions R1 and R3 reveal a symmetry which resembles the rhombohedral structure, although the corresponding lattice parameter in the  $[001]_{pc}$  direction is elongated. On the other hand, the SAED pattern from Region R2 indicates the presence of the  $M_c$  phase in this region.

Additionally, a geometrical phase analysis (GPA) was performed, based on the HR-TEM images, to acquire the strain maps in the  $[110]_{pc}$  and  $[001]_{pc}$  direction. The reference

for strain calculation is the LAO structure. The relative strain increases from the green color to red color. The consistent green color visible in the strain maps obtained in the  $[110]_{pc}$  direction in both films (Figures 5.9c, g and j) indicate that there is no or minimal strain in the in-plane direction. This validates that the films (20 and 60 nm) completely adopt the lattice parameter of the substrate which also was proven in the X-ray studies. The red color visible in the strain maps in the  $[001]_{pc}$  direction for both films (Figure 5.9d and h) depicts a strain of about 23% in the out-of-plane direction and translates into a  $c_{pc}$  between 4.61 Å and 4.67 Å which corresponds to the  $M_c$  phase. However the strain map in the  $[001]_{pc}$  direction for the stripe-like region (Figure 5.9k) is a bit more complex with shades of red and green. The greenish color in regions R1 and R3 indicates lesser strain, with  $c_{pc}$  closer to that of LAO. This also supports the interpretation from the SAED patterns where the existence of a rhombohedral-like phase in this region is proposed. Region R2 has a reddish shade indicating higher  $c_{pc}$  that corresponds to the  $M_c$  phase. Hence it can be concluded that the stripes in these films are composed of rhombohedral-like and  $M_c$  phase.

The nature and structure of these stripes has been under some deliberation in the recent past. In the very first report from Zeches et. al. [28], the stripes were considered to be composed of the tetragonal-like T and rhombohedral-like R phase of BFO. Additionally, the bulk of the film, within which these stripes were embedded, was proposed to be the T-phase with slight monoclinic distortion. In the subsequent works from Damodaran [136] and Chen et. al. [135] it was proven that the bulk in these films is made up of the  $M_c$  phase whereas the stripes are composed of a mixture of tilted  $M_a/M_b$  and  $M_c$  phase [136]. In a more recent work from Beekman et.al. [140], involving temperature dependent studies, the stripes are shown to comprise of  $S'$  and  $M_c$  phase. The  $c/a$  ratio for the  $S'$  phase was calculated to be 1.09 but the symmetry of this  $S'$  phase advertently was not defined. Nevertheless, from temperature studies, primarily two factors which contribute towards the formation of these stripes were found, namely: relaxation of stresses induced due to lattice mismatch and the different thermal expansion coefficients [140].

Our work on thick films, based on the images shown in Figure 5.9, largely is in agreement with the results of Beekman et. al. [140]. However, we indicate the so called  $S'$  phase as the rhombohedral-like phase since the symmetry and lattice parameters resemble the rhombohedral symmetry although there is an evident elongation along the  $c$ -direction. Moreover, the tilting within these stripes (shown in Figure 5.8) makes the detection of the rhombohedral-like phase rather tedious in the RSM studies. But in thin film of thickness approximately 20 nm, our work [141], lead by Dr.Y.H.Kim, indicates the presence of tetragonal phase in the stripes. It must be mentioned here that the bulk of the film still consists of  $M_c$  phase with extremely small traces of stripe region which were investigated by TEM and were found to be composed of tetragonal and  $M_c$  phase. From this one might speculate different relaxation mechanisms adopted by the films of different thickness.

### 5.2.2 BiFeO<sub>3</sub> films on (La<sub>0.7</sub>Sr<sub>0.3</sub>)MnO<sub>3</sub>-buffered substrates

The  $2\theta - \omega$  scans to investigate the structure of the BFO films grown on LAO with LSMO serving as the bottom electrode were performed for the  $(001)_{pc}$  plane. The scans for films which were deposited at different frequencies of target ablation are shown in Figure 5.10. The LSMO and BFO film thickness are 10 and 20 nm, respectively, for all the scans presented in Figure 5.10a. It can be observed from Figure 5.10a, that when

BFO is deposited at a frequency of 10 Hz, there is hardly any formation of the  $M_c$  phase of BFO. The out-of-plane lattice parameter obtained from the BFO (001) peak is 4 Å which indicates towards the presence of the rhombohedral phase since  $c_{pc}(\text{rhombohedral}) = 3.96 \text{ \AA}$  (the morphology of such a film was presented in Figure 5.4a.) Additionally, the peak originating from the rhombohedral BFO overshadows the  $(001)_{pc}$  peak from LSMO. As stated in section 5.1.2, due to the 2.64 % lattice mismatch with LAO, the LSMO grows under compressive stress on LAO. As a result the out-of-plane parameter expands to 4 Å, which is in accordance with reported results [129].

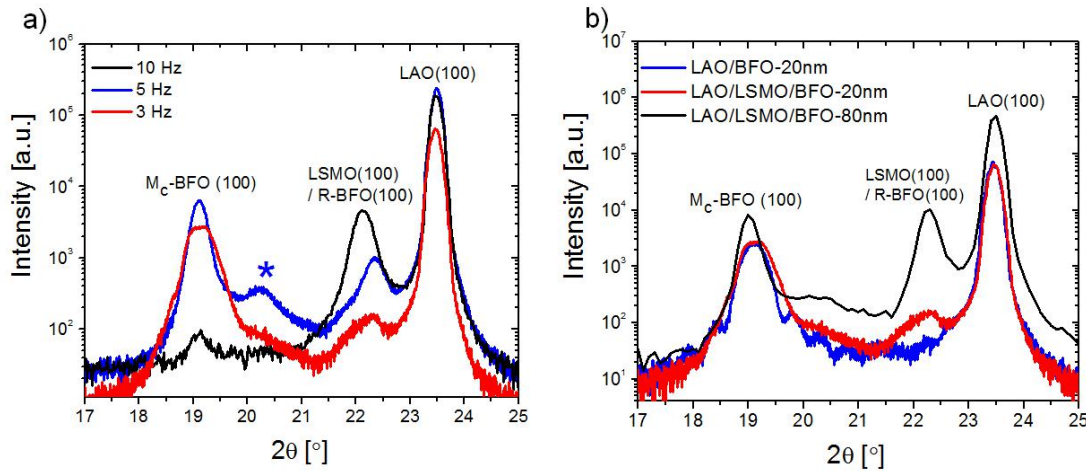


**Figure 5.10:** a)  $2\theta - \omega$  scans of films comprising of BFO and LSMO layers grown on LAO substrates by varying the ablation frequency during the deposition process. The blue star indicates an intermediate phase of BFO. b) Comparison of  $2\theta - \omega$  scans obtained from BFO films grown on LAO with and without LSMO buffer layer.

When the ablation rate during the deposition was reduced to 5 Hz, the nucleation of the  $M_c$  phase of BFO is observed as is evident in Figure 5.10a. As a result there is a steep decrease in the intensity from the rhombohedral BFO phase. Additionally, the nucleation of an intermediate phase is also observed (marked with a blue star in Figure 5.10a) which has a  $c$  parameter of approximately 4.38 Å that lies between  $c_{pc}$  of the  $M_c$  phase and  $c_{pc}$  of the rhombohedral phase. A further decrease in the ablation rate to 3 Hz results in a BFO film (morphology shown in Figure 5.4c) which crystallizes completely in the  $M_c$  phase with a corresponding  $c_{pc}$  of 4.67 Å. This value is the same which is obtained in the BFO film deposited on bare LAO that is also evident when the  $2\theta - \omega$  scans of the two films are compared as shown in Figure 5.10b.

However, as the BFO film thickness is increased to 80 nm, while continuing with 3 Hz ablation frequency, in addition to the crystallization of the  $M_c$  phase of BFO, there is an evident increase in the peak which corresponds to both LSMO  $(001)_{pc}$  and rhombohedral BFO  $(001)_{pc}$  (Figure 5.10b). This indicates that as the film thickness increases, the BFO film grown on LSMO eventually tends to relax by crystallizing in the rhombohedral phase, and the occurrence of a gradual loss of pseudomorphy with the substrate.

RSM contours were obtained around the  $(103)_{pc}$  plane in order to further elucidate the epitaxial relation between the different layers and the substrate. Figure 5.11a depicts the RSM for a 20 nm thick BFO film grown with an ablation frequency of 3 Hz on top of 10 nm LSMO. The RSM, presented in out-of-plane and in-plane lattice parameters,

clearly reveals the distinct peaks arising from the  $M_c$  phase of BFO and the “tetragonal-like” phase of LSMO. Both the films apparently adopt the value of  $a_{pc}$  of the substrate.

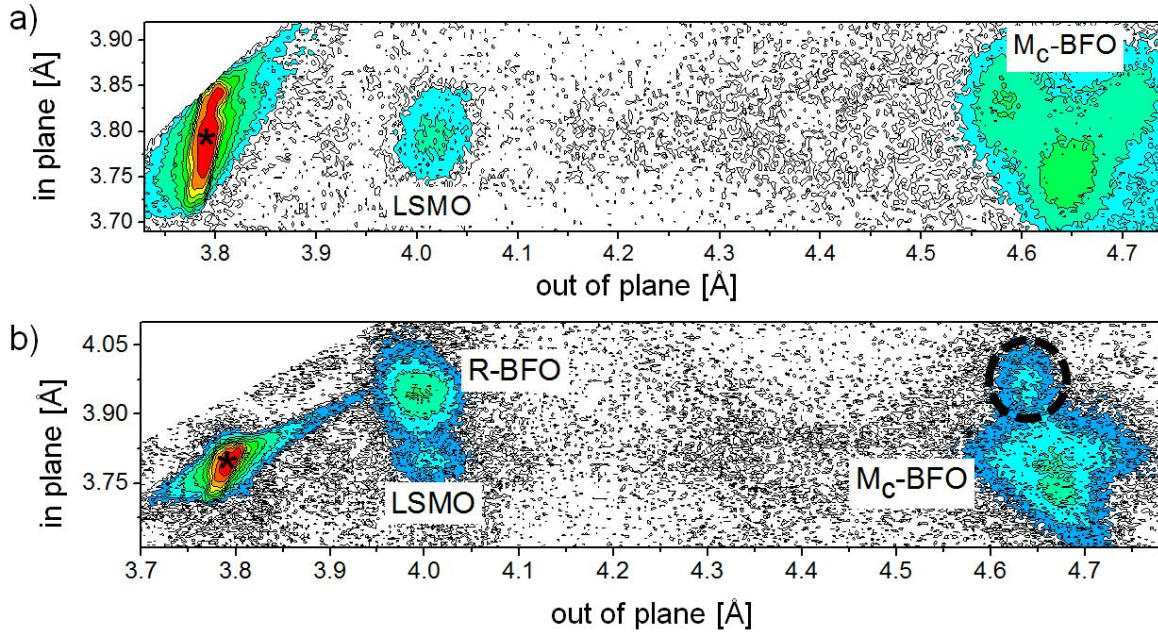


**Figure 5.11:** a) RSM obtained around the  $(103)_{pc}$  plane for a sample with a 20 nm BFO film grown on top of 10 nm LSMO with LAO as substrate. b) RSM obtained around the  $(103)_{pc}$  plane for a sample with an 80 nm thick BFO film grown on top of 10 nm LSMO with LAO as substrate. The star indicates the position of the peak from the substrate.

In the case when the thickness of BFO is increased to about 80 nm, with the thickness of LSMO maintained at 10 nm and persisting with an ablation frequency of 3 Hz, the peak from BFO is split into two phases, namely the  $M_c$  phase and the rhombohedral phase as is shown in Figure 5.11b. The rhombohedral phase of BFO has  $a = 3.94 \text{ \AA}$ , and  $c = 3.99 \text{ \AA}$ , which indicates that the rhombohedral unit cell is slightly elongated along the  $c$  direction. Surprisingly the RSM reveals another phase of BFO which has been encircled in Figure 5.11b. The lattice parameters for this phase are  $a = 3.96 \text{ \AA}$ , and  $c = 4.63 \text{ \AA}$ . The phase exhibits an enhanced  $c$  parameter although the  $a$  parameter resembles that of a relaxed rhombohedral BFO. Such a phase of BFO might be one of the variants with a parent monoclinic cell.

It can be concluded here that the relaxation behavior of BFO is largely changed with LSMO as the buffer layer. Without the buffer layer, BFO grows completely in the  $M_c$  phase on bare LAO at a high ablation frequency of 10 Hz, and the effect of in-plane strain persists up to a thickness of 80 nm. In contrast, when grown on LSMO, despite LSMO being completely strained, the ablation frequency for BFO must be reduced to 3 Hz to obtain the  $M_c$  phase. Moreover the BFO tends to relax much earlier in terms of thickness.

One of the possible explanations could be the suppression of octahedra rotations at the LSMO-BFO interface. Unlike other conventional ferroelectric materials, BFO allows large degrees of rotation of its oxygen octahedra [40]. To a certain extent, the tilting and rotation of these octahedra can be held responsible for a strain accommodation in large lattice mismatch conditions [142] [143]. Additionally such mechanisms have also been



discussed to allow for a large magnetoelectric effect in BFO [144]. As a result, the effect of strain persists for larger thickness values when deposited on bare LAO. However, studies have shown that when BFO grows epitaxially on top of LSMO, the octahedra tilting in BFO is largely suppressed due to smaller tilt angles in LSMO [145]. Due to this restriction of octahedra rotation, the strain in BFO cannot be accommodated for higher thickness which eventually is relaxed *via* nucleation of the rhombohedral phase and other phases as indicated in Figure 5.11b.

The results of the structural investigations performed on BFO films, of different thickness, grown on LAO substrates with and without LSMO layer are summarized in table 5.1.

**Table 5.1:** Evolution of different phases

Thickness of BFO	BFO/LAO	BFO/LSMO/LAO
20 nm	$M_c$	Dominant $M_c$ with minimal evolution of stripes
80 nm	Dominant $M_c$ + stripes ( $M_c$ and R)	$M_c + R$ + intermediate phases

### 5.3 PFM studies

As stated in section 5.2.1, each of the monoclinic distortion variants of the  $M_c$  phase is a ferroelastic or ferroelectric domain. The ferroelectric  $M_c$  phase has also been explored in PMN-PT crystals, and the various possible domain configurations have been analyzed [146]. In the  $M_c$  phase, the spontaneous polarization lies in the  $\{010\}$  family of planes. The possible variants for polarization orientation are shown in Figure 5.12a. Each face of the cube has the possibility to accommodate four polarization variants resulting in overall 24 polarization variants. In Figure 5.12a, 12 orientations are presented, each having its own ferroelastic distortion (not shown). Likewise in the case mentioned in section 2.1.3.3,  $\pm P_i$  will give the same ferroelastic distortion. However by applying strain or poling *via* an electric field, the number of possible polarization variants or the number of ferroelastic distortions can be reduced. This is presented in Figure 5.12b where only four polarization variants are present due to an in-plane epitaxial strain. The orientation of the domain walls which separate these domains has been theoretically predicted by incorporating the conditions of mechanical coherency and electrical neutrality between two successive domains. As a result, the domain walls allowed in the  $M_c$  phase are oriented along the  $\langle 110 \rangle$  family of directions [146] [147]. For instance, the domain walls which separate the variants 1 and 2 in Figure 5.12b are along the  $[110]$  direction when observed in the (001) plane as is shown in Figure 5.12c. However the variants 2 – 3 are separated by domain walls which are aligned along  $[1\bar{1}0]$  when observed in the (001) plane as shown in Figure 5.12d. Similarly, the traces of domain walls corresponding to variant pairs 3 – 4 and 4 – 1 will also be lying in the (001) plane.

Keeping in perspective the above discussion regarding the domain/domain wall orientations in the  $M_c$  phase, one might suspect a rather complicated domain pattern in (001)-oriented BFO films grown on LAO (001). But, like for the case depicted in Figure

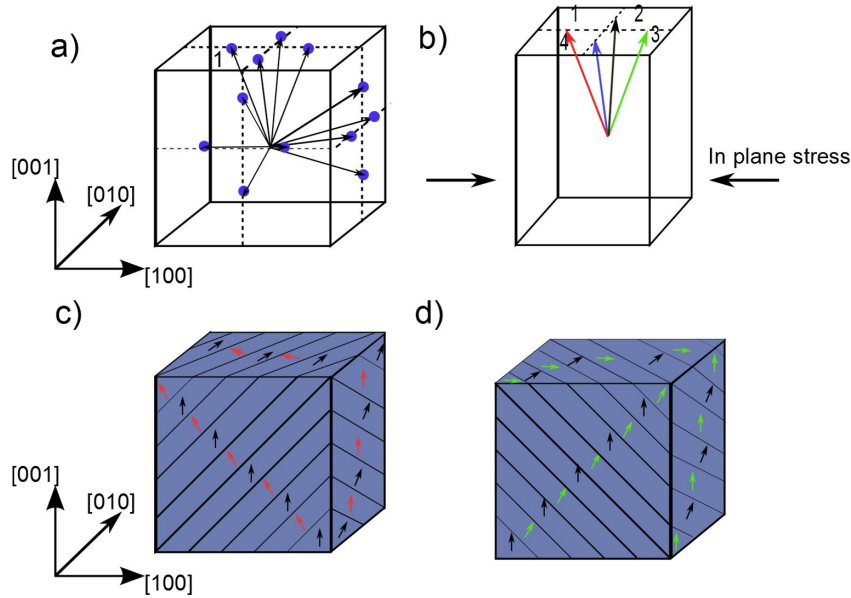


**Figure 5.12:** a) Schematic of 12 out of 24 polarization variants possible in the ferroelectric  $M_c$  phase. b) Four polarization variants possible under the application of in-plane strain. The orientation of domains and domain walls between polarization variants c) 1 and 2, d) 2 and 3.

5.12b, the number of possible domain configurations are reduced because of the in-plane strain persistent in BFO when grown on LAO. Figures 5.13a-h show the AFM and corresponding PFM images of a 20 nm thick BFO film grown on LAO. The cantilever was oriented along the  $[1\bar{1}0]$  direction for visualizing the domains (as explained in section 3.2.3). The vertical PFM (VPFM) images of the amplitude (Figure 5.13b) and phase (Figure 5.13c) are largely consistent in their respective colors which means that the out-of-plane projection of the polarization vector is completely in one direction i.e. upwards $\uparrow$  and resembles the case depicted in Figure 5.12b. The lateral PFM (LPFM) images of the amplitude (Figures 5.13d) and phase (Figures 5.13e) reveal the presence of stripe domain patterns. The corresponding domain walls are running in  $[110]$  direction as proposed by the theory [146] [147]. The sizes of the stripe domains range from 20 to 30 nm. The presence of such patterns indicates the dominance of only one type of domain pair variant out of the four possible, i.e. either (1-2), (2-3), (3-4) or (4-1). It is also noteworthy to mention the direction of the stripe domains with respect to the steps observed in the topography. It can be observed that the steps make an angle of  $45^\circ$  with the domains. However this relation is not valid in all the cases. In Figures 5.13f-g, the steps in the morphology (acquired from a different sample) are aligned along with the stripe domains. The domains, however, still persist along one of the  $\langle 110 \rangle$  directions.

In case of thick BFO films (about 80 nm), the domain pattern, as does the morphology, gets more complicated and complex to decipher. Figures 5.14b-e show the typical PFM response obtained from a thick BFO film grown on LAO. It can be observed that the VPFM-phase image (Figure 5.14c) is again consistent in one direction with uniform color. In VPFM-amplitude (Figure 5.14b) image, the stripe like features from the morphology (Figure 5.14a) are visible but they leave no such trace in the VPFM phase image (Figure 5.14c). Thus one might suspect a cross-talk between the VPFM and morphology signal. In the LPFM images, the presence of different kinds of domain pair variants is evident

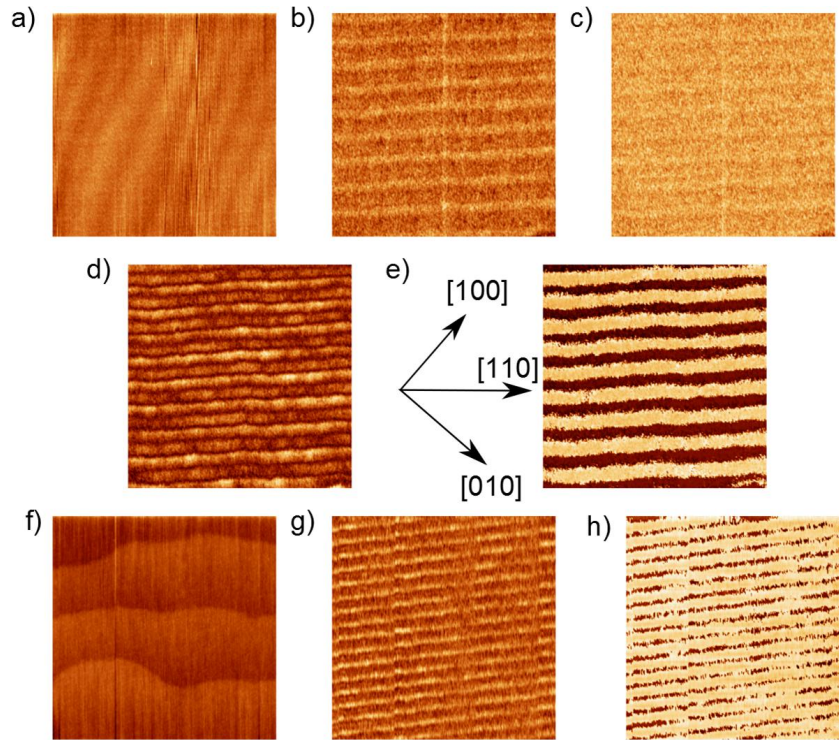


**Figure 5.13:** a) AFM image of size  $0.5 \times 0.5 \mu\text{m}$  for a 20 nm BFO film grown on LAO and the corresponding PFM images showing b) VPFM-amplitude, c) VPFM-phase, d) LPFM-amplitude, e) LPFM-phase. f) AFM image of size  $0.8 \times 0.8 \mu\text{m}$  for a 20 nm BFO film grown on LAO and the corresponding PFM images showing g) LPFM-amplitude and h) LPFM-phase.

due to the presence of different colors. By combining the information obtained from the LPFM amplitude image (Figure 5.14d) and LPFM phase image (Figure 5.14e) it is possible to understand, although not conclusively, the domain configurations. The region marked I and III in the LPFM-amplitude show domain walls running at  $90^\circ$  with respect to each other. However in the LPFM-phase image these areas come in the red region. This clearly indicates that the polarization projections in these two regions lie on the same side (R side) of the cantilever as depicted in the schematic in Figure 5.14f. Thus the domain walls in region I belong to variants (2-3), whereas the domain walls in region III belong to the (1-2) variant. Additionally, the domain walls in region II have the same orientation as in region III. However in the LPFM-phase image they appear as yellow region which means that the polarization in the two regions is opposite to each other. From this it can be postulated that the domain walls in region II belong to variants (3-4).

In Figure 5.14g-h, a zoomed in area from the same sample is presented. The steps in the morphology are clearly visible and have been sub-marked as region IV and V in Figure 5.14g. The corresponding LPFM-phase image from the two regions reveals the presence of stripe domains however with different periodicity. The PFM image was obtained with the cantilever along one of the  $\langle 110 \rangle$  directions. The different periodicity of the domains in the two regions could be only due to different pairs of polarization variants. From the schematic shown in Figure 5.14i, it is clear that when the scanning is performed in the  $\langle 110 \rangle$  direction, only the domain walls corresponding to variants (1-2) and (3-4) are possible. The stripe like region in the morphology seems to be acting like a bridge between these two kinds of domain wall variants. One might speculate here

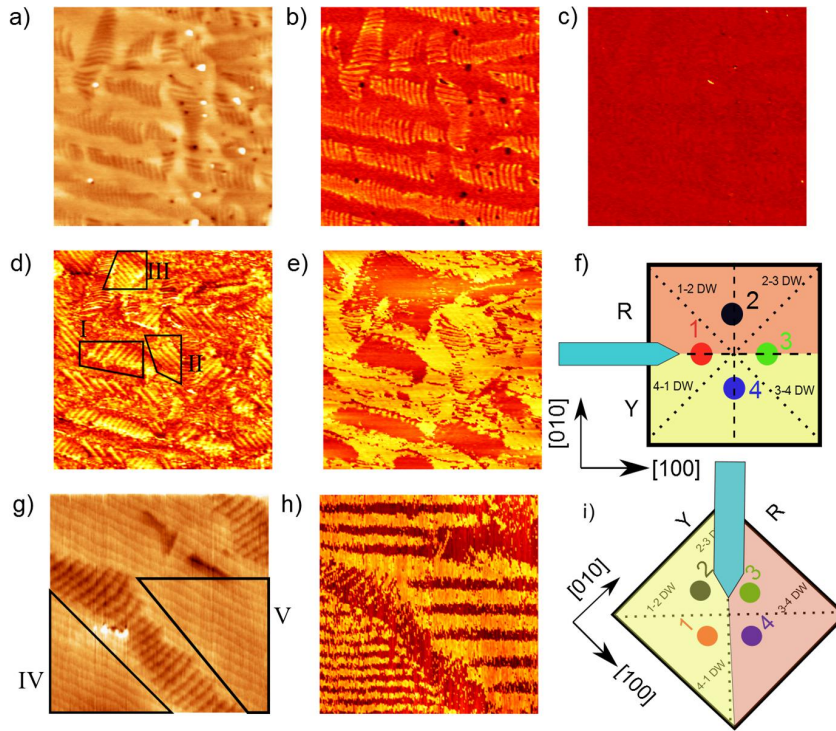


**Figure 5.14:** AFM image of size  $4 \times 4 \mu\text{m}$  for an 80 nm BFO film grown on LAO and the corresponding PFM images showing b) VPFM-amplitude, c) VPFM-phase, d) LPFM-amplitude, e) LPFM-phase. f) Orientation of the cantilever with respect to the sample valid for figures a-e, and the possible domain variants which can be detected. g) AFM image of size  $1 \times 1 \mu\text{m}$  for an 80 nm thick BFO film grown on LAO and the corresponding h) LPFM-phase image, i) orientation of the cantilever with respect to the sample valid for figures g-h.

that in a hypothetical scenario where the stripe feature in the morphology is assumed to be absent, the interface between regions IV and V will be electrically charged and not neutral. Thus the existence of stripe like features in the morphology can be explained to some extent.

## 5.4 Ferroelectric characteristics

The ferroelectric characteristics were investigated in films with LSMO as the buffer layer which acts as a bottom electrode. The thickness of the LSMO and BFO were 10 and 20 nm, respectively. As was proven in section 5.2.2, BFO films with a thickness upto 20 nm exhibit the monoclinic  $M_c$  phase when grown on top of LSMO.

In order to test the ferroelectric properties, polarization loops and the corresponding switching current loops were obtained by using the technique as stated in section 3.4.1. It is evident from the measurements at room temperature, which are shown in Figure 5.15a, that the response from the BFO film is highly affected by leakage mechanisms. The loss of polarization via leakage current is known to be inherent within the stable rhombohedral phase of BFO [95] [96]. Chemical doping with elements such as *La* and *Mn* has been one of the pathways to reduce the effect of leakage currents in BFO films. Likewise in the case of strained BFO films grown on LAO, enhanced polarization values have been achieved by *Mn* doping [27].

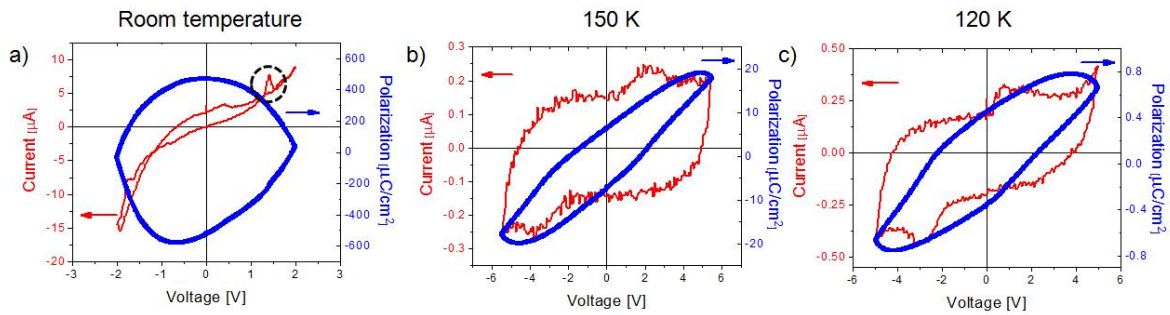


**Figure 5.15:** Investigation of ferroelectric characteristics by measuring the ferroelectric polarization (blue) and switching current (red) loops at a) room temperature, b) 150 K and c) 120 K.

Nevertheless, even though the polarization curve at room temperature is heavily plagued with leakage currents, in the switching current plot (Figure 5.15a) a peak is observed which might be due to the switching of polarization as marked in Figure 5.15a. When the temperature is reduced to 150 K, a more reasonable polarization loop is obtained with obvious presence of peaks in the current loop which correspond to switching of polarization (Figure 5.15b). The appearance of these peaks is a necessary condition for validating the ferroelectric nature of a material. A further decrease in temperature to 120 K makes the switching peaks in the current loop more distinct (Figure 5.15c). However leakage still seems to be affecting the resultant polarization curves.

To further elaborate on the ferroelectric nature of these films, PFM was used to microscopically change the polarization of small areas by applying a *dc* voltage to the tip and thereafter removing the *dc* bias to image the same area.

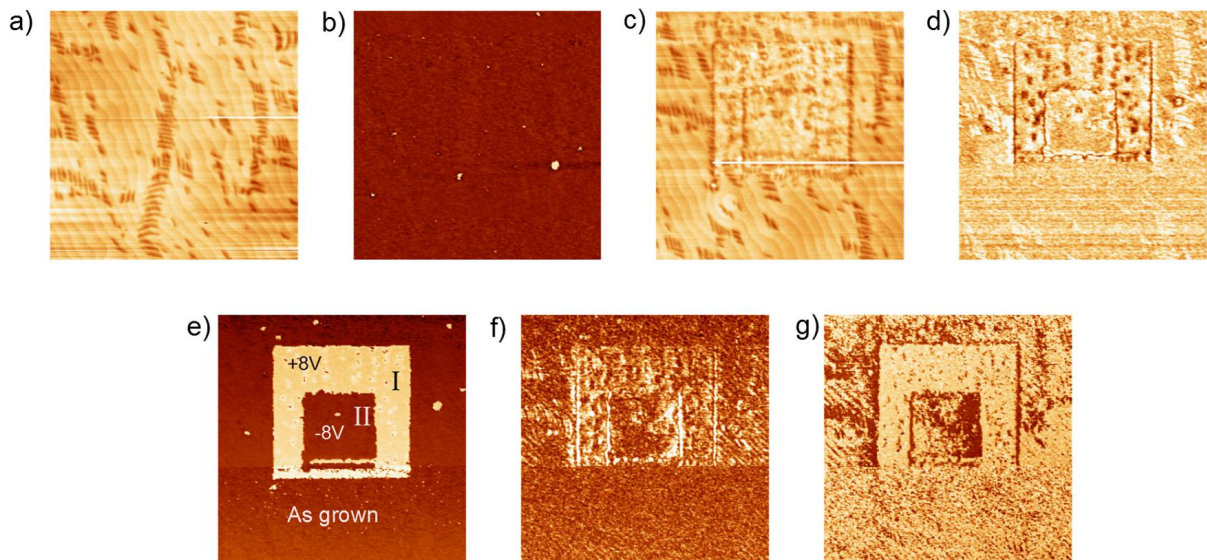


**Figure 5.16:** a) AFM image of size  $3.9 \times 3.9 \mu\text{m}$  for a 20 nm thick BFO film grown on 10 nm LSMO, and the corresponding PFM image showing b) VPFM-phase. c) AFM image of size  $3.7 \times 3.7 \mu\text{m}$  of the same area after switching and corresponding d) VPFM-amplitude e) VPFM-phase f) LPFM-amplitude and g) LPFM-phase.

In Figure 5.16a, the morphology of the area which was selected to switch the polarization is shown. Figure 5.16b shows the VPFM-phase image indicating uniform polariza-

tion in downward direction indicated by a uniform color. Thereafter, a bias of +8 V was applied to the tip but the scanning area was reduced to 2x2  $\mu\text{m}$ . Subsequently, the bias at the tip was changed to -8 V, with scanning size further reduced to 1x1  $\mu\text{m}$ , to switch back the polarization direction to the as grown state. The *dc* bias from the tip was then removed and all the areas were rescanned in the conventional PFM mode.

In Figure 5.16c, the morphology of the switched area is shown. The topography of the switched area is apparently changed. In the switched area, the step flow growth pattern has vanished accompanied with the formation of stripe like features. The VPFM-amplitude (Figure 5.16d) shows the domain walls between positive and negative poled areas. The VPFM-phase image (Figure 5.16e) reveals the existence of oppositely poled areas. Interestingly, the effect of poling is also visible in the LPFM images (Figure 5.16f-g). The polarization vector in the  $M_c$  phase is not perpendicular to the  $(001)_{pc}$  or  $(100)_{pc}$  planes due to which the LPFM signal is substantial. As a result, if due to the application of an electric field in the out-of-plane direction there is a change in the orientation of the polarization vector, then a variation in the LPFM response can also be visible.

Additionally, the change in the morphology, from step-like features to stripe formation, under a bias *dc* voltage means the phase is changing from  $M_c$  to the mixed phase ( $M_a$ ,  $M_b$  or  $M_c$ ) of the stripe. This must be also true when macroscopic measurements for polarization estimation are being performed. Hence it is rather tedious to measure the true polarization value corresponding to the  $M_c$  phase of strained BFO, and there will be always some contribution from mixed phases.

## 5.5 Electronic characterization

The electrical characterization was performed for BFO films with 20 nm and 80 nm thickness which were grown directly on bare LAO substrates. Platinum electrodes were fabricated on top of the BFO films following the techniques mentioned in section 3.1.2. For all the measurements, unless mentioned otherwise, the gap between the electrodes was roughly 15  $\mu\text{m}$ .

### 5.5.1 Current-voltage characteristics

In Figure 5.17 the current-voltage (IV) characteristics for BFO films with (photo) and without illumination (dark) are shown. For illumination, a laser of 405 nm wavelength and 80 mW power was used. The apparent linear IV behavior proves that electrodes form an ohmic contact with the film. Such linear characteristics have also been reported in single crystals [23] and thin films [22] of BFO in the rhombohedral phase. In either of the films, 20 nm (Figure 5.17a) and 80 nm thick (Figure 5.17b), there is a marked increase in the current magnitudes under illumination relative to the dark current. Such massive difference in the current values indicates that the intrinsic number of charge carriers in these films can be considered to be negligible when compared to the additional amount of photo-excited charge carriers i.e.  $n_i \ll \Delta n$ .

Despite the generation of a large number of photo-generated carriers, there is no substantial build up of an open circuit voltage ( $V_{oc}$ ). A higher intrinsic dark and photo conductivity of the material might be one of the reasons for a low photo-voltage in a ferroelectric material as can be implied from equation 2.15 stated in section 2.2.2. Addi-

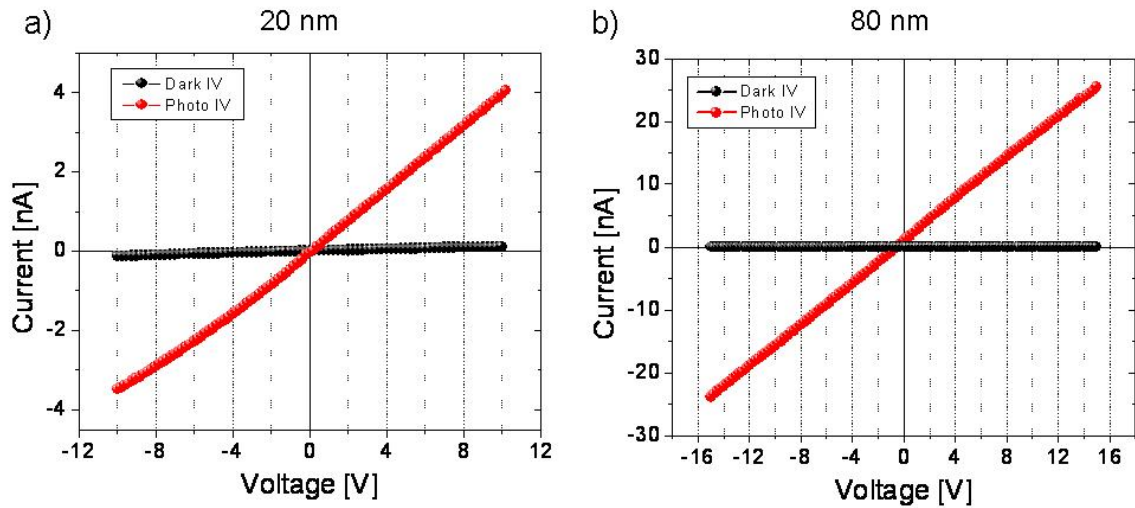


**Figure 5.17:** Current-voltage (IV) characteristics with (photo, red) and without (dark, black) illumination for a) 20 nm and b) 80 nm BFO films grown on LAO.

tionally, the photoconductivity ( $\sigma_{ph}$ ) of a material largely depends upon the lifetime of the carriers and can be described as [108]

$$\sigma_{ph} = g \cdot \tau \cdot e \cdot \mu \quad (5.2)$$

where  $g$  is the generation rate of carriers,  $\tau$  is the lifetime of a carrier and  $\mu$  is the mobility. It has been proven in ferroelectric materials like  $\text{LiNbO}_3$ , that by doping with appropriate elements the effective lifetimes and generation rates can be changed which assists in tuning the photo and dark conductivities of the material. Moreover, as discussed in section 5.3, both thin and thick films of BFO exhibit the  $M_c$  phase with a corresponding high density of domain walls. The domain walls have been found to be more conducting relative to the bulk, at least in the case of rhombohedral BFO [5]. Cumulatively, the different types of conductivities can add up resulting in an overall higher conductivity of the measurement gap, which eventually culminates into lower  $V_{oc}$  values.

An intriguing aspect was observed in the IV characteristics after the illumination was switched off. The IV curve acquired, after the illumination was switched off, displayed a much higher conductivity when compared to the conductivity measured before the illumination. Figure 5.18a shows the IV curves measured, which were obtained before and after the illumination for an 80 nm thick BFO film. The difference in slopes between the two IV curves is a measure of change in the conductivity. The difference in the conductivity is approximately two orders of magnitude.

However, the enhanced conductivity which was observed after turning off the illumination gradually decayed over a long period of time. This was observed in separate measurements where a constant bias voltage was applied during and after the illumination was switched off. The decay in conductivity was then measured as a function of time as it is shown in Figure 5.18b. The conductivity continued to degrade over a time span of roughly 11 hours till it reached its original value measured before illumination. The

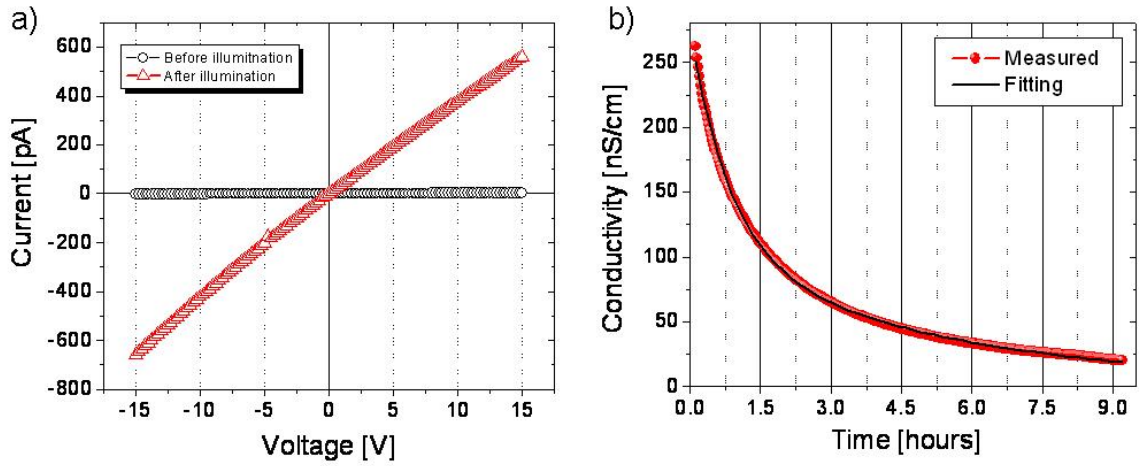


**Figure 5.18:** a) Current-voltage characteristic for an 80 nm thick BFO film acquired before and after the illumination was switched off. b) Conductivity measured as a function of time after the illumination is switched off for an 80 nm thick BFO film.

decay behavior of the conductivity, shown in Figure 5.18b can be replicated by using a double exponential equation of the type

$$\sigma(t) = \sigma_{01} \exp\left(\frac{-t}{\tau_1}\right) + \sigma_{02} \exp\left(\frac{-t}{\tau_2}\right) \quad (5.3)$$

where  $\sigma_{01}$  and  $\sigma_{02}$  are constants.  $\tau_1$  and  $\tau_2$  are two different decay times for the charge carriers which have values of 52 min and 5.4 hours, respectively. The conformity between the measured values and the equation 5.3 is evident from Figure 5.18b. It must be emphasized here that these calculated decay times are not characteristic of the material and have been calculated with the assumption of a simple decay process by neglecting any kind of thermally activated processes or temperature dependency. Nevertheless, the relaxation times obtained are rather long and apparently indicate that charge carriers generated in the material upon illumination prevailed in the material for a long time before they eventually recombine.

In a conventional band-band transition, the recombination proceeds via radiative or Auger processes (section 2.3). In either of the cases, the lifetime of the photo-generated carriers remains in the range of  $10^{-12} - 10^{-9}$  seconds [148]. Such short lifetimes cannot result in an augmented conductivity for longer times. The presence of two decay times and the gradual decay of conductivity over an extended period of time indicate the existence of sub-band levels capable of trapping and emission of carriers. Additionally the presence of two decay times, in a crude approximation, might also indicate either the presence of two levels or a band of levels.

The enhanced conductivity observed after switching off the illumination has often been referred to as “persistent photoconductivity” in previous works. Lately, such kind of behavior has been reported in heterostructures including interfaces between LaAlO<sub>3</sub> (LAO) and SrTiO<sub>3</sub> (STO) [149] [150]. These interfaces have also been investigated for the occurrence of a 2-dimensional electron gas between two insulating materials [151]. When such interfaces are illuminated, the additional number of charge carriers that are generated tend to get trapped in the interfacial potential wells and thus are inhibited from recombining which results in a low resistance state in comparison to the non-illuminated



previous state [150]. But the recent discovery of this effect in pure annealed SrTiO<sub>3</sub> substrates [152] has brought the principle of persistent conductivity and 2-D electrons in the STO/LAO system to question. However, only the annealed STO samples with deliberate inclusion of oxygen vacancies exhibited the effect. Likewise, the phenomenon has also been reported in perovskite based manganite materials like La<sub>0.7</sub>Ce<sub>0.3</sub>MnO<sub>3</sub> [153] and La<sub>2/3</sub>Sr<sub>1/3</sub>MnO<sub>3</sub> [154] where the samples were intentionally annealed to induce oxygen vacancies. Such observations were also made in superconducting materials like YBa<sub>2</sub>Cu<sub>3</sub>O<sub>6+x</sub> ( $x \approx 0.4$ ) where the effect has been attributed to localized microscopic barriers due to atomic level defects [155] [156] [157].

In general, the phenomenon of persistent photoconductivity can be explained by the presence of trap levels which have been found to be imperative to cause extended lifetime of charge carriers resulting in enhanced conductivity [63] [64]. The trap level lies just below the conduction band and its *shallowness* or *deepness* is determined by the temperature. A variation of this explanation was also proposed to elaborate on some anomalous observations in case of semiconductor compounds like Al<sub>x</sub>Ga<sub>1-x</sub>As and GaAs<sub>1-x</sub>P<sub>x</sub> where the trap levels, despite getting activated at low temperatures, possessed high activation energies. To incorporate the anomalies, the model assumes a presence of the trap level above the conduction band in equilibrium conditions, which subsequently moves below the conduction band when the system is perturbed [158]. In ferroelectric materials, such kind of behavior pertaining to enhanced conductivity after illumination has been reported in SbSI [159] which is known to possess an orthorhombic structure [160] with a band gap of approximately 1.97 eV.

It must be mentioned here that the enhanced conductivity observed in the strained BFO films, as shown in Figure 5.18a-b, was obtained by only subjecting the sample to illumination without any annealing or any intentional creation of oxygen vacancies as was the case in the cited studies regarding STO, LSMO and LCMO. Also one of the common factors, in all of the studies mentioned above, is the presence of STO as the substrate. This is rather intriguing and one might suspect that the levels which are present within the band gap of STO [152] have any kind of effect in all the measurements. On the contrary, there have been no reports regarding activated levels in the band structure of LAO that has a wide band gap of approximately 5.6 eV and is considered to be a rather strong dielectric material [151] [161].

### 5.5.2 Thermally stimulated current/conductivity

Thermally stimulated currents (TSC) or conductivities were investigated to analyze the origin of persistent conductivity in strained BFO films grown on LAO substrate. As is stated in section 3.4.3, the technique involves stimulating the material by light of appropriate wavelength which in this case was 405 nm (3.06 eV). The temperature during stimulating the material should be low enough so that the excited carriers that are trapped in the levels do not have sufficient thermal energy to be released. For these measurements this temperature was chosen to be room temperature, since this is also the temperature where persistent conductivity is observed. The electrode area was uniformly illuminated with an applied bias voltage of 10 V. Thereafter the illumination was switched off and the sample quickly cooled down to 80 K, and the current was allowed to stabilize. The sample was henceforth heated following a definite heating scheme of 5 K/min up to 450 K with an applied bias voltage of 10 V. The current/conductivity values were measured simultaneously via a high impedance electrometer.

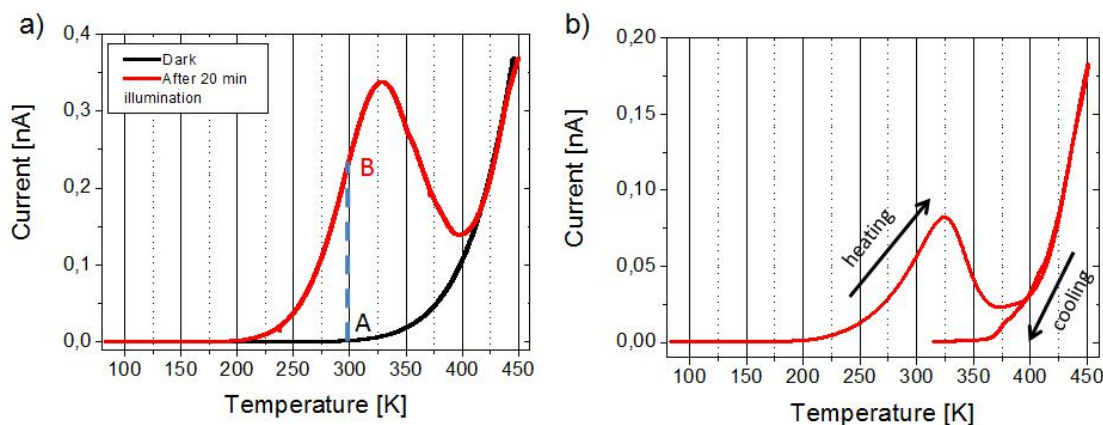


**Figure 5.19:** a) TSC measurement, for an 80 nm thick BFO film, which was (red) and was not illuminated (black) at room temperature. The heating rate in both cases is 5 K/min. b) TSC measurement, for an 80 nm thick BFO film, which was illuminated for 20 min and subsequently cooled down to approximately room temperature.

Figure 5.19 depicts the typical response obtained from the TSC measurements for an 80 nm thick BFO film grown on LAO. In Figure 5.19a the black curve represents the current response that was acquired when the sample was heated up to 450 K without any prior exposure to illumination at room temperature. In a separate measurement, the sample was illuminated for approximately 20 min at room temperature with subsequent cooling to low temperature. Thereafter the current response, which was measured by linearly increasing the temperature, is depicted by the red curve. The difference between the two responses, viz. black and red curves, is evident with a peak appearing at a temperature of 329 K in the case when the sample was stimulated by light at room temperature. Interestingly, as marked in Figure 5.19a, the difference in current values between the two curves at room temperature is two orders of magnitude (3 pA at point A and 230 pA at point B) which also translates into a similar change in conductivity values (1.35 nS/cm at point A and 151 nS/cm at point B). Additionally, Figure 5.19b depicts a measurement, similar to the one shown by the red curve of Figure 5.19a, where after reaching the temperature of 450 K the sample was cooled at a steady rate. The peak which appears during the ramping up of temperature at 324 K is absent when the same temperature is reached while cooling down.

From the above observations it can be postulated here that, indeed, the conduction in strained BFO films is not via band-band transition, and the involvement of a sub-band or a trap level is evident. Moreover, it can be commented, based on Figure 5.19b, that the activity of the trap level is massively decreased if the sample is heated to a high temperature with a subsequent cooling down process, which eventually results in retaining the inherent conductivity values, i.e.  $\approx 1.35$  nS/cm.

The observation pertaining to the TSC measurements can be assimilated to understand the conduction mechanism, to an extent, that is relevant in strained BFO films. When the sample is illuminated at room temperature, large amounts of carriers are generated in the material and the Fermi level in the material splits into two quasi Fermi levels. Under these conditions, the trap level, if in equilibrium with the conduction band, will be filled up with charge carriers as well, and the entire charge generation process occurs via the trap level. This consequently also means that the recombination of carriers will

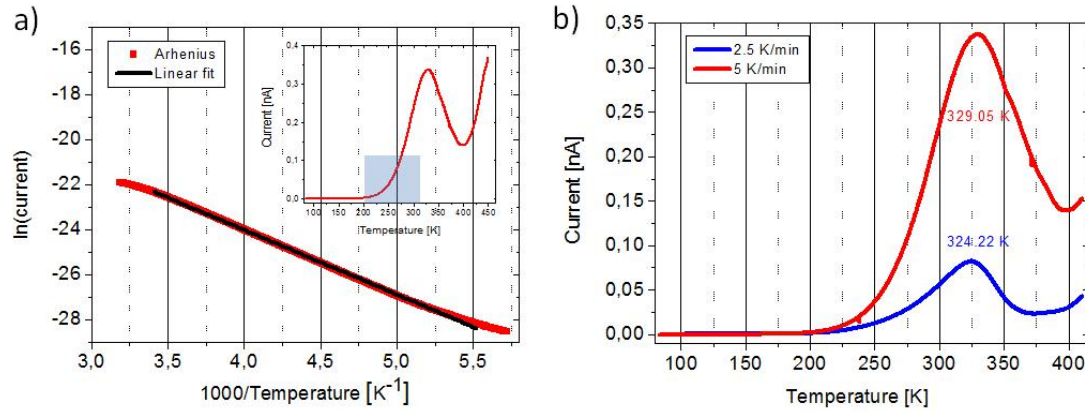


**Figure 5.20:** a) Arrhenius plot at low temperature for an 80 nm thick BFO film. The corresponding TSC measurement is depicted in the inset. b) TSC measurements when the film was heated at 5 K/min (red) and 2.5 K/min (blue).

also occur via the trap level. As a result, the overall decay time of the current is higher than the characteristic lifetime of a carrier, which is in contrast to a material that has no trap levels, and therefore the decay time of current is massively dictated by the lifetime of the carriers.

Thereafter, when the sample is cooled down to a lower temperature, the quasi Fermi levels corresponding to the different type of carriers tend to move towards their band edges. The carriers in the traps are frozen in their state. When the sample is heated again for the TSC measurement, the quasi Fermi levels move towards each other and cross the trap levels at a certain temperature. The trapped carriers become mobile again and get in equilibrium with their respective bands, which results in enhanced conductivity. This is visible in the TSC measurement as the current begins to increase at a temperature between 150 and 200 K, and peaks at 323 K. With most of the carriers from the trapped levels freed, the recombination process tends to dominate and the carriers reduce in number. Likewise it is apparent in the TSC measurement as well, where the current decreases after peaking at 323 K. The investigation of the TSC measurement at a low temperature, when the traps are still full of carriers, can provide an estimate of the depth of the trap below the corresponding band, which is referred to as  $E_a$ .

Figure 5.20a shows the Arrhenius plot in the low temperature regime of the TSC measurement which is depicted in Figure 5.19a. From the linear fitting of the Arrhenius plot, the value of the slope yields the  $E_a$  value to be 0.26 eV, proving the existence of a trap level that is 0.26 eV below an allowed band (valence or conduction band). It must be mentioned here that since via TSC measurements the type of majority carriers (electrons or hole) cannot be determined, it is also not possible to validate the character of the trap level (donor type or acceptor type). Complimentary measurements such as optical charge spectroscopy (OCR) or deep level transient spectroscopy (DLTS) need to be combined with the TSC data to unveil the character of a trap level. Figure 5.20b depicts a comparison between two measurements where all the experimental parameters were kept the same but the heating rate of the sample in one case is 5 K/min, whereas in the other case it is 2.5 K/min. There is an apparent change in the magnitude of the TSC peaks along with a shift in the temperature ( $T_m$ ) corresponding to the maximum current. When the sample is heated at 5 K/min, the current peaks at 329 K, while it reaches its

maximal value at 324.22 K when heated at 2.5 K/min. Nevertheless, the activation energy remains the same in either of the case, being roughly 0.26 eV. With a higher heating rate, the quasi Fermi level tends to approach the trap level sooner, as a result of which the number of trapped carriers needs to be released in a shorter time. Hence the current peak shifts to a higher temperature. The higher magnitude of the current and larger area under the current peak when heated at 5 K/min can be explained by the relation given in equation (3.21) in section 3.4.3 according to which the area under the peak is directly proportional to the heating rate.

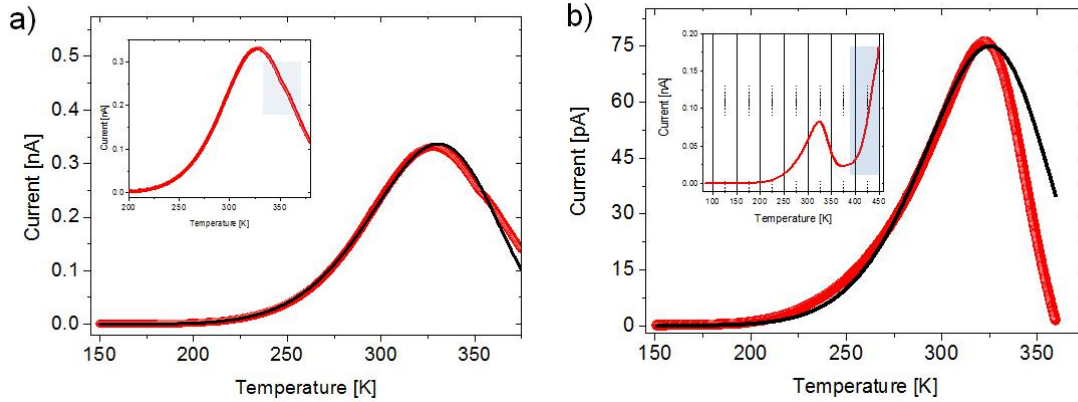


**Figure 5.21:** a) Simulated (black) and measured (red) TSC response for the film heated at 5 K/min. b) Simulated (black) and measured (red) TSC response for the film heated at 2.5 K/min. Inset shows the zoomed out version of the actual TSC measurement.

The TSC behavior can be described by a relation stated in equation (3.19) in section 3.4.3. Such analysis can provide some insights regarding information about lifetime of carriers ( $\tau$ ) and the related capture cross-sections ( $\beta$ ). For this purpose, the dark current must be subtracted from the TSC curve which will yield the effective current generated due to the emptying of trap levels. Figure 5.21a depicts the plot which is obtained when the dark current is subtracted from the TSC measurement for a sample heated at 5 K/min. The resultant peak is a characteristic of the trap level. It is noteworthy to mention the shoulder-like feature arising just after the peak. By using the values of activation energy calculated previously and substituting the values of heating rate in equation (3.19), it is possible to simulate the TSC response acquired from the sample as is shown in Figure 5.21a. The conformity between the simulated curve and the response from the sample is evident. From the fitting, the value of the product of capture cross-section and effective number of states in the conduction band, i.e.  $N_{eff}\beta_t$ , can be calculated which is about  $1.37 \times 10^{-6}$ . However, the simulated curve seems to deviate from the sample response as it approaches the shoulder-like feature. One of the reasons could be the existence of two trap levels in close proximity to each other. The shoulder like feature cannot be incorporated in the simulation since equation (3.19) describes the conduction mechanism that is affected by the presence of a single trap level. In addition, the validity of the equation is under the assumption that the carrier will recombine after it is emitted from the trap. A second trap level or a distribution of traps can cause re-trapping which can further delay the recombination and thus contribute to the lifetime

of a carrier. The time constant ( $\tau_0$ ) due to the presence of a single trap level can be reasonably approximated by the relation

$$\tau_0 = \frac{1}{N_{eff}\beta_t v \exp\left(\frac{-E_a}{k_b T}\right)} \quad (5.4)$$

The value of  $\tau_0$  is calculated to be 160 sec at room temperature which is indeed smaller than the measured time constants from time dependent conductivity measurement. This explicitly proves the existence of other levels not visible in the temperature range used in the present TSC measurement. Nevertheless, the  $\tau_0$  calculated is several orders of magnitude higher than the lifetime of a carrier. Such huge difference validates the trap assisted conduction in strained BFO films.

A similar analysis was performed for the sample which was heated at 2.5 K/min. The activation energy of the trap level remained the same. However the value of the product, i.e.  $N_{eff}\beta_t$ , had to be modulated to induce a better conformity with the experimental data. This means, assuming that the number of states in the conduction band remains constant, the capture cross-section is different in this case due to which the lifetime of the carrier is also varied. Using equation 5.4, the value of  $\tau_0$  calculated for room temperature is 115 sec. From this we can postulate, although not conclusively, that the peak obtained in the lower heating rate is probably from the first of the two trap levels. This is also evident when the activation energy is measured in the region after the current peaks (inset of Figure 5.21b) which gives 0.63 eV. The activation energy that is calculated from the dark current measurement (black curve in Figure 5.19a) is between 0.8 and 1.09 eV. The difference in these values indicates that indeed there is another trap level which lies rather deep within the band gap.

Additionally, measurements were performed by varying the level of excitation in terms of illumination time and power. In Figure 5.22a shows the TSC curves obtained by varying the illumination intensity ( $I$ ). For the same time of illumination, the intensity was changed from  $I_1$  to  $I_2$  where  $I_1 < I_2$ . By increasing the intensity, the number of photons incident on the sample are escalated. The higher TSC response corresponding to higher illumination power is evident from Figure 5.22a. This can be attributed to a larger number of carriers that are generated, which are available for trapping when the incident number of photons is increased. Figure 5.22b shows the comparison between two measurements where the intensity of illumination was kept constant, but the duration of illumination was changed from 10 to 30 minutes. Likewise, the TSC response for 30 min of illumination is higher than for the 10 min illumination. From these measurements it can be implied that due to the activity of these trap levels near room temperature, it is possible to tune the conducting properties of the strained BFO films.

Figure 5.22c depicts the result of a TSC measurement performed on a sample with 20 nm thickness. The sample was illuminated at room temperature for 20 min and the subsequent treatment was the same as in the other measurements. The acquired response is largely similar to the curves obtained from thicker films. It was proven in section 5.2 that both 20 nm and 80 nm thick BFO films grown on LAO exhibit the  $M_c$  phase. However in the thick film, stripe-like features appear, while in thin films they do not. Since the TSC response from thin and thick films are congruent to one another, it can be concluded that the stripe-like features have no effect on the TSC response and thus are not responsible for the trapping phenomenon. Nevertheless one might suspect that

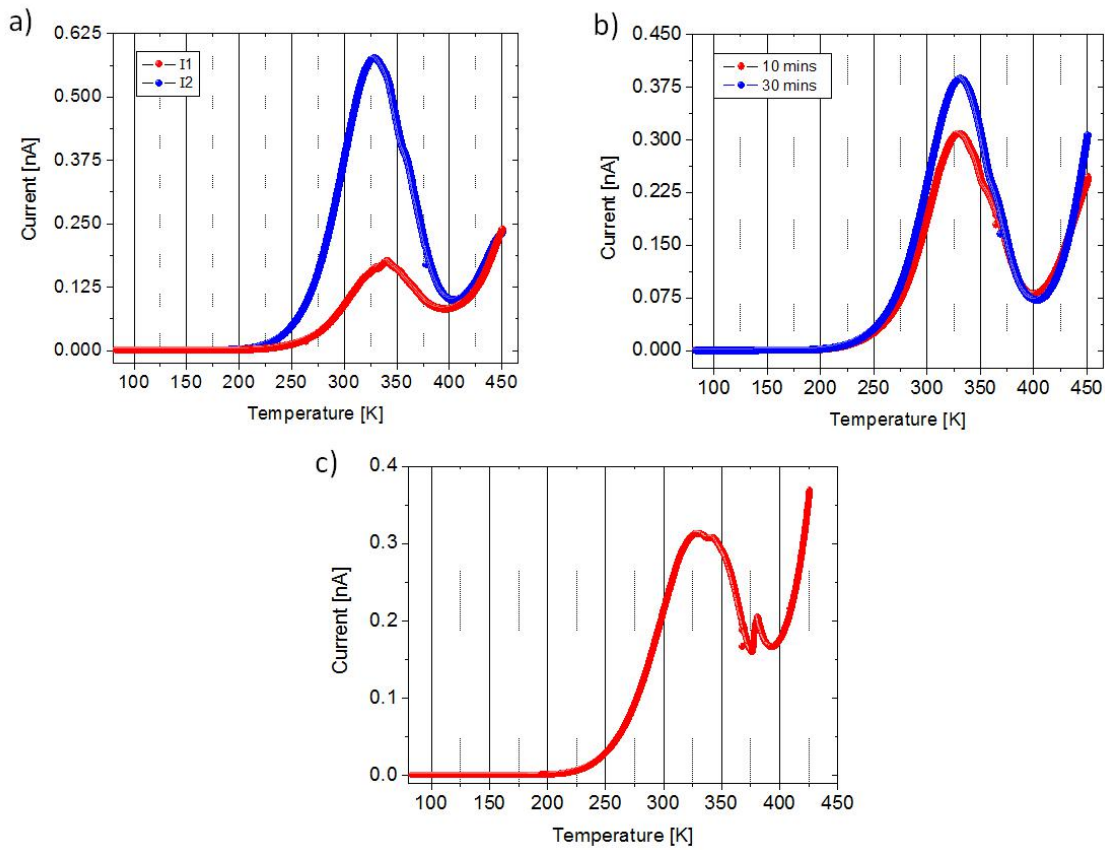


**Figure 5.22:** Comparison of TSC measurements subjected to a) different intensities of illumination where  $I_1 < I_2$ , b) different duration of illumination. c) TSC measurement for a 20 nm thick BFO film.

the amplitude of the response might be affected, if the stripes are more conducting than the bulk of the sample.

### 5.5.3 Spectral distribution

The spectral distribution of the thick (Figure 5.23a) and thin (Figure 5.23b) films was measured by varying the wavelength of the illumination between 205 and 750 nm, and acquiring the resultant photocurrent under a constant bias voltage of 20 V. The effective response is calculated by normalizing the acquired photocurrent at each wavelength with the corresponding power available at the wavelength. The measurement consisted of two cycles: in the first cycle the wavelength is varied from a higher to a lower wavelength (from 750 nm to 250 nm), in the the second cycle the wavelength is varied from lower to higher wavelength. The direction of wavelength variation is indicated in Figures 5.23a-b. The bias voltage is maintained in either of the cycles. In a material without any kind of trapping levels, the spectral distribution will exhibit a maximum in its response at the wavelength which corresponds to the band gap of the material. At lower wavelengths, or higher energy, the absorption increases exponentially and most of the light is absorbed within the first few nanometers according to Beer-Lambert law [75]. In this regime, the photo-conduction is heavily affected by surface recombination and the response decreases dramatically. For BFO, one might suspect this region to be lying between 205 and 300

nm in Figures 5.23a-b. The peak corresponding to the band gap occurs roughly between wavelengths 405 and 420 nm in either of the film thicknesses. The wavelength translates into a band gap energy between 2.95 and 3.06 eV which are in good agreement with the experimentally reported values of about 3.1 eV [162] but larger than the theoretically predicted values [163] [164]. Interestingly, in either of the films when the wavelength is changing from high to low, or alternatively when the energy of the illumination is increased, the onset of photo-conduction is below the actual band gap value. In the thin films (Figure 5.23d) it starts at 485 nm (2.55 eV) and in the thick film (Figure 5.23c) it begins at 515 nm (2.40 eV). From there on, the photoconductivity or the response gradually increases up to the energy corresponding to the band gap. Additionally, a peak appears in the thick film at 580 nm (2.13 eV), and at 565 nm (2.19 eV) in the thin film (star marked in Figures 5.23c-d). The peak tends to decay before the onset of eventual photo-conduction.

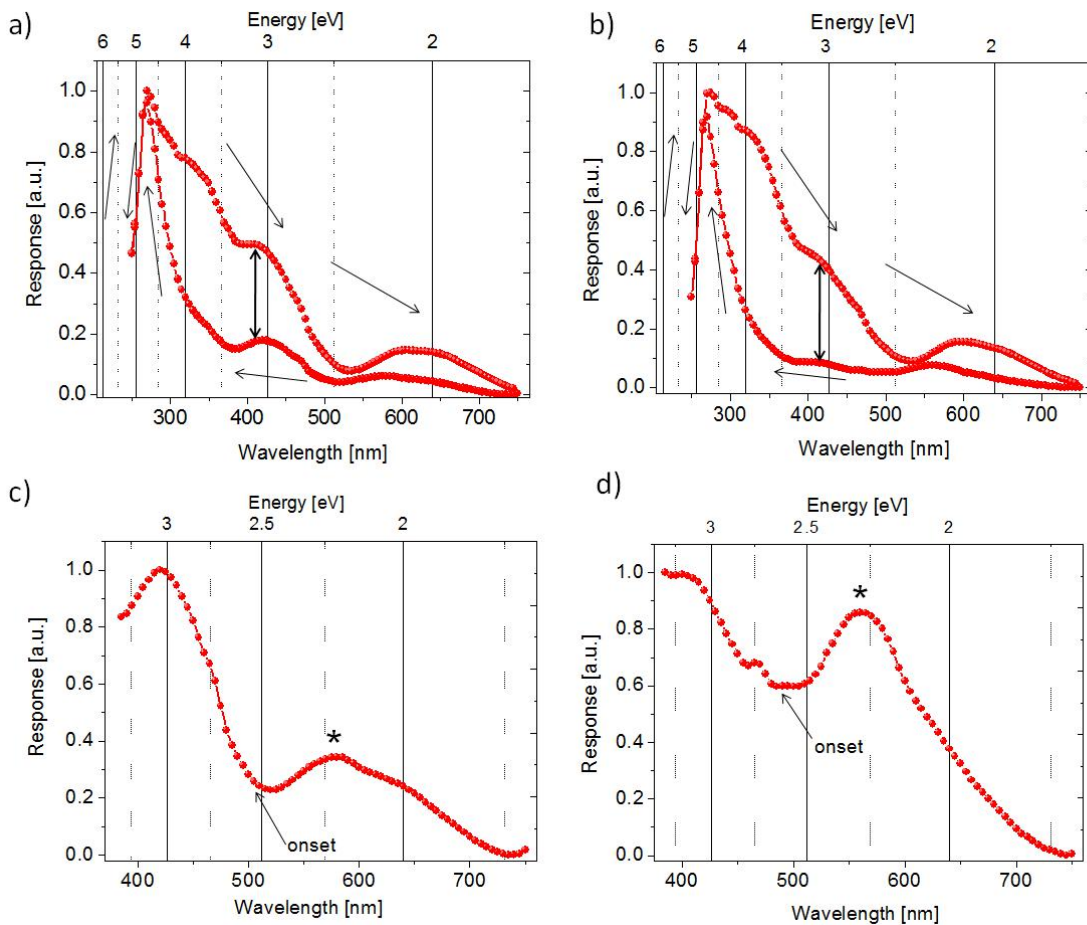


**Figure 5.23:** Spectral distribution acquired for a) 80 nm, b) 20 nm film by varying the wavelength from 750 to 205 to 750 nm. Spectral distribution acquired for c) 80 nm, d) 20 nm film by varying the wavelength from 750 to 205 nm.

The features observed in the wavelength range of 300 to 700 nm can be explained by the help of band diagrams shown previously in the basics sections. Under equilibrium conditions, if the system has electrons as the majority carriers, the Fermi level ( $E_F$ ) of the system can be assumed to be positioned towards the conduction ( $E_c$ ) band as shown in Figure 5.24a. Additionally, we might assume the existence of two levels, viz.

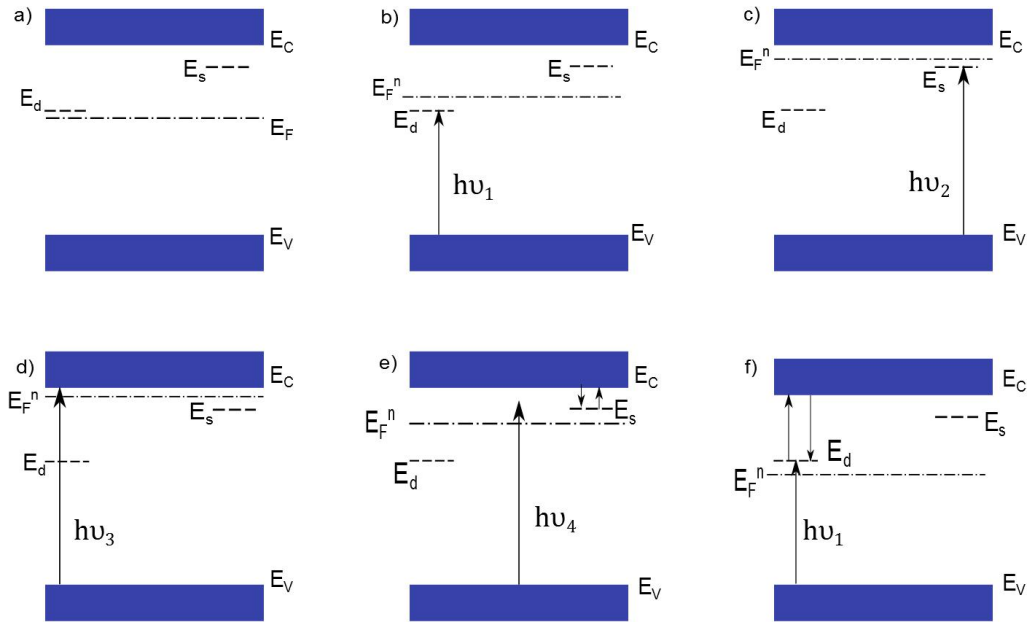


**Figure 5.24:** Energy band diagram to depict a) the equilibrium state, b-d) the possible states when the wavelength is decreasing from 750 to 250 nm, e-f) the possible states when the wavelength is increasing from 250 to 750 nm.  $h\nu_1$ ,  $h\nu_2$ ,  $h\nu_3$ ,  $h\nu_4$  indicate the incident illumination energies corresponding to energy levels  $E_d$ ,  $E_s$ ,  $E_c$ , between  $E_c$  and  $E_s$  respectively.

a deep ( $E_d$ ) and a shallow ( $E_s$ ), which are empty in equilibrium as shown in Figure 5.24a. Thereafter, when the system is illuminated by the photons of certain energy or wavelength, the Fermi level is split into quasi Fermi levels of electrons ( $E_F^n$ ) and holes ( $E_F^p$ ) [61] as shown in Figure 5.24b. Assuming that the majority carriers in the system are electrons, we only consider the case of the quasi Fermi level of the electrons. The deep levels, which lie below the  $E_F^n$  level, are filled up first as the energy begins to increase from 750 nm (Figure 5.24b). Since this level is below  $E_F^n$ , the electrons excited to this level can be considered as trapped and will have a high probability to be recombined. The excitation of electrons to this level is suggested by the presence of a peak in the response between 750 and 485 nm (Figure 5.23c and d) indicating the absorption of photons for electron excitation. The peak tends to decay as the energy of the incident light increases which depicts a lack of levels beyond the energy of 485 nm.

Thereafter, as the incident energy is increased, the response begins to increase again: from 485 nm in a thin film and 515 nm in a thick film. The onset of photoconductivity or the response few nanometers below the actual band gap indicates the excitation of electrons to the shallow level at  $E_s$  which is in close proximity to  $E_c$ . In addition as the incident energy is increased, the level of  $E_F^n$  moves closer to  $E_c$  as a result of which the electrons at level  $E_s$  get trapped (Figure 5.24c) like those present at level  $E_d$ . Eventually, the incident energy equals the energy of the band gap and the conduction is predominantly *via* band-band excitation as shown in Figure 5.24d. Henceforth, with higher incident energy, indirect band excitations also occur. These indirect band transitions can also contribute in filling up trap levels. Hence the first cycle (750-250 nm) involves filling up of levels,  $E_s$  and  $E_d$ , with charge carriers.

As was mentioned in section 2.3, the recombination processes initiate as soon as the system is perturbed from its equilibrium condition. Consequently, the  $E_F^n$  level will tend



to move back to the middle of the gap and cross the level at  $E_s$ . This will bring the previously trapped carriers at level  $E_s$  in equilibrium with  $E_c$  as shown in Figure 5.24e. However there is also another possibility where in the carriers which were previously excited to the  $E_c$  level will get trapped in the  $E_s$  level and push the  $E_F^n$  level towards  $E_c$ . Hence the  $E_F^n$  level might fluctuate in that energy region till an equilibrium is reached. Nevertheless, in either of the possibilities there are additional number of carriers that are available for conduction in level  $E_s$ . This is also visible in the second cycle when the energy is reduced from high to low values. In the region of energy that is near the band gap (as indicated in Figure 5.23a and b), the response is approximately 3 and 5 times higher in the thick and thin film, respectively during the second cycle. Another reason for a higher conductivity that can be speculated is an increase in the effective lifetime of the carriers due to trap assisted recombination [63]. A similar explanation might also be valid when the incident energy is further decreased and it reaches around 600 nm in the second cycle (Figure 5.24f). The peaks around 600 nm (Figure 5.23a and b) are typical for carrier excitation from previously charged traps.

Thus it can be proposed here that the distribution statistics of the carriers is largely modified by the presence of traps, when under or, after illumination. Even though the effect of this modification in statistics is evident by analyzing the spectral distribution, but it is not possible to clearly identify the exact mechanism.

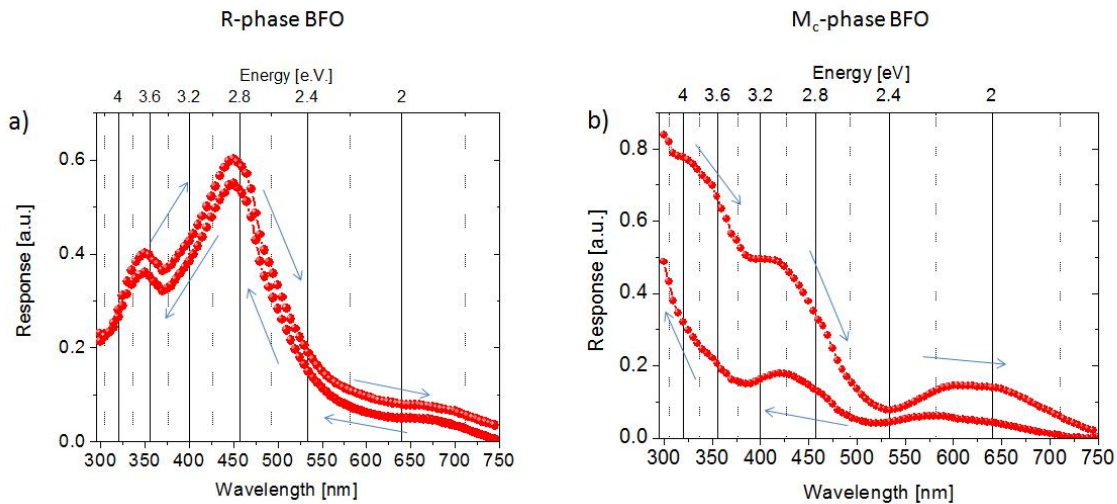


**Figure 5.25:** Spectral distribution acquired for a BFO film in a) rhombohedral and b) monoclinic phase by varying the wavelength from 750 to 205 to 750 nm.

Additionally, the onset of photoconductivity in the thick film, at an energy of 2.4 eV (515 nm), is comparable to the onset of photoconductivity in the BFO film with a rhombohedral phase. The BFO films in rhombohedral phase were also discussed in chapter 4. Figure 5.25a shows the spectral distribution obtained from a 100 nm thick BFO film in the rhombohedral phase that was deposited on  $\text{TbScO}_3$  substrate. In figure 5.25b, the spectral distribution shown in Figure 5.23a has been replotted for comparison between the two phases. Likewise, as in the case of a BFO film in the monoclinic phase, the photoconductivity in the BFO film with rhombohedral phase starts from an energy of 2.4 eV and gradually increases till the photoconduction occurs via band-band transition. The band gap in the rhombohedral phase is approximately 2.8 eV and is in agreement with the previously reported value [165]. This means that the level which is present at

an energy of 2.4 eV is inherent to BFO and exists in both the phases, i.e. rhombohedral and  $M_c$  phases. The presence of this level in the rhombohedral phase has also been reported by cathodoluminescence studies [166]. However, it is noteworthy to mention that even though this level is common in both phases, its activity is largely subdued in the rhombohedral phase. This is evident from the fact that the response in the BFO film with rhombohedral phase does not change drastically during the second cycle when the energy is gradually decreased. This is in contrast to the response from the BFO film with  $M_c$  phase in which the response increases by 3 times during the second cycle. From this one might speculate that a change in the symmetry of BFO, due to the in-plane strain, causes the level at 2.4 eV to have a higher capture cross-section ( $\beta_t$ ).

The onset of photoconduction below the band gap energy and the higher response obtained when the incident energy is reduced in the second cycle, explicitly validates the trap level assisted conduction in BFO films grown on LAO. Based on the TSC measurement, the existence of a level at 2.8 eV or 0.26 eV below the conduction band was proved and the presence of another level in close proximity was also proposed. The onset of photoconduction with a lesser energy of illumination (2.40 eV) supports the activity of two levels or a band of levels near the conduction band.

## 5.6 Summary

Strained BFO films grown on LAO substrates were investigated and analyzed in this chapter. From the growth perspective, it was proven that a high repetition rate (10 Hz) during deposition is essential to achieve a better film quality when the film is grown on bare LAO. On the contrary, the repetition rate must be reduced (3 Hz) in case of LSMO buffered substrates. One of the probable reasons could be the restriction of octahedra tilts imposed by the LSMO layer which also causes a loss of the pseudomorphic relation with the substrate at a lower thickness when compared to growth on bare LAO substrate. The structural analysis *via* XRD and TEM reveals the existence of the  $M_c$  phase in the thick and thin films on bare substrates. Additionally the thick films are accompanied with evolution of stripe-like features which can be attributed to strain relaxation phenomena. The ferroelectric properties were found to be plagued with leakage mechanisms at room temperature that is considered inherent in BFO. Nevertheless, the ferroelectric nature of the BFO films was elaborated by low temperature hysteresis measurements and microscopic domain switching by PFM. The replacement of terraces from the film with stripe-like features under *dc* voltage proves the inevitable influence of the stripes during polarization measurement.

The electronic properties were investigated by acquiring IV characteristics, TSC curves and photocurrent spectral distribution measurement. Enhanced and persistent conductivity were observed at room temperature after switching off the illumination. From the TSC measurements, the presence and activity of a trap level 0.26 eV below the conduction band was clearly established that is responsible for the persistent conductivity. The appearance of two peaks in some measurements indicates the activity of another level as well. Additionally, the activity of the level and so the conductivity of the film can be tuned by controlling the population of carriers in the trap level with varying illumination intensities and corresponding time. The trap level assisted conduction is evident from the enhanced responses acquired in the spectral distribution when the wavelength increases from the high to low energy. The manifestation of enhanced conductivity only in the  $M_c$

phase of BFO might be a consequence of the different symmetry in comparison to the rhombohedral and relaxed system of BFO.

## Summary and Outlook

In the present Thesis, electronic and photoelectronic phenomena in strained and unstrained BiFeO<sub>3</sub> (BFO) thin films were studied. Primarily, two different cases of BFO were chosen as the subject for this study.

In the first case, epitaxial films of BFO were deposited on TbSO<sub>3</sub> (TSO) and SrTiO<sub>3</sub> (STO) single crystalline substrates by pulsed laser deposition. Owing to a minimal in-plane lattice parameter mismatch between either of the substrates and the rhombohedral phase of BFO, the resultant films on both the substrates crystallized in the rhombohedral phase. The phase purity and the structure of the films were validated by employing XRD and TEM techniques. The domain configuration was analyzed in the films by PFM. It was observed that the BFO films deposited on conventionally annealed TSO substrates consist of 109° domain walls (DWs), whereas films on O<sub>2</sub>-annealed TSO consist of 71° DWs. The different termination at the surface of the scandate substrate after O<sub>2</sub> annealing might be a possible explanation. Also, it was proven that either of the films consist of the same pair of structural variants but they have different active polarization variants.

The electrical and photoelectrical measurements were performed on BFO films with 109° and 71° DWs to investigate the abnormal photovoltaic effect in BFO. The measurements were carried out in two geometries, i.e. in PLDW and PPDW. The appearance of open circuit voltages ( $V_{oc}$ ) higher than the band gap in both geometries proves that the previously assumed model given in ref. [22] is not valid. By performing angle dependent measurements, the bulk photovoltaic (BPV) effect was found to be the origin of the photovoltaic (PV) effect in BFO films. Thereafter, the manifestation of the BPV effect in BFO films with periodic domains was explained via mathematical analysis. By the analysis it was proven that high  $V_{oc}$  values can be achieved irrespective of the measurement geometry and controlling the conductivity of the DWs.

In the second case, epitaxial BFO films were grown on LaAlO<sub>3</sub> (LAO) substrates. Due to the large mismatch between the in-plane lattice parameters, the BFO crystallized in the monoclinic phase which was proven by XRD and TEM investigations. In the subsequent electrical measurements the phenomenon of persistent photoconductivity was observed. By analyzing the thermally stimulated current (TSC) it was found that a sub-band level at an energy of 2.8 eV, due to its trap character, is responsible for higher conductivities. However by changing the heating rate, the presence of another level which lies a bit deeper was also proposed. Thereafter, the spectral distribution was acquired by measuring the response from the film while varying the wavelength of the illumination. The activity of the sub-band levels was validated by a higher response obtained when

---

the energy of the illumination was sequentially reduced. Additionally it was found that a level exists at an energy of 2.4 eV in BFO films irrespective of their phase. However this level seems to have a higher capture cross-section in the monoclinic phase as a result of which it contributes heavily to the conduction mechanism. Eventually it can be concluded that the conduction mechanism in the strained BFO films is massively affected by the presence of sub-band levels and the conductivity can be enhanced drastically by controlling the population of carriers in these levels.

Primarily, in this Thesis, the manifestation of two phenomena, i.e. photovoltaic effect and trap assisted conductivity, which are usually related to semiconducting materials, have been demonstrated in a multiferroic material like BFO. The common factor in both of the phenomena has been the role of illumination. In the rhombohedral phase of BFO, illumination resulted in an abnormal photovoltaic effect but the role of the ferroelectric character of BFO (the domains and DWs) was also evident. On the other hand, the same illumination in the monoclinic phase of BFO resulted in enhanced and persistent conductivities. It became thus obvious that the *interaction* between the ferroelectric and semiconducting properties of this multiferroic material is decisive for its physical properties. This aspect can be regarded as the primary outcome of this Thesis and should be investigated further, both for BFO and for other multiferroic materials.



## Bibliography

- [1] H. Schmid, “Multi-ferroic magnetoelectrics,” *Ferroelectrics*, vol. 162, pp. 317–338, 1994.
- [2] S. W. Cheong and M. Mostovoy, “Multiferroics: a magnetic twist for ferroelectricity,” *Nature Materials*, vol. 6, pp. 13–12, 2007.
- [3] R. Ramesh and N. A. Spaldin, “Multiferroics: progress and prospects in thin films,” *Nature Materials*, vol. 6, pp. 21–29, 2007.
- [4] N. A. Spaldin and M. Fiebig, “The renaissance of magnetoelectric multiferroics,” *Science*, vol. 309, pp. 391–392, 2005.
- [5] J. Seidel, L. W. Martin, Q. He, Q. Zhan, Y. . H. Chu, A. Rother, M. E. Hawkrige, P. Maksymovych, P. Yu, M. Gajek, N. Balke, S. V. Kalinin, S. Gemming, F. Wang, G. Catalan, J. F. Scott, N. A. Spaldin, J. Orenstein, and R. Ramesh, “Conduction at domain walls in oxide multiferroics,” *Nature Materials*, vol. 8, pp. 229–234, 2009.
- [6] J. Seidel, P. Maksymovych, Y. Batra, A. Katan, S.-Y. Yang, Q. He, A. Baddorf, S. Kalinin, C.-H. Yang, J.-C. Yang, Y.-H. Chu, E. Salje, H. Wormeester, M. Salmeron, and R. Ramesh, “Domain Wall Conductivity in La-Doped BiFeO<sub>3</sub>,” *Physical Review Letters*, vol. 105, pp. 2010–2012, 2010.
- [7] G. Catalan, J. Seidel, R. Ramesh, and J. F. Scott, “Domain wall nanoelectronics,” *Review of Modern Physics*, vol. 84, pp. 119–156, 2012.
- [8] G. A. Smolenskii and V. A. Bokov, “Coexistence of Magnetic and Electric Ordering in Crystals,” *Journal of Applied Physics*, vol. 35, pp. 915–918, 1964.
- [9] G. A. Smolenskii and I. E. Chupis, “Ferroelectromagnets,” *Soviet Physics Uspekhi*, vol. 25, p. 475, 1982.
- [10] J. Wang, J. B. Neaton, H. Zheng, V. Nagarajan, S. B. Ogale, B. Liu, D. Viehland, V. Vaithyanathan, D. G. Schlom, U. V. Waghmare, N. A. Spaldin, K. M. Rabe, M. Wuttig, and R. Ramesh, “Epitaxial BiFeO<sub>3</sub> multiferroic thin film heterostructures,” *Science*, vol. 299, pp. 1719–1722, 2003.

- [11] J. Li, J. Wang, M. Wuttig, R. Ramesh, N. Wang, B. Ruetter, A. P. Pyatakov, A. K. Zvezdin, and D. Viehland, “Dramatically enhanced polarization in (001), (101), and (111) BiFeO<sub>3</sub> thin films due to epitaxial-induced transitions,” *Applied Physics Letters*, vol. 84, pp. 5261–5263, 2004.
- [12] F. Zavaliche, R. R. Das, D. M. Kim, C. B. Eom, S. Y. Yang, P. Shafer, and R. Ramesh, “Ferroelectric domain structure in epitaxial BiFeO<sub>3</sub> films,” *Applied Physics Letters*, vol. 87, p. 182912, 2005.
- [13] F. Zavaliche, S. Y. Yang, T. Zhao, Y. H. Chu, M. P. Cruz, C. B. Eom, and R. Ramesh, “Multiferroic BiFeO<sub>3</sub> films: domain structure and polarization dynamics,” *Phase Transitions*, vol. 79, pp. 991–1017, 2006.
- [14] J. Neaton, C. Ederer, U. Waghmare, N. Spaldin, and K. Rabe, “First-principles study of spontaneous polarization in multiferroic BiFeO<sub>3</sub>,” *Physical Review B*, vol. 71, p. 014113, 2005.
- [15] S. J. Clark and J. Robertson, “Energy levels of oxygen vacancies in BiFeO<sub>3</sub> by screened exchange,” *Applied Physics Letters*, vol. 94, p. 022902, 2009.
- [16] S. H. Wemple, “Polarization Fluctuations and the Optical-Absorption Edge in BaTiO<sub>3</sub>,” *Physical Review B*, vol. 2, pp. 2679–2689, 1970.
- [17] S. de Lazaro, E. Longo, J. R. Sambrano, and A. Beltrán, “Structural and electronic properties of PbTiO<sub>3</sub> slabs: a DFT periodic study,” *Surface Science*, vol. 552, pp. 149 – 159, 2004.
- [18] D. Redfield and W. J. Burke, “Optical absorption edge of LiNbO<sub>3</sub>,” *Journal of Applied Physics*, vol. 45, pp. 4566–4571, 1974.
- [19] A. Kholkin, O. Boiarkine, and N. Setter, “Transient photocurrents in lead zirconate titanate thin films,” *Applied Physics Letters*, vol. 72, pp. 130–132, 1998.
- [20] S. Y. Yang, L. W. Martin, S. J. Byrnes, T. E. Conry, S. R. Basu, D. Paran, L. Reichertz, J. Ihlefeld, C. Adamo, a. Melville, Y.-H. Chu, C.-H. Yang, J. L. Musfeldt, D. G. Schlom, J. W. Ager, and R. Ramesh, “Photovoltaic effects in BiFeO<sub>3</sub>,” *Applied Physics Letters*, vol. 95, p. 062909, 2009.
- [21] T. Choi, S. Lee, Y. J. Choi, V. Kiryukhin, and S.-W. Cheong, “Switchable ferroelectric diode and photovoltaic effect in BiFeO<sub>3</sub>,” *Science*, vol. 324, pp. 63–6, 2009.
- [22] S. Y. Yang, J. Seidel, S. J. Byrnes, P. Shafer, C.-H. Yang, M. D. Rossell, P. Yu, Y.-H. Chu, J. F. Scott, J. W. Ager, L. W. Martin, and R. Ramesh, “Above-bandgap voltages from ferroelectric photovoltaic devices,” *Nature Nanotechnology*, vol. 5, pp. 143–7, 2010.
- [23] M. Alexe and D. Hesse, “Tip-enhanced photovoltaic effects in bismuth ferrite,” *Nature Communications*, vol. 2, doi: 10.1038/ncomms1261, 2011.
- [24] M. Alexe, “Local Mapping of Generation and Recombination Lifetime in BiFeO<sub>3</sub> Single Crystals by Scanning Probe Photoinduced Transient Spectroscopy,” *Nano Letters*, vol. 12, pp. 2193–2198, 2012.



- [25] A. M. Glass, D. von der Linde, and T. J. Negran, “High-voltage bulk photovoltaic effect and the photorefractive process in  $\text{LiNbO}_3$ ,” *Applied Physics Letters*, vol. 25, p. 233, 1974.
- [26] A. Chynoweth, “Surface space-charge layer in barium titanate,” *Physical Review*, vol. 102, pp. 705–714, 1956.
- [27] H. Béa, B. Dupé, S. Fusil, R. Mattana, E. Jacquet, B. Warot-Fonrose, F. Wilhelm, A. Rogalev, S. Petit, V. Cros, A. Anane, F. Petroff, K. Bouzehouane, G. Geneste, B. Dkhil, S. Lisenkov, I. Ponomareva, L. Bellaiche, M. Bibes, and A. Barthélémy, “Evidence for room-temperature multiferroicity in a compound with a giant axial ratio,” *Physical Review Letters*, vol. 102, pp. 1–5, 2009.
- [28] R. J. Zeches, M. D. Rossell, J. X. Zhang, A. J. Hatt, Q. He, C.-H. Yang, A. Kumar, C. H. Wang, A. Melville, C. Adamo, G. Sheng, Y.-H. Chu, J. F. Ihlefeld, R. Erni, C. Ederer, V. Gopalan, L. Q. Chen, D. G. Schlom, N. A. Spaldin, L. W. Martin, and R. Ramesh, “A strain-driven morphotropic phase boundary in  $\text{BiFeO}_3$ ,” *Science*, vol. 326, pp. 977–80, 2009.
- [29] D. Sando, A. Agbelele, D. Rahmedov, J. Liu, P. Rovillain, C. Toulouse, I. C. Infante, A. P. Pyatakov, S. Fusil, E. Jacquet, C. Carretero, C. Deranlot, S. Lisenkov, D. Wang, J.-M. Le Breton, M. Cazayous, A. Sacuto, J. Juraszek, A. K. Zvezdin, L. Bellaiche, B. Dkhil, A. Barthelemy, and M. Bibes, “Crafting the magnonic and spintronic response of  $\text{BiFeO}_3$  films by epitaxial strain,” *Nature Materials*, vol. 12, pp. 641–646, 2013.
- [30] A. M. Mulders, “Multiferroics: Magnetic moments under stress,” *Nature Physics*, vol. 9, p. 398399, 2013.
- [31] M. E. Lines and A. M. Glass, *Principles and applications of ferroelectrics and related materials*. Oxford: Clarendon Press, 2004.
- [32] T. Mitsui, I. Tatsuzaki, and E. Nakamura, *An Introduction to the Physics of Ferroelectrics*. New York: Gordon and Breach Science Publishers, 1976.
- [33] J. Nye, *Physical properties of crystals*. Oxford: Clarendon Press, 1960.
- [34] H. F. Kay, “Preparation and properties of crystals of barium titanate,  $\text{BaTiO}_3$ ,” *Acta Crystallographica*, vol. 1, pp. 229–237, 1948.
- [35] H. T. Evans, “The crystal structure of tetragonal barium titanate,” *Acta Crystallographica*, vol. 4, p. 377, 1951.
- [36] R. E. Cohen and H. Krakauer, “Electronic structure studies of the differences in ferroelectric behavior of  $\text{BaTiO}_3$  and  $\text{PbTiO}_3$ ,” *Ferroelectrics*, vol. 136, pp. 65–83, 1992.
- [37] N. A. Hill, “Why are there so few magnetic ferroelectrics?,” *The Journal of Physical Chemistry B*, vol. 104, pp. 6694–6709, 2000.
- [38] E. Speranskaya, V. Skorikov, E. Rode, and V. Terekhov *Bull. Acad. Sci. USSR, Div. Chem. Sci.*, vol. 5, p. 874, 1965.

- [39] R. Palai, R. Katiyar, H. Schmid, P. Tissot, S. Clark, J. Robertson, S. Redfern, G. Catalan, and J. Scott, “ $\beta$  phase and  $\gamma$ - $\beta$  metal-insulator transition in multiferroic  $\text{BiFeO}_3$ ,” *Physical Review B*, vol. 77, pp. 1–11, 2008.
- [40] G. Catalan and J. F. Scott, “Physics and Applications of Bismuth Ferrite,” *Advanced Materials*, vol. 21, pp. 2463–2485, 2009.
- [41] J. Moreau, C. Michel, R. Gerson, and W. James, “Ferroelectric  $\text{BiFeO}_3$  X-ray and neutron diffraction study,” *Journal of Physics and Chemistry of Solids*, vol. 32, pp. 1315 – 1320, 1971.
- [42] F. Kubel and H. Schmid, “Structure of a ferroelectric and ferroelastic monodomain crystal of the perovskite  $\text{BiFeO}_3$ ,” *Acta Crystallographica Section B Structural Science*, vol. 46, pp. 698–702, 1990.
- [43] J. D. Bucci, B. K. Robertson, and W. J. James, “The precision determination of the lattice parameters and the coefficients of thermal expansion of  $\text{BiFeO}_3$ ,” *Journal of Applied Crystallography*, vol. 5, pp. 187–191, 1972.
- [44] R. Seshadri and N. A. Hill, “Visualizing the role of Bi 6s ”Lone Pairs” in the off center distortion in ferromagnetic  $\text{BiMnO}_3$ ,” *Chemistry of Materials*, vol. 13, pp. 2892–2899, 2001.
- [45] S. K. Streiffer, C. B. Parker, a. E. Romanov, M. J. Lefevre, L. Zhao, J. S. Speck, W. Pompe, C. M. Foster, and G. R. Bai, “Domain patterns in epitaxial rhombohedral ferroelectric films. I. Geometry and experiments,” *Journal of Applied Physics*, vol. 83, no. 5, p. 2742, 1998.
- [46] P. Fischer, M. Polomska, I. Sosnowska, and M. Szymanski, “Temperature dependence of the crystal and magnetic structures of  $\text{BiFeO}_3$ ,” *Journal of Physics C: Solid State Physics*, vol. 13, p. 1931, 1980.
- [47] I. Sosnowska, T. P. Neumaier, and E. Steichele, “Spiral magnetic ordering in bismuth ferrite,” *Journal of Physics C: Solid State Physics*, vol. 15, no. 23, p. 4835, 1982.
- [48] D. Lebeugle, D. Colson, A. Forget, M. Viret, A. M. Bataille, and A. Gukasov, “Electric-Field-Induced Spin Flop in  $\text{BiFeO}_3$  Single Crystals at Room Temperature,” *Physical Review Letters*, vol. 100, p. 227602, 2008.
- [49] D. Lebeugle, D. Colson, A. Forget, M. Viret, P. Bonville, J. F. Marucco, and S. Fusil, “Room-temperature coexistence of large electric polarization and magnetic order in  $\text{BiFeO}_3$  single crystals,” *Physical Review B*, vol. 76, pp. 1–8, 2007.
- [50] A. Kadomtseva, A. Zvezdin, Y. Popov, A. Pyatakov, and G. Vorob’ev, “Space-time parity violation and magnetoelectric interactions in antiferromagnets,” *JETP Letters*, vol. 79, pp. 571–581, 2004.
- [51] S. M. Sze, *Physics of semiconductor devices*. New York: John Wiley & Sons, INC., 1981.

- [52] V. M. Fridkin, *Photoferroelectrics*. Springer-Verlag Berlin Heidelberg New York, 1979.
- [53] D. A. Neamen, *Semiconductor Physics And Devices*. New Delhi: Tata McGraw Hill, 2007.
- [54] B. I. Sturman and V. Fridkin, *The Photovoltaic and Photorefractive Effects in Noncentrosymmetric Materials*. Philadelphia: Gordon and Breach Science, 1992.
- [55] V. M. Fridkin, "Review of recent work on the bulk photovoltaic effect in ferro and piezoelectrics," *Ferroelectrics*, vol. 53, pp. 169–187, 1984.
- [56] W. Ruppel, R. Von Baltz, and P. Wurfel, "The origin of the photo-emf in ferroelectric and non-ferroelectric materials," *Ferroelectrics*, vol. 43, pp. 109–123, 1982.
- [57] H. Ibach and H. Lüth, *Solid -State Physics*. Springer-Verlag Berlin Heidelberg New York, 2002.
- [58] V. Fridkin, "The possible mechanism for the bulk photovoltaic effect and optical damage in ferroelectrics," *Applied Physics*, vol. 13, pp. 357–359, 1977.
- [59] V. Fridkin, A. Grekov, and A. Rodin, "The bulk photovoltaic effect in the crystals without a center of symmetry," *Ferroelectrics*, vol. 43, pp. 99–108, 1982.
- [60] V. Fridkin, "Parity nonconservation and bulk photovoltaic effect in a crystal without symmetry center," *IEEE Transactions on Ultrasonics, Ferroelectrics and Frequency Control*, vol. 60, pp. 1551–1555, 2013.
- [61] W. Shockley and J. W.T. Read, "Statistics of the recombination of holes and electrons," *Physical Review*, vol. 87, pp. 835–842, 1952.
- [62] P. Bräunlich, ed., *Thermally stimulated Relaxation in Solids*. Springer-Verlag Berlin Heidelberg New York, 1979.
- [63] A. Rose, "Recombination processes in insulators and semiconductors," *Physical Review*, vol. 97, pp. 322–333, 1955.
- [64] A. Rose, "An outline of some photoconductive processes," *Radio Cooperation of America Review*, vol. 12, pp. 362–414, 1951.
- [65] R. Eason, ed., *Pulsed laser deposition of thin films*. New Jersey: Wiley - Interscience, 2007.
- [66] C. Harnagea, *Local piezoelectric response and domain structures in ferroelectric thin films investigated by voltage-modulated force microscopy*. PhD thesis, Martin-Luther-Universität Halle-Wittenberg, 2001.
- [67] F. Johann, *Control of ferroelectric domains in epitaxial BiFeO<sub>3</sub> thin films and submicron structures*. PhD thesis, Martin-Luther-Universität Halle-Wittenberg, 2012.
- [68] E. Soergel, "Piezoresponse force microscopy (PFM)," *Journal of Physics D: Applied Physics*, vol. 44, p. 464003, 2011.

- [69] A. Gruverman, O. Kolosov, J. Hatano, K. Takahashi, and H. Tokumoto, “Domain structure and polarization reversal in ferroelectrics studied by atomic force microscopy,” *Journal of Vacuum Science & Technology B*, vol. 13, pp. 1095–1099, 1995.
- [70] A. Morelli, *Piezoresponse force microscopy of ferroelectric thin films*. PhD thesis, University of Groningen, 2009.
- [71] B. Cullity and S. Stock, *Elements of X-ray diffraction*. New Jersey: Prentice Hall, 2001.
- [72] D. B. Williams and C. B. Carter, *Transmission electron microscopy : A textbook for materials science*. Springer-Verlag Berlin Heidelberg New York, 2009.
- [73] J. C. Schug, A. Lilly, and D. Lowitz, “Schottky currents in dielectric films,” *Physical Review B*, vol. 1, pp. 4811–4818, 1970.
- [74] G. Dussel and R. Bube, “Theory of thermally stimulated conductivity in a previously photoexcited crystal,” *Physical Review*, vol. 155, pp. 764–779, 1967.
- [75] R. H. Bube, *Photoelectronic properties of semiconductors*. Cambridge: Cambridge University Press, 1992.
- [76] R. H. Bube, *Photoconductivity of Solids*. New York: John Wiley & Sons, INC., 1960.
- [77] J. Simmons and G. Taylor, “High field isothermal currents and thermally stimulated currents in insulators having discrete trapping levels,” *Physical Review B*, vol. 5, pp. 1619–1629, 1972.
- [78] R. Guo, L. You, L. Chen, D. Wu, and J. Wang, “Photovoltaic property of BiFeO<sub>3</sub> thin films with 109° domains,” *Applied Physics Letters*, vol. 99, p. 122902, 2011.
- [79] D. Lee, S. H. Baek, T. H. Kim, J.-G. Yoon, C. M. Folkman, C. B. Eom, and T. W. Noh, “Polarity control of carrier injection at ferroelectric/metal interfaces for electrically switchable diode and photovoltaic effects,” *Physical Review B*, vol. 84, p. 125305, 2011.
- [80] R. Moubah, O. Rousseau, D. Colson, A. Artemenko, M. Maglione, and M. Viret, “Photoelectric effects in single domain BiFeO<sub>3</sub> crystals,” *Advanced Functional Materials*, vol. 22, pp. 4814–4818, 2012.
- [81] C.-S. Tu, C.-M. Hung, V. H. Schmidt, R. R. Chien, M.-D. Jiang, and J. Anthoninappen, “The origin of photovoltaic responses in BiFeO<sub>3</sub> multiferroic ceramics,” *Journal of Physics: Condensed Matter*, vol. 24, p. 495902, 2012.
- [82] A. Lempicki, “Anomalous photovoltaic effect in ZnS single crystals,” *Physical Review*, vol. 113, pp. 1204–1209, 1959.
- [83] G. F. Neumark, “Theory of the anomalous photovoltaic effect of ZnS,” *Physical Review*, vol. 125, pp. 838–845, 1962.

- [84] S. M. Young, F. Zheng, and A. M. Rappe, “First-Principles calculation of the bulk photovoltaic effect in bismuth ferrite,” *Physical Review Letters*, vol. 109, p. 236601, 2012.
- [85] R. P. Liferovich and R. H. Mitchell, “A structural study of ternary lanthanide orthoscamdate perovskites,” *Journal of Solid State Chemistry*, vol. 177, pp. 2188 – 2197, 2004.
- [86] A. Okazaki and M. Kawaminami, “Lattice constant of strontium titanate at low temperatures,” *Materials Research Bulletin*, vol. 8, pp. 545 – 550, 1973.
- [87] M. Kawasaki, K. Takahashi, T. Maeda, R. Tsuchiya, M. Shinohara, O. Ishiyama, T. Yonezawa, M. Yoshimoto, and H. Koinuma, “Atomic control of the SrTiO<sub>3</sub> crystal surface,” *Science*, vol. 266, pp. 1540–1542, 1994.
- [88] G. Koster, B. L. Kropman, G. J. H. M. Rijnders, D. H. A. Blank, and H. Rogalla, “Quasi-ideal strontium titanate crystal surfaces through formation of strontium hydroxide,” *Applied Physics Letters*, vol. 73, pp. 2920–2922, 1998.
- [89] R. Dirsyte, J. Schwarzkopf, G. Wagner, R. Fornari, J. Lienemann, M. Busch, and H. Winter, “Thermal-induced change in surface termination of DyScO<sub>3</sub> (110),” *Surface Science*, vol. 604, pp. L55 – L58, 2010.
- [90] F. Johann, A. Morelli, D. Biggemann, M. Arredondo, and I. Vrejoiu, “Epitaxial strain and electric boundary condition effects on the structural and ferroelectric properties of BiFeO<sub>3</sub> films,” *Physical Review B*, vol. 84, p. 094105, 2011.
- [91] G. Rijnders, D. H. A. Blank, J. Choi, and C.-B. Eom, “Enhanced surface diffusion through termination conversion during epitaxial SrRuO<sub>3</sub> growth,” *Applied Physics Letters*, vol. 84, pp. 505–507, 2004.
- [92] C. W. Huang, Z. H. Chen, J. W. T. Sritharan, and L. Chen, “Stability and crossover of 71° degrees and 109° degrees domains influenced by the film thickness and depolarization field in rhombohedral ferroelectric thin films,” *Journal of Applied Physics*, vol. 110, p. 014110, 2011.
- [93] C. M. Folkman, S. H. Baek, H. W. Jang, C. B. Eom, C. T. Nelson, X. Q. Pan, Y. L. Li, L. Q. Chen, A. Kumar, V. Gopalan, and S. K. Streiffer, “Stripe domain structure in epitaxial (001) BiFeO<sub>3</sub> thin films on orthorhombic TbScO<sub>3</sub> substrate,” *Applied Physics Letters*, vol. 94, p. 251911, 2009.
- [94] Y.-H. Chu, Q. He, C.-H. Yang, P. Yu, L. W. Martin, P. Shafer, and R. Ramesh, “Nanoscale control of domain architectures in BiFeO<sub>3</sub> thin films,” *Nano Letters*, vol. 9, pp. 1726–1730, 2009.
- [95] G. W. Pabst, L. W. Martin, Y.-H. Chu, and R. Ramesh, “Leakage mechanisms in BiFeO<sub>3</sub> thin films,” *Applied Physics Letters*, vol. 90, p. 072902, 2007.
- [96] H. Yang, M. Jain, N. a. Suvorova, H. Zhou, H. M. Luo, D. M. Feldmann, P. C. Dowden, R. F. DePaula, S. R. Foltyn, and Q. X. Jia, “Temperature-dependent leakage mechanisms of Pt/BiFeO<sub>3</sub>/SrRuO<sub>3</sub> thin film capacitors,” *Applied Physics Letters*, vol. 91, p. 072911, 2007.

- [97] X. Qi, J. Dho, R. Tomov, M. G. Blamire, and J. L. MacManus-Driscoll, “Greatly reduced leakage current and conduction mechanism in aliovalent-ion-doped  $\text{BiFeO}_3$ ,” *Applied Physics Letters*, vol. 86, p. 062903, 2005.
- [98] C. Wang, M. Takahashi, H. Fujino, X. Zhao, E. Kume, T. Horiuchi, and S. Sakai, “Leakage current of multiferroic  $(\text{Bi}_{0.6}\text{Tb}_{0.3}\text{La}_{0.1})\text{FeO}_3$  thin films grown at various oxygen pressures by pulsed laser deposition and annealing effect,” *Journal of Applied Physics*, vol. 99, p. 054104, 2006.
- [99] C.-F. Chung, J.-P. Lin, and J.-M. Wu, “Influence of Mn and Nb dopants on electric properties of chemical-solution-deposited  $\text{BiFeO}_3$  films,” *Applied Physics Letters*, vol. 88, p. 242909, 2006.
- [100] E. Igarashi, “FeRAMs to Provide Very Low Power, High Speeds for New Mobile Electronic Products,” tech. rep., Fujitsu Microelectronics America, Inc., 2006.
- [101] C. Daumont, W. Ren, I. C. Infante, S. Lisenkov, J. Allibe, C. Carrétéro, S. Fusil, E. Jacquet, T. Bouvet, F. Bouamrane, S. Prosandeev, G. Geneste, B. Dkhil, L. Bellaiche, A. Barthélémy, and M. Bibes, “Strain dependence of polarization and piezoelectric response in epitaxial  $\text{BiFeO}_3$  thin films,” *Journal of Physics: Condensed Matter*, vol. 24, p. 162202, 2012.
- [102] J. Seidel, D. Fu, S.-Y. Yang, E. Alarcón-Lladó, J. Wu, R. Ramesh, and J. W. Ager, “Efficient photovoltaic current generation at ferroelectric domain walls,” *Physical Review Letters*, vol. 107, p. 126805, 2011.
- [103] Q. He, C.-H. Yeh, J.-C. Yang, G. Singh-Bhalla, C.-W. Liang, P.-W. Chiu, G. Catalan, L. W. Martin, Y.-H. Chu, J. F. Scott, and R. Ramesh, “Magnetotransport at domain walls in  $\text{BiFeO}_3$ ,” *Physical Review Letters*, vol. 108, p. 067203, 2012.
- [104] Y.-P. Chiu, Y.-T. Chen, B.-C. Huang, M.-C. Shih, J.-C. Yang, Q. He, C.-W. Liang, J. Seidel, Y.-C. Chen, R. Ramesh, and Y.-H. Chu, “Atomic-scale evolution of local electronic structure across multiferroic domain walls,” *Advanced Materials*, vol. 23, pp. 1530–4, 2011.
- [105] P. Gunter, “Photovoltages, photocurrents and photorefractive effects in  $\text{KNbO}_3\text{:Fe}$ ,” *Ferroelectrics*, vol. 22, pp. 671–674, 1978.
- [106] W. T. H. Koch, R. Munser, W. Ruppel, and P. Würfel, “Anomalous photovoltage in  $\text{BaTiO}_3$ ,” *Ferroelectrics*, vol. 13, pp. 305–307, 1976.
- [107] W. Koch, R. Munser, W. Ruppel, and P. Würfel, “Bulk photovoltaic effect in  $\text{BaTiO}_3$ ,” *Solid State Communications*, vol. 17, pp. 847 – 850, 1975.
- [108] E. Krätzig, “Photorefractive effects and photoconductivity in  $\text{LiNbO}_3\text{:Fe}$ ,” *Ferroelectrics*, vol. 21, pp. 635–636, 1978.
- [109] E. Avakyan, K. Belabaev, S. Odulov, and O. Oleinik, “Photogalvanic currents in reduced Lithium-Titanate crystals,” *Izvestiya Akademii Nauk SSSR. Seriya Fizicheskaya*, vol. 47, pp. 656–659, 1983.

- [110] D. W. Wilson, E. N. Glytsis, N. F. Hartman, and T. K. Gaylord, “Beam diameter threshold for polarization conversion photoinduced by spatially oscillating bulk photovoltaic currents in  $\text{LiNbO}_3: \text{Fe}$ ,” *Journal of the Optical Society of America B*, vol. 9, p. 1714, 1992.
- [111] R. Weis and T. Gaylord, “Lithium niobate: Summary of physical properties and crystal structure,” *Applied Physics A*, vol. 37, pp. 191–203, 1985.
- [112] W. Ji, K. Yao, and Y. C. Liang, “Evidence of bulk photovoltaic effect and large tensor coefficient in ferroelectric  $\text{BiFeO}_3$  thin films,” *Physical Review B*, vol. 84, p. 094115, Sept. 2011.
- [113] R. E. Newnham, *Properties of materials*. New York: Oxford University Press, 2005.
- [114] H. G. Festl, P. Hertel, E. Krätzig, and R. von Baltz, “Investigations of the photovoltaic tensor in doped  $\text{LiNbO}_3$ ,” *Physica Status Solidi (b)*, vol. 113, pp. 157–164, 1982.
- [115] M. Ahart, M. Somayazulu, R. E. Cohen, P. Ganesh, P. Dera, H.-k. Mao, R. J. Hemley, Y. Ren, P. Liermann, and Z. Wu, “Origin of morphotropic phase boundaries in ferroelectrics,” *Nature*, vol. 451, pp. 545–8, 2008.
- [116] P. Groth, “Ueber Beziehungen zwischen Krystallform und chemische Constitution bei einigen organischen Verbindungen,” *Ann. Phys. Chem.*, vol. 31, p. 217, 1870.
- [117] B. Noheda, D. E. Cox, G. Shirane, J. A. Gonzalo, L. E. Cross, and S.-E. Park, “A monoclinic ferroelectric phase in the  $\text{Pb}(\text{Zr}_{1-x}\text{Ti}_x)\text{O}_3$  solid solution,” *Applied Physics Letters*, vol. 74, pp. 2059–2061, 1999.
- [118] B. Noheda, D. E. Cox, G. Shirane, S.-E. Park, L. E. Cross, and Z. Zhong, “Polarization rotation via a monoclinic phase in the piezoelectric 92%  $\text{PbZn}_{1/3}\text{Nb}_{2/3}\text{O}_3$ -8% $\text{PbTiO}_3$ ,” *Physical Review Letters*, vol. 86, pp. 3891–3894, 2001.
- [119] S.-E. Park and T. R. Shrout, “Ultrahigh strain and piezoelectric behavior in relaxor based ferroelectric single crystals,” *Journal of Applied Physics*, vol. 82, p. 1804, 1997.
- [120] A. Herklotz, J. D. Plumhof, A. Rastelli, O. G. Schmidt, L. Schultz, and K. Dörr, “Electrical characterization of PMN-28%PT(001) crystals used as thin-film substrates,” *Journal of Applied Physics*, vol. 108, p. 094101, 2010.
- [121] C. Ederer and N. Spaldin, “Effect of epitaxial strain on the spontaneous polarization of thin film ferroelectrics,” *Physical Review Letters*, vol. 95, no. 25, pp. 2–5, 2005.
- [122] R. K. Vasudevan, Y. Liu, J. Li, W.-I. Liang, A. Kumar, S. Jesse, Y.-C. Chen, Y.-H. Chu, V. Nagarajan, and S. V. Kalinin, “Nanoscale control of phase variants in strain-engineered  $\text{BiFeO}_3$ ,” *Nano Letters*, vol. 11, pp. 3346–54, 2011.

- [123] H. Yamada, V. Garcia, S. Fusil, S. Boyn, M. Marinova, A. Gloter, S. Xavier, J. Grollier, E. Jacquet, C. Carretero, C. Deranlot, M. Bibes, and A. Barthelemy, "Giant electroresistance of super-tetragonal BiFeO<sub>3</sub>-based ferroelectric tunnel junctions," *ACS Nano*, vol. 7, pp. 5385–5390, 2013.
- [124] S. Geller and V. Bala, "Crystallographic studies of perovskite-like compounds .2. rare earth aluminates," *Acta Crystallographica*, vol. 9, pp. 1019–1025, 1956.
- [125] H. Boschker, M. Huijben, A. Vailionis, J. Verbeeck, S. van Aert, M. Luysberg, S. Bals, G. van Tendeloo, E. P. Houwman, G. Koster, D. H. A. Blank, and G. Rijnders, "Optimized fabrication of high-quality La<sub>0.67</sub>Sr<sub>0.33</sub>MnO<sub>3</sub> thin films considering all essential characteristics," *Journal of Physics D-Applied Physics*, vol. 44, p. 205001, 2011.
- [126] T. H. Kim, S. H. Baek, S. Y. Jang, S. M. Yang, S. H. Chang, T. K. Song, J.-G. Yoon, C. B. Eom, J.-S. Chung, and T. W. Noh, "Step bunching-induced vertical lattice mismatch and crystallographic tilt in vicinal BiFeO<sub>3</sub> (001) films," *Applied Physics Letters*, vol. 98, p. 022904, 2011.
- [127] J. Tersoff, Y. H. Phang, Z. Zhang, and M. G. Lagally, "Step-bunching instability of vicinal surfaces under stress," *Physical Review Letters*, vol. 75, pp. 2730–2733, 1995.
- [128] H. Boschker, M. Mathews, P. Brinks, E. Houwman, A. Vailionis, G. Koster, D. H. A. Blank, and G. Rijnders, "Uniaxial contribution to the magnetic anisotropy of La<sub>0.67</sub>Sr<sub>0.33</sub>MnO<sub>3</sub> thin films induced by orthorhombic crystal structure," *Journal of Magnetism and Magnetic Materials*, vol. 323, pp. 2632–2638, 2011.
- [129] A. Tebano, C. Aruta, P. G. Medaglia, F. Tozzi, G. Balestrino, A. A. Sidorenko, G. Allodi, R. De Renzi, G. Ghiringhelli, C. Dallera, L. Braicovich, and N. B. Brookes, "Strain-induced phase separation in La<sub>0.7</sub>Sr<sub>0.3</sub>MnO<sub>3</sub> thin films," *Physical Review B*, vol. 74, p. 245116, 2006.
- [130] V. Nagarajan, I. G. Jenkins, S. P. Alpay, H. Li, S. Aggarwal, L. Salamanca-Riba, A. L. Roytburd, and R. Ramesh, "Thickness dependence of structural and electrical properties in epitaxial lead zirconate titanate films," *Journal of Applied Physics*, vol. 86, pp. 595–602, 1999.
- [131] H. Béa, M. Bibes, M. Sirena, G. Herranz, K. Bouzehouane, E. Jacquet, S. Fusil, P. Paruch, M. Dawber, J.-P. Contour, and A. Barthélémy, "Combining half-metals and multiferroics into epitaxial heterostructures for spintronics," *Applied Physics Letters*, vol. 88, p. 062502, 2006.
- [132] D. H. Kim, H. N. Lee, M. D. Biegalski, and H. M. Christen, "Effect of epitaxial strain on ferroelectric polarization in multiferroic BiFeO<sub>3</sub> films," *Applied Physics Letters*, vol. 92, p. 012911, 2008.
- [133] Y. Uratani, T. Shishidou, F. Ishii, and T. Oguchi, "First-principles predictions of giant electric polarization," *Japanese Journal of Applied Physics*, vol. 44, pp. 7130–7133, 2005.



- [134] J. Íñiguez, D. Vanderbilt, and L. Bellaiche, “First-Principles study of  $(\text{BiScO}_3)_{1-x}(\text{PbTiO}_3)_x$  piezoelectric alloys,” *Physical Review B*, vol. 67, p. 224107, 2003.
- [135] Z. Chen, Z. Luo, C. Huang, Y. Qi, P. Yang, L. You, C. Hu, T. Wu, J. Wang, C. Gao, T. Sritharan, and L. Chen, “Low-symmetry monoclinic phases and polarization rotation path mediated by epitaxial strain in multiferroic  $\text{BiFeO}_3$  thin films,” *Advanced Functional Materials*, vol. 21, pp. 133–138, 2011.
- [136] A. R. Damodaran, C.-W. Liang, Q. He, C.-Y. Peng, L. Chang, Y.-H. Chu, and L. W. Martin, “Nanoscale structure and mechanism for enhanced electromechanical response of highly Strained  $\text{BiFeO}_3$  thin films,” *Advanced Materials*, vol. 23, pp. 3170–5, 2011.
- [137] D. Vanderbilt and M. H. Cohen, “Monoclinic and triclinic phases in higher-order devonshire theory,” *Physical Review B*, vol. 63, p. 094108, 2001.
- [138] K. Saito, A. Ulyanenkov, V. Grossmann, H. Ress, L. Bruegemann, H. Ohta, T. Kurosawa, S. Ueki, and H. Funakubo, “Structural characterization of  $\text{BiFeO}_3$  thin films by reciprocal space mapping,” *Japanese Journal of Applied Physics*, vol. 45, pp. 7311–7314, 2006.
- [139] K.-T. Ko, M. H. Jung, Q. He, J. H. Lee, C. S. Woo, K. Chu, J. Seidel, B.-G. Jeon, Y. S. Oh, K. H. Kim, W.-I. Liang, H.-J. Chen, Y.-H. Chu, Y. H. Jeong, R. Ramesh, J.-H. Park, and C.-H. Yang, “Concurrent transition of ferroelectric and magnetic ordering near room temperature,” *Nature Communications*, vol. 2, doi:10.1038/ncomms1576, Nov 2011.
- [140] C. Beekman, W. Siemons, T. Z. Ward, M. Chi, J. Howe, M. D. Biegalski, N. Balke, P. Maksymovych, A. K. Farrar, J. B. Romero, P. Gao, X. Q. Pan, D. A. Tenne, and H. M. Christen, “Phase transitions, phase coexistence, and piezoelectric switching behavior in highly strained  $\text{BiFeO}_3$  films,” *Advanced Materials*, vol. 25, pp. 5561–5567, 2013.
- [141] Y. H. Kim, A. Bhatnagar, E. Pippel, M. Alexe, and D. Hesse, “Microstructure of highly strained  $\text{BiFeO}_3$  thin films: Transmission electron microscopy and electron-energy loss spectroscopy studies,” *Journal of Applied Physics*, vol. 115, p. 043526, 2014.
- [142] P. Woodward, “Octahedral tilting in perovskites. 2. Structure stabilizing forces,” *Acta Crystallographica Section B-Structural Science*, vol. 53, pp. 44–66, 1997.
- [143] I. C. Infante, S. Lisenkov, B. Dupé, M. Bibes, S. Fusil, E. Jacquet, G. Geneste, S. Petit, A. Courtial, J. Juraszek, L. Bellaiche, A. Barthélémy, and B. Dkhil, “Bridging multiferroic phase transitions by epitaxial strain in  $\text{BiFeO}_3$ ,” *Physical Review Letters*, vol. 105, p. 057601, 2010.
- [144] J. C. Wojdel and J. Iniguez, “Ab initio indications for giant magnetoelectric effects driven by structural softness,” *Physical Review Letters*, vol. 105, p. 037208, 2010.
- [145] A. Y. Borisevich, H. J. Chang, M. Huijben, M. P. Oxley, S. Okamoto, M. K. Niranjan, J. D. Burton, E. Y. Tsymlal, Y. H. Chu, P. Yu, R. Ramesh, S. V. Kalinin,

- and S. J. Pennycook, "Suppression of octahedral tilts and associated changes in electronic properties at epitaxial oxide heterostructure interfaces," *Physical Review Letters*, vol. 105, p. 087204, 2010.
- [146] A. Bokov and Z. Ye, "Domain structure in the monoclinic Pm phase of  $\text{Pb}(\text{Mg}_{1/3}\text{Nb}_{2/3})\text{O}_3\text{-PbTiO}_3$  single crystals," *Journal of Applied Physics*, vol. 95, pp. 6347–6359, 2004.
- [147] J. Sapriel, "Domain-wall orientations in ferroelastics," *Physical Review B*, vol. 12, pp. 5128–5140, 1975.
- [148] R. Klann, T. Hfer, R. Buhleier, T. Elsaesser, and A. Lambrecht, "Picosecond recombination processes in lead selenide," *Applied Physics Letters*, vol. 61, pp. 2866–2868, 1992.
- [149] H.-L. Lu, Z.-M. Liao, L. Zhang, W.-T. Yuan, Y. Wang, X.-M. Ma, and D.-P. Yu, "Reversible insulator-metal transition of  $\text{LaAlO}_3/\text{SrTiO}_3$  interface for nonvolatile memory," *Scientific Reports*, vol. 3, doi: 10.1038/srep02870, 2013.
- [150] A. Tebano, E. Fabbri, D. Pergolesi, G. Balestrino, and E. Traversa, "Room-temperature giant persistent photoconductivity in  $\text{SrTiO}_3/\text{LaAlO}_3$  heterostructures," *ACS Nano*, vol. 6, pp. 1278–1283, 2012.
- [151] A. Ohtomo and H. Hwang, "A high-mobility electron gas at the  $\text{LaAlO}_3/\text{SrTiO}_3$  heterointerface," *Nature*, vol. 427, pp. 423–426, 2004.
- [152] M. C. Tarun, F. A. Selim, and M. D. McCluskey, "Persistent photoconductivity in strontium titanate," *Physical Review Letters*, vol. 111, p. 187403, 2013.
- [153] E. Beyreuther, A. Thiessen, S. Grafstrom, L. M. Eng, M. C. Dekker, and K. Dörr, "Large photoconductivity and light-induced recovery of the insulator-metal transition in ultrathin  $\text{La}_{0.7}\text{Ce}_{0.3}\text{MnO}_{3-\delta}$  films," *Physical Review B*, vol. 80, p. 075106, 2009.
- [154] R. Cauro, A. Gilabert, J. P. Contour, R. Lyonnet, M.-G. Medici, J.-C. Grenet, C. Leighton, and I. K. Schuller, "Persistent and transient photoconductivity in oxygen-deficient  $\text{La}_{2/3}\text{Sr}_{1/3}\text{MnO}_3$  thin films," *Physical Review B*, vol. 63, p. 174423, 2001.
- [155] V. Kudinov, A. Kirilyuk, N. Kreines, R. Laiho, and E. Lahderanta, "Photoinduced superconductivity in YBCO films," *Physics Letters A*, vol. 151, pp. 358–364, 1990.
- [156] N. Kreines and V. Kudinov, "Metastable photoinduced superconductivity in YBaCuO films close to metal-semiconductor transition," *Modern Physics Letters B*, vol. 6, pp. 289–307, 1992.
- [157] V. Pena, T. Gredig, J. Santamaria, and I. K. Schuller, "Interfacially controlled transient photoinduced superconductivity," *Physical Review Letters*, vol. 97, p. 177005, 2006.
- [158] D. V. Lang and R. A. Logan, "Large-lattice-relaxation model for persistent photoconductivity in compound semiconductors," *Physical Review Letters*, vol. 39, pp. 635–639, 1977.

- 
- [159] E. V. Burtsev, A. A. Grekov, V. G. Lazarev, N. P. Protsenko, A. I. Rodin, and S. D. Samko, “Anomalies of photoconductivity in ferroelectrics near the phase transition,” *Ferroelectrics*, vol. 22, no. 1, pp. 669–670, 1978.
- [160] A. Kikuchi, Y. Oka, and E. Sawaguchi, “Crystal structure determination of SbSI,” *Journal of the Physical Society of Japan*, vol. 23, pp. 337–354, 1967.
- [161] R. W. Simon, C. E. Platt, A. E. Lee, G. S. Lee, K. P. Daly, M. S. Wire, J. A. Luine, and M. Urbanik, “Low-loss substrate for epitaxial growth of high temperature superconductor thin films,” *Applied Physics Letters*, vol. 53, pp. 2677–2679, 1988.
- [162] P. Chen, N. J. Podraza, X. S. Xu, A. Melville, E. Vlahos, V. Gopalan, R. Ramesh, D. G. Schlom, and J. L. Musfeldt, “Optical properties of quasi-tetragonal BiFeO<sub>3</sub> thin films,” *Applied Physics Letters*, vol. 96, p. 131907, 2010.
- [163] H. M. Tütüncü and G. P. Srivastava, “Electronic structure and lattice dynamical properties of different tetragonal phases of BiFeO<sub>3</sub>,” *Physical Review B*, vol. 78, p. 235209, 2008.
- [164] D. Ricinschi, K.-Y. Yun, and M. Okuyama, “A mechanism for the 150 $\mu$ C/cm<sup>2</sup> polarization of BiFeO<sub>3</sub> films based on first-principles calculations and new structural data.,” *Journal of Physics: Condensed Matter*, vol. 18, pp. L97–L105, 2006.
- [165] J. F. Ihlefeld, N. J. Podraza, Z. K. Liu, R. C. Rai, X. Xu, T. Heeg, Y. B. Chen, J. Li, R. W. Collins, J. L. Musfeldt, X. Q. Pan, J. Schubert, R. Ramesh, and D. G. Schlom, “Optical band gap of BiFeO<sub>3</sub> grown by molecular-beam epitaxy,” *Applied Physics Letters*, vol. 92, p. 142908, 2008.
- [166] A. J. Hauser, J. Zhang, L. Mier, R. A. Ricciardo, P. M. Woodward, T. L. Gustafson, L. J. Brillson, and F. Y. Yang, “Characterization of electronic structure and defect states of thin epitaxial BiFeO<sub>3</sub> films by UV-visible absorption and cathodoluminescence spectroscopies,” *Applied Physics Letters*, vol. 92, p. 222901, 2008.

## Curriculum vitae et studiorum

# Akash Bhatnagar

### Personal information

**Date of birth** 12<sup>th</sup> September 1986

**Place of birth** New Delhi, India

**Nationality** Indian

**Civil status** Single

### Education

**Period** **University/Institution**

02/2011-present PhD student at Max-Planck-Institut für Mikrostrukturphysik, Halle, Germany

09/2008-10/2010 M.Sc (Masters of Science) in Material Science and Engineering from Christian-Albrechts-Universität, Kiel, Germany

08/2004-08/2008 B.Tech (Bachelors of Technology) in Mechanical and Automation Engineering from Indraprastha University, New Delhi, India

### Publications **Journals**

A. Bhatnagar, A. Roy Chaudhuri, Y. Heon Kim, D. Hesse, and M. Alexe, "Role of domain walls in the abnormal photovoltaic effect in BiFeO<sub>3</sub>," *Nature Communications*, vol. 4, doi: 10.1038/ncomms3835, 2013.

Y. H. Kim, A. Bhatnagar, E. Pippel, M. Alexe, and D. Hesse, "Microstructure of highly strained BiFeO<sub>3</sub> thin films: Transmission electron microscopy and electron-energy loss spectroscopy studies," *Journal of Applied Physics*, vol. 115, p. 043526, 2014.

- A. Bhatnagar, Y. Heon Kim, D. Hesse, and M. Alexe, “Persistent photoconductivity in BiFeO<sub>3</sub> films,” *Under preparation*, 2014.
- H. Deniz and A. Bhatnagar et. al., “Observation of Aurivillius type of defects in BiFeO<sub>3</sub> thin films by electron microscopy: meta stable nano-scale Bi<sub>2</sub>FeO<sub>6-x</sub> precipitates,” *Under preparation*, 2014.

## Conferences Talks

- A. Bhatnagar, J. Lee, Y. H. Kim, A. R. Chaudhuri, D. Hesse, and M. Alexe, “Anomalous Photovoltaic effect in BiFeO<sub>3</sub>,” in *E-MRS Spring Meeting, Strasbourg, France*, May 2013.
- A. Bhatnagar, J. Lee, Y. H. Kim, A. R. Chaudhuri, D. Hesse, and M. Alexe, “Anomalous Photovoltaic effect in BiFeO<sub>3</sub>,” in *MRS Spring Meeting, San Francisco, USA*, April 2013.
- A. Bhatnagar, Y. H. Kim, J. Lee, D. Hesse, and M. Alexe, “Effect of domain wall conductivity and strain on anomalous photovoltaic effect in BiFeO<sub>3</sub> thin films,” in *Leverhulme Workshop, Mallorca, Spain*, January 2013.
- A. Bhatnagar, A. R. Chaudhuri, Y. H. Kim, D. Hesse, and M. Alexe, “Anomalous photovoltaic effect in BiFeO<sub>3</sub> thin films,” in *ISAF-IEEE-PFM, Aveiro, Portugal*, July 2012.
- A. Bhatnagar, A. R. Chaudhuri, D. Hesse, and M. Alexe, “Electronic processes in BiFeO<sub>3</sub> thin film,” in *DPG Spring Meeting, Berlin, Germany*, March 2012.

February 2014

## Acknowledgments

The present Thesis would not have been possible without the help of many people who were involved, directly and indirectly, in this work. Here I would like to acknowledge all the support and encouragement I received from these people and also wish them success in their future endeavors.

First and foremost, my heart felt gratitude to Prof. Hesse and Prof. Alexe for giving me the opportunity to initiate my PhD work in their group in Max Planck Institute (MPI), Halle. I would like to thank Prof. Hesse for not only his ever helping attitude and motivation but for also providing inspiration to perform better in personal and professional life.

Probably, no words will be enough to express my respect for Prof. Alexe who introduced me to the world of multiferroic materials. The present Thesis might not have been possible without his expert guidance and I find myself extremely fortunate for being able to work under his supervision. The skills and lessons imparted by him in these years, will for sure guide me in my future career.

I would like to thank Dr. Ayan Roy Chaudhuri for helping and training me in the initial days of my work, Dr. Y.H. Kim and Dr. Hakan Deniz for providing TEM and structural analysis and Norbert Schammelt for the preparation of TEM samples.

It is always desirable to have a good and joyful atmosphere to accomplish goals in professional life and I was lucky to be a part of such group. I must mention here my colleagues Dr. Johann, Dr. Lee (Flora), Dr. Deniz, Dr. Kim, Dr. Lu, Daniele, Simon, Andy for always being there to lighten the atmosphere during some tense moments and giving a great company during our frequent breaks from work. I will always embrace the fond memories I have of all the tennis and table tennis matches I had with Prof. Alexe, Dr. Kim, Dr. Deniz, Dr. Lu and Daniele.

Also I would like to acknowledge the support from our technical (electrical and mechanical workshop) and administrative staff. Especially I would like to thank Frau Pohlink, Frau Frankenstein, Frau Schneider and Frau Amm from the administrative department of our institute for providing all the help in housing, visa and other regulatory issues which allowed me to focus better on my work. I must thank the International Max Planck Research School (IMPRS) for funding my work and stay in MPI, Halle. I will always be indebted to MPI, Halle for maintaining an international environment in the institute that allowed me to have many fruitful interactions with people from different countries and nationalities.

Lastly, but definitely not the least, I would like to express my love and regards to my parents and my sister. They always have been, and will always be, a pillar of support and a source of inspiration in my life.

## **Eidesstattliche Erklärung**

Hiermit erkläre ich eidesstattlich, dass ich meine Dissertation selbständig und ohne fremde Hilfe verfasst und keine anderen als die von mir angegebenen Quellen und Hilfsmittel zur Erstellung meiner Dissertation verwendet habe. Die wörtlich und inhaltlich entnommenen Stellen habe ich als solche gekennzeichnet und den entnommenen Werken zugeordnet. Die Arbeit ist in vorliegender oder ähnlicher Form bei keiner anderen Prüfungsbehörde zur Erlangung eines Doktorgrades eingereicht worden.

Halle an der Saale, Februar 2014

Akash Bhatnagar